Wrocław University
of Science and Technology

FIELD OF SCIENCE:
NATURAL SCIENCES

DISCIPLINE OF SCIENCE:
CHEMICAL SCIENCES

DOCTORAL DISSERTATION

Synthesis and characterization of lanthanide ions doped materials showing concurrent emission in UV and NIR spectral ranges

Patryk Fałat, MSc Eng

Supervisor:
Dominika M. Wawrzyńczyk, DSc, PhD, Eng
Associate Professor at Wrocław University of Science and Technology

Keywords:
lanthanides, nanoparticles, microcrystals, up-conversion, down-conversion, ultraviolet, visible radiation, near-infrared

WROCŁAW 2025

Acknowledgments

First and foremost, I would like to express my deepest gratitude to my supervisor, **Prof. Dominika Wawrzyńczyk**, for introducing me to the fascinating world of lanthanide-doped materials at the nano- and microscale, and their spectroscopic properties. Your guidance, patience, and scientific creativity shaped my growth throughout these doctoral years. I am especially grateful for the trust you placed in me at the very beginning of this scientific journey.

I would also like to acknowledge the support of the institutions that made this work possible: the **National Science Centre of Poland** for funding the SHENG project (2018/30/Q/ST5/00634), the **Polish National Agency for Academic Exchange (NAWA)** and **the Doctoral School of Wrocław University of Science and Technology** for enabling my research stay at Utrecht University through the *InterDocSchool* program. I am also grateful to the **German Academic Exchange Service (DAAD)** for giving me the opportunity to explore new research ideas in Germany.

A special thank you goes to **Prof. Andries Meijerink** from Utrecht University in the Netherlands for warmly welcoming me into his group and allowing me to work in his optical labs during two short-term research stays in 2023. Your insights into electronic transitions and energy transfer processes between lanthanide ions have been incredibly valuable, and I am grateful for the time and attention you dedicated to my work.

To my colleagues – **Ivy Tsang, Magda Antoniak, Szymon Zelewski, and Piotr Kuich** – thank you for your help, advice, and for making the long hours in the lab easier and more enjoyable. It was great to have your support along the way!

Most importantly, I want to thank the amazing people who have been there for me since the very start — **my family, friends, and the loved one**. Your constant support and belief in me helped me get through everything. This accomplishment is as much yours as it is mine.

And now, finally, when someone asks me “When will you finish writing your PhD?”, I can smile and say — “I already have.”

Abstract (English version)

This doctoral dissertation is focused on synthesis, physicochemical characterization, and validation of potential application of inorganic phosphors, doped with lanthanide ions, particularly Pr^{3+}, Tm^{3+}, Gd^{3+}, Yb^{3+}, and Nd^{3+} ones. These materials, prepared in the form of colloidal nanoparticles (NPs) or microcrystals (MCs) powders were engineered in a way to emit both ultraviolet (UV) and near-infrared (NIR) radiation. The spectral regions of interest are of great importance for biomedical applications due to their utility in non-invasive high-contrast *in vivo* bioimaging, deep-tissue penetration, light-triggered disinfection, or photodynamic therapy. Within the research, I explored various strategies to enhance the luminescent properties of these materials, all aimed at improving the efficiency and versatility for advanced biomedical applications. The materials were synthesized under controlled conditions using thermal decomposition, hydrothermal, and solid-state synthesis methods, tailored to achieve specific size and structure. The characterizations of structure, morphology, and elemental composition were performed using X-ray diffraction (XRD), scanning and transmission electron microscopy (SEM, TEM), and energy-dispersive X-ray spectroscopy (EDS), respectively. Optical properties were investigated with the means of photoluminescence (PL) spectroscopy, with the main focus on emission intensities in UV and NIR regions of radiation, and luminescence lifetimes (LTs) registration.

In particular, I developed and optimized Pr^{3+},Yb^{3+}-co-doped β-$NaYF_4$ NPs and $LiYF_4$ NPs with bimodal optical properties for biomedical use. Under 447 nm excitation, they exhibited intense Visible(Vis)-to-UV up-conversion (UC) luminescence, the resultant UV-C radiation was sufficiently strong to damage double-stranded DNA (dsDNA). On the other hand, their NIR-to-NIR emission, occurring under 980 nm laser excitation and peaking at ca. 1320 nm, enabled effective imaging in an oral-cavity-mimicking model. To further enhance upconverted UV emission, I employed co-doping with another UV-emitting lanthanide ion, i.e., Gd^{3+}, and synthesized core@shell nanostructures. These modifications improved UV-C emission from Pr^{3+} ions and reduced surface quenching, respectively. Transferred into aqueous phase, the materials in the form of suspensions served as effective UV-emitting disinfectants, capable of inactivating human virus species under Vis irradiation. Furthermore, in order to minimize parasitic energy migration processes occurrence, I designed and synthesized core@multi-shell nanostructures in which optically active ions were spatially separated from each other.

This approach enabled the maximization of emission intensity in both the UV and NIR regions, strongly required for theranostic applications. In the next step, I explored Pr^{3+} co-doping in Tm^{3+}-based β-$NaYF_4$ MCs. By utilization of this lanthanide ions pair, I generated the enhanced both UV-C and NIR emissions, compared to solely Tm^{3+}-doped material, due to efficient energy transfer (ET) between ladder-like energy level structure of lanthanide ions. Lastly, I conducted investigation on Pr^{3+}-doped $Y_2Si_2O_7$ crystalline powders for light-triggered antimicrobial applications. The results showed that tuning the optically-active lanthanide dopants improved the efficiency of the material in inactivating widespread bacteria and fungi, simultaneously presenting a safer alternative to conventional UV-based disinfection methods.

The presented research introduces innovative strategies for enhancing luminescence performance of lanthanide-doped colloidal NPs and MCs powders in both UV and NIR spectral regions. Their successful use in proof-of-concept applications – ranging from NIR-guided *in vivo* bioimaging to visible light-induced inactivation of viruses, bacteria, and fungi based on UV emission generation – demonstrates their strong potential for real-world biomedical use.

Abstract (Polish version)

Niniejsza praca doktorska dotyczy syntezy oraz fizykochemicznej charakteryzacji luminoforów nieorganicznych, domieszkowanych jonami lantanowców (w szczególności Pr^{3+}, Tm^{3+}, Gd^{3+}, Yb^{3+} i Nd^{3+}), a także weryfikacji ich skuteczności w potencjalnych zastosowaniach biologicznych. Materiały te, otrzymane w formie koloidalnych nanocząstek lub proszków mikrokryształów, zostały zaprojektowane tak, aby emitować promieniowanie zarówno w zakresie ultrafioletu (UV), jak i bliskiej podczerwieni (NIR). Te zakresy spektralne są niezwykle ważne, jeśli chodzi o zastosowania biomedyczne, ponieważ są wykorzystywane np. w nieinwazyjnym bioobrazowaniu *in vivo*, dezynfekcji promieniowaniem UV oraz terapii fotodynamicznej.

W ramach badań wykorzystano różne strategie mające na celu poprawę właściwości luminescencyjnych otrzymywanych materiałów w zakresach UV i NIR, aby zwiększyć ich efektywność w potencjalnych zastosowaniach biomedycznych. Materiały zostały zsyntetyzowane w kontrolowanych warunkach, przy użyciu takich metod jak termiczny rozkład prekursorów w mieszaninach surfaktantów o wysokiej temperaturze wrzenia, metoda hydrotermalna oraz synteza w stanie stałym. Dzięki nim nanocząstki i mikrokryształy wykazywały pożądane strukturę krystaliczną, morfologię oraz skład chemiczny, co zostało potwierdzone przy pomocy odpowiednio dyfrakcji rentgenowskiej (XRD), mikroskopii elektronowej (SEM, TEM) oraz spektroskopii rentgenowskiej (EDS). Właściwości luminescencyjne zbadano za pomocą spektroskopii fotoluminescencyjnej, koncentrując się na emisji w zakresie UV i NIR oraz pomiarze czasów życia luminescencji.

W ramach badań opracowano i zoptymalizowano serię nanocząstek β-$NaYF_4$:Pr^{3+},Yb^{3+} oraz $LiYF_4$:Pr^{3+},Yb^{3+}, które pod wpływem wzbudzenia falą o długości 447 nm wykazywały intensywną emisję w zakresie UV, będącą skutkiem kombinacyjnej konwersji energii fotonów w górę. Uzyskane promieniowanie z zakresu UV-C było wystarczająco silne, aby uszkodzić podwójne nici DNA. Z kolei klasyczna Stokesowska emisja w zakresie NIR, zachodząca przy wzbudzeniu laserem o długości fali 980 nm i osiągająca maksimum przy około 1320 nm, umożliwiła skuteczne obrazowanie kanału zęba, pokrytego tkanką mięśniową. Następnie, w celu zwiększenia intensywności emisji w UV, zastosowano domieszkowanie innym jonem lantanowca, również emitującym w UV, tj. Gd^{3+}, oraz zsyntetyzowano nanostruktury typu

rdzeń@powłoka. Te modyfikacje w znaczący sposób poprawiły emisję w zakresie UV-C, pochodzącą z jonów Pr^{3+}, oraz ograniczyły występowanie wygaszania luminescencji poprzez oddziaływanie z defektami powierzchniowymi. Po transferze z fazy organicznej do fazy wodnej, materiały te w postaci koloidalnych zawiesin okazały się skutecznymi dezynfektantami emitującymi promieniowanie z zakresu UV pod wpływem promieniowania z zakresu widzialnego, zdolnymi do unieszkodliwiania ludzkich wirusów. Ponadto, aby zminimalizować występowanie niepożądanych procesów migracji energii, zaprojektowano i zsyntetyzowano nanostruktury typu rdzeń z wielowarstwową powłoką, w których optycznie aktywne jony były względem siebie rozdzielone. Takie podejście pozwoliło na maksymalizację intensywności emisji w obu regionach UV i NIR, co jest istotne przy zastosowaniach teranostycznych. Następnie, zbadano mikrokryształy współdomieszkowane $\beta\text{-NaYF}_4\text{:Tm}^{3+}\text{,Pr}^{3+}$. Dzięki połączeniu takiej pary lantanowców uzyskano wzmocnienie emisji zarówno w zakresie UV, jak i NIR, w porównaniu do materiału domieszkowanego jedynie jonami Tm^{3+}, co było skutkiem efektywnego transferu energii pomiędzy poziomami energetycznymi tych jonów. Na koniec przeprowadzono badania krystalicznych proszków $Y_2Si_2O_7$ domieszkowanych jonami Pr^{3+}, które po domieszkowaniu jonami Tm^{3+} oraz Yb^{3+} okazały się być skuteczne w zwalczaniu bakterii oraz grzybów, jednocześnie stanowiąc bezpieczniejszą alternatywę dla konwencjonalnych metod dezynfekcji UV.

Przedstawione badania wprowadzają innowacyjne strategie na zwiększenie intensywności luminescencji koloidalnych nanocząstek oraz mikrokryształów w formie proszków domieszkowanych jonami lantanowców, emitujących w zakresie promieniowania UV i NIR. Ich skuteczne zastosowanie w testach funkcjonalnych, obejmujących m.in. obrazowanie *in vivo* z wykorzystaniem promieniowania NIR oraz unieszkodliwianie wirusów, bakterii i grzybów promieniowaniem UV generowanym pod wpływem promieniowania z zakresu widzialnego, potwierdza ich wysoki potencjał do praktycznych zastosowań biomedycznych.

List of abbreviations

ACT	Activator
ATCC	American Type Culture Collection
C NPs	Core nanoparticles
CFU	Colony forming unit
CPE	Cytopathic effect
CS NPs	Core@shell nanoparticles
CSS NPs	Core@shell@shell nanoparticles
CSSS NPs	Core@shell@shell@shell nanoparticles
CUC	Co-operative up-conversion
CW	Continuous-wave
DC	Down-conversion
DCFDA	2′,7′-dichlorodihydrofluorescein diacetate
DMEM	Dulbecco's Modified Eagle's Medium
DNA	Deoxyribonucleic acid
dsDNA	Double-stranded DNA
EDS	Energy-Dispersive X-ray Spectroscopy
EDTA	Ethylenediaminetetraacetic acid
ESA	Excited state up-conversion
ET	Energy transfer
ETU	Energy transfer up-conversion
FADU	Fluorescence analysis of dsDNA unwinding
FBS	Fetal bovine serum
FT-IR	Fourier transform infrared spectroscopy
HAdV-C5	Human Adenovirus type C serotype 5
HSV-1	Herpes Simplex Virus type 1
ICDD PDF	International Centre for Diffraction Data Powder Diffraction File
ICSD	Inorganic Crystal Structure Database
IR	Infrared region
LED	Light-emitting diode
LT	Luminescence lifetime
MCs	Microcrystals
MCS	Multichannel scaling

MTT	3-(4,5-dimethylthiazol-2-yl)-2,5-diphenyltetrazolium bromide
NIR	Near infrared region
NIR-I	First near-infrared biological window
NIR-II	Second near-infrared biological window
NIR-III	Third near-infrared biological window
NPs	Nanoparticles
PBS	Phosphate buffer saline
PCM	Polish Collection of Microorganisms
PLE	Photoluminescence excitation
PMT	Photomultiplier tube
QC	Quantum cutting
RE^{3+}	Rare-earth ion
RNA	Ribonucleic acid
ROS	Reactive oxygen species
SEM	Scanning electron microscope
SEN	Sensitizer
ssDNA	Single-stranded DNA
SWIR	Short-wave infrared region
TEM	Transmission electron microscope
UC	Up-conversion
UV	Ultraviolet
UV-A	Ultraviolet type A
UV-B	Ultraviolet type B
UV-C	Ultraviolet type C
Vis	Visible
WHO	World Health Organization
XRD	X-ray diffraction

List of symbols

$\vec{E}$	Electric field
$\vec{M}$	Magnetic field
$\vec{v}$	Velocity
A	Absorbance
a.u.	Arbitrary unit
c	Speed of light in vacuum
c_{dsDNA}	dsDNA concentration
d	Interplanar spacing of the crystal lattice
E_1, E_2, E_1', E_2', …	Following excited energy state of a lanthanide ion
G, G’	Ground state of a lanthanide ion
$h\nu$	Quantum of light
$\hbar\omega$	Phonon cut-off energy
I_{int}	Integrated intensity
kbp	Kilobase pairs
l	Optical path length
n	Order of diffraction
ε	Molar absorption coefficient
θ	Bragg angle
λ	Wavelength
λ_{em}	Emission wavelength
λ_{ex}	Excitation wavelength
τ	Luminescence lifetime value
τ_1	Short component of luminescence lifetime
τ_2	Long component of luminescence lifetime

Table of content

Chapter 1

Introduction

1.1. Problem statement and objectives

The field of lanthanide-doped inorganic phosphors has experienced significant advances over the last few decades, with the strong focus on the development of nano- and microcrystalline materials. Thanks to their small size, they have shown great potential for a variety of applications, particularly in biomedical and technological fields. Despite these advances, challenges remain – particularly in achieving high-intensity emission in ultraviolet (UV) and near-infrared (NIR) spectral ranges. These limitations still prevent the materials from being used efficiently in real-life applications, including *in vivo* bioimaging, photodynamic therapy, and light-triggered disinfection. As a result, the core of ongoing research is the design and synthesis of materials capable of efficient emission in both regions of interest.

Within the presented doctoral dissertation, I focus on the development and fabrication of lanthanide-doped nanoparticles (NPs) and microcrystals (MCs), along with a detailed investigation of their luminescent properties in UV and NIR spectral ranges. My main goal is to explore how different co-doping ions and adjustments to the size, structure, and architecture of these materials can enhance the efficiency of both Stokes (down-conversion, DC) and anti-Stokes (up-conversion, UC) emissions. Furthermore, some of the materials are tested in proof-of-concept experiments, demonstrating their potential for use in real-life biomedical applications. The specific aims of the doctoral dissertation include:

- development of lanthanide-doped colloidal NPs which can be utilized as bimodal optical nanoplatforms for theranostic purposes, since they are capable to emit concurrently in UV and NIR spectral regions;
- design and implementation of a proof-of-concept experiment allowing me to demonstrate both qualitatively and quantitatively the ability of the upconverted UV radiation emitted by the manufactured materials to degrade double-stranded DNA (dsDNA);
- design of a proof-of-concept experiment demonstrating the potential of the synthesized materials for *in vivo* bioimaging;

- experimental exploration of various strategies to enhance the up-converted UV emission materials at the nano- and microscale for light-triggered eradication of human virus species;
- implementation of organic-to-aqueous phase transfer of the oleic-acid-capped NPs for light-triggered eradication of human virus species;
- design and fabrication of complex core@multi-shell NPs to engineer the spatial distribution of dopants within distinct layers of a single NP to enhance emission in divergent spectral regions, simultaneously minimizing quenching effects;
- synthesis of lanthanide-co-doped inorganic phosphors in the form of crystalline powders to get a better insight into photon management processes leading to the concurrent emission enhancement in UV and NIR spectral ranges upon Visible (Vis) laser excitation;
- engineering of the upconverted UV emission output by manufacturing triply-lanthanide-co-doped powders and their performance validation in light-triggered germicidal action against commonly known bacteria and fungi as plankton suspensions and biofilms.

In the presented doctoral dissertation, I do not only focus on the synthesis and optical characterization of these lanthanide-doped materials, but I also highlight the strategies utilized to tailor their luminescence behavior for specific applications, such as simultaneous light-triggered therapy and *in vivo* bioimaging within UV and NIR spectral ranges, respectively. The research I present here aims to contribute to the growing field of multifunctional inorganic lanthanide-based colloidal NPs and MCs as well as powders, and their potential use in biomedical applications, in which their ability to convert lower-energy light into higher-energy emissions can significantly enhance the sensitivity and effectiveness of diagnostic and therapeutic tools.

1.2. Dissertation overview

This doctoral dissertation is organized into nine chapters. In **Chapter 2,** I acquaint the Reader with the current state of the knowledge in physicochemical properties of lanthanide-doped materials. I mainly describe light-matter interactions within the ladder-like energy level structure of lanthanides, focusing on the importance of the UV and NIR spectral ranges for biological applications. I also briefly describe how the choice of host matrix and its form (i.e., as colloidal NPs or MCs powders) can influence on the spectroscopic behavior of the material. **Chapter 3** outlines various synthesis methods, leading to NPs (thermal decomposition reaction of precursors in high-boiling-point surfactants), MCs (microwave-assisted hydrothermal synthesis and solid-state synthesis), and powders formation (sol-gel method). Moreover, I briefly describe the characterization methods of the manufactured lanthanide-doped materials, with the particular focus on structural analysis and spectroscopic features investigation. In **Chapter 4,** I synthesize and investigate Pr^{3+},Yb^{3+}-co-doped β-$NaYF_4$ and $LiYF_4$ NPs for their bimodal optical potential in theranostics, including UV-C disinfection and NIR *in vivo* bioimaging. I present results of the proof-of-concept experiments, demonstrating their ability to exhibit both functions effectively under appropriate excitation. **Chapter 5** is devoted to strategies leading to the up-converted UV-C emission enhancement of Pr^{3+}-based β-$NaYF_4$ and $LiYF_4$ NPs (i.e., passivation of the optically active core with the optically inert shell or co-doping with another type of lanthanide ions, i.e., Gd^{3+}), optimizing them for light-triggered disinfection. In this chapter, I highlight the successful utilization of these materials in inactivating common human viruses (adenovirus and herpes simplex virus), which supports their prospective utilization for biomedical applications. In **Chapter 6**, I present the careful engineering of complex core@multi-shell β-$NaYF_4$ nanoarchitectures. Within this chapter I examine the enhancement of emission in both UV and NIR spectral ranges for theranostic purposes, particularly for medical treatment and *in vivo* bioimaging, accordingly. In **Chapter 7**, I explore how co-doping Tm^{3+}-based β-$NaYF_4$ MCs with Pr^{3+} ions improves their luminescence properties. The improved performance is linked to the efficient energy transfer between the dopants, offering a promising approach for tuning optical output in materials designed for light-triggered disinfection and *in vivo* bioimaging. In **Chapter 8**, I explore Pr^{3+}-doped $Y_2Si_2O_7$ crystalline powders for light-triggered antimicrobial applications, harnessing both Vis-to-UV and NIR-to-UV UC. By varying the optically active lanthanide dopants, I show that the UV emission output can be tuned, significantly enhancing the effectiveness of the material against bacterial and fungal pathogens and offering a safer alternative to conventional UV-based disinfection methods. Finally, **Chapter 9** summarizes the main findings of this doctoral dissertation and outlines potential future directions in the field of lanthanide-doped inorganic phosphors. It emphasizes how the materials developed throughout the conducted research could contribute to advancing multifunctional platforms for theranostic applications, particularly in the areas of targeted bioimaging and light-activated therapy.

Chapter 2

Theoretical framework

The optical behavior of lanthanide-doped materials is strongly governed by fundamental principles of light-matter interactions. To deeply analyze their luminescence properties, it is thus essential to understand the electromagnetic spectrum as the light of specific wavelengths interacts with their ladder-like energy level structure. Particular attention within the framework of this doctoral dissertation must be given to the UV and NIR regions as photons within these spectral ranges can be of critical importance for bio-related applications, such as light-based disinfection, cancer treatment, and deep-tissue imaging.

Since lanthanide ions cannot exist freely as solid materials due to the charge conservation principle, they must be incorporated as doping ions into crystalline host matrices. The careful selection of hosts, preferably those with low phonon energy in their crystal lattice, is crucial to minimize non-radiative energy losses and optimize photoluminescence (PL) intensity. Furthermore, lanthanide ions, doped within the selected materials, facilitate various photon management processes, including ET, UC, and DC, by absorbing and emitting photons across different energy levels. In addition to the choice of host material, the physical dimensions of the material significantly influence its luminescence performance. NPs and MCs, in form of colloids or powders, exhibit variations in surface related effects, energy migration processes available, and defect states, all of which impact the overall emission characteristics.

This chapter introduces the key concepts necessary for the scope of this research, focusing on the luminescent features of lanthanide-doped materials. It familiarizes the Reader with the fundamental principles discussed above and provides a solid foundation for the experimental investigations presented in the following chapters of the doctoral dissertation.

2.1. Electromagnetic spectrum

Electromagnetic radiation is defined as the oscillating electric ($\vec{E}$) and magnetic ($\vec{M}$) fields that are perpendicularly aligned to each other as well as to the direction of their propagation, indicated as $\vec{v}$ in Fig. 1 [1]. As a consequence, electromagnetic waves are formed, which consist of photons, massless and chargeless particles exhibiting corpuscular-wave duality. Phenomena such as interference and diffraction support the wave hypothesis, whereas the photoelectric and Compton effects demonstrate the particle nature of light quanta. In vacuum, such waves travel at the speed of light ($c \approx 3 \cdot 10^8$ m s^{-1}) and are capable to undergo reflection, refraction, and diffraction phenomena [1,2].

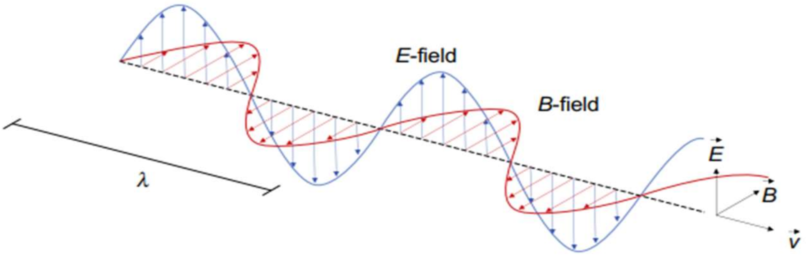

Fig. 1. The graphical representation of an electromagnetic wave (reprinted with the permission from reference no. [2], Copyright © 2017 Elsevier Ltd)

When electromagnetic waves are classified with respect to wavelengths (λ), understood as the distance between two repeating points in a wave, the formed sequence is named as electromagnetic spectrum (Fig. 2). Even though it spans roughly 15 orders of magnitude and is continuous with no sharp boundaries, several radiation ranges can be distinguished. Each of them has unique properties, including the way of generation and its interaction with matter [1]. Understanding these processes allows for developing novel materials and technologically advanced devices that can harness and process electromagnetic waves.

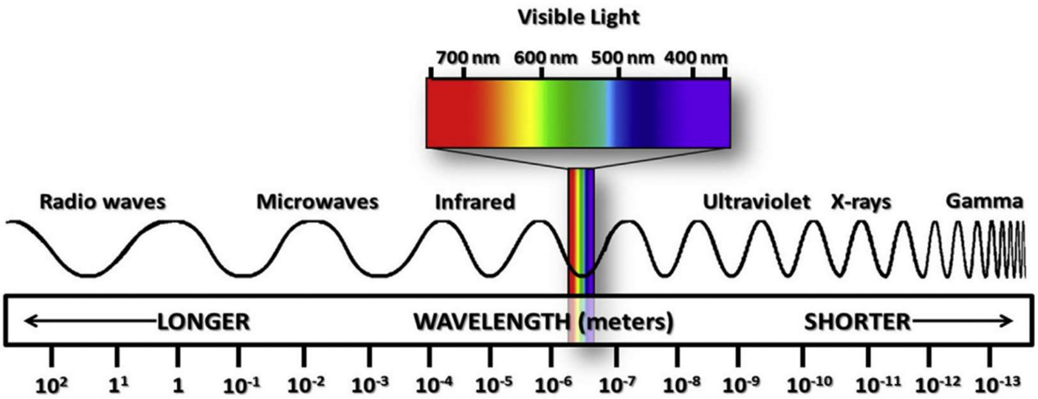

Fig. 2. Electromagnetic waves spectrum (reprinted with permission from reference no. [3], Copyright © 2019 Elsevier Inc)

The ability to generate and control radiation of specific wavelengths has led to the development of innovative solutions, e.g., in spectroscopy, remote sensing, and quantum computing. Research into the influence of electromagnetic waves on biological systems has also opened new possibilities for medical treatment and diagnostics. As provided in the doctoral dissertation, prospective applications of radiation-emitting materials can still emerge, simultaneously demonstrating the importance of the light-matter interactions in modern science and state-of-the-art technology.

Since the presented research focuses on the UV and NIR spectral regions, their brief overview is provided to familiarize the Reader with their relevance in the field.

2.1.1. Ultraviolet (UV)

UV radiation is the part of the electromagnetic spectrum spanning between 100÷400 nm. The photons associated with this spectral range are of high enough energy, which is sufficient to induce electron transitions in high-bandgap semiconductors or in organic dye molecule, resulting in charge separation or fluorescence [4,5]. In terms of biology, UV radiation is known to strongly interact and potentially damage biological soft matter, like nucleic acids, proteins or membrane cells. However, since it is robustly emitted by the Sun, it has also been proven to have a beneficial impact on human health due to mediation of vitamin D and endorphins synthesis in human body [6,7].

Within the UV spectral range, one can distinguish three sub-regions, namely UV-A (320÷400 nm), UV-B (280÷320 nm), and UV-C (100÷280 nm) (Fig. 3). Each of them has its own key properties, thus they exhibit different effects on biological tissues [8]. Understanding these mechanisms is important for the development of new materials for light-triggered disinfection or prospective *in vivo* cancer treatment.

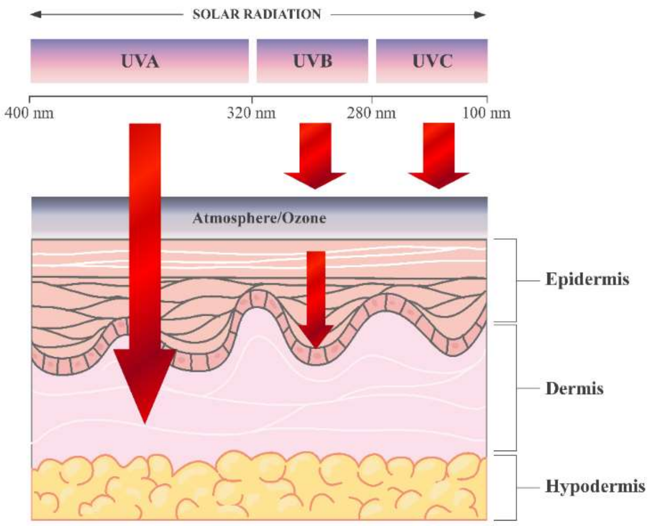

Fig. 3. UV penetration into the layers of the skin (reprinted from the reference no. [6] under Creative Commons Attribution (CC BY) license)

UV-A radiation constitutes around 95% of the UV rays passing through the Earth's atmosphere and reaching its surface. Spanning between 315÷400 nm, it is the least energetic type of UV radiation. However, it penetrates through human skin up to 1 mm, causing long-term damage of dermis, associated with premature aging and risk of melanoma development [9]. In bacteria, fungi, and viruses, UV-A photons sensitize endogenous protoporphyrins, leading to the oxidative stress increase, by generating reactive oxygen species (ROS) such as free radicals and H_2O_2, and damage deoxyribonucleic acid (DNA) or ribonucleic acid (RNA), proteins, and lipids [10,11].

On the contrary, roughly 5% of the UV radiation emitted by the Sun and reaching the Earth is UV-B (280÷320 nm), primarily due to strong absorption by the ozone layer and scattering by atmospheric particles (Fig. 3). UV-B photons barely penetrate human tissues, however, the prolonged exposure can lead to severe sunburns [12]. Although only a small portion of UV-B traverses epidermis, its photons have higher energy compared to UV-A, which allows them to directly damage nucleic acids at the cellular level. The degradation occurs through the formation of mutagenic photolesions, such as thymine or uracil dimers and 6-4 photoproducts [13].

Among all UV subregions, UV-C (100÷280 nm) is the most energetic, but is largely absorbed by the ozone layer (Fig. 3), which limits its direct impact on living organisms on Earth. UV-C photons do not only disrupt microbial DNA and RNA, preventing cell replication, but can also destroy cell walls and membranes, ultimately leading to death of cells [14]. Therefore, it can be utilized for localized cancer treatment. Besides that, it is the most effective UV radiation type for disinfection purposes, since it kills a broad range of pathogens, including antibiotic-resistant bacteria, viruses, and fungal spores. Due to severe health hazards, artificial sources of UV-C, such as high-power lamps or light-emitting diodes (LEDs), are only used for disinfection when no one is in the irradiated area. Beyond healthcare, UV-C is also used in water purification, air sterilization, and food processing to ensure microbial safety [15–17].

2.1.2. Near-infrared (NIR) radiation

NIR radiation refers to electromagnetic waves with wavelengths spanning between 700÷2500 nm, which are not visible to humans. Compared to UV, NIR is easier to generate as laser radiation, making it an ideal source for modern technologies. It is commonly utilized in spectroscopy, imaging, and optical communication due to its ability to penetrate various materials while minimizing scattering and absorption losses [18]. Many organic and inorganic compounds exhibit characteristic vibrational overtones in the NIR region, which makes this radiation applicable for chemical identification and analysis [19]. Unlike ionizing types of radiation such as gamma rays or X-rays, NIR does not cause molecular damage. Therefore, it is suitable for biomedical applications, e.g., tissue oxygenation monitoring [20]. In telecommunications, NIR wavelengths are preferred due to minimal signal attenuation in silica-based fibers. Additionally, they are extensively applied in remote sensing, night vision technology, and real-time industrial process monitoring [21].

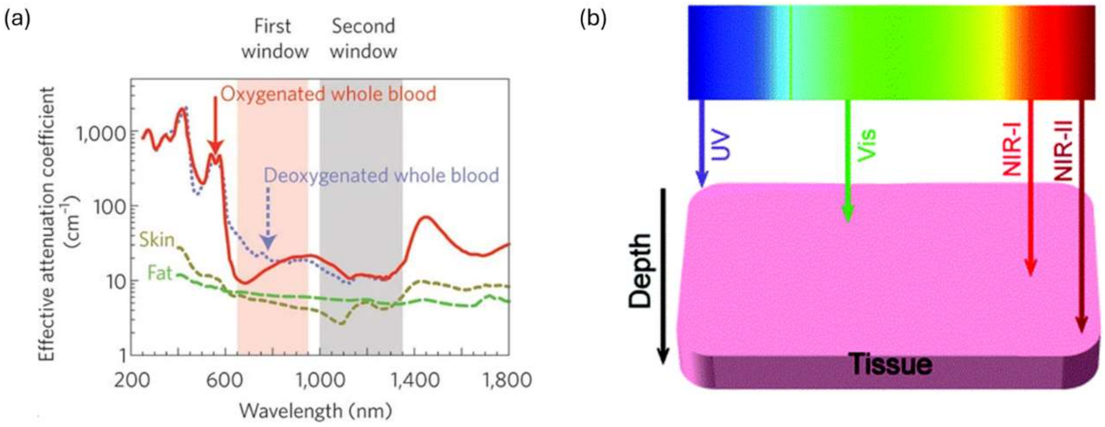

Fig. 4. (a) Effective attenuation coefficients plotted against wavelength for oxygenated blood, deoxygenated blood, skin, and fat with marked areas for the first (in pink) and second (in grey) window of biological tissue transparency, (reprinted with the permission from reference no. [22], Copyright © 1969, Springer Nature Limited), (b) A scheme presenting the penetration depth of UV, Vis, NIR-I, and NIR-II radiation within a human tissue (reprinted with the permission from reference no. [23], Copyright © 2013, Royal Society of Chemistry)

Within the NIR spectrum, three interesting subtypes can be distinguished: NIR-I (700÷1000 nm), NIR-II (1000÷1400 nm), and NIR-III (1500÷1800 nm). They partially overlap with the so-called first, second, and third optical transmission windows of biological tissues, respectively. This means that waves within these spectral ranges can deeply penetrate complex biological tissues as the effective attenuation coefficients for deoxygenated and oxygenated whole blood, fat, and skin reach their minima (*vide* Fig. 4a) [22]. NIR is only weakly absorbed by water, the major component of biological tissues, which further enhances its penetration depth [24]. Moreover, NIR-affected live cells experience minimal photodamage. Due to these properties, light from NIR-I, NIR-II, and NIR-III wavelength regions are widely employed in bio-related applications, such as *in vivo* material excitation and high-contrast bioimaging, which are particularly relevant to this doctoral dissertation [25]. However, due to increased scattering and potential autofluorescence from flesh, bones, and body fluids, NIR-I exhibits a more limited penetration depth in living organisms compared to NIR-II and NIR-III radiation types (Fig. 4b) [23]. NIR-II, operating within the second window of biological tissue transparency, is particularly advantageous for *in vivo* bioimaging as it provides significantly enhanced spatial image resolution and signal-to-noise ratios. This enables superior visualization of blood vessels, tumors, and tissues up to several millimeters deep [18]. Furthermore, NIR-II time-gated imaging techniques are commonly applied to suppress autofluorescence, thereby increasing the contrast of captured images [26,27].

2.2. Lanthanide ions

The lanthanide series (also referred as rare-earth metals) is a set of 15 elements with atomic numbers ranging from 57 (lanthanum, La) to 71 (lutetium, Lu), which are located in the f block of the periodic table of elements (Fig. 5). They are characterized by the progressive filling of the 4f orbitals, which are shielded from external interactions by the 5s and 5p electrons, making the 4f electrons relatively inert in chemical reactions. The +3 oxidation state dominates for the majority of rare-earth ions (RE^{3+}) in compounds [28].

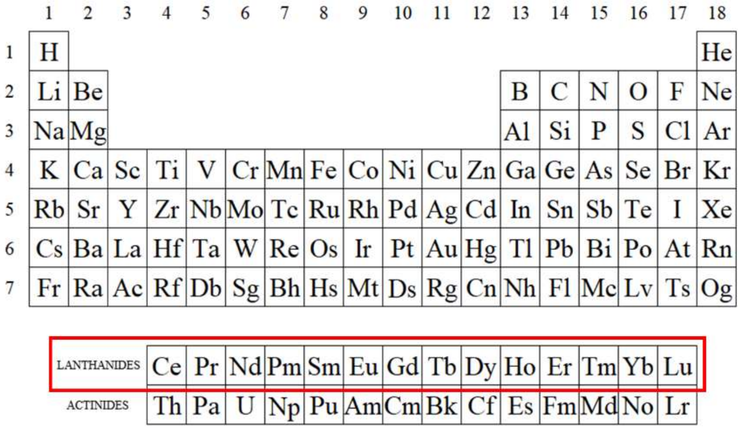

Fig. 5. The periodic table of elements with lanthanides highlighted in red

Consequently, lanthanides exhibit unique physical and chemical properties that are invaluable for advances in technology, e.g., manufacturing of artificial light sources of tunable power density [29]. The photoluminescent properties of lanthanides result from the intrashell f-f transitions, which are generally forbidden by the Laporte parity selection rules stating that electric dipole transitions cannot occur between states of the same parity [30]. However, mixing of opposite-parity configurations can weaken those selection rules, allowing for otherwise forbidden electric dipole transitions. In an asymmetric crystal field, the probability of these transitions increases significantly. Hence, modifying the crystal structure to lower symmetry around lanthanide ions can enhance luminescence emission intensity [31].

The reduced perturbation by the host crystal field implies that lanthanide ions in crystals have 4f electronic states that are relatively discrete and differ little from those of the same ions in vacuum. Therefore, the approximate 4f excited state positions of rare earth ions in any material can be foreseen with help of the Dieke diagram (Fig. 6) [28,32,33]. It was created in the 1950s by G.H. Dieke to organize the vast amount of spectroscopic data collected up to date, and nowadays serves as an important tool to understand the robust ladder-like energy level structure of trivalent lanthanide ions and to predict absorption and emission transitions within and between lanthanides. Thanks to their unique physical character, lanthanide ions are also named as photon managers, as they enable engineered control and manipulation of the number of excitation to emission photons ratio. In fact, rare-earth-doped materials can be used as efficient converters of excitation light into PL at almost any desired wavelength [34].

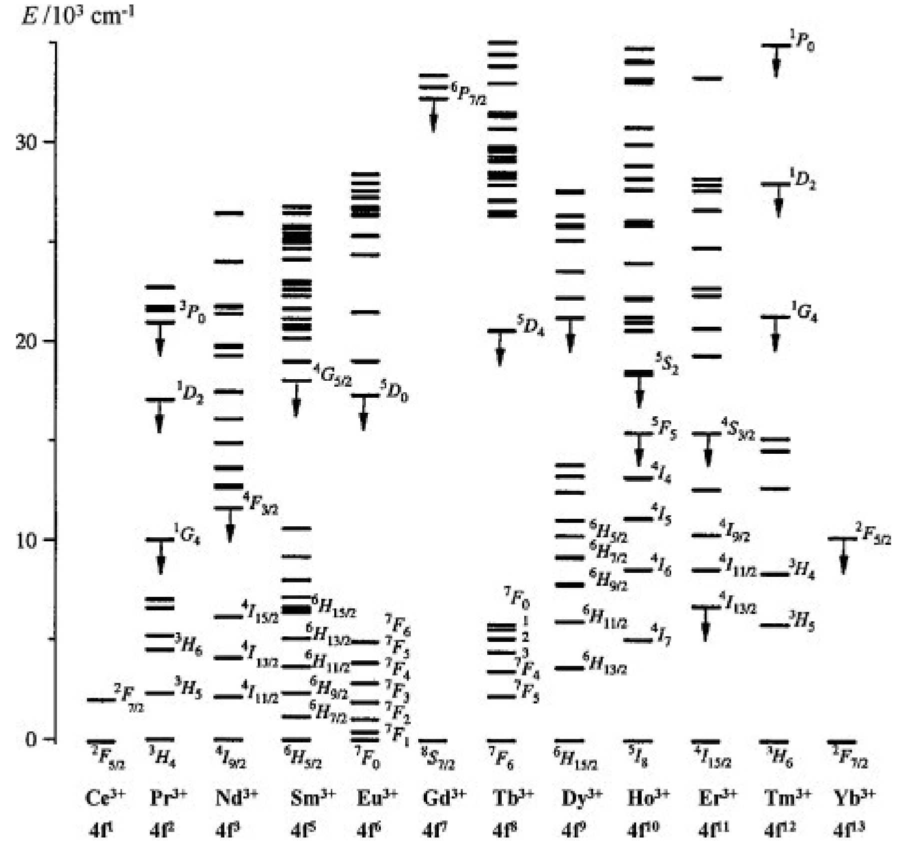

Fig. 6. Dieke diagram showing 4f energy levels of the trivalent lanthanide ions (reprinted with the permission from reference no. [32], Copyright © 2011 Elsevier B.V.)

2.3. Photon management processes in lanthanide ions

As provided in the Dieke diagram in Fig. 6, lanthanide ions exhibit ladder-like structure of well-defined energy levels. Since they are only to small extent influenced by the surrounding matrix, fine-tuning of their emission wavelength is challenging. Besides, they demonstrate intraconfigurational transitions with low extinction coefficients, around 1 M^{-1} cm^{-1}, and narrow bandwidths [27,35]. On the other hand, the difference in position and narrow character of absorption bands between various lanthanide ions makes it challenging to effectively excite multiple activators with a use of single wavelength.

However, some of rare-earth ions are characterized with long luminescence lifetimes (LTs), usually measured in the μs or ms range [36]. Therefore, they are ideal candidates for the realization of various photon management processes, allowing for manipulation with the spectral properties of incident photons. The Reader of the presented dissertation becomes acquainted with three major processes – energy transfer (ET), photon up-conversion (UC), and down-conversion (DC) – which are highly important within the research scope. Their simplified mechanisms were presented in Fig. 7a-c, respectively, where G stands for the ground state of RE^{3+} ions, whereas E_1 and E_2 for their following excited states. The efficiency of photon management processes in lanthanide-doped systems can be fine-tuned mainly by the careful selection of dopants type, and their concentrations optimization, with an additional quite weaker effect of host matrices.

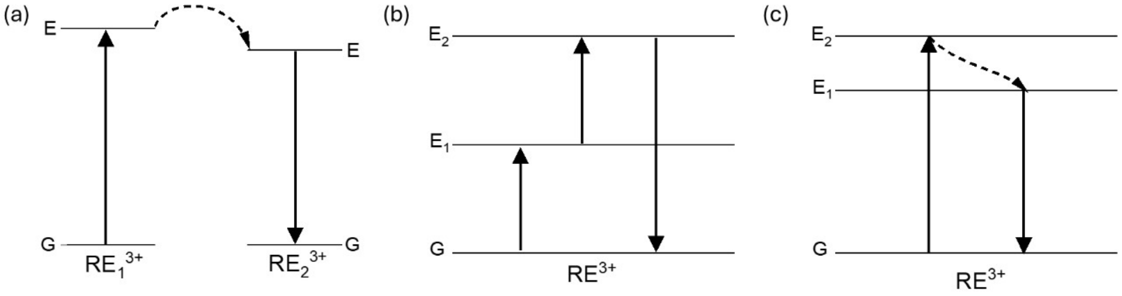

Fig. 7. The schematic representation of photon management processes within the ladder-like energy level structure of lanthanide ions (RE^{3+}, RE_1^{3+}, and RE_2^{3+}): (a) ET, (b) UC, (c) DC. G stands for the ground state of RE^{3+} ions, whereas E_1, E_2 for their following excited states. Full arrows represent radiative processes whereas the dashed represent non-radiative ones

2.3.1. Energy transfer (ET) between lanthanide ions

ET processes occur in a system where absorption and emission happen in separate lanthanide ions, with some energy levels in their electronic structures overlapping.

In this situation, a sensitizer (SEN) absorbs incident photons and radiatively or non-radiatively transfers the associated energy to an emitting lanthanide ion, i.e., an activator (ACT). The process is dependent on the distance between ions in the host matrix, with ET becoming less probable as the ions are further apart [37]. Consequently, certain lanthanide ions are able to emit radiation even when the excitation energy does not precisely correspond to their electronic transitions [36,38].

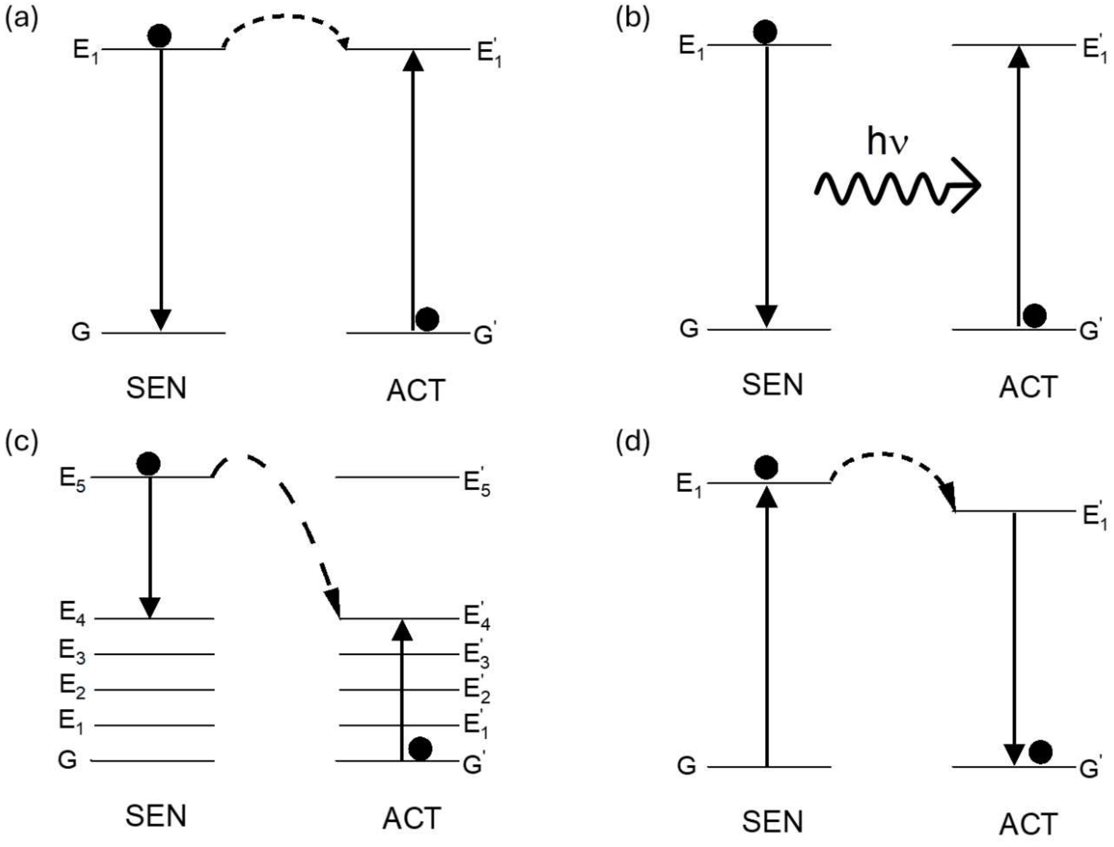

Fig. 8. ET processes between two lanthanide ions: (a) resonant non-radiative transfer, (b) resonant radiative transfer; (c) cross-relaxation; (d) phonon-assisted non-radiative transfer. G stands for the ground state of RE^{3+} ions, whereas E_1, E_2,... – for their following excited states. All ACT energy levels were additionally denoted with an apostrophe. Doubled arrows symbolize the Coulombic interaction (adapted based on: [39])

One can distinguish four following ET processes: resonant non-radiative ET, resonant radiative ET, cross-relaxation (CR), and phonon-assisted non-radiative ET, for which simplified schemes were presented in Fig. 8a-d. Resonant non-radiative ET (Fig. 8a) involves direct energy exchange between SEN and ACT without photon emission. The distance between lanthanide ions participating in resonant non-radiative ET is usually 1÷3 nm, since the spectral overlap is required [34]. It strongly depends on SEN and ACT concentration and their spatial distribution in the investigated material. On the contrary, resonant radiative ET (Fig. 8b) happens as SEN ions emit photons from E_1 energy level, which are then absorbed by ACT ions, being in their G' state. The process occurs between SEN and ACT located close to each other, but the distance can reach up to a few µm [34]. Interestingly, non-radiative ET can also contribute to concentration quenching through CR (Fig. 8c). The excited ions exchange the energy with the neighbor ions in their G' state, which can have either beneficial or negative impact on emission intensity, depending on the electronic transitions involved. It happens particularly when identical ions are incorporated into host matrix at high concentration, i.e., SEN and ACT are the same rare-earth ion. Lastly, phonon-assisted non-radiative ET (Fig. 8d) occurs when energy is transferred through phonon interactions, facilitating transitions between energy levels in the presence of vibrational modes [39].

By careful selection of lanthanide dopants, their concentration and spatial distribution in the chosen host matrix, one can optimize ET mechanisms, which eventually assure the emission peaking at a specific wavelength as intense as possible.

2.3.2. Photon up-conversion (UC)

Photon up-conversion (UC) is an optical process in which two or more low-energy photons are sequentially absorbed within ladder-like energy level structure of lanthanide ions, resulting in one higher energy photon emission. Such an anti-Stokes process was first theoretically predicted by N. Bloembergen in 1959 and experimentally confirmed in 1966 by F. Auzel in Er^{3+},Yb^{3+}- and Tm^{3+},Yb^{3+}-co-doped materials [40,41]. Initially, research was focused on bulk glass or crystalline materials until the late 1990s, when nanotechnology became popular worldwide [36].

The UC strongly relies on intermediate excited energy levels of rare-earth ions, which should exhibit sufficiently long luminescence LTs to facilitate the sequential absorption of the following photon. The ability of the optically active ion(s) to sequentially absorb photons or accept energy through intermediate states is critical as it allows for the capture of multiple photons over a longer timescale. Since the energy can be step-wisely accumulated in the ions, light sources of moderate intensities, e.g., unfocused continuous wave (CW), cheap, and widely available laser diodes, can be used for excitation. For that reason, UC is pronounced as a more efficient process of photon energy conversion, compared to second harmonic generation or two-photon absorption, a third-order nonlinear process requiring extremely high photon flux, e.g., emitted by high power, expensive amplified femtosecond laser sources, since non-stationary quantum mechanical states are involved, through which probability of simultaneous two-photon absorption is extremely low [36].

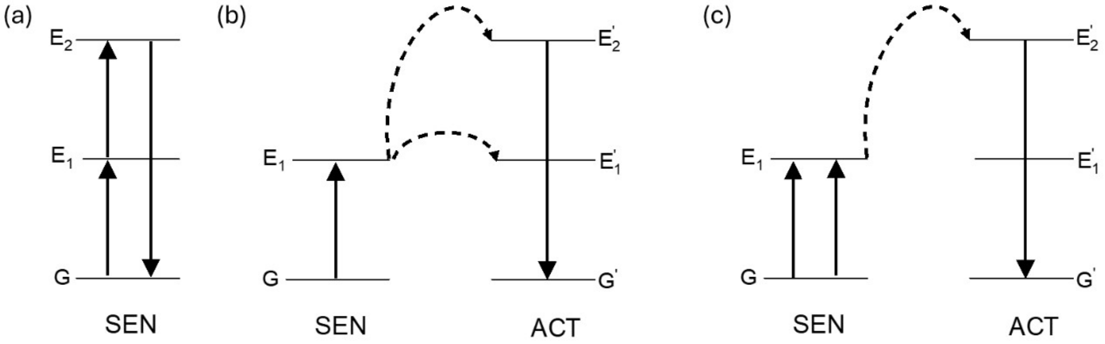

Fig. 9. The schematic representation of UC mechanisms: (a) excited state absorption (ESA), (b) energy transfer UC (ETU), (c) cooperative UC (CUC). All ACT energy levels were additionally denoted with an apostrophe. Adapted based on: [42]

In general, there have been three major UC mechanisms identified experimentally (Fig. 9a-c), each of them involving the sequential absorption of at least two excitation photons, followed by the emission of one photon of higher energy. Additionally, these processes are shown to occur independently or in combination. Excited state absorption (ESA, Fig. 9a), one of the least efficient UC mechanisms, relies on sequential photon absorption by a single ion. When the energy of incident photons matches the energy gap between G and E_1 states, an electron is promoted to E_1. The sufficiently long LT of E_1, along with an energy match between the photons and a higher excited state (E_2), allows the lanthanide ion to absorb another photon. Upon radiative relaxation back to G, the excited lanthanide ion emits a photon of higher energy (shorter wavelength) than those absorbed. On the other hand, energy transfer UC (ETU, Fig. 9b), also named by F. Auzel as *addition de photon par transferts d'energie*, is the most effective and widely used UC mechanism, with the efficiency up to two orders of magnitude higher than ESA. It follows the same principles as ESA, but differs by involving non-radiative ET between neighboring ions. In ETU, both SEN and ACT ions initially occupy their ground states (i.e., G and G′ respectively). SEN absorbs a photon and is excited to E_1. ET from E_1 state of SEN to G' state of ACT promotes ACT to its E_1' state. To enable sequential ET, the E_1 and E_1' states in both SEN and ACT must possess sufficiently long LTs. The second photon absorbed by SEN excites it again to E_1, followed by ET to ACT (E_1' state), promoting it to a higher excited state (E_2'). This ET occurs through dipole-dipole interactions and depends on the overlap of the ions' electric fields. If the energy levels align, direct ET occurs, otherwise, phonon-assisted ET is needed. Interestingly, a related mechanism – cooperative sensitization UC (CSU, Fig. 9c) – also involves the absorption of multiple photons by two or more SEN ions, but instead of sequential ET, energy is cooperatively exchanged between SEN ions to directly excite the ACT to a higher excited state, resulting in UC emission.

Despite significant progress in engineering of up-converting materials, several challenges still remain in generating sufficiently bright radiation at desired wavelengths. One of them is non-radiative energy loss in host matrices, thereby diminishing UC efficiency. To mitigate it, low-phonon-energy hosts should be chosen as they facilitate the process (more details are provided in Section 2.4). Additionally, if lanthanide ions are incorporated into the host matrix at excessively high concentrations, ET can occur between neighboring ions, leading to partial energy loss. Consequently, concentration quenching reduces the intensity of up-converted radiation [37]. Interestingly, sequential two-photon absorption presents less of a hindrance compared to multiple-photon absorption. The total probability for two Vis photons UC into one UV photon is higher than for the UC of three or more NIR photons [43]. To address all of these challenges, researchers optimize lanthanide ions concentrations and synthesize various sophisticated structures, sometimes preceded by *in silico* calculations through machine learning approach [44].

2.3.3. Down-conversion (DC)

In contrast to UC, down-conversion (DC), commonly referred to as standard PL, is a Stokes-shifted process in which a high-energy photon is absorbed and re-emitted as a lower-energy photon. This energy loss occurs due to non-radiative relaxations and ET processes within the ladder-like energy level structure of lanthanide ions. Importantly, the number of emitted photons remains unchanged relative to the number of absorbed photons. This inherent one-to-one photon process limits the overall energy efficiency to values below 100%. The phenomenon has been employed for optoelectronic solutions, e.g., solid-state lighting technologies, display manufacturing, and phosphor-based coatings for efficient UV-to-Vis conversion [45].

Interestingly, quantum cutting (QC) can be considered as a special type of DC. This process allows a single absorbed photon to be split into two or more photons of lower energy through sequential ET or cascade emission, which may lead to quantum yield exceeding 100% [46–48]. Consequently, it is particularly useful for improving the efficiency of solar cells as photons from the UV or Vis spectral ranges can be converted into multiple NIR photons, which better match the absorption band of silicon solar cells, thus improving overall power conversion efficiency.

Similarly to the UC process, both DC and QC efficiencies depend on the choice of host matrix. Researchers strive to optimize the concentration of optically active ions in synthesized materials to balance luminescence efficiency and quenching effect. For solving the challenge, machine learning is more and more eagerly employed. It helps predict the most efficient dopant-host combinations and ET pathways.

2.3.4. Electronic transitions investigated in the doctoral dissertation

As mentioned above in Sections 2.3.1-2.3.3, lanthanide ions undergo specific electronic transitions that are fundamental for luminescent properties of the synthesized doped materials. They are usually summarized in a form of graphs, as transitions within the ladder-like energy level structure of the investigated ions. Therefore, for the better clarity of the doctoral dissertation, I collected the energy level structures of all lanthanide ions that I will discuss within the dissertation, i.e., Pr^{3+}, Tm^{3+}, Gd^{3+}, Yb^{3+}, and Nd^{3+} (*vide* Fig. 10). These graphical interpretations will be utilized to explain to the Reader various processes leading to Stokes and anti-Stokes emissions from particular lanthanide ions.

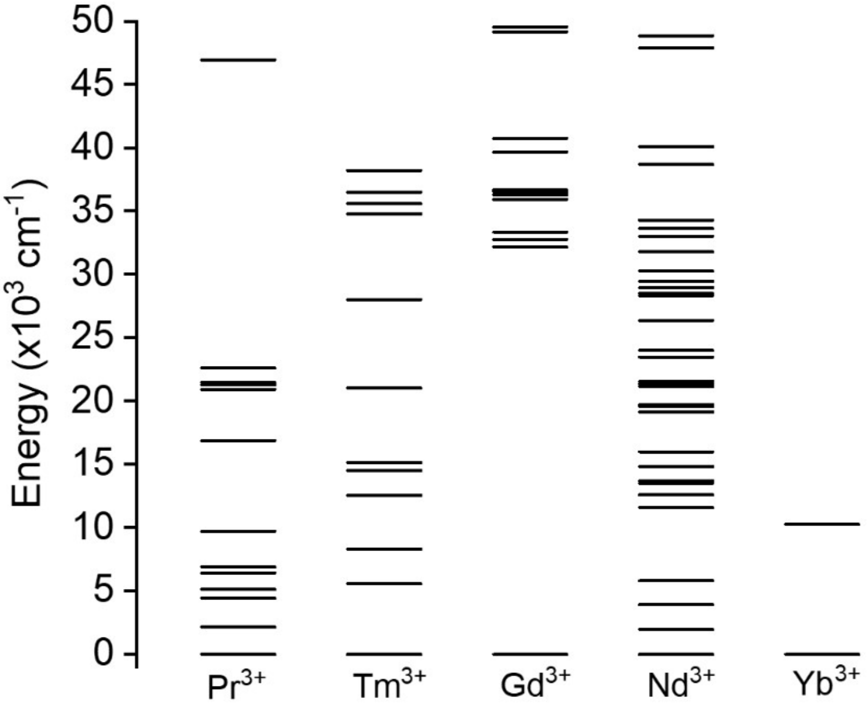

Fig. 10. Energy levels diagrams for Pr^{3+},Tm^{3+}, Gd^{3+}, Nd^{3+}, and Yb^{3+} – lanthanide ions utilized in this doctoral dissertation (adapted based on: [49])

Moreover, to clarify the origin and interpretation of all registered excitation and emission spectra, in each experimental chapter I prepared detailed energy level diagrams of the investigated lanthanide ions, indicating both intra- and inter-level transitions leading to the observed emission lines in UV, Vis, and NIR spectral ranges.

2.4. Host matrices

Due to the charge conservation principle, the overall charge of cations must be balanced with the charge of anions. Therefore, lanthanide dopants in the ionic form cannot exist on their own and there is a strong need to incorporate them into host matrices – crystalline or vitreous ones. Hosts can also modify the intensity of optical transitions within ladder-like energy level structure of lanthanide ions through lattice vibrations of small magnitude – i.e., phonons. Therefore, to understand the optical behavior of rare-earth ions in solid-state hosts in more detail, the Judd-Ofelt theory was proposed in the 1960s [50,51]. It provides insight into how the local environment around the ion influences the probability of f–f electronic transitions, which makes the theory particularly useful when designing host lattices for efficient radiation emission. Materials with lower symmetry and appropriate ligand fields can enhance specific transitions, thus improving luminescent performance [52].

For biological applications, the considered host matrices for lanthanide ions incorporation should exhibit long-term chemical stability to withstand aqueous conditions as well as sufficiently low phonon energies and/or ability to alter crystal lattice field to ensure high luminescence efficiency. Since fluoride and silicate materials doped with lanthanide ions have been widely studied in terms of their unique optical properties for real-life applications, I decided to exploit them in my research, thus I describe them briefly in the following sections.

2.4.1. Alkali-metal-based yttrium fluorides

In the literature, alkali-metal-based yttrium fluorides (AYF_4, A = Li, Na, K) have been identified among the most promising host matrices for co-doping with lanthanide ions to ensure high efficiency of photon management processes such as UC, DC, and ET. The low values of their phonon cut-off energy ($\hbar\omega_{LiYF4} \approx 425\ \mathrm{cm}^{-1}$, $\hbar\omega_{\mathrm{NaYF4}} \approx 370\ \mathrm{cm}^{-1}$, and $\hbar\omega_{\mathrm{KYF4}} \approx 328\ \mathrm{cm}^{-1}$) provide the information that these hosts suppress unwanted photon-assisted non-radiative relaxation processes, thereby allowing most of the energy absorbed by rare-earth ions to be efficiently converted into radiative emission [53].

Furthermore, alkali metal ions expand the crystal lattice of host matrices, altering local symmetry in a way that enhances ET between the incorporated ions and eventually can increase luminescence intensity. In case of some ions, the high doping capacity allows for nearly 100% substitution of Y^{3+} ions with some lanthanide ions, e.g., Yb^{3+}, Gd^{3+} or Lu^{3+} [37]. Additionally, as discussed in Sections 3.1 and 3.2, well-established wet chemistry and solid-state synthesis methods enable the manufacturing of such materials with diverse sizes and morphologies.

Numerous research papers have shown the possibility to effectively tune the emission color output by UC, DC, and ET processes with the largest interest in sodium yttrium fluoride ($NaYF_4$) and its derivatives (e.g., $NaYbF_4$ and $NaLuF_4$), obtained due to Y^{3+} ions substitution [37]. There are two polymorphs to be distinguished within this material, the cubic α-$NaYF_4$ phase and the hexagonal β-$NaYF_4$ phase. The cubic phase has less ordered crystal structure with higher degree of symmetry, whereas the hexagonal phase exhibits more structured arrangement within crystal lattice with reduced symmetry [54,55]. This lowered symmetry creates in β-$NaYF_4$ crystals an asymmetrical crystal field around the dopant ion, which enhances electronic coupling between 4f energy levels, hence it increases the probability of Laporte-forbidden f-f electronic transitions. This portrays β-$NaYF_4$ as a host lattice with low affinity toward non-radiative energy losses, thereby enhancing PL intensity [56]. Therefore, this structure is associated with unique and enhanced optical properties.

Lanthanide-doped alkali-metal-based yttrium fluorides are additionally chemically inert and resistant to degradation under various environmental conditions, ensuring the preservation of the optical properties of doping lanthanide ions over prolonged time. This makes them highly suitable for applications in harsh environments. When functionalized with organic functional groups, such as –OH, $-NH_2$, –COOH, or –SH, or encapsulated in biocompatible polymers, e.g., ethylene glycol, poly(ethylene glycol), poly(vinylpyrrolidone), β-$NaYF_4$ and $LiYF_4$ materials become non-cytotoxic, which positions them as strong candidates for biomedical applications [57]. Once delivered into the body, these materials remain intact, preventing the formation of harmful by-products. The pronounced biocompatibility is particularly advantageous for *in vivo* bioimaging and cancer treatment, enabling high-contrast visualization of complex biological structures and facilitating targeted photodynamic therapies – all with no harm caused to living organisms [58]. Beyond medicine, the non-toxic properties of alkali-metal-based host matrices are essential in antimicrobial and disinfection technologies as they can be used in coatings and surfaces to prevent microbial growth without posing risks to human health.

2.4.2. Yttrium silicates

Yttrium silicates, particularly Y_2SiO_5 and $Y_2Si_2O_7$, are among widely studied host matrices for Vis-to-UV UC due to their structural versatility and ability to influence rare-earth ion emissions. Although these materials exhibit a relatively high phonon cut-off energy ($\hbar\omega \approx 970 \div 1000$ cm^{-1}), which typically suggests high non-radiative relaxation rates of excited states, they simultaneously lower the host-dependent edge energy of the 4f5d band of rare-earth ions [53,59]. This effect enables efficient UC under Vis excitation, particularly when ET mechanisms between lanthanide ions are optimized. With different polymorphic forms providing distinct local environments for lanthanide ions, structural versatility of yttrium silicates is important for Stokes- and anti-Stokes emissive properties. Despite their strong potential for photonic applications, there are still some challenges regarding fine-tuning of crystal field effects to optimize rare-earth ions interactions and maximize radiative emission efficiency.

Y_2SiO_5 exists in two crystallographic phases (X1 and X2), both of which providing low-symmetry sites that strongly influence optical transitions within the incorporated lanthanide ions. This feature makes Y_2SiO_5 particularly valuable for applications requiring sharp emission lines, such as quantum memory and bioimaging [60,61]. The host matrix is commonly prepared *via* solid-state or sol-gel methods, which allow for fine control over its chemical composition and facilitate targeted doping strategies to enhance PL intensity in the region of interest while maintaining high crystal structure purity. Characterized by high thermal stability and good mechanical properties, the material is able to withstand harsh conditions, simultaneously preserving its optical features [62].

On the other hand, $Y_2Si_2O_7$ exhibits UC properties strongly dependent on its crystalline phase. Among its four known polymorphs (α, β, γ, and δ), the α-phase is particularly valued for its structural purity, which contributes to efficient UC performance. However, achieving a single-phase material remains a challenge due to the tendency of different polymorphs to co-exist, often influenced by synthesis conditions such as temperature, precursor selection, and impurity levels. Phase control strategies, including optimized calcination procedures and doping modifications, are actively investigated to improve homogeneity and optical properties of $Y_2Si_2O_7$ [63].

2.5. Material size and its influence on lanthanide ions luminescence properties

Prospective applications impose size and morphology of inorganic lanthanide-ion-doped phosphors. For instance, in order to introduce them into a living organism for cancer treatment or bioimaging and to functionalize with specific chemical species for sensitive biomolecules targeting (e.g., DNA, RNA, proteins or receptors), the ideal size of materials should be below 50 nm [64]. However, technological solutions requiring high emission intensity from lanthanide ions rely on bigger particles as they do not show high numbers of surface defects, prone to quench PL. They are also easier in further processing, e.g., to be integrated into polymeric surfaces without complex stabilization strategies or to be compressed as pellets [65,66]. Therefore, to meet the presented requirements for applications, well-developed and feasible synthesis protocols have been developed to fabricate lanthanide-ion-doped at nano- and micro-scale, in the form of colloids or powders.

2.5.1. Nanoparticles

According to the European Union standards, nanoparticles (NPs) are defined as particles in which at least 50% have one or more dimensions ranging from 1 to 100 nm, exhibiting unique features compared to bulk materials [67]. While materials at macroscale typically show consistent physical properties regardless of their size, this is not always true at the nanoscale, at which size-dependent properties emerge, able to enhance PL emission. Furthermore, they form stable colloidal suspensions and their large surface area, typically ranging $100\div1000\ m^2\ g^{-1}$, provides opportunities for additional modifications to meet the demands of specific applications, such as sensing, drug delivery, and *in vivo* bioimaging [58,68]. In dried form, nano-sized phosphors can be utilized for solid-state lighting, providing high packaging density within ultrathin layers due to reduced number of voids between the particles, in contrast to the micron-sized counterparts [69].

2.5.1.1. Core nanoparticles

The term *core nanoparticles (C NPs)* typically refers to NPs in which rare-earth ions are distributed throughout the entire volume. These nanomaterials gained significant attention in the late 1990s and were recognized as a breakthrough in research on lanthanide-doped materials, as nanoscale effects introduce several new features that distinguish them from their bulk counterparts [27]. The unique optical properties of lanthanide ions, which remain stable over time, are confined within particles no larger than several ten nanometers, making them highly suitable for applications in deep-tissue imaging, biological molecule sensing, and solar energy conversion [25,70]. Core-only NPs offer good colloidal stability and their surface can be easily modified to improve dispersibility in aqueous environments. They also serve as an alternative to organic fluorophores, which are prone to photobleaching and degradation, making them highly attractive for biological applications [71].

However, core-only NPs often suffer from reduced PL efficiency due to surface-related quenching effects [27]. A significant proportion of dopant ions are located near the NPs surface, where they interact with high-energy vibrational modes from surface ligands, solvent molecules, and other external quenchers possibly present in the suspensions. The presence of –OH and $–NH_2$ functional groups in capping ligands and solvents introduces additional non-radiative relaxation pathways through multi-phonon relaxation processes [53]. As a result, energy absorbed by dopants is often lost non-radiatively instead of being emitted as luminescence, thus PL efficiency is substantially reduced, compared to the corresponding bulk materials. The high surface-to-volume ratio of C NPs amplifies these effects, particularly in smaller ones (<10 nm) [36]. ET occurring between closely spaced dopant ions within C NPs can promote energy migration toward the surface, where quenching centers dissipate the excitation energy. Another limiting factor in the performance of core-only NPs is the presence of structural defects formed during synthesis, which serve as additional non-radiative recombination sites [72]. While advances in synthetic chemistry have allowed for better control over particle size, morphology, and surface properties, intrinsic defects remain a significant challenge for optimizing PL intensity in C NPs. Therefore, within the ongoing research scientists continue to explore various strategies for mitigating these effects, with particular focus on developing more complex architectures, such as core@shell NPs or even systems composed of multiple epitaxially grown shells (i.e., core@multi-shell NPs) [38].

2.5.1.2. Core@shell nanoparticles

Lanthanide-doped core@shell NPs (CS NPs) are structures in which the lanthanide-doped core is coated with an epitaxially grown shell, in the vast majority of cases made of the same material as the host matrix. This modification is particularly beneficial for ultra-small NPs (<10 nm), where high surface-to-volume ratios amplify quenching effects. After passivation with the inert (i.e., undoped) shell, the PL intensity of CS NPs tends to increase significantly due to a reduction of possible interactions between doping ions and surface defects or quenching centers introduced by ligands and solvents. For instance, studies have reported UC intensity enhancements ranging from several-fold to hundreds, depending on factors such as core size, composition, and excitation power density [38]. Interestingly, advancements in wet chemistry synthesis techniques allow for precise engineering of shell layers with tailored composition and thickness. However, excessively thick shells (≥3 nm) have been shown to limit efficiency gains by inhibiting ET processes [62].

Initial designs featured undoped shells to reduce surface energy loss and enhance PL intensity by minimizing non-radiative decay pathways. This protective shell physically shields the core from surface quenchers, thereby preserving excitation energy within the NP, thus improving PL efficiency. However, while undoped shells effectively suppress quenching, they do not actively contribute to ET processes. Therefore, optically active shells have been introduced, where dopant ions are incorporated into the shell itself to fine-tune the excitation and emission properties of lanthanide-doped CS NPs. By carefully selecting dopants concentration and spatial distributions, researchers have achieved enhanced energy migration pathways [39,73]. Furthermore, this spatial separation prevents unwanted energy losses and promotes efficient PL intensity, ultimately enhancing the stability and performance of CS NPs across various applications.

In some systems, the shell is composed of different material than the core, and, resultantly, heterogeneous CS structure is formed. This strategy can effectively suppress ion migration from the core to the shell and minimize non-radiative losses at the interface. Host matrices like SrF_2 and CaF_2 possess phonon energies of lower magnitude, compared to $NaYF_4$ ($\hbar\omega_{SrF2} \approx 290\ cm^{-1}$, $\hbar\omega_{CaF2} \approx 350\ cm^{-1}$), which further reduces multi-phonon relaxation processes [53]. For instance, it has been proven for $NaYF_4$:Tb^{3+},Yb^{3+}@CaF_2 and $NaYF_4$:Yb^{3+},Er^{3+}@SrF_2 CS nanostructures, where the lattice mismatch and lower phonon energy of the shell material act as a physical barrier, improving PL efficiency and stability in time [74,75].

2.5.1.3. Core@multi-shell nanoparticles

Although CS NPs provide substantial benefits, defects can still form at the surface and core@shell interface. They can arise due to lattice mismatches, surface irregularities, or incomplete shell coverage, all of which potentially leading to non-radiative losses, thus reduced PL efficiency. To address these limitations, scientists have explored core@multi-shell NPs, where multiple shells are epitaxially grown through layer-by-layer coating process [38]. Such an approach allows for spatial separation of optically active ions, which can lead to optimized ET processes. Additionally, divergent optical properties can be exploited, combining multiple functionalities within a single NP, e.g., concurrent emission in UV and NIR spectral ranges coming from separated lanthanide ions, which can be applied for simultaneous *in vivo* cancer treatment and bioimaging [76].

Foremostly, efforts to limit concentration quenching in lanthanide-doped nanophosphors have led to various strategies development, particularly in the research on efficient up-converting materials. The active-core and active-shells architectures have been introduced to minimize CR between lanthanide dopants. For instance, spatial distribution of Yb^{3+}, Gd^{3+}, and Ho^{3+} ions within core@multi-shell β-$NaYF_4$ NPs allowed for the generation of UC emission of the lowest wavelength observed upon 980 nm excitation, coming from Gd^{3+} ions at 204 nm, which was never reported for NPs of simple core architecture [77]. The observed UV-C emission was of low magnitude as it required high-order multi-photon processes, including sequential absorption and ET between ions in different layers. Nevertheless, the method has proven its effectiveness for multiple optical processes combination within a single NP.

2.5.2. Microcrystals (MCs)

Microcrystals (MCs) doped with lanthanide ions are particles with relatively large sizes, typically exceeding 1 μm in each dimension. Their morphology, homogeneity, and crystalline phase purity can be easily tuned during simple and scalable synthesis methods as capping agents [e.g., ethylenediaminetetraacetic acid (EDTA) or citric acid] are usually required to mediate the growth within particular structures [78]. If no ligands are intended to be utilized within the synthesis, solid-state method at elevated temperatures or sol-gel method followed by calcination are conducted. However, the formed powders consist of large particles with broad size distribution [59,70].

Compared to the NPs co-doped with rare-earth ions at corresponding concentrations, MCs possess fewer surface defects due to their reduced surface-to-volume ratio. As a result, within their structure, quenching effects occur rather rarely, which leads to improved and stable PL characteristics. Consequently, it makes MCs a valuable solution for various photonic applications, but simultaneously though their larger size can limit their use *in vivo* (e.g., bioimaging [64]).

When suspended, the MCs do not form aggregates, even after the removal of surface ligands utilized during the synthetic procedure. However, due to relatively big size, they tend to sediment, which is an important factor in terms of storing, handling, and further processing. With the utilization of an appropriate method, they can be embedded into solid host matrices, polymer coatings, and composite materials without the need for additional surface modifications [65]. Such stability makes them ideal for applications requiring long-term durability and consistent performance. This ease of integration, combined with their high luminescence efficiency, makes them attractive for solid-state lighting or light-triggered disinfection.

Chapter 3

Experimental methods

In the experimental section of this doctoral dissertation, I provide a brief overview of the methods incorporated into the research strategy for the successful synthesis and characterization of various lanthanide-doped materials, including colloidal NPs and MCs in the form of powders. The synthesis procedures were conducted under controlled and optimized conditions to achieve precise tuning of particle size, morphology, and structural properties. By varying the stoichiometry of reagents, the effects on crystallinity, phase composition, and optical behavior were systematically examined.

Structural characterization was performed using advanced analytical techniques, such as XRD to determine phase composition and crystallographic properties as well as electron microscopy methods, including SEM and TEM to analyze surface morphology, particle size distribution, and internal structure at the micro- and nano-scale. Particular attention was given to the luminescent properties of those synthesized rare-earth-doped materials, investigated through spectroscopic techniques to examine excitation and emission behaviors, including the LTs of selected excited energy levels. In addition, I also present the examples of potential applications of the obtained materials, including experiments on bacteria, fungi, and human virus species inactivation and fluorimetric analysis of dsDNA unwinding, performed by me within the research.

The step-by-step methodology presented in this study reveals how particle size and lanthanide ions concentration affect spectroscopic properties. Understanding these effects enables the fine-tuning of material characteristics for bio-related applications, e.g., light-triggered disinfection or *in vivo* bioimaging.

3.1. Methods of lanthanide-doped fluoride-based NPs synthesis

The scientists performing research on nanotechnology and its prospective applications have developed various chemical methods to synthesize nanocrystals of good chemical and optical quality. In the literature, there are four commonly reported, well established wet chemistry techniques: co-precipitation, hydro(solvo)thermal synthesis, thermal decomposition, and microwave-assisted method [79–81]. Each of them, although leading to the successful obtaining of lanthanide-doped fluoride-based NPs, has advantages and disadvantages, which were briefly summarized in Table 1.

Table 1. Advantages and disadvantages of commonly utilized wet chemistry techniques for NPs manufacturing (based on: [79–81])

Synthesis technique	Advantages	Disadvantages
co-precipitation	• facile procedure • no expensive equipment required • fast NPs growth rate • high reaction yield	• products are of high size and shape dispersibility • annealing needed as post-treatment to improve NPs crystallinity
hydro(solvo)thermal synthesis	• one-step facile method • relatively cheap reagents • good control on NPs size and shape • pure crystalline phases at lowered temperatures • no post-treatment needed	• prolonged reaction time • autoclave needed, resisting high pressure and temperature of solvents in their critical point • low reaction yield
thermal decomposition	• high quality not aggregated nanocrystals • narrow size distribution • relatively cheap reagents	• air-sensitive precursors – inert atmosphere needed • toxic by-products formed during the process • low reaction yield
microwave-assisted methods	• shorter reaction time in comparison with hydro-(solvo)thermal synthesis • synthesis is performed at low temperatures	• needed autoclave or reactor with the microwave source

The research papers on lanthanide-doped nanophosphors focus on the relationship between their size and the expected emission output, i.e., relative or integral intensity, luminescence LTs in the spectral region of interest. When the NPs size is below 10 nm, their luminescence starts to strongly depend on the phonon confinement effect [82]. As the dimensions increase, it leads to lowering of the surface defects density, prone to quench luminescence by interactions with the local surroundings (e.g., solvent or ligand molecules) [82]. Additionally, it has been highlighted for biological applications that inorganic nanophosphors ought to exhibit size below 50 nm with narrow size distribution to target sensitive biomolecules, such as DNA, RNA, proteins or receptors [83]. The chosen protocols for the synthesis should thus be reproducible, eventually leading to the good repeatability of the investigated spectroscopic features of the obtained materials [79]. These factors were of great significance for the successful accomplishment of the performed research within the presented doctoral dissertation. Therefore, since thermal decomposition reaction of precursors in high-boiling point surfactants fulfils all of the aforementioned requirements, I decided to synthesize the lanthanide-doped fluoride-based NPs concurrently emitting UV and NIR radiation with this technique.

Thermal decomposition reaction is based on heating of relatively inexpensive, simple precursors of both corresponding lanthanides and host matrix elements in mixtures of high-boiling-point surfactants (e.g., octadec-1-ene, Therminol® 66). Although the first protocols were reported without organic capping agents, such as oleic acid, oleylamine, or trioctylphosphine, nowadays, fluoride NPs formation by the decomposed reagents is always by them mediated [79]. Their utilization is mandatory to promote the growth of the NPs of particular crystal structure, size, and morphology, all of which having then tremendous impact on the luminescent properties. Additionally, the presence of organic ligands on the surface allows to stabilize the NPs not only in the reaction mixture, but also in organic solvents for long-period storage as transparent, colloidal stock solutions [79]. Such a form is extremely convenient to perform any further modifications needed for prospective applications, e.g., functionalization, surface modification, ligand exchange or organic-to-inorganic phase transfer [84]. Furthermore, the feasibility of the method to manufacture sophisticated core@multi-shell nanostructures has been proven, simultaneously allowing for the enhancement of specific spectroscopic features in the spectral range of interest [85].

Primarily, rare-earth and alkali metals trifluoroacetates were used in the synthesis. However, during their decomposition highly toxic fluorinated volatile side-products are usually formed [86]. Consequently, the researchers decided to shift toward safer rare-earth acetates, usually obtained right before the synthesis from the corresponding oxides and transformed in the subsequent step to rare-earth oleates. They react with NH_4F or alkali metal fluorides (like LiF or NaF) in a mixture of high boiling point surfactants and capping agents, which ratio can easily be manipulated, eventually yielding NPs with varying sizes and morphologies while maintaining monodispersity within the same batch [79]. In the research I decided to utilize two protocols, allowing for the synthesis of lanthanide-doped alkali-metal-based fluoride NPs of two different sizes, i.e., ~20÷30 nm and ~100 nm, however, the workflow is identical for both of them (Fig. 11). They were presented in the following Sections 3.1.1 and 3.1.2.

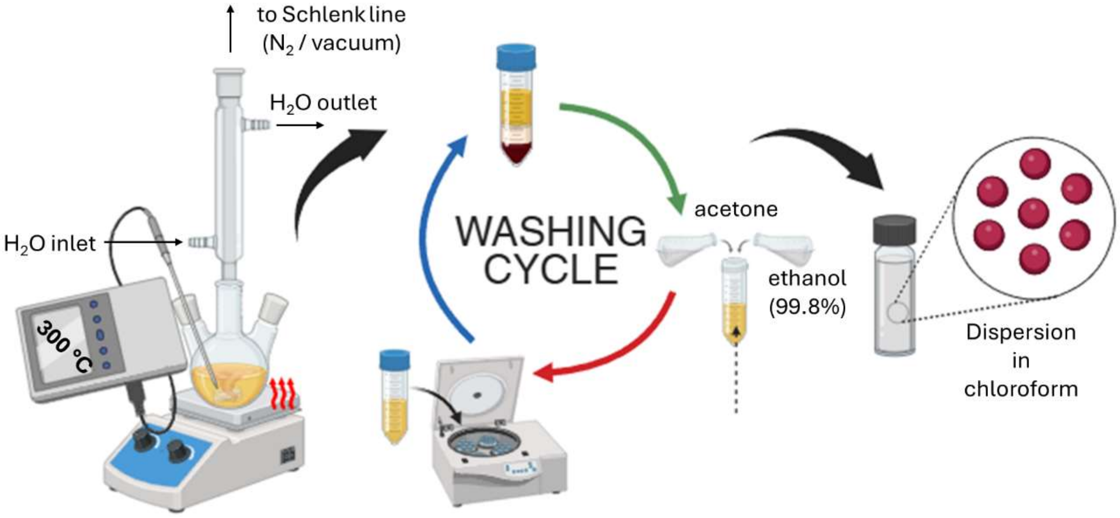

Fig. 11. The schematic representation of lanthanide-doped NPs synthesis workflow

3.1.1. Synthesis of lanthanide-doped alkali-metal-based yttrium fluoride C NPs

The protocol described by Abel et al. and altered to my needs was utilized to synthesize the C NPs [87]. I chose it as the NPs manufactured according to it are usually of small sizes (ca. 20÷40 nm, depending on the intended host matrix) and of narrow size distribution. Furthermore, the possibility to use different alkali hydroxides and various lanthanide dopants makes the synthetic procedure feasible to fabricate NPs of desired spectroscopic features.

I utilized the protocol to synthesize the following NPs series:

- Pr^{3+},Yb^{3+}-co-doped β-$NaYF_4$ of dual optical functionality, exhibiting concurrent UC and DC emissions – for more precise information see Section 4.2.1 in Chapter 4;

- Pr^{3+}-based $LiYF_4$, β-$NaYF_4$, and $Na_{0.5}K_{0.5}YF_4$ C NPs for human naked and enveloped virus species inactivation – more details in Section 5.2.1 in Chapter 5.

The anhydrous $RE(CH_3COO)_3$ salt (RE = Y, Pr, Gd, Tm, Nd) in the total amount of 2.00 mmol was obtained by dissolution of the corresponding lanthanide oxides in a small volume of the acetic acid and water mixture (1:1 v/v) at 100 °C under reflux. The transparent solution was evaporated, followed by the powder-like precursor transfer to a three-neck round bottom flask with a magnetic stirring bar. Then 30 mL of octadec-1-ene and 12 mL of oleic acid were added. Heated at 120 °C under vacuum to remove water and oxygen residues, the mixture was cooled down to 50 °C. In the subsequent step, 10 mL of the methanolic solution of NH_4F (8.00 mmol) and the corresponding amount of alkali hydroxides (in total 5.00 mmol) was instilled carefully. The cloudy mixture was stirred for 30 minutes under reflux and in nitrogen purge to become homogeneous. Followingly, methanol, residual water, and oxygen were evaporated from the system at 120 °C. Once the mixture stopped foaming, it was heated swiftly to 300 °C (for β-$NaYF_4$ and $Na_{0.5}K_{0.5}YF_4$ host matrices) and 320 °C (for $LiYF_4$ host matrix), and left under reflux and constant nitrogen flow for 1 h. The yellowish mixture was cooled down to room temperature naturally, quenched with acetone and anhydrous ethanol (1:1 v/v), and centrifuged at 6,000 rpm for 10 min. The supernatant was discarded and the precipitate was re-dispersed in small portions of hexane, followed by washing three times with the mixture of acetone and ethanol (1:1 v/v). The final dispersions were prepared by suspending the obtained oleic-acid-capped NPs in 5 mL of chloroform. However, when shelling was planned to be conducted, 6 mL of C NPs dispersion in hexane was prepared – 1 mL was kept for the characterization with regard to crystal structure, morphology, and the chosen spectroscopic features, whereas the remaining 5 mL was used for further shelling.

3.1.2. Synthesis of lanthanide-doped alkali-metal-based yttrium fluoride CS, CSS, and CSSS NPs

The protocol presented by Abel et al., which I described in Section 3.1.1, was also proven to be handy for the synthesis of more complex nanostructures, even consisting of multiple shells (i.e., core@multi-shell NPs) [87]. Grown epitaxially, each shell varied in both lanthanide ion dopants and their molar concentration.

The synthetic procedure reported below enabled me to obtain various NPs:

- Pr^{3+}-based $LiYF_4$ and β-$NaYF_4$ CS NPs for human naked and enveloped virus species inactivation – more details provided in Section 5.2.1 in Chapter 5;
- complex Pr^{3+}-based β-$NaYF_4$ CS, CSS, and CSSS NPs showing concurrent emission in divergent spectral regions – more information available in Section 6.2 in Chapter 6.

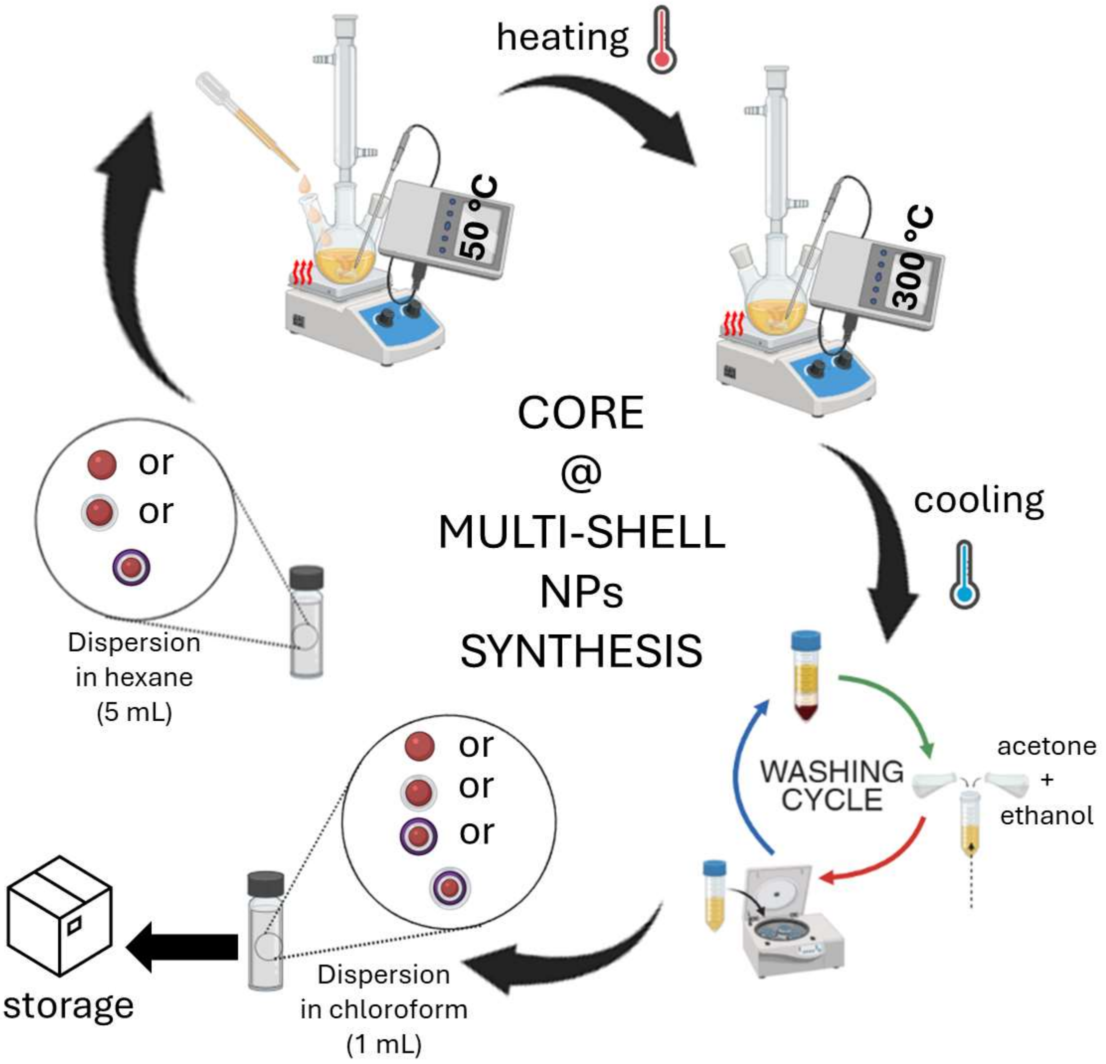

Fig. 12. The schematic representation of lanthanide-doped CSSS NPs synthesis workflow

Since the workflow of CSSS NPs synthesis is complex, I decided to summarize it in Fig. 12 for the enhanced clarity. Briefly, the anhydrous $RE(CH_3COO)_3$ salt (RE = Y, Pr, Gd, Tm, Nd) in the total amount of 2.00 mmol was obtained by dissolution of the corresponding lanthanide oxides in a small volume of the acetic acid and water mixture (1:1 v/v) at 100 °C under reflux. The transparent solution was evaporated, followed by the powder-like precursor transfer to a three-neck round bottom flask with a magnetic stirring bar. Then 30 mL of octadec-1-ene and 12 mL of oleic acid were added. Heated at 120 °C under vacuum to remove water and oxygen residues, the mixture was then cooled down to 50 °C. Depending on the number of the shell to be epitaxially grown, 5 mL of the stock dispersion of C, CS or CSS NPs was added drop-wisely and the solution was left for 10 minutes for homogenization. In the subsequent step, 10 mL of the methanolic solution of NH_4F (8.00 mmol) and the corresponding amount of alkali hydroxides (in total 5.00 mmol) was instilled carefully. The cloudy mixture was stirred for 30 minutes under reflux and in nitrogen purge to become homogeneous. Followingly, methanol, residual water, and oxygen were evaporated from the system at 120 °C. Once the mixture stopped foaming, it was heated swiftly to 300 °C (for β-$NaYF_4$ host matrix) and 320 °C (for $LiYF_4$ host matrix), and left under reflux and constant nitrogen flow for 1 h. The yellowish mixture was cooled down to room temperature naturally, quenched with acetone and anhydrous ethanol (1:1 v/v), and centrifuged at 6,000 rpm for 10 min. The supernatant was discarded and the precipitate was re-dispersed in small portions of hexane, followed by washing three times with the mixture of acetone and ethanol (1:1 v/v). The final dispersions of CSSS NPs were prepared by suspending the obtained oleic-acid-capped NPs in 5 mL of chloroform.

3.1.3. Synthesis of $LiYF_4$ NPs in the size range of 100÷120 nm

The synthesis protocol adapted from the research paper by Chen et al. was introduced to obtain the series of Pr^{3+},Yb^{3+}-co-doped $LiYF_4$ NPs of dual optical functionality, exhibiting concurrent UC and DC emissions [25]. More comprehensive information can be found in Section 4.2.1 in Chapter 4. According to the procedure, the size of the reported NPs exceeded 100 nm. Nevertheless, I decided to follow it to obtain lanthanide-doped $LiYF_4$ NPs of well-defined morphology, for which the density of surface defects is relatively low. As a consequence, their influence on spectroscopic properties, especially on Vis-to-UV UC emission, should be negligible.

Shortly, the anhydrous $RE(CF_3COO)_3$ (RE = Y, Pr) and $Li(CF_3COO)$ salts were simultaneously obtained by dissolution of the corresponding lanthanide oxides (in total amount of 1.25 mmol) and 2.25 mmol Li_2CO_3 in a small volume of the trifluoroacetic acid and water mixture (1:1 v/v) at 100 °C under reflux. The transparent solution was evaporated, followed by the powder-like precursor transfer to a three-neck round bottom flask with a magnetic stirring bar. In the following step, 30 mL of octadec-1-ene and 30 mL of oleic acid were added. The mixture was heated up to 120 °C under nitrogen purge, followed by evacuation of water and oxygen residues for ca. 30 min. Having been dried, the solution was heated slowly up to 320 °C. The reaction system was kept at this temperature for 1 h to react, under reflux and nitrogen purge. After that time, the temperature was lowered to room temperature naturally, the post-reaction mixture was quenched with acetone and anhydrous ethanol (1:1 v/v), and centrifuged at 8,000 rpm for 5 min. The supernatant was discarded and the precipitate was re-dispersed in small portions of chloroform, followed by washing twice with the mixture of acetone and ethanol (1:1 v/v). The final dispersions were prepared by suspending the obtained oleic-acid-capped NPs in 5 mL of chloroform.

3.2. Methods of lanthanide-doped fluoride-based MCs synthesis

Lanthanide-doped fluoride-based MCs usually exhibit more intense and stable in time luminescent properties than the corresponding NPs, which pictures them as more reliable phosphors for the long-term implementation in optical and biological fields [64]. Regarding the targeted applications, their phase, size, morphology, and surface should be carefully tuned during the manufacturing process. Up to now, various synthetic methods have been investigated, including hydrothermal synthesis or solid-state synthesis, which were briefly discussed in the following Sections 3.2.1 and 3.2.2, respectively.

3.2.1. Hydrothermal synthesis

Hydrothermal synthesis is a facile, low-cost method, in which high-quality crystalline inorganic materials grow from water suspension of precursors at temperatures significantly exceeding its boiling point. The process is usually conducted in a closed system, capable to resist high pressures induced by solvent vapors (more than 1 bar), e.g., in an autoclave or a reactor. At extreme conditions water enables the formation of crystal structures with controlled morphology and size, which are difficult to achieve through other methods. The compounds crystallization is commonly mediated with help of such organic capping agents as EDTA or citric acid [88,89]. Hydrothermal synthesis can also be conducted using various heat sources, e.g., in drying ovens or microwave-assisted heating devices. The latter provide rapid and uniform heating of the reaction setup, simultaneously accelerating the MCs nucleation, thus reducing the reaction time, depending on the type of the material, from days to hours or even minutes [90].

3.2.1.1. Microwave-assisted hydrothermal synthesis of lanthanide-doped alkali-metal-based yttrium fluoride MCs

In the research paper by Qiu et al. a facile manufacturing method of lanthanide-doped $LiYF_4$ MCs is reported [65]. The process can be easily adjusted for various alkali-metal-based yttrium fluoride MCs fabrication. Therefore, within the research scope I utilized it to obtain Pr^{3+}-based $LiYF_4$ and β-$NaYF_4$ MCs for human naked and enveloped virus species inactivation. Since the size of the synthesized microphosphors falls in the microscale region, defects present on the materials surface diminish their emission intensity in much more smaller rate than in the case of NPs. It was a key factor to manufacture up-converting materials at the microscale, tailored for the prospective light-triggered disinfection. Additionally, the presence of organic ligands on their surface allows for their further modification to e.g. embed them into polymeric surfaces. More details on the synthesis conditions, regarding exact amounts of reagents, were provided in Section 5.2.2 in Chapter 5.

The synthetic procedure was preceded each time with the precursor synthesis. Shortly, RE_2O_3 (RE = Y, Pr, Gd) in the total amount of 3.75 mmol reacted at 100 °C with 20 mL of the mixture of HNO_3 and water (1:1 v/v) for 1 h under reflux and nitrogen purge. After that time the excess of acid and water was evaporated with the usage of a rotary evaporator, and the powder-like nitrates were washed several times with distilled water. When pH of the last portion was neutral, the dried precursor was dissolved in 10 mL of distilled water along with 1.35 mmol of EDTA and then transferred to a Teflon vessel. Simultaneously, 7.5 mmol of LiF or NaF and 22.5 mmol of NH_4F were dissolved in 10 mL of distilled water to form another solution, which was drop-wisely added to the Teflon vessel. The mixture was vigorously stirred for 30 min to form homogeneous, milky dispersion. The vessel was sealed and placed into the microwave reactor (MAGNUM V2, ERTech, Poland) for 8 h (for $LiYF_4$ host matrix) or 12 h (for β-$NaYF_4$ host matrix) at 200 °C. The obtained MCs were centrifuged at 6,000 rpm for 5 min and washed with the mixture of water and ethanol (1:1 v/v) three times, to be finally suspended in 5 mL of distilled water.

3.2.2. Solid state synthesis

Solid state synthesis is a versatile method of manufacturing various types of inorganic materials, including fluorides. At elevated temperatures in advanced tube furnaces and usually under inert gas flow, the mixture of finely ground, solid reagents undergo a chemical reaction, in which a new compound is formed. The applied temperature is high enough to assure the ions diffusion across the solid phases, but at the same time does not exceed the melting point of its each component [70]. In order to manufacture materials of high crystal phase purity, it is required to precisely control time and temperature during the process, the crystallites morphology is not adjustable, though. In the mixture there are no organic ligands promoting crystals growth along particular crystallographic faces. Consequently, the formed microcrystalline particles are of irregular shape.

3.2.2.1. Solid state synthesis of β-$NaYF_4$ MCs

The synthesis protocol presented in the work by Aarts et al. was used to obtain ligand-free Tm^{3+},Pr^{3+}-co-doped β-$NaYF_4$ MCs [70]. The method was chosen to avoid organic capping agents, which present on the surface of the materials could quench the emissive properties in the regions of interest [91]. The materials were synthesized for the investigation of ET processes occurring within and between the ladder-like energy level structures of Tm^{3+} and Pr^{3+} ions, leading to the concurrent enhancement of the Stokes and anti-Stokes emissions in NIR and UV spectral ranges, respectively. The detailed specification was provided in Section 7.2 of Chapter 7.

In brief, the total amount of 10.6 mmol of corresponding REF_3 (RE = Y, Pr, Tm) and 10.6 mmol of NaF were dried overnight at 120 °C in an oven under inert atmosphere to evaporate any water traits. In the subsequent step, the dried fluorides were ground collectively in an agate mortar with 13.5 mmol of NH_4F. Transferred into a corundum crucible, the mixed substrates were placed in a tube furnace along with an additional crucible filled with the excess of $(NH_4)HF_2$. The synthesis was conducted in the constant flow of N_2/H_2 gas mixture (95:5 v/v) at 650 °C for 5 h. In the end, the obtained materials were cooled down naturally and finely ground in a mortar with a pestle to form powders for further studies.

3.2.3. Sol-gel method

Sol-gel method is a highly-reproducible technique for fabrication of inorganic materials in the form of powders or thin films. The process is clamed as cost-effective since it does not require expensive reagents. Generally, the procedure involves hydrolysis and polycondensation of precursors present in the initial solution (sol), leading to a network of interconnected particles with trapped between them solvent molecules. In the so-called gelation the sol becomes thicker and, as its temperature is sufficiently high, the solvent evaporates, thus the gel is prepared. The final solid material with desired properties is obtained after calcination at high temperatures, usually above 1000 °C.

By simple changes in the amount of starting reagents, it is possible to dope materials with various lanthanide ions at chosen concentrations. Therefore, I synthesized the lanthanide-doped $Y_2Si_2O_7$ crystalline powders for the photoactivated eradication of common bacteria and fungi according to the protocol described by Cates et al. with slight modifications [66]. For further clarification see Section 8.2.1 in Chapter 8.

In general, the total amount of 4.43 mmol of corresponding RE_2O_3 (RE = Y, Pr, Tm, Yb) was dissolved in the mixture of nitric acid and water (1:1 v/v) in a three-neck round-bottom flask under reflux and nitrogen purge for 1 h. The remaining acid and water were evaporated with a rotary evaporator. Each time the obtained powder was washed several times with distilled water until pH of the last portion was neutral. Having been dried overnight on a hot plate at 130 °C in ambient air, the powdered precursor was dissolved in 3.25 mL of ethanol and 1.02 mL of distilled water, followed by the addition of 0.98 mL of tetraethoxysilane (TEOS). The solution was slowly stirred and heated at 70 °C to form a clear gel, which was later dried in an oven in the air for 17 h at 104 °C. The formed powders were finely ground in a mortar and transferred into corundum crucibles and heated in a muffle furnace in ambient atmosphere for 3 h at 1000 °C. The calcinated phosphors were cooled down naturally to room temperature and ground for further studies.

3.3. Crystal structure and morphology characterization

3.3.1. X-ray diffraction (XRD)

X-ray diffraction (XRD) is a fundamental technique for qualitative analysis of crystalline structure of materials under X-ray radiation exposition. Its core principle is based on the Braggs law [Formula (1.1)], describing the condition for constructive interference when X-rays interact with a crystal lattice of the considered material:

$$n\,\lambda = 2d\,\sin\theta, \qquad (1.1)$$

where:

- n – order of diffraction;
- λ – incident X-ray wavelength (here the filtered CuKα_1, λ = 1.54056 Å);
- d – interplanar spacing of the crystal lattice (Å);
- θ – Bragg angle, measured between the incident X-ray and the lattice plane (°).

In a typical XRD experiment an X-ray tube generates X-rays, which are directed toward the finely ground sample, evenly spread on a sample holder to minimize orientation effects. As the monochromatic X-ray beam irradiates the specimen, it is diffracted at specific angles that depend on the atomic arrangement of the crystal structure and interplanar spacings. The X-ray detector moves along a fixed path to record intensities of the diffracted radiation as a 2θ function (the diffraction angle). The measurement is typically conducted in Bragg-Brentano geometry, in which the incident and diffracted beams remain symmetrical with respect to the sample surface. Therefore, within the research scope an STOE X-ray diffractometer or Malvern Panalytical Aeris benchtop powder X-ray diffractometer were utilized.

Since each crystalline material has its unique XRD diffraction pattern, also known as *crystallographic fingerprint*, the obtained powder diffractograms are compared with the ones deposited in standard reference databases, such as Powder Diffraction File (ICDD PDF) or Inorganic Crystal Structure Database (ICSD). If the collected XRD pattern of the powdered specimen indicates for the presence of two or more crystal phases, Rietveld refinement is usually used to determine phase composition.

3.3.2. Scanning electron microscopy (SEM)

Scanning electron microscopy (SEM) is an imaging technique widely used in materials science or biology to reveal fine surface details and structural properties. It uses a focused beam of electrons, accelerated by high voltage reaching up to 30 kV, to scan a specimen. While interacting with the sample, they cause the emission of electrons of lower energy (e.g., secondary or back-scattered electrons), which are detected by dedicated detectors. Consequently, the collected signals are converted into high-resolution images. Since the clarity of the images captured by any microscope is limited by the diffraction limit, determined by the wavelength of the radiation used for imaging, SEM allows for imaging with resolutions ranging in the nanometers range. This feature far surpasses the capabilities of traditional light microscopes, which are limited to a resolution of about 200 nm. As a result, SEM is an essential tool for observing fine surface details and nanostructures that conventional optical techniques cannot resolve. It also provides a significant depth of field, allowing surfaces at different distances from the magnetic lens to appear in focus.

SEM imaging is performed on samples that are capable to conduct electrons. However, if the investigated specimen is not conductive (e.g., polymers or biological matter), it is additionally coated with a thin layer of carbon, gold or platinum. It ensures that the sample does not charge during measurements, otherwise the quality of captured micrographs can be severely affected. The appropriately prepared specimen is then placed in the high-vacuum chamber, where there are no air-suspended particles that could scatter the electron beam, generated by the electron gun and focused with a set of magnetic lenses. As the beam scans across the surface of the sample, the latter emits secondary and backscattered electrons, which are detected and processed in order to generate topographical imaging or compositional contrast. Within the research scope, the Jeol JSM-6610LVnx SEM was utilized, being simultaneously connected to an Oxford Aztec Energy X-ray energy dispersive spectrometer (EDS). This equipment allows for conducting elemental analysis of samples in both qualitative and quantitative manner. The method utilizes unique lines of X-ray radiation emitted by the elements present in the specimen upon interaction with high-energy electrons.

3.3.3. Transmission electron microscopy (TEM)

Similarly to SEM, transmission electron microscopy (TEM) is another advanced imaging technique utilizing electrons as a source for materials investigation at the nanoscale. In comparison with the scanning method, the coherent high-energy electron beam interacts with an ultrathin specimen (typically less than 100 nm thick) prepared on a copper grid, which is placed in the vacuum chamber right behind the magnetic lenses. While passing it through, the electrons are affected by the variations in density and atomic composition of the sample. Consequently, high-contrast real-space image is created on a fluorescent screen or a digital detector with extremely high resolutions, reaching a few nanometers. Within the research scope of this doctoral dissertation, the TEM images of the synthesized nanomaterials were captured using an FEI Tecnai G^2 20 X-TWIN electron microscope.

3.4. Optical spectroscopy

3.4.1. UV-Vis spectroscopy

UV-Vis spectroscopy allows to analyze how strong UV and Vis radiation is absorbed by a sample. The method's basic principle relies on the capability of molecules to absorb light, which simultaneously causes electronic transitions between molecular orbitals of investigated compounds. These transitions typically involve the excitation of electrons from lower-energy occupied orbitals (e.g., bonding or non-bonding orbitals) to higher-energy unoccupied orbitals (e.g., anti-bonding orbitals), depending on the nature of the molecule and its conjugated system. For instance, molecules with conjugated π-systems, aromatic rings, or other chromophores exhibit characteristic absorption bands within the UV-Vis region due to $\pi \rightarrow \pi^*$ and $n \rightarrow \pi^*$ electronic transitions.

The technique is commonly employed in research and industry laboratories worldwide due to its simplicity, rapid data acquisition, and minimal sample preparation requirements. A typical UV-Vis measurement is performed in a spectrophotometer, an instrument consisting of two polychromatic light sources (deuterium lamp for UV and tungsten lamp for Vis), a monochromator (diffraction grating or prism) to select specific wavelengths, and a detector, typically a photodiode or a photomultiplier tube (PMT) to measure the intensity of radiation transmitted through the sample. Typically, the monochromatic radiation is split by a beam splitter – the halved intensity passes through a quartz cuvette filled with a solution of the investigated substance, whereas the other one passes through a quartz cuvette containing the corresponding solvent, serving as a reference.

Within specific concentration range, the intensity of absorbed radiation obeys the Lambert-Beer law, provided as a linear Formula (1.2):

$$A = \varepsilon c l, \tag{1.2}$$

where:

- A – absorbance (a.u.);
- ε – molar absorption coefficient (M^{-1} cm^{-1});
- c – molar concentration (M);
- l – optical path length (cm).

As a consequence, having registered the calibration curve within the concentration range, one can estimate the concentration of the substance in the investigated solution, for which the absorbance was measured.

3.4.2. PL spectroscopy of lanthanide-doped materials

PL spectroscopy allows for the investigation of the optical properties of lanthanide-doped materials by analyzing their emission spectra upon excitation with an external light source of a specific wavelength, e.g., a xenon (Xe) arc lamp, a CW or pulsed laser, and monitoring their temporal evolution. When the energy of the incident photons matches the energy difference between electronic states, the ions transition from the ground state to a higher excited energy level. Various ET processes occurring within and between the ladder-like structures of rare-earth ions (e.g., UC, DC, CR) as well as the local environment of the dopant ions, influence their emissive properties. As a result, the PL spectra and decay curves, collected as the material relaxes back to its ground state, provide valuable insights into the electronic structure of the doped materials.

PL spectroscopy measurements are typically performed using a spectrometer on materials in various forms – thin films, powders, solutions, and suspensions. A sample, in either solid or liquid form, is excited by a Xe lamp, a CW or pulsed laser at a wavelength selected based on previously collected absorption/excitation characteristics (for more information, see Section 3.4.3). The excitation wavelength is set using a monochromator (only for Xe lamps) and further modulated with short-pass or long-pass optical filters (for both aforementioned light sources), ensuring that only the chosen wavelength reaches the sample. The emitted photons are then collected by an optical system consisting of lenses and mirrors, analyzed by another monochromator, and directed toward a detector (e.g., PMT) to record the emission spectrum. PL decay curves are typically recorded using the multichannel scaling (MCS) technique, which is based on detecting photon arrival times in discrete time bins.

The data collected from these measurements provide key parameters, such as emission band positions and excited-state LTs, revealing essential details about the photophysical properties of the investigated materials. This information helps optimize their performance in various applications, including bio-related ones.

3.4.3. PL excitation (PLE) spectroscopy

PLE spectroscopy provides information on wavelengths capable to excite higher energy states of lanthanide ions incorporated into luminescent phosphors or organic molecules.

As already mentioned in Section 2.2, f-f electronic transitions within robust energy level structures of lanthanide ions are generally forbidden by selection rules in free ions, but become partially allowed due to interactions with the host lattice. They appear in PLE spectra as narrow, sharp spectral lines, being a result of the outer 5s and 5p orbitals shielding effect, protecting 4f electrons from any external perturbations. Similarly, organic molecules such as dyes, absorb radiation over a broad wavelength range, covering UV and Vis regions. This behavior arises from the presence of chromophores in their molecular structure. Such functional groups interact with light owing to their conjugated π-electron systems. Upon irradiation, electrons in the chromophores are promoted to higher excited states. Since vibrational relaxation occurs spontaneously as a non-radiative energy loss, radiation at longer wavelengths is emitted, typically in the Vis or NIR regions. The shift in emission wavelength compared to excitation is known as the Stokes shift. Because emission can occur from different vibrational sublevels of the excited state to various vibrational levels of the ground state, the fluorescence spectrum of the dye appears as a broad band rather than a sharp peak, which strongly contrasts with the emission behavior of lanthanide ions.

The majority of setups to measure PLE are based on the right-angle (90°) geometry to minimize Rayleigh and Raman scattering of the excitation beam. The source of light, usually a Xe lamp, is located perpendicularly to the detector. It emits a continuous radiation spectrum (UV-Vis-NIR), from which a monochromator isolates selectively a specific excitation wavelength. Only when the energy of incident photons matches the energy difference between the ground state and a chosen higher excited state, the excitation occurs. Followingly, the excited energy levels depopulate, which is observed as emission bands peaking at its characteristic wavelengths.

Due to the need to meet specific experimental requirements, various measurement setups were employed in this study. The detailed description of each setup is provided in the particular chapters.

3.4.4. Fourier transform infrared spectroscopy (FT-IR)

IR spectroscopy is a non-destructive method used to determine the structure of organic molecules and identify their functional groups. It is based on measuring the absorption of IR radiation, which induces molecular vibrations, including stretching, bending, and twisting of chemical bonds. The specific frequencies at which a molecule absorbs strongly depend on the type of the bonds and the atomic masses of the elements involved, thus making IR spectroscopy a powerful tool for chemical identification in organic chemistry and materials science. However, since the principle approach of dispersive IR spectroscopy requires a few-minute-long measurement each time, Fourier transform infrared (FT-IR) spectroscopy was developed to shorten the acquisition time needed to capture the spectra within the broad span of IR frequencies. This method exploits an interferometric approach, where an interferometer modulates IR radiation before it reaches the detector. Instead of directly measuring absorption at individual frequencies, FT-IR collects an interferogram, recording intensity variations as a function of the optical path difference. As a consequence, the information from all IR wavelengths is recorded simultaneously and then processed with Fourier transform. With the mathematical formulas the collected raw data is swiftly converted into a conventional IR absorption spectrum with absorption peaks corresponding to specific molecular vibrations, usually denoted as characteristic *fingerprints* of different chemical compositions. IR spectra are unique for each organic compound as molecules differ in the number of atoms and their arrangement within molecular structure. This provides a valuable piece of information whether the processes conducted on materials surface, e.g., functionalization or etching, were completed successfully.

In the presented doctoral dissertation, the measurements were conducted with an FT-IR vacuum spectrometer Bruker Optic GmbH Vertex70v.

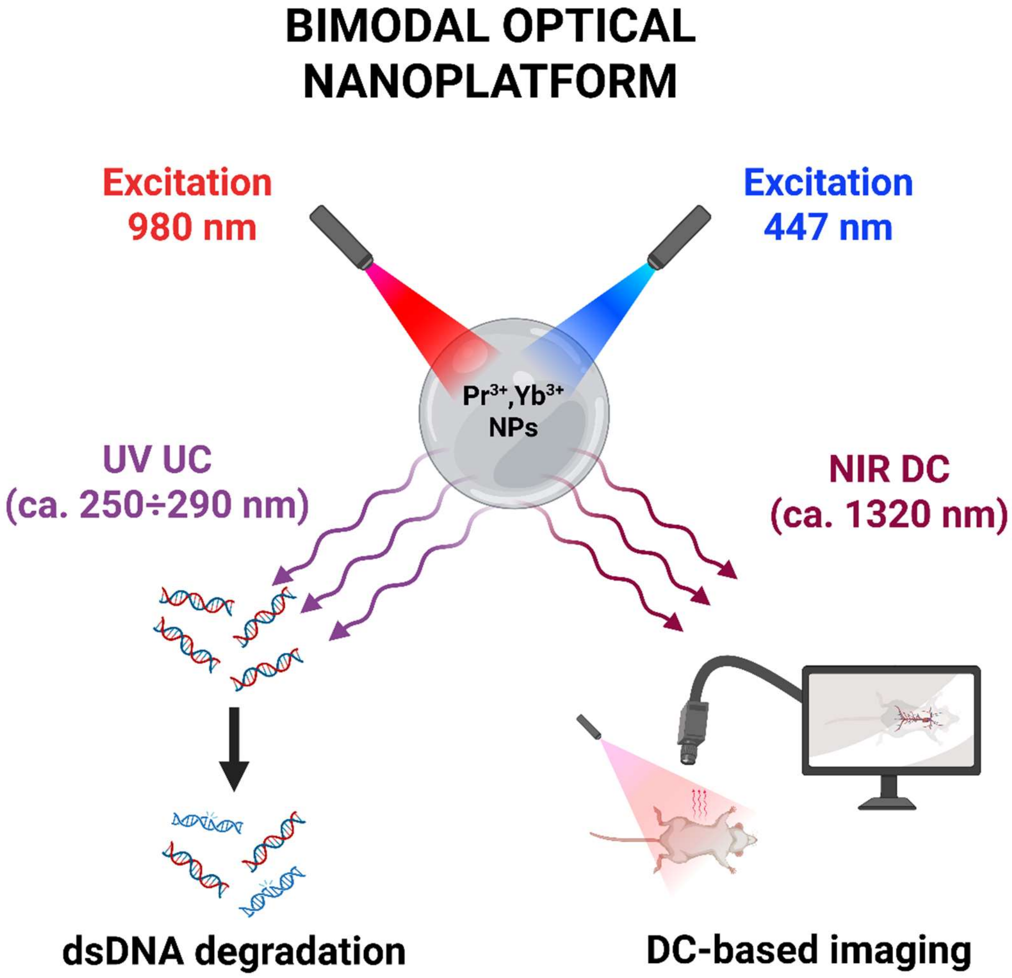

Fig. 13. The general concept of Pr^{3+}*,*Yb^{3+}*-co-doped β-*$NaYF_4$ *and* $LiYF_4$ *NPs as a dual optical functionality nanoplatform for biomedical purposes*

Chapter 4

Pr^{3+},Yb^{3+}-co-doped β-$NaYF_4$ and $LiYF_4$ NPs exhibiting concurrent Vis-to-UV UC and NIR-to-NIR DC for biomedical applications

In this chapter, I conduct a thorough evaluation of the application potential of Pr^{3+}-co-doped β-$NaYF_4$ and $LiYF_4$ NPs as dual optical functionality nanomaterials for biomedical applications (Fig. 13). These NPs have the capability to emit radiation concurrently in UV and NIR spectral ranges. Pr^{3+} ions, incorporated into nanocrystalline host matrices, exhibit Vis-to-UV UC emission under 447 nm CW excitation. The emission was registered with a custom spectroscopic setup designed for UV radiation detection. In two independent proof-of-concept experiments, I demonstrate that the up-converted UV radiation can be utilized to photodamage dsDNA. Additionally, by measuring the fluorescence of a dsDNA-labelling dye, I estimate the concentration of dsDNA remaining in the solution after exposure to UV-C radiation. This approach facilitates the identification of the most promising materials for prospective *in vitro* tests of photoinduced viruses and bacteria eradication, which is presented in Chapters 5 and 8 of the doctoral dissertation, respectively.

Conversely, co-doping of the studied materials with Yb^{3+} ions allows the NPs to be excited at 980 nm. ET between Yb^{3+} and Pr^{3+} ions results in NIR emission from the latter peaking at approximately 1320 nm, within the second window of biological tissue transparency. Bioimaging experiments conducted on a bovine tooth and chicken flesh provide solid evidence that NIR-to-NIR DC emission from Pr^{3+} ions is sufficiently intense and long-lasting to perform high-contrast and deep-tissue bioimaging, thus opens up the possibility for their use in prospective *in vivo* bioimaging applications.

The studied Pr^{3+}-co-doped β-$NaYF_4$ and $LiYF_4$ NPs offer dual optical functionality, enabling germicidal action through the interaction of up-converted UV-C radiation with DNA and RNA of bacteria, viruses, or other microorganisms of more complex structure. Simultaneously, they exhibit high-contrast NIR-II emission of long luminescence LTs which is suitable for bioimaging in both steady-state and time-gated modes. Therefore, the synthesized nanomaterials could be utilized as bimodal optical nanoplatforms for theranostic purposes in e.g., dentistry.

4.1. Introduction to the scientific problem

Lanthanide-doped NPs have recently emerged as intriguing nanomaterials for multiple biomedical applications. Owing to their unique optical properties stemming from a robust energy level structure, precise manipulation of the excitation-to-emission photon ratio is possible [92]. Hence, it allows for photon emission at any desired wavelength from UV, Vis, and NIR spectral ranges [93–96]. Moreover, straightforward wet chemistry synthesis methods of lanthanide-doped alkali-metal-based yttrium fluorides at nanoscale enable the control over their shape and size, which are important parameters for customizing the nanomaterials for specific bio-related applications, including targeted functionalization toward molecules sensing [97,98], imaging of biological systems [99–101], or microbial inactivation [102–104].

The vast majority of research papers on lanthanide-doped fluoride NPs for biomedical applications present them as efficient, non-cytotoxic *in vivo* bioimaging nanoprobes, some of which functionalized with antibodies to achieve targeted delivery [105–107]. The Yb^{3+}-, Nd^{3+}-, or Er^{3+}-doped NPs exploit emission bands in NIR-I and NIR-II, corresponding to the first and second window of biological tissue transparency, respectively. The radiation within these spectral ranges shows the feature of deep penetration through tissues due to their insignificant autofluorescence and reduced light scattering [108–110]. Additionally, NIR-II emission bands from lanthanide ions are characterized by sufficiently long luminescence LTs, which paves the way for high-quality images acquisition in both steady-state and time-gated modes [111]. Nevertheless, the research on lanthanide-doped NPs development exhibiting the NIR-to-NIR DC of the significantly increased yield is still ongoing. Naturally, as fluoride host matrices are proven to incorporate trivalent lanthanide ions without significant crystal lattice distortion due to matching ionic radii to the Y^{3+} ionic radius, NPs based on two or even three optically active rare-earth elements are thoroughly investigated [112,113].

For instance, the enhanced emission intensity in the NIR-II spectral region was shown by Nunes et al. for the Pr^{3+},Yb^{3+} ion combination in β-$NaYF_4$ NPs. It was proven that due to Yb^{3+} ions sensitization at 980 nm, followed by ET to Pr^{3+} ions, the NIR-to-NIR DC luminescence from the latter occurs at approximately 1320 nm [113]. It implies that Pr^{3+} ions are well-suited for bioimaging purposes. Nevertheless, the energy level structure of Pr^{3+} ions includes 4f5d level, after which excitation the emission in UV-C range is attainable. This energy level can be also excited by sequential absorption of two photons from 440÷490 nm spectral range due to energy difference matching between the levels, which eventually leads to Vis-to-UV UC emission [114]. It is noteworthy that the research area of lanthanide-based UV-C up-converting nanophosphors is yet largely undiscovered. Therefore, given the beneficial features of UV-C radiation in pathogens inactivation, as thoroughly described in Section 2.1.1, there is a strong need to investigate and engineer such nanomaterials for new and emerging biomedical applications.

What is intriguing about the Pr^{3+},Yb^{3+} pair is its potential to provide the NPs or MCs with dual functionality when incorporated into the nano- or microscale host matrix. The concurrent emission in UV-C and NIR spectral ranges occurring within a single lanthanide-doped NPs or MCs system has not been described in the literature. Therefore, my motivation to conduct research on this topic stems from its possible recognition as one of the significant contributions in the field of advanced luminescent nanomaterials. I hypothesized that by leveraging various photon management processes within Pr^{3+},Yb^{3+}-co-doped β-$NaYF_4$:Pr^{3+},Yb^{3+} and $LiYF_4$:Pr^{3+},Yb^{3+} NPs, the emission bands could occur in both regions of interest when corresponding laser excitation wavelengths are applied. Moreover, the prospective applications of such nanophosphors could be expanded, especially for theranostic purposes at infection sites caused by microorganisms. It implies that the UV-C radiation generated *in situ* could be harnessed for remarkably selective and localized antimicrobial therapy, owing to its capacity for targeted dsDNA degradation [115,116]. Meanwhile, the affected site could be precisely imaged using NIR radiation, providing exceptionally high contrast [117].

4.2. Chemicals and materials used

4.2.1. β-$NaYF_4$:Pr^{3+},Yb^{3+} and $LiYF_4$:Pr^{3+},Yb^{3+} NPs synthesis

For the β-$NaYF_4$ and $LiYF_4$ NPs synthesis the following chemicals were used: Pr_2O_3 (99.99%), Y_2O_3 (99.99%), Yb_2O_3 (99.99%), NaOH (≥ 98.0%), NH_4F (≥ 99.99%), Li_2CO_3 (≥ 90.0%), trifluoroacetic acid (reagent grade, ≥ 99%), acetic acid (pure for analysis, 99.5÷99.9%), oleic acid (technical grade, 90%), octadec-1-ene (technical grade, 90%), methanol (99%), ethanol (99.9%), chloroform, and acetone. All reagents were purchased from Sigma Aldrich and used without prior purification.

The β-$NaYF_4$:Pr^{3+},Yb^{3+} NPs series was prepared in accordance with the protocol described in Section 3.1.1. The masses of the corresponding solid compounds used in the syntheses were provided below in Table 2.

Table 2. Summary for the amount of solid compounds used to synthesize Pr^{3+},Yb^{3+}-co-doped β-$NaYF_4$: Pr^{3+},Yb^{3+} NPs series

β-$NaYF_4$ NPs dopants	**Compound mass [g]**				
	Pr_2O_3	**Y_2O_3**	**Yb_2O_3**	**NaOH**	**NH_4F**
1% Pr^{3+}, 5% Yb^{3+}	0.0067	0.4245	0.0394	0.2000	0.2964
1% Pr^{3+}, 10% Yb^{3+}		0.4019	0.0788		
1% Pr^{3+}, 20% Yb^{3+}		0.3568	0.1576		
1% Pr^{3+}, 40% Yb^{3+}		0.2665	0.3153		
1% Pr^{3+}, 60% Yb^{3+}		0.1761	0.4729		

For the $LiYF_4$:Pr^{3+},Yb^{3+} NPs series the protocol from Section 3.1.3 was applied. The masses of corresponding solid compounds used in the syntheses were charted below as Table 3.

Table 3. Summary for the amount of solid compounds used to synthesize Pr^{3+},Yb^{3+}-co-doped $LiYF_4$: Pr^{3+},Yb^{3+} NPs series

$LiYF_4$ NPs dopants	**Compound mass [g]**			
	Pr_2O_3	**Y_2O_3**	**Yb_2O_3**	**Li_2CO_3**
2% Pr^{3+}, 2% Yb^{3+}	0.0083	0.2710	0.0099	0.1663
2% Pr^{3+}, 5% Yb^{3+}		0.2625	0.0246	
2% Pr^{3+}, 10% Yb^{3+}		0.2484	0.0493	
2% Pr^{3+}, 20% Yb^{3+}		0.2202	0.0985	

4.2.2. dsDNA photodegradation with up-converted UV-C radiation

Salmon sperm dsDNA was purchased from Sigma Aldrich and used without further purification. The dsDNA solution (concentration: 50 $\mu g\ mL^{-1}$) was prepared in Milli-Q quality water (resistivity: 18.2 $M\Omega\ cm^{-1}$ at 25 °C) right before the measurements.

Hoechst 33258 dye was purchased from Sigma Aldrich and used without prior purification. The stock solution of Hoechst 33258 at the concentration of 1 $mg\ mL^{-1}$ was prepared in Milli-Q quality water (resistivity: 18.2 $M\Omega\ cm^{-1}$ at 25 °C).

4.2.3. NIR-to-NIR DC-based bioimaging

To demonstrate the usability of the selected β-$NaYF_4:Pr^{3+},Yb^{3+}$ and $LiYF_4:Pr^{3+},Yb^{3+}$ colloidal NPs, an oral cavity resembling model was applied. It consisted of two types of biological tissues – a bovine tooth with a cavity drilled along its axis and a thin piece of chicken breast. All animal tissues were handled with the utmost care and in the accordance with the regulations introduced by the Administrative Panel of Shenzhen University on Laboratory Animal Care and confirmed by the Animal Ethical and Welfare Committee at Shenzhen University (approval no. SZUHSC-01).

4.3. Characterization methods

4.3.1. Crystal structure

The crystal structure of all synthesized β-$NaYF_4:Pr^{3+},Yb^{3+}$ and $LiYF_4:Pr^{3+},Yb^{3+}$ colloidal NPs was investigated with an STOE powder X-ray diffractometer. The NPs suspensions were drop-casted on the Si-wafer holder to form the uniform layer of solid residue after chloroform evaporation. The Ge-filtered $CuK\alpha_1$ radiation operated in the 15-75° 2θ range in the Bragg-Brentano geometry.

4.3.2. Morphology and size distribution

The TEM images were captured using an FEI Tecnai G^2 20 X-TWIN TEM at the Faculty of Chemistry at University of Wroclaw, Poland. Before drop-casting onto the carbon-coated Cu grids, all colloidal suspensions were diluted in 2 mL of chloroform. The NPs size distribution analysis was performed in OriginPro Software as the diameter size of 100 NPs in the micrographs had been measured in ImageJ Software.

4.3.3. Spectroscopic features

The Vis-to-UV UC spectra of the samples drop-casted onto a glass slide and then air-dried were recorded under ambient conditions with the custom setup assembled in the Institute of Advanced Materials at Wrocław University of Science and Technology, Poland. The Vis-to-UV UC radiation was induced with either a 447 nm or 980 nm fiber-coupled semiconductor laser diode (CNI MDL-XD-447 or CNI FC-W-980A, respectively). The laser was focused with a 200 mm focal length lens so that the power density at the focal point was ~2000 W cm^{-2}. The emitted UV radiation was captured with the UV-grade fused silica lenses. Additionally, into the optical path a set of filters (two short-pass filters with cut-off wavelengths at 400 nm and 425 nm, respectively, and a UV band-pass filter) was inserted for blocking the scattered laser light from reaching the detection setup. The Vis-to-UV UC spectra were analyzed with a Horiba iHR320 grating monochromator (focal length – 320 nm, grating density – 1800 lines mm^{-1}, blaze wavelength – 330 nm), coupled with a pre-amplified PMT (Hamamatsu H5784-04). The custom setup sensitivity enhancement was achieved *via* synchronous phase-sensitive detection. Additionally, the laser light modulation at 40 Hz using a mechanical chopper was introduced to enable the intensity enhancement. Emission intensity was measured indirectly *via* monitoring the PMT output voltage with a lock-in amplifier (EG&G 7260).

The Stokes PL spectra in Vis spectral range (λ_{ex} = 447 nm) were recorded with FLS980 Edinburgh Instruments spectrophotometer in Czerny-Turner configuration. The NPs dispersed in chloroform were excited with a 450 W Xe arc lamp in ambient conditions. Additionally, the anti-Stokes NIR-to-Vis UC spectra were captured, having been induced with a 980 nm CW semiconductor laser diode (8 W, Spectra Laser, Poland).

The NIR emission spectra of the diluted β-$NaYF_4$:Pr^{3+},Yb^{3+} and $LiYF_4$:Pr^{3+},Yb^{3+} NPs suspended in chloroform (concentration ~100 mg mL^{-1}) were recorded in ambient conditions with a fiber-coupled, thermoelectrically cooled InGaAs CCD spectrometer (Hamamatsu C9913GC). A two-lens optical system collected the PL emission and coupled it to the fiber. Additionally, in order to cut off the scattered light, a 1050 nm long-pass filter was introduced.

4.3.4. Qualitative validation of dsDNA photodegradation *via* up-converted UV radiation

The potential applicability of the Vis-to-UV UC emission generated within the synthesized β-$NaYF_4$:Pr^{3+},Yb^{3+} and $LiYF_4$:Pr^{3+},Yb^{3+} NPs was qualitatively validated in a proof-of-concept experiment of dsDNA degradation. dsDNA is prone to absorb UV-C radiation, which leads to the eventual bonds breakage between the strands [118]. As a consequence, the amount of dsDNA in the solution decreases. It was confirmed that at the same time dsDNA absorbance, peaking at 260 nm, tends to increase [119]. Therefore, the idea of the proposed proof-of-concept experiment is based on observation of the so-called hyperchromic effect *via* UV-Vis absorption spectra registration of dsDNA solutions both non-exposed and exposed to up-converted UV-C radiation generated by the synthesized nanomaterials.

The setup utilized for dsDNA Vis-to-UV UC-based photodegradation (presented in Fig. 14) included a fiber-coupled 447 nm CW laser diode, a quartz cuvette containing 0.5 mL of dsDNA solution (concentration: 50 µg mL^{-1}) and a thin layer of NPs drop-casted and dried on a glass substrate. The glass slide was positioned in close proximity behind the cuvette. During each experiment the collimated laser beam with the power density of ~11 W cm^{-2} at the focal point traversed the solution and reached the glass substrate. Under Vis irradiation the nanomaterials generated anti-Stokes UV-C radiation within the ladder-like energy level structure of trivalent Pr^{3+} ions incorporated into the host matrices as dopants. The dsDNA solution was exposed to the backscattered up-converted UV-C radiation for either 20 or 40 min; after that time its UV-Vis absorption spectra of the dsDNA solution were collected with a JASCO V650 spectrophotometer (scan rate: 400 nm min^{-1}).

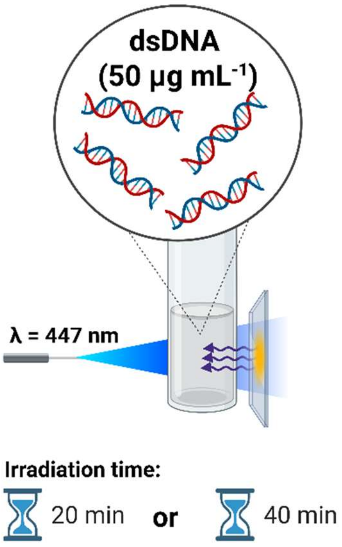

Fig. 14. A proof-of-concept experiment of Vis-to-UV UC-based dsDNA denaturation

4.3.5. Quantitative validation of dsDNA photodegradation *via* up-converted UV radiation

The method based on UV-Vis absorption spectra registration allows only to confirm whether dsDNA denaturation occurs under exposition to UV-C radiation. However, the amount of dsDNA damaged within the specified period of time remains unknown. Nevertheless, this piece of information could be useful in order to compare the Vis-to-UV up-converting materials efficiency and thus identify the most promising candidates for further biological applications, such as Vis-to-UV UC-based bacteria and viruses photoeradication. Hence, within the research scope of my doctoral dissertation there was a strong need to utilize a method to quantitatively measure the dsDNA concentration after exposition to the up-converted UV-C radiation.

For that purpose, I chose a well-described protocol of fluorescence analysis of dsDNA unwinding (FADU) [120]. It requires the utilization of organic dye molecules which are only fluorescent while intercalating dsDNA and simultaneously not binding to its photodegradation products, e.g., single-stranded DNA (ssDNA). The dye applied in my studies was Hoechst 33258, widely used in molecular biology and biochemistry as a dsDNA staining agent [121,122]. If only bound to the minor groove of dsDNA, it exhibits fluorescence peaking at ~460 nm when excited at the absorption maximum of 365 nm. Additionally, the fluorescence signal tends to be strong, even though the dye concentration in the investigated solution is ultralow, i.e., 1÷10 μg mL^{-1}. The chemical structure, UV-Vis absorption spectrum, and fluorescence spectrum of Hoechst 33258 dye were provided in Fig. 15a-b.

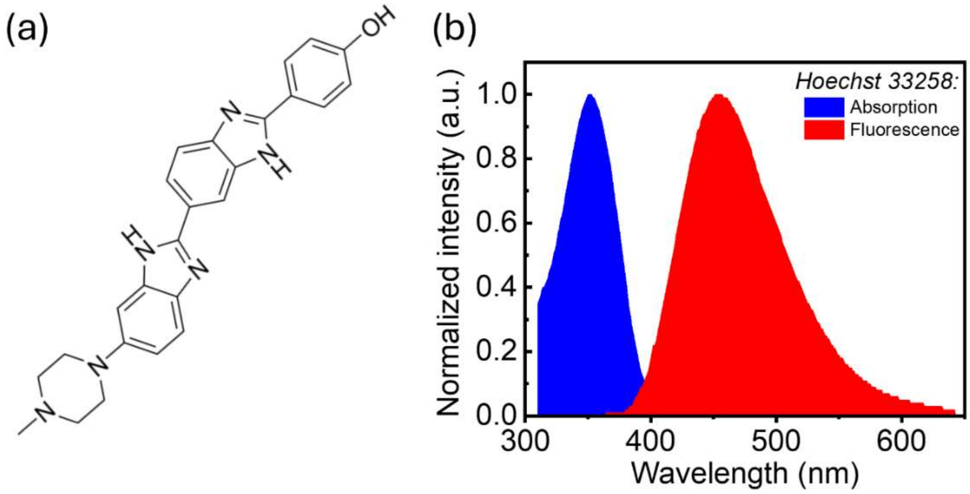

Fig. 15. Hoechst 33258 dye:
(a) Chemical structure, (b) UV-Vis absorption spectrum and fluorescence spectrum

The general concept of quantitative validation of dsDNA photodegradation is derived from the fluorescence spectra registration of the dye bound to dsDNA. The procedure could be divided into 5 main steps, which are shortly described below:

- ***Step 1.*** Calibration curve preparation

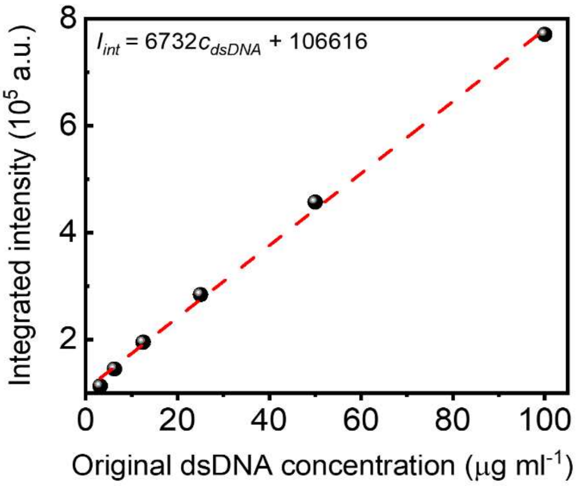

Fig. 16. Calibration curve for establishing the concentration of dsDNA remaining after the exposition to upconverted UV-C radiation. c_{dsDNA} is issued in μg mL^{-1}

Hoechst 33258 is fluorescent only when attached to dsDNA and its fluorescence intensity increases linearly with the concentration of dsDNA in the solution. Therefore, fluorescence spectra for a series of dsDNA solutions at specific model concentrations (i.e., 3.125, 6.25, 12.5, 25, 50, and 100 μg mL^{-1}) were registered before the start of the irradiation experiment. After their integration, the calibration curve integrated intensity I_{int} vs. dsDNA concentration c_{dsDNA} was constructed, as depicted in Fig. 16. Based on this calibration curve, the dsDNA concentration in the irradiated solution was then estimated.

- ***Step 2.*** dsDNA solution irradiation

  The quartz cuvette containing 0.5 mL of dsDNA solution (concentrated at 50 μg mL^{-1}) was placed in the experimental setup for qualitative validation of dsDNA photodegradation, described in Section 4.3.4. The exposition time to up-converted UV-C radiation was either 20 or 40 min.

- ***Step 3.*** dsDNA intercalation with the dye

  After the irradiation for specified time, 250 μL of the solution was sampled and mixed with 2 mL of the Hoechst 33258 dye assay, prepared in accordance with the protocol described by S.R. Gallagher [123]. To ensure that all dsDNA molecules remaining in the solution after the irradiation could be intercalated by the dye molecules, the mixture prepared in a quartz cuvette was gently shaken. Furthermore, within the procedure optimization it was established that the mixture ought to be left for 2÷3 min to allow the dye molecules to bind with dsDNA.

- ***Step 4.*** Fluorescence registration

  The quartz cuvette was placed in a Hitachi F-4500 fluorescence spectrophotometer. The fluorescence of Hoechst 33258 bound to dsDNA was induced upon 365 nm excitation, i.e., in the dye maximum absorption. The fluorescent emission was measured from 385 to 635 nm with a scan rate 100 nm min^{-1}.

- ***Step 5.*** Data post-processing

  The collected fluorescence spectra of the samples exposed to the up-converted UV-C radiation generated by the synthesized nanomaterials was integrated. Knowing I_{int} and having the calibration curve from Fig. 16, I was able to the dsDNA concentration left in the solution after the irradiation.

4.3.6. NIR-to-NIR DC bioimaging application

The NIR-II PL bioimaging was performed with a short-wave infrared (SWIR) imaging camera (Xeva-1.7-320, Xenics, Belgium) equipped with focusing optics (TECM55MPW, Computar, USA) for signal enhancement. The bovine tooth, filled with the selected NPs samples and covered with thin chicken breast tissue, was irradiated with the unfocused 980 nm laser beam with power density of 100 mW cm^{-2} (laser diode QSP-975-10, QPhotonics, USA). Bioimaging was performed in accordance with the regulations introduced by the Administrative Panel of Shenzhen University on Laboratory Animal Care and confirmed by the Animal Ethical and Welfare Committee at Shenzhen University (approval no. SZUHSC-01).

4.4. Results and discussion

4.4.1. Crystal structure and morphology characterization

The utilization of standard thermal decomposition methods of precursors in high boiling points surfactants resulted in formation of β-$NaYF_4$ and $LiYF_4$ NPs. They were doped with a fixed low molar concentration of Pr^{3+} ions (1% or 2% to minimize the possibility of concentration quenching and to maximize the Pr^{3+} ions emission intensity in all spectroscopic studies) and with Yb^{3+} ions in a broad range of molar concentration (1%, 2%, 5%, 10%, 20%, 40%, and 60%). The XRD measurements (Fig. 17a-b) of the dried samples revealed the matching peaks to those observed for undoped β-$NaYF_4$ (space group: *P*-6) and $LiYF_4$ (space group: $I4_1$/a) host matrices standard patterns (ICSD #51916 and #27896, respectively). It is noteworthy that both host matrices were prone to incorporate substantial amount of Yb^{3+} ions along with low concentration of Pr^{3+} ions without significant crystal lattices alteration. It is due to the similar ionic radii of Y^{3+}, Pr^{3+}, and Yb^{3+} ions of ninefold coordination for β-$NaYF_4$ host matrix (1.075 Å, 1.179 Å and 1.042 Å, respectively) and of eightfold coordination for $LiYF_4$ host matrix (1.019 Å, 1.126 Å, and 0.985 Å, respectively) [124].

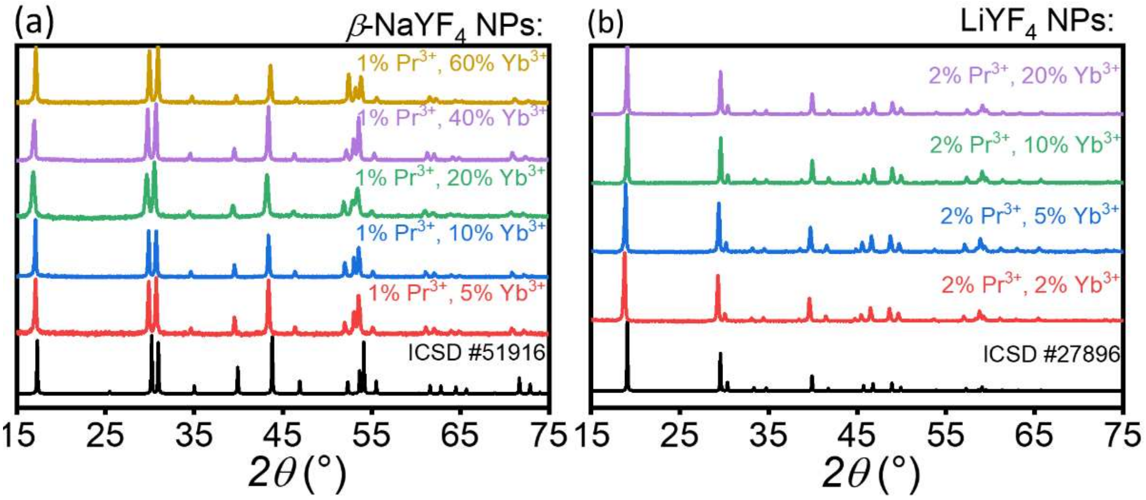

Fig. 17. XRD patterns of the synthesized Pr^{3+},Yb^{3+}-co-doped (a) β-$NaYF_4$ and (b) $LiYF_4$ NPs series, with the theoretical patterns of undoped host matrices provided

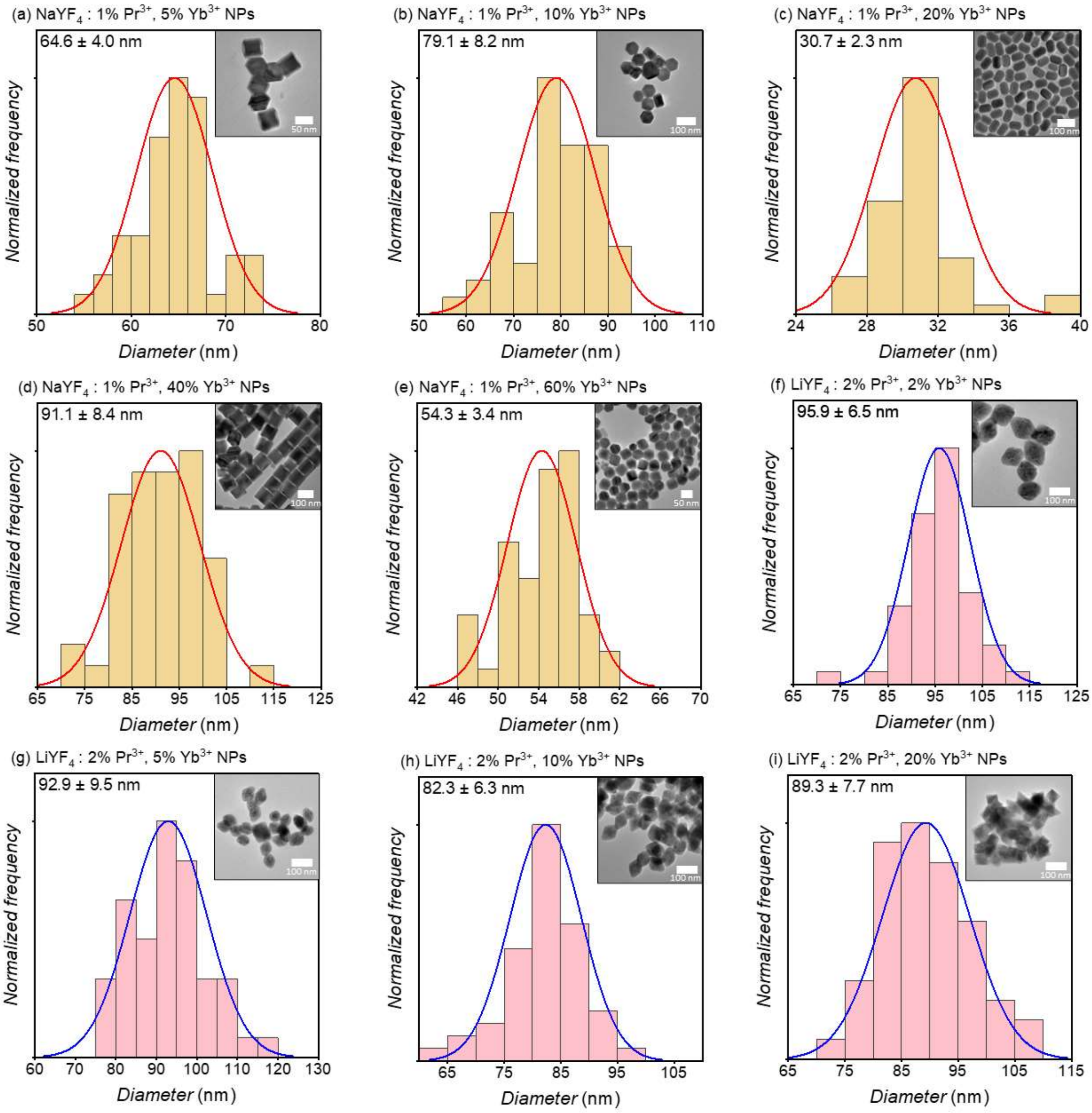

Fig. 18. Size distribution histograms of Pr^{3+},Yb^{3+}-co-doped (a-e) β-$NaYF_4$ and (f-i) $LiYF_4$ NPs series. In the right corner of each histogram, as the inset, the corresponding TEM images were provided

After capturing TEM images of the synthesized NPs, I analyzed their mean size distribution by plotting size distribution histograms and fitting Gaussian distribution curves. An overview of the histograms, along with TEM images (added as insets of each histogram) is provided in Fig. 18a-e for β-$NaYF_4$:Pr^{3+},Yb^{3+} NPs and in Fig. 18f-i for $LiYF_4$:Pr^{3+},Yb^{3+} NPs. All of the synthesized β-$NaYF_4$:Pr^{3+},Yb^{3+} NPs batches contained NPs of uniform size distribution, exhibiting hexagonal shape. The mean diameter sizes were as follows: 64.6 ± 4.0 nm (for β-$NaYF_4$:1%Pr^{3+},5%Yb^{3+}), 79.1 ± 8.2 nm (for β-$NaYF_4$:1%Pr^{3+},10%Yb^{3+}), 30.7 ± 2.3 nm (for β-$NaYF_4$:1%Pr^{3+}, 20%Yb^{3+}), 91.1 ± 8.4 nm (for β-$NaYF_4$:1%Pr^{3+},40%Yb^{3+}), and 54.3 ± 3.4 nm (for β-$NaYF_4$:1%Pr^{3+},60%Yb^{3+}). On the contrary, the obtained $LiYF_4$:Pr^{3+},Yb^{3+} NPs were tetragonal, which is consistent with the $LiYF_4$ NPs synthesized by Chen et al [25].

The mean diameter size of $LiYF_4$ NPs was as follows: 95.9 ± 6.5 nm (for $LiYF_4$:2%Pr^{3+}, 2%Yb^{3+}), 92.9 ± 9.5 nm (for $LiYF_4$:2%Pr^{3+},5%Yb^{3+}), 82.3 ± 6.3 nm (for $LiYF_4$:2%Pr^{3+}, 10%Yb^{3+}), and 89.3 ± 7.7 nm (for $LiYF_4$:2%Pr^{3+},20%Yb^{3+}).

4.4.2. Spectral characterization

In the next step, the spectroscopic properties of the synthesized β-$NaYF_4$:Pr^{3+},Yb^{3+} and $LiYF_4$:Pr^{3+},Yb^{3+} NPs were investigated. For the better chapter clarity, the energy level diagrams of Pr^{3+} and Yb^{3+}, with all radiative and non-radiative transitions, were provided in Fig. 19a-b.

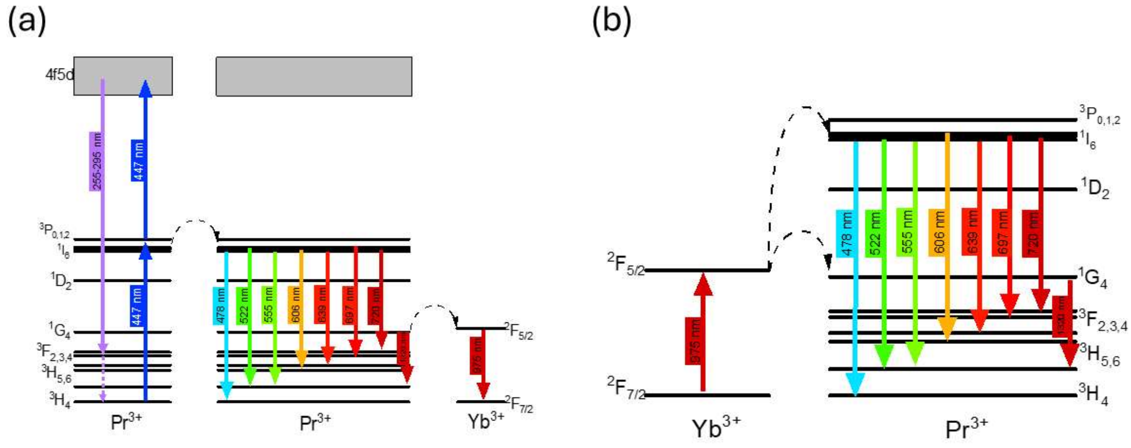

Fig. 19. Energy level diagrams with radiative and non-radiative transitions occurring in Pr^{3+} and Yb^{3+} ions incorporated into β-$NaYF_4$ and $LiYF_4$ NPs under (a) 447 nm excitation, (b) 975 nm excitation

Since Pr^{3+} ions exhibit strong absorption bands in 440÷490 nm spectral range, I utilized the 447 nm wavelength as the excitation wavelength in my research [125]. The radiation emitted by either a Xe lamp or a laser diode induced $^3H_4 \rightarrow {}^3P_J$ electronic transitions in the energy level structure of Pr^{3+} ions. In the Vis-to-Vis Stokes PL spectra under 447 nm Xe lamp excitation for both types of NPs typical f-f emission lines from Pr^{3+} ions peaking at ca. 478, 522, 555, 606, 639, 697, and 720 nm were observed (Fig. 20a-b). These emission lines corresponded to $^3P_0 \rightarrow {}^3H_4$, $^1I_6 \rightarrow {}^3H_5$, $^3P_1 \rightarrow {}^3H_5$, $^3P_0 \rightarrow {}^3H_6$, $^3P_0 \rightarrow {}^3F_2$, $^3P_1 \rightarrow {}^3F_3$, and $^3P_0 \rightarrow {}^3F_4$ transitions, respectively, (for energy level structure of Pr^{3+} ions see Fig. 19a) and were consistent with the ones reported for Pr^{3+},Yb^{3+}-co-doped fluoride phosphate glasses [126]. Within the β-$NaYF_4$:Pr^{3+},Yb^{3+} NPs series the highest emission intensity for all bands was registered for β-$NaYF_4$:1%Pr^{3+},5%Yb^{3+} NPs, whereas within the $LiYF_4$:Pr^{3+},Yb^{3+} NPs series for $LiYF_4$:2%Pr^{3+},2%Yb^{3+} NPs. Additionally, Yb^{3+} ions concentration increase in the host matrix led to the overall emission intensity decrease, which could be connected with ET from the excited Pr^{3+} ions to Yb^{3+} ions in their ground state, as suggested by Borrero-González et al [127]. The PL was strongly quenched at lower Yb^{3+} ions concentration (i.e., 20%) for $LiYF_4$ host matrix, in which Pr^{3+} ions were co-doped at 2%, meanwhile this effect was observed for Yb^{3+} ions at the concentration of 40% in β-$NaYF_4$ host matrix. Additionally, the same emission lines were registered under 980 nm laser excitation (see Fig. 20c-d for spectra and Fig. 19b for energy level structures of Pr^{3+} and Yb^{3+} ions). It implies that after $^2F_{7/2}\rightarrow{}^2F_{5/2}$ transition in Yb^{3+}, the ions were able to transfer energy to neighboring Pr^{3+} ions. The multiple ET processes allowed by the match between NIR photon energy and energy difference between corresponding energy levels as well as sufficiently long LTs of the excited states in Pr^{3+} ions resulted in the ^3P_J excited states population, thus NIR-to-Vis UC emission occurred. Primarily, for β-$NaYF_4$:Pr^{3+},Yb^{3+} NPs the UC emission intensity increased with the increase of Yb^{3+} ions concentration to reach the maximum emission intensity for β-$NaYF_4$:1%Pr^{3+},10%Yb^{3+} NPs. The further co-doping resulted in the UC of lower magnitude for all emission bands, which is in good agreement for other Pr^{3+},Yb^{3+}-co-doped materials, e.g., for yttria-stabilized zirconia single crystals [128].

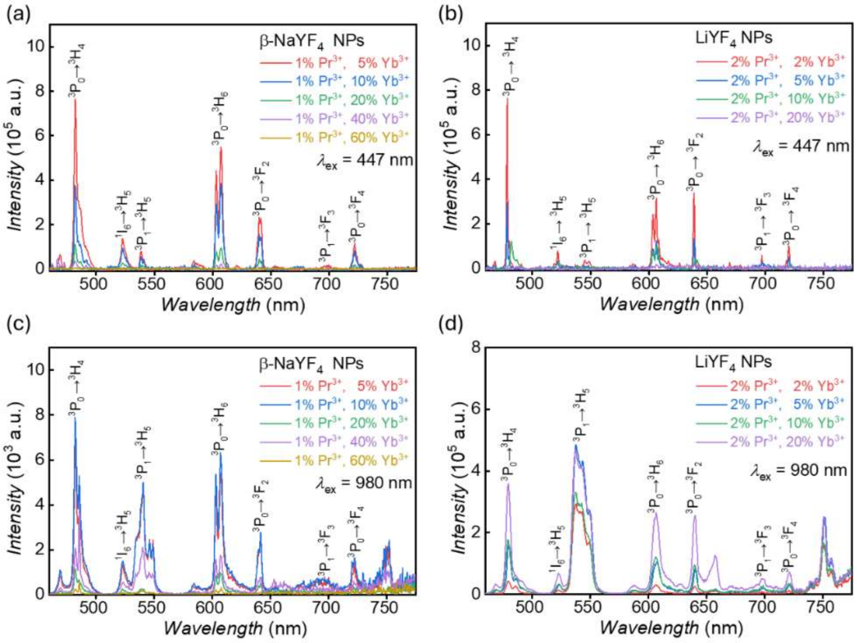

Fig. 20. Vis emission spectra of β-$NaYF_4$:Pr^{3+},Yb^{3+} (left column) and $LiYF_4$:Pr^{3+},Yb^{3+} NPs (right column), dispersed in chloroform. (a),(b) Vis-to-Vis Stokes PL spectra (λ_{ex}=447 nm, Xe lamp) (c),(d) NIR-to-Vis UC emission spectra (λ_{ex}=980 nm, laser diode)

It is noteworthy that while Pr^{3+}-doped MCs and bulk materials have been shown to emit Vis-to-UV UC radiation, knowledge on nanomaterials exhibiting such functionality remains scarce [59,129]. Therefore, I investigated the ability of the synthesized β-$NaYF_4$:Pr^{3+},Yb^{3+} and $LiYF_4$:Pr^{3+},Yb^{3+} NPs, drop-casted onto glass substrates and air-dried, to sequentially absorb two 447 nm photons and emit up-converted UV-C radiation (Fig. 21a-b). The first photon leads to the population of ^3P_J states in Pr^{3+} ions, with the LTs of these excited states being long enough to allow the absorption of the second photon. Consequently, the 4f5d excited state is populated. Its depopulation resulted in UV-C emission band peaking at *ca.* 275 nm due to 4f5d→^3H_J/^3F_J transitions (see energy level diagram of Pr^{3+} ions in Fig. 19a). Spectral analysis revealed that the optimal molar concentration of Yb^{3+} ions in both investigated host matrices was 10% and the sequential two-photon absorption was proven to be a convenient method of inducing UV-C UC emission in Pr^{3+}-co-doped materials. Co-doping with higher amounts of Yb^{3+} ions reduced Vis-to-UV UC emission intensity from both host matrices, especially for β-$NaYF_4$, in which 40% mol or more of Yb^{3+} ions quenched UC emission. On the contrary, sequential absorption of multiple NIR photons, aiming for NIR-to-UV UC emission in the investigated NPs series (Fig. 21c-d) was not attainable, even though ET between Yb^{3+} and Pr^{3+} ions was proven to occur (*vide supra*). The reason is connected with the high value of energy mismatch between the 980 nm photon energy and the energy difference between ^3P_J and 4f5d excited states (see energy level diagrams of Pr^{3+} and Yb^{3+} ions in Fig. 19b).

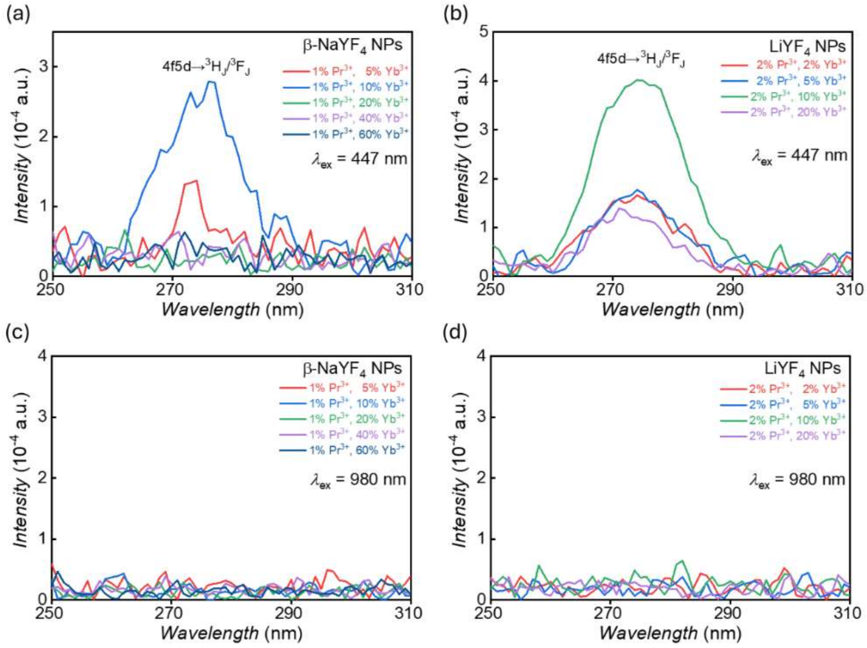

Fig. 21. UC spectra of β-$NaYF_4$:Pr^{3+},Yb^{3+} (left column) and $LiYF_4$:Pr^{3+},Yb^{3+} NPs (right column)
(a),(b) Vis-to-UV UC emission, induced under 447 nm excitation (laser diode)
(c),(d) NIR-to-UV UC emission, induced under 980 nm excitation (laser diode)

Not only did the absorption of 447 nm photon induce Vis-to-Vis Stokes PL from the synthesized NPs, but also emissions in NIR-I and NIR-II spectral regions

(Fig. 22a-b). Whereas the latter occurred at ca. 1320÷1325 nm within ladder-like energy level structure of Pr^{3+} ions ($^1G_4 \rightarrow {}^3H_5$ transition, the bands were provided in insets at the tenfold magnification of Fig. 22a-b, for the energy level structures of Pr^{3+} and Yb^{3+} ions see Fig. 19a), the former was the result of ET from the excited ^3P_J state of Pr^{3+} ion to $^2F_{5/2}$ energy level of Yb^{3+} ion and consequently $^2F_{5/2} \rightarrow {}^2F_{7/2}$ transition was observed as a band peaking at ca. 1000 nm. This constitutes the strong evidence on ET between Pr^{3+} and Yb^{3+} ions, which could occur interchangeably, regardless of the excitation wavelength and thus excited ionic species. The most intense emission bands within each synthesis series were observed for β-$NaYF_4$:1%Pr^{3+},10%Yb^{3+} NPs and $LiYF_4$:2%Pr^{3+}, 20%Yb^{3+} NPs.

Furthermore, Yb^{3+} ions sensitized under 975 nm excitation provided the NIR-II emission from Pr^{3+} ions incorporated into both host matrices (Fig. 22c-d). The $^1G_4 \rightarrow {}^3H_5$ transition arose from the $^2F_{5/2}$ (Yb^{3+})$\rightarrow$$^1G_4$ (Pr^{3+}) ET (see Fig. 19b for the energy level structures of Pr^{3+} and Yb^{3+} ions) and, as a result, the emission band spanned between 1250÷1450 nm with the maximum intensity at ca. 1325 nm for the β-$NaYF_4$:Pr^{3+},Yb^{3+} NPs series and ca. 1320 nm for the $LiYF_4$:Pr^{3+},Yb^{3+} NPs series. The similar findings were reported for the 980 nm sensitized Pr^{3+},Yb^{3+},Ho^{3+}-co-doped CSS β-$NaGdF_4$ NPs, differing in the spatial ions distribution in the core and shells [130].

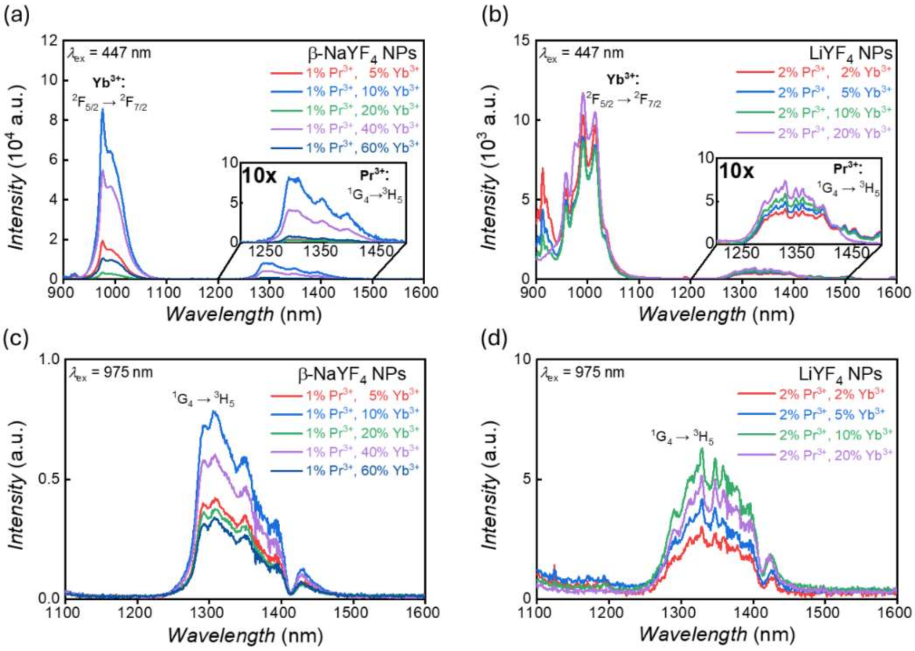

Fig. 22. NIR emission of β-$NaYF_4$:Pr^{3+},Yb^{3+} (left column) and $LiYF_4$:Pr^{3+},Yb^{3+} NPs (right column)
(a)(b) Vis-to-NIR DC spectra induced under 447 nm excitation (laser diode)
(c)(d) NIR-to-NIR DC spectra induced under 975 nm excitation (laser diode)

Additionally, upon 975 nm pulsed laser excitation, the luminescence decay curves for $^2F_{5/2} \rightarrow ^2F_{7/2}$ transition in Yb^{3+} ions (Fig. 23a-b) and $^1G_4 \rightarrow ^3H_5$ transition occurring in Pr^{3+} ions (Fig. 23c-d) were recorded for the synthesized β-$NaYF_4$:Pr^{3+},Yb^{3+} and $LiYF_4$:Pr^{3+},Yb^{3+} NPs series. The former were registered at 1000 nm for both host matrices, whereas the latter were registered at 1325 nm and 1320 nm for β-$NaYF_4$ and $LiYF_4$, respectively. All the curves were approximated with a single exponential model to extract the LT values (τ), which were summarized in insets of each Fig. 23a-d as a function of Yb^{3+} ions concentration. The Yb^{3+}:$^2F_{5/2}$ excited state LT was shorter as more Yb^{3+} ions were incorporated into β-$NaYF_4$ host (Fig. 23a), the highest value was extracted for β-$NaYF_4$:1%Pr^{3+},5%Yb^{3+} NPs (171 µs) and the lowest one for β-$NaYF_4$:1%Pr^{3+},60%Yb^{3+} NPs (8 µs). Such decrease in LT values could be connected with concentration quenching between lanthanide ions [131].

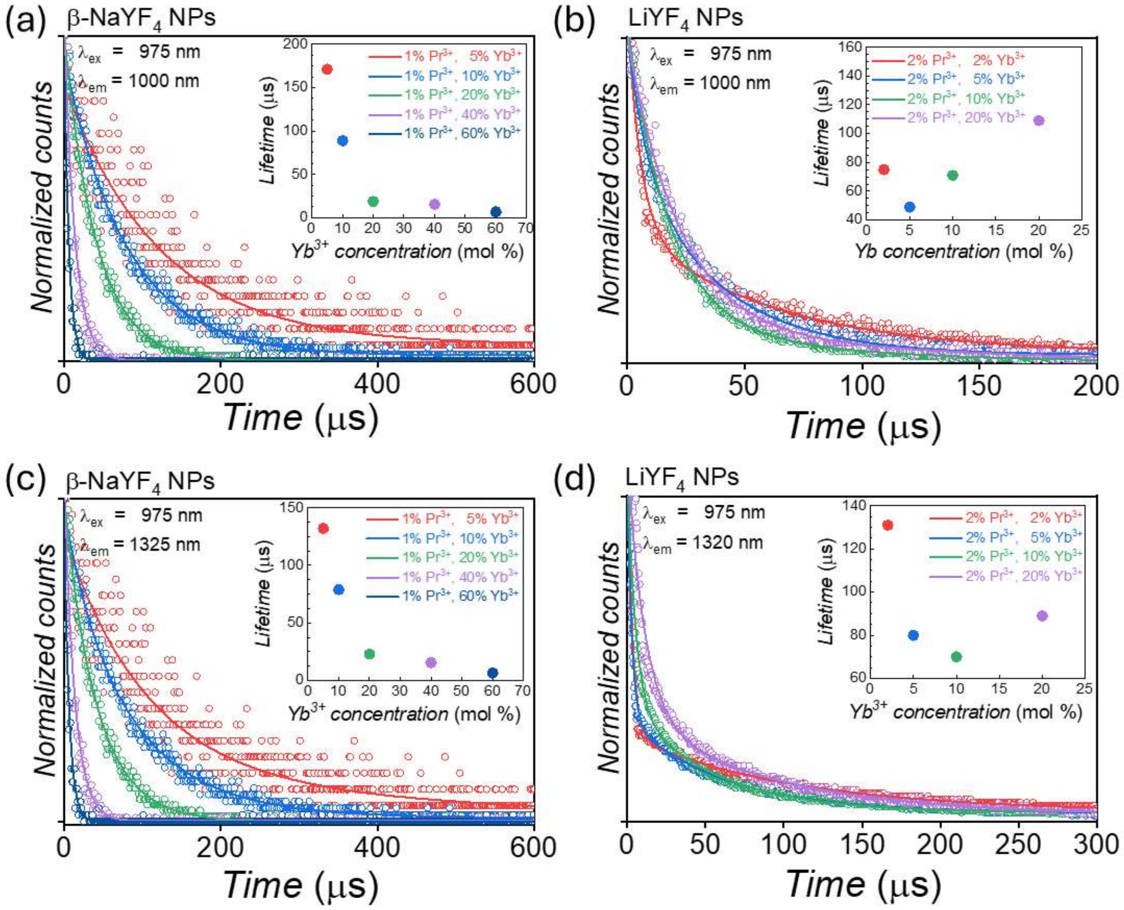

Fig. 23. Normalized luminescence decay curves induced under 975 nm pulse laser, registered for (a)(b) Yb^{3+}:$^2F_{5/2}$ excited energy level at 1000 nm, corresponding to $^2F_{5/2} \rightarrow ^2F_{7/2}$ transition (c)(d) Pr^{3+}:$^1G_4$ excited energy level at 1325 and 1320 nm, corresponding to $^1G_4 \rightarrow ^3H_5$ transition for β-$NaYF_4$:Pr^{3+},Yb^{3+} NPs (left column) and $LiYF_4$:Pr^{3+},Yb^{3+} NPs (right column) Insets: LT values as a function of Yb^{3+} molar concentration

4.4.3. The results of proof-of-concept experiments

For enhanced clarity, the nanomaterials chosen for the proof-of-concept experiments are denoted hereinafter as β-$NaYF_4:Pr^{3+},Yb^{3+}$ NPs (for β-$NaYF_4:1\%Pr^{3+},10\%Yb^{3+}$ NPs) and $LiYF_4:Pr^{3+},Yb^{3+}$ NPs (for $LiYF_4:2\%Pr^{3+},10\%Yb^{3+}$ NPs).

The UV-Vis absorption spectrum of dsDNA solution peaks in UV-C region at approximately 260 nm and partially overlaps with the registered Vis-to-UV UC emission spectra of β-$NaYF_4:Pr^{3+},Yb^{3+}$ and $LiYF_4:Pr^{3+},Yb^{3+}$ NPs, as illustrated in Fig. 24. The interaction of UV-C radiation with dsDNA leads to bond breakage between the strands and consequent unwinding of the dsDNA molecule. In more complex systems, such as microorganisms, the formed photodegradation products are irreplicable. It implies that when exposed to UV-C radiation, microbes are no longer able to reproduce, which ultimately leads to their death. Therefore, the idea to expose dsDNA directly to UV-C radiation emerged, aiming to demonstrate in a straightforward manner the capability of Vis-to-UV UC emission to damage dsDNA.

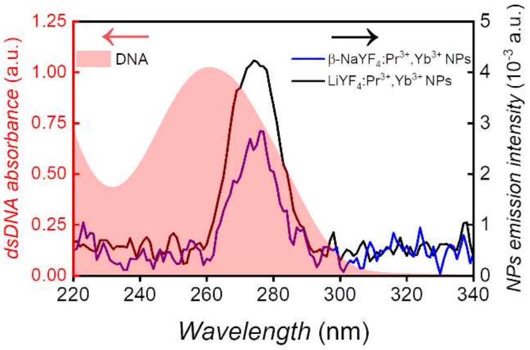

Fig. 24. The Vis-to-UV UC emission spectra of $LiYF_4:Pr^{3+},Yb^{3+}$ NPs (black line) and β-$NaYF_4:Pr^{3+},Yb^{3+}$ NPs (blue line) under 447 nm laser excitation in the comparison with dsDNA absorption spectrum (red area)

The method based on hyperchromicity effect observation allowed me to confirm the photodegradation of dsDNA in a qualitative way, which I described in more detail in Section 4.3.4. The results were summarized in Fig. 25-26 and the exact values of normalized absorbance were provided in Table 4 for the enhanced clarity. The control experiment conducted both in the absence of NPs (Fig. 26a) and in the presence of undoped nanocrystalline host matrix (Fig. 26b) showed that the absorption

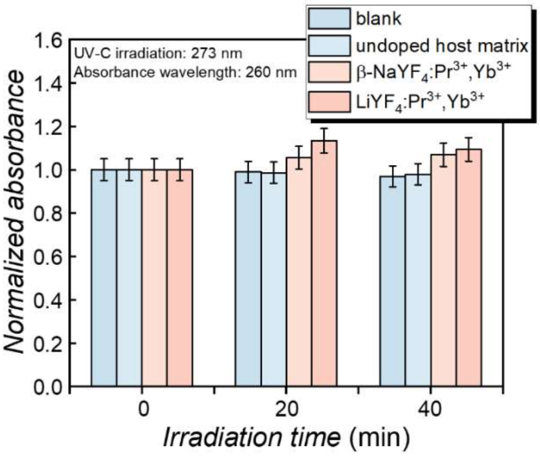

Fig. 25. Normalized absorbance of dsDNA solution at 260 nm after irradiation under 447 nm CW laser diode for 0, 20 and 40 min in the presence of glass substrate (denoted as blank), undoped host matrix, β-$NaYF_4:Pr^{3+},Yb^{3+}$ NPs, and $LiYF_4:Pr^{3+},Yb^{3+}$ NPs

spectra did not change after 20 and 40 min of irradiation, thus 447 nm CW laser radiation did not affect dsDNA molecules in the suspension. When β-$NaYF_4$:Pr^{3+},Yb^{3+} and $LiYF_4$: Pr^{3+},Yb^{3+} NPs were exposed to 447 nm wavelength for 20 min, the dsDNA absorbance at 260 nm registered after 20 min increased by ca. 13% and 6%, respectively. The observation of hyperchromic effect indicates that a significant amount of dsDNA in the aqueous solution was unwound under UV-C up-converted emission from Pr^{3+} ions incorporated into the investigated nanoscale host matrices. After the prolonged irradiation time to 40 min, the dsDNA absorbance at 260 nm dropped to 1.094 ± 0.054 a.u. for β-$NaYF_4$:Pr^{3+},Yb^{3+} NPs whereas it slightly increased to 1.069 ± 0.053 a.u. for $LiYF_4$:Pr^{3+},Yb^{3+} NPs.

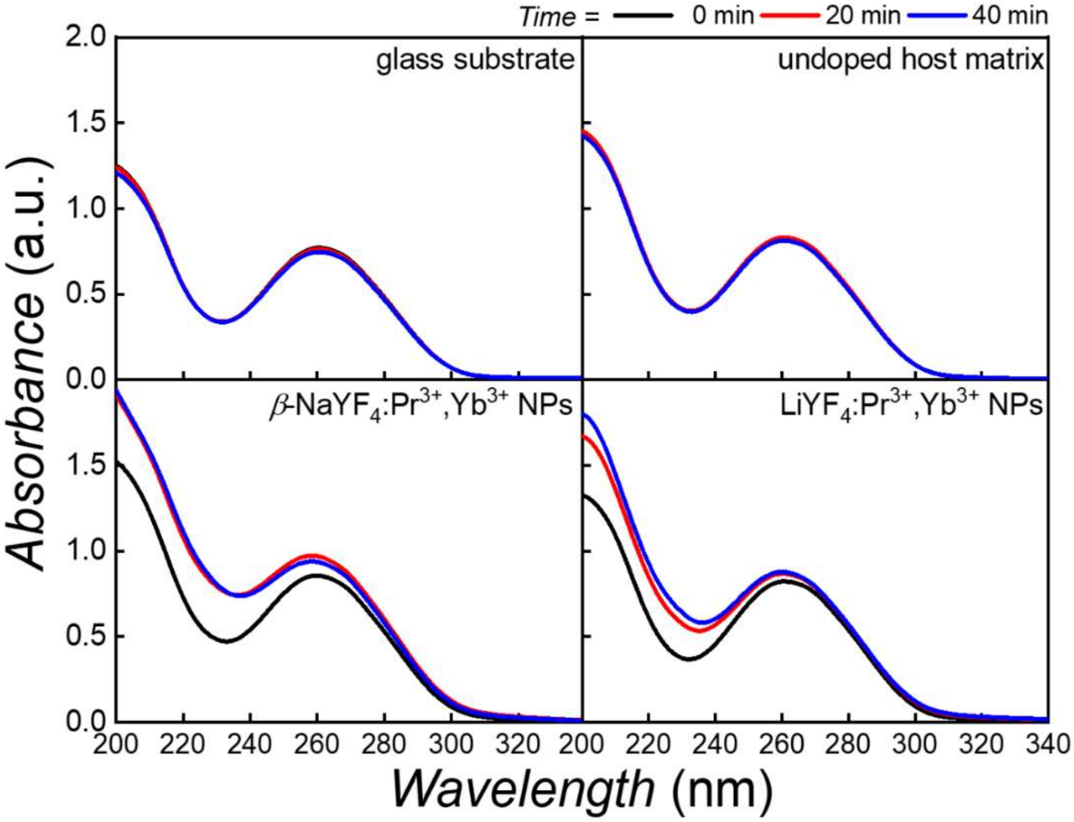

Fig. 26. UV-Vis absorption spectra of dsDNA solution after exposition to 447 nm CW laser diode for 0, 20, and 40 min in the presence of glass substrate (denoted as blank), undoped host matrix, β-$NaYF_4$:Pr^{3+},Yb^{3+} NPs, and $LiYF_4$:Pr^{3+},Yb^{3+} NPs

Table 4. Normalized absorbance of dsDNA solution at 260 nm after irradiation under 447 nm CW laser diode for 0, 20 and 40 min in the presence of glass substrate (blank), undoped host matrix, β-$NaYF_4$:Pr^{3+},Yb^{3+} NPs, and $LiYF_4$:Pr^{3+},Yb^{3+} NPs

	Irradiation time (min)		
	0	**20**	**40**
Investigated sample	**Normalized absorbance (a.u.)**		
glass substrate (blank)	1.000 ± 0.050	0.989 ± 0.049	0.969 ± 0.048
undoped host matrix	1.000 ± 0.050	0.986 ± 0.049	0.979 ± 0.048
β-$NaYF_4$:Pr^{3+},Yb^{3+} NPs	1.000 ± 0.050	1.133 ± 0.056	1.094 ± 0.054
$LiYF_4$:Pr^{3+},Yb^{3+} NPs	1.000 ± 0.050	1.055 ± 0.053	1.069 ± 0.053

On the contrary, by the means of FADU, I was able not only to confirm dsDNA photoinduced denaturation, but also to estimate the amount of dsDNA unwound. The results were summarized in Fig. 27-28 and the exact values of dsDNA concentration were provided in Table 5 for enhanced clarity. The calibration curve based on the dsDNA denaturation quantification (see Section 4.3.5), clearly indicates that even small fluctuations in dsDNA concentration are noticeable as the Hoechst 33258 fluorescence intensity changes drastically. Initially, irradiating the solution with 447 nm radiation either for 20 or 40 min did not cause a significant change in dsDNA concentration – the values were within the measurement uncertainty. It implies that dsDNA does not denature under exposure to blue radiation, which is consistent with the aforementioned UV-Vis spectra registered for both the glass substrate and the undoped host matrix (*vide supra*). The presence of the Pr^{3+},Yb^{3+}-co-doped NPs drop-casted onto the glass substrate and placed behind the quartz cuvette significantly influenced dsDNA concentration – for β-$NaYF_4$:Pr^{3+},Yb^{3+} NPs it decreased by ~19% (to 40.27 ± 5.87 μg mL^{-1}) and ~21% (to 39.67 ± 3.07 μg mL^{-1}) after 20 and 40 min of the exposure to UV-C radiation, respectively, whereas for $LiYF_4$:Pr^{3+},Yb^{3+} NPs it decreased by ~21% (to 39.43 ± 2.75 μg mL^{-1}) and ~24% (to 38.05 ± 5.25 μg mL^{-1}), correspondingly. Therefore, the dsDNA denaturation study provides strong evidence that

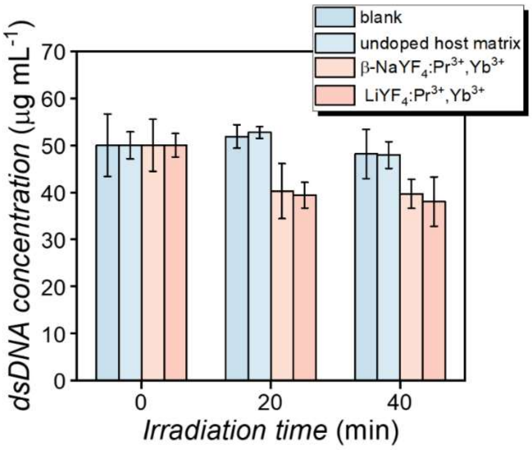

Fig. 27. Concentration of dsDNA solution after irradiation with 447 nm CW laser diode for 0, 20 and 40 min in the presence of glass substrate (denoted as blank), undoped host matrix, β-$NaYF_4$:Pr^{3+},Yb^{3+} NPs, and $LiYF_4$:Pr^{3+},Yb^{3+} NPs

Vis-to-UV UC exhibited by Pr^{3+},Yb^{3+}-co-doped β-$NaYF_4$ and $LiYF_4$ NPs could be used for antibacterial and antiviral purposes.

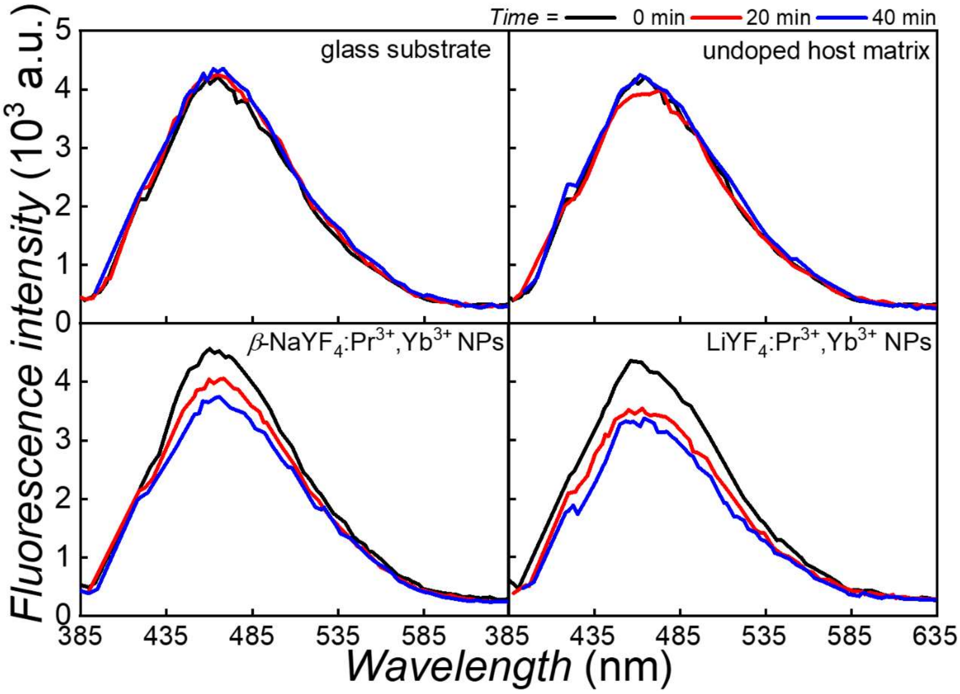

Fig. 28. Fluorescence spectra of Hoechst 33258 dye excited at 365 nm and attached to dsDNA remaining in the solution after exposition to 447 nm CW laser diode for 0, 20, and 40 min in the presence of glass substrate, undoped host matrix, β-$NaYF_4$:Pr^{3+},Yb^{3+} NPs, and $LiYF_4$:Pr^{3+},Yb^{3+} NPs

Table 5. Concentration of dsDNA solution estimated with FADU procedure after irradiation with 447 nm CW laser diode for 0, 20, and 40 min in the presence of glass substrate (blank), undoped host matrix, β-$NaYF_4$:Pr^{3+},Yb^{3+} NPs, and $LiYF_4$:Pr^{3+},Yb^{3+} NPs

	Irradiation time (min)		
	0	**20**	**40**
Investigated sample	**dsDNA concentration (μg mL^{-1})**		
glass substrate (blank)	50.00 ± 6.61	51.87 ± 2.50	48.16 ± 5.23
undoped host matrix	50.00 ± 2.85	52.73 ± 1.26	47.94 ± 2.83
β-$NaYF_4$:Pr^{3+},Yb^{3+} NPs	50.00 ± 5.51	40.27 ± 5.87	39.67 ± 3.07
$LiYF_4$:Pr^{3+},Yb^{3+} NPs	50.00 ± 2.48	39.43 ± 2.75	38.05 ± 5.25

The synthesized co-doped NPs are prone to emit NIR-II radiation peaking at approximately 1320÷1325 nm under 980 nm radiation, which falls within the windows of biological tissue transparency, owing to ET from Yb^{3+} to Pr^{3+} ions. I decided to have a series of bioimaging experiments conducted for the selected β-$NaYF_4$:Pr^{3+},Yb^{3+} and $LiYF_4$:Pr^{3+},Yb^{3+} NPs to assess their application potential. The transparency of both dental enamel and the majority of compounds forming stains on teeth surface in NIR-I and NIR-II spectral regions is advantageous in dentistry applications [132]. Hence, bioimaging was performed using an oral-cavity-resembling model, consisting of a bovine tooth with a cavity drilled along its axis and a 4 mm thick chicken breast tissue. Initially, the NIR-to-NIR imaging capability of NPs suspensions in chloroform in the Eppendorf tubes (concentration: ~100 mg mL^{-1}) was assessed. As shown in Fig. 29a, the β-NaYF$_4$:Pr^{3+},Yb^{3+} NPs exhibited a higher signal-to-noise ratio compared to LiYF$_4$:Pr^{3+},Yb^{3+} NPs, and thus were selected for further investigation. A drop of the suspension was introduced into the drilled dental cavity, enabling the visualization of its shape and depth in various modes (Fig. 29b-d), even after covering the tooth with the chicken breast flesh (Fig. 29e-g). Therefore, the sufficiently long LT of Pr^{3+} ions at 1320 nm, which is approximately 80 μs, suggests that the NPs of choice could be also utilized the time-gated NIR-II imaging. In this technique, the extended LT allows for temporal separation of the short-lived luminescent signal from background autofluorescence, thereby improving imaging contrast. It was proven that the delay of only 1 μs between laser pulse and *in vivo* image acquisition can eliminate autofluorescence [133]. The method was also effectively demonstrated for NIR-to-NIR emitting NaGdF$_4$:Nd^{3+} NPs exhibiting similar LT value (~100 μs for $^4F_{3/2}\rightarrow{}^4I_{11/2}$ transition in Nd^{3+} ions, peaking at ca. 1060 nm) [26]. In this case, the synthesized Pr^{3+}-doped NPs are a promising bioimaging nanoprobe, capable to provide detailed insights into complex biological systems with high resolution.

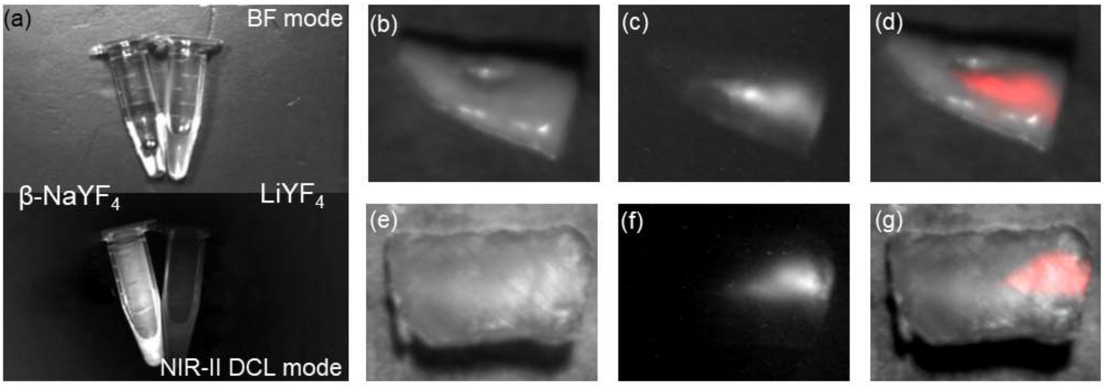

Fig. 29. NIR-to-NIR-II bioimaging capacity verification of β-NaYF$_4$:Pr^{3+},Yb^{3+} NPs and LiYF$_4$:Pr^{3+},Yb^{3+} NPs performed under 980 nm excitation: (a) bright field (up) and NIR-II (down) images of the Eppendorf tubes containing the investigated NPs, (b) bright field image of the bovine tooth, (c) NIR-II DC image of the drilled cavity with the NPs suspension introduced, (d) merged (bright field and NIR-II DC) image of the bovine tooth, (e) BF image of the tooth covered with 4 mm thick chicken breast tissue, (f) NIR-II DC image of the tooth covered with 4 mm thick chicken breast tissue, (g) merged (bright field and NIR-II DC) image of the tooth covered with 4 mm thick chicken breast tissue

4.5. Conclusions

In this chapter of the doctoral dissertation, I present the successful synthesis, characterization and a series of the proof-of-concepts experiments regarding potential bio-related application of Pr^{3+},Yb^{3+}-doped alkali-metal-based yttrium fluoride NPs. These NPs exhibit Vis-to-UV UC under 447 nm laser excitation as well as NIR-to-NIR DC emission under 980 nm excitation. The UV-C radiation, peaking at ca. 275 nm, leads to a significant decrease in dsDNA concentration in the irradiated aqueous solution due to dsDNA unwinding. This phenomenon was confirmed both qualitatively (through hyperchromicity effect observation) and quantitatively (*via* fluorescent analysis of dsDNA unwinding with Hoechst 33258 dye). Concurrently, the NPs exhibit NIR-to-NIR DC emission at ca. 1320 nm, occurring after ET to Pr^{3+} to Yb^{3+} ions, sensitized under 980 nm excitation. The NIR-II emission renders the synthesized NPs suitable candidates for bioimaging purposes in the steady state mode. With sufficiently long luminescence LTs (~70 us for $LiYF_4$:Pr^{3+},Yb^{3+} NPs and ~130 us for β-$NaYF_4$: Pr^{3+},Yb^{3+}) their application could be extended to time-gated NIR-II bioimaging or even to photoluminescence lifetime imaging.

Therefore, my thorough research provides solid evidence that bimodal β-$NaYF_4$:Pr^{3+},Yb^{3+} and $LiYF_4$:Pr^{3+},Yb^{3+} NPs could be of great interest within the emerging field of theranostics, integrating diagnosis and therapy in a single platform. Their ability to up-convert Vis-to-UV radiation enables localized photodynamic or germicidal treatment, whereas NIR-II emission provides non-invasive imaging. Such materials offer a promising route toward targeted, light-triggered theranostic *in vivo* solutions, minimizing side effects and enhancing clinical precision.

4.6. Acknowledgments and comments

This chapter is partially based on the data presented in the research paper *Pr^{3+}-doped $NaYF_4$ and $LiYF_4$ nanocrystals combining visible-to-UVC upconversion and NIR-to-NIR-II downconversion luminescence emissions for biomedical applications.* M.Y. Tsang, **P. Fałat**, M.A. Antoniak, R. Ziniuk, S.J. Zelewski, M. Samoć, M. Nyk, J. Qu, T.Y. Ohulchanskyy, D. Wawrzyńczyk. Nanoscale 14, 2022, pp. 14770-14778.

Within the research scope I synthesized the batches of β-$NaYF_4$:Pr^{3+},Yb^{3+} and $LiYF_4$:Pr^{3+},Yb^{3+} NPs with the invaluable help of M.A. Antoniak. I conducted the Vis/NIR-to-UV UC emission measurements using the dedicated optical setup assembled by S.J. Zelewski. The Vis-to-Vis Stokes emission and NIR-to-Vis UC emission measurements were conducted on the courtesy of B. Cichy. The development of both qualitative and quantitative methods to validate the efficiency of dsDNA photodegradation through up-converted UV-C radiation was performed with the assistance of M.Y. Tsang. Additionally, the Vis-to-NIR Stokes emission, NIR-to-NIR DC spectra, and luminescence LTs curves were registered by R. Ziniuk and T.Y. Ohulchanskyy along with the NIR-II bioimaging provided.

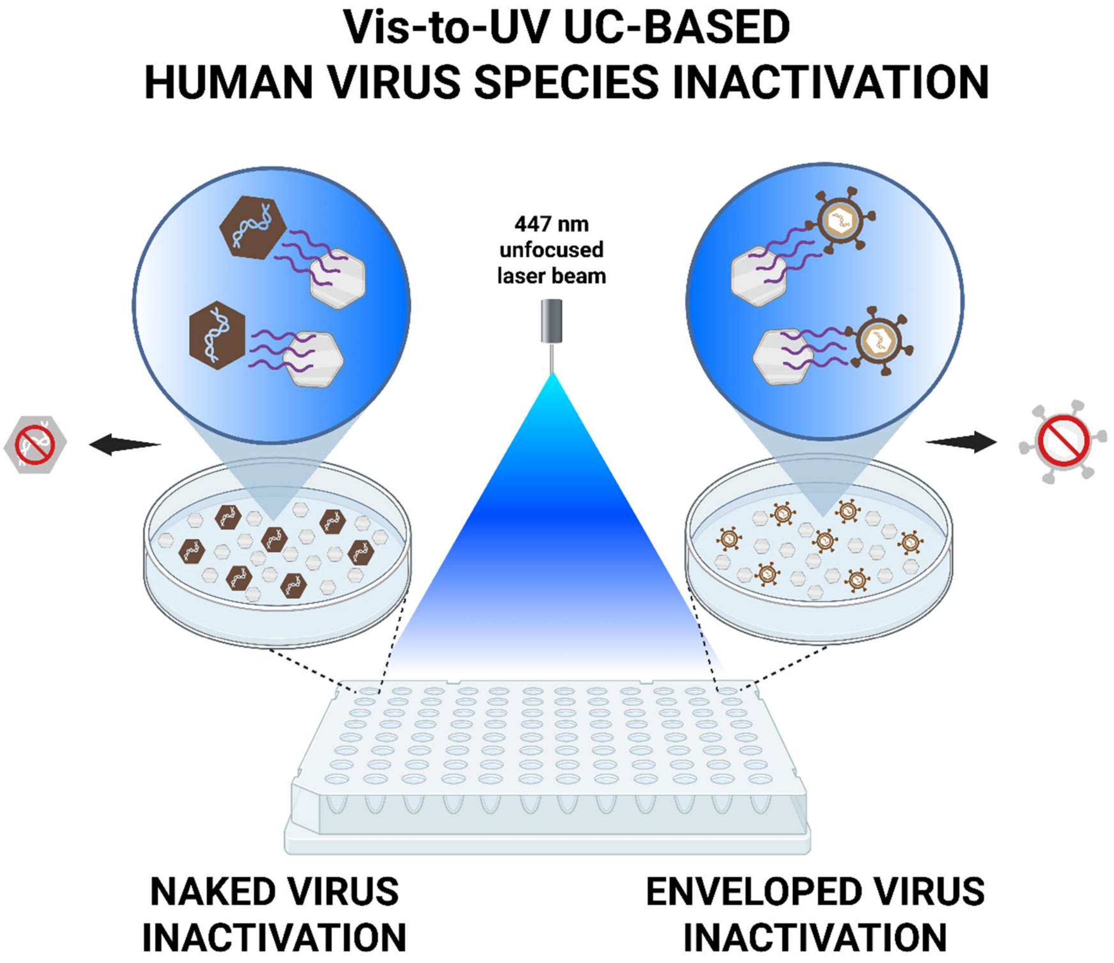

Fig. 30. The general concept of naked and enveloped human viruses photoinactivation experiment, exploiting Vis-to-UV UC emission of Pr^{3+}-co-doped alkali-metal-based yttrium fluoride NPs and MCs

Chapter 5

Vis-to-UV UC of Pr^{3+}-co-doped alkali-metal-based yttrium fluoride NPs and MCs for human virus species inactivation

As provided in Chapter 4, Pr^{3+}-co-doped β-NaYF$_4$ and LiYF$_4$ NPs are capable to harvest Vis photons in such a way that the emission falls in UV-C spectral range. This radiation is of higher energy and interacts with dsDNA. When living cells are irradiated with UV-C, the genetic material is destroyed and cannot replicate, which ultimately leads to the death of the exposed microorganisms. For that very reason, there is a strong need to improve brightness of Vis-to-UV UC emission so that the up-converting materials could be used as highly-efficient disinfectants. Therefore, in this part of my doctoral dissertation, I decided to focus on colloidal Pr^{3+}-doped alkali-metal-based yttrium fluoride NPs and the possibilities to enhance their anti-Stokes emission in UV-C spectral range through co-doping with Gd^{3+} ions and covering the optically active C NPs with the inert shell, leading to the formation of CS NPs. Additionally, I compare their emissive properties in the region of interest with the ones exhibited by the synthesized MCs bearing corresponding lanthanide ions at selected molar concentration.

In accordance with the registered Vis-to-UV UC emission spectra upon 447 nm laser excitation and the capability to degrade dsDNA within the particular timespan, I select the most promising materials for a biological experiment of light-triggered human virus species eradication (Fig. 30). Having been transferred from organic phase to water through acidic etching, the chosen NPs and MCs are mixed with suspensions of the naked adenovirus HAdV-C5 and the enveloped herpes simplex virus HSV-1, followed by exposition to the unfocused 447 nm laser beam. Due to differences in both genome size and morphology, these viruses are inactivated in a diverse way, thus photoeradication efficiency rates are various. The results gathered in the conducted *in vitro* experiment prove that nanophotonics-based solutions could be promising in terms of germicidal action. Additionally, the designed Pr^{3+}-co-doped colloidal NPs and MCs are a versatile class of materials that can be further processed with the ease to be utilized in the fabrication of light-activated disinfecting surfaces and fabrics.

5.1. Introduction to the scientific problem

As antimicrobial resistance was first discovered, it was not even thought that it would become a severe issue which the modern world would be forced to struggle with. Initially classified as a scientific trivia, it was over time recognized as a threat for humanity, mainly due to the misuse of antibiotics for infections treatment and strong oxidizing agents as surface disinfectants [134]. In the document *Global Strategy for Containment of Antimicrobial Resistance*, issued in the beginning of 21st century, World Health Organization (WHO) anticipated that the promoted cross-resistance would eventually convert the vast majority of pathogens into super-resistant bacteria, superviruses, and fungi populations [135]. As difficult as they are to be eliminated with traditional chemical treatment, they could easily spread on frequent-touch surfaces. For instance, some bacteria are prone to adhere to surfaces, where they can survive for an extended period, even up to 3 months, reciprocating at the same time. On the other hand, the survival time of virus particles outside the host can vary from a few hours to even a few weeks. To illustrate, coronavirus SARS-CoV-2 particles, responsible for the COVID-19 pandemic outbreak, were found to remain contagious for up to 24 hours on fabric, but up to 48 hours on stainless steel [136–138]. Not to mention, the high mutation rates of virus species also pose a serious health hazard to all members of society, regardless of their medical conditions, as vaccine development and market release are time-consuming processes. Therefore, there is a strong need to foster new solutions for high-touch surfaces disinfection, e.g., at public transportation, healthcare facilities or in commonly accessible sanitary rooms.

For these purposes, nanotechnology-based solutions show the great potential since the number of validated applications has been constantly growing, in which the spread of virus is inhibited [139]. Additionally, the physicochemical properties of nano- and micro-size materials, such as high surface area, allow for their designed and engineered modification. It results then in the enhancement of properties which could be effectively utilized directly against virus species, e.g., photocatalytic activity, ROS generation capability, or externally triggered UV emission. The last one seems to be highly fascinating, since UV radiation is a factor proven in many experiments to inactivate microorganisms, especially when the UV-C type of radiation is considered (for more detailed information see Section 2.1.1). One of the possible ways to generate the UV-C emission in inorganic materials is *via* sequential photon absorption in the ladder-like energy level structure of lanthanide ions, as already presented in Chapter 4 of the doctoral dissertation for Pr^{3+}-based $LiYF_4$ and β-$NaYF_4$ NPs [140]. In order to provide germicidal action of high efficiency, there is an urgent call to design and synthesize up-converting NPs exhibiting this emission of the sufficient intensity. Usually the research path toward it starts with finding a suitable configuration of various lanthanide ions, of which the synergic effect after incorporation into the host matrix and concentration optimization could result in the enhanced emission in the region of interest. Not to mention, one of the universal strategies to enhance UC luminescence, commonly reported in the literature, relies on manufacturing core@undoped-shell NPs. As a consequence, the shell protects the emitting lanthanide ions from parasitic energy migration processes and surface quenching. For example, such an approach allows the NIR-to-Vis UC emission to be intensified [38]. In particular, Fischer et al. demonstrated that precise tuning of the epitaxially grown inert shell thickness enables both significant enhancement and further optimization of NIR-to-Vis UC and NIR-to-NIR DC emission intensities within the core@undoped-shell nanostructure [141].

Taking into consideration the information mentioned above, in this part of the doctoral dissertation I assume that Vis-to-UV UC emission could be of higher magnitude when the Pr^{3+}-based optically active C NPs are co-doped with an additional amount of Gd^{3+} ions. These ions have been reported not only to alter the crystal structure of the host matrix in such a way that Vis-to-UV UC is enhanced, but also to contribute to UV-B emission under Vis excitation [59]. As a consequence, Gd^{3+} co-doping could be considered as beneficial for anti-germ-oriented applications. In the next step, this effect is further enhanced by passivating the C NPs with an inert shell made of the same host matrix type, thus forming a CS nanoarchitecture. The presented research of mine also focuses on finding the answer if the up-converted UV-C emission could be enhanced when the lanthanide ions are incorporated into different alkali-metal-based yttrium fluoride NPs, even alkali-metal-mixed ones. As the addition, I provide the comparison of the emissive properties gathered for the synthesized MCs. To present the potential application of the most promising materials at nano- and microscale, I decided to have a biological experiment conducted, using common human virus species, which are morphologically different, even though having dsDNA genome. According to the European standards, the effectiveness of physical agents, like UV radiation, tends to be similar for the viruses with similar shapes and structures [142]. In essence, the morphological characteristics often influences how these agents interact with the virus, making them effective across related virus types. The non-enveloped virus chosen for study, human adenovirus type C5 (HAdV-C5) can survive in harsh environmental conditions. It usually causes mild respiratory infections such as sore throat and bronchitis, as well as conjunctivitis and diarrhea, particularly in children or immunocompromised people [143,144]. On the other hand, the enveloped herpes simplex virus (HSV-1), around which genome the lipid bilayer is present, is prone to cause a variety of illnesses, including oral or genital herpes (sore colds) and, in more severe cases, encephalitis, leading to serious neurological complications. The lipid envelope surrounding HSV-1 enhances its ability to interact with host cells and influences its stability and sensitivity to environmental factors and antiviral treatments [145,146].

I am convinced that the materials synthesized in a well-controlled manner in both shape and size at nano- and microscale *via* wet-chemistry-based techniques and emitting UV-C radiation in the process of sequential two-photon absorption opens up the way to utilize them as efficient emitters for light-triggered disinfection. Their ability to form stable colloidal dispersions in various environments is surely advantageous from a technological point of view, since it facilitates surface functionalization procedures for specific applications, such as fabrication of antiviral photoactivated surfaces or fabrics.

5.2. Chemicals and materials used

5.2.1. Synthesis of Pr^{3+}-co-doped alkali-metal-based NPs

For the synthesis of Pr^{3+}-co-doped alkali-metal-based yttrium fluoride C and CS NPs the following chemicals were used: Pr_2O_3 (99.99%), Gd_2O_3 (99.99%), Y_2O_3 (99.99%), $LiOH \cdot H_2O$ (99.99%), NaOH (≥ 98.0%), KOH (99.99%), NH_4F (≥ 99.99%), acetic acid (pure for analysis, 99.5÷99.9%), oleic acid (technical grade, 90%), octadec-1-ene (technical grade, 90%), methanol (99%), ethanol (99.8%), hexane, chloroform, and acetone. All reagents were purchased from Sigma Aldrich and utilized without prior purification.

All of the NPs were prepared in accordance with the protocol described in Sections 3.1.1 and 3.1.2. The masses of the corresponding solid compounds utilized in the syntheses were provided below in Table 6.

Table 6. Summary for the amount of solid compounds used in C and CS NPs syntheses

Dopants	**Host matrix**	**Compound mass [g]**						
		Y_2O_3	**Pr_2O_3**	**Gd_2O_3**	**$LiOH \cdot H_2O$**	**NaOH**	**KOH**	**NH_4F**
2% Pr^{3+}	$LiYF_4$	0.2766	0.0083	-	0.2098	-	-	0.2964
2% Pr^{3+}, 15% Gd^{3+}	$LiYF_4$	0.2343	0.0083	0.0682	0.2098	-	-	0.2964
2% Pr^{3+}	$NaYF_4$	0.2766	0.0083	-	-	0.2000	-	0.2964
2% Pr^{3+}, 15% Gd^{3+}	$NaYF_4$	0.2343	0.0083	0.0682	-	0.2000	-	0.2964
2% Pr^{3+}	$Na_{0.5}K_{0.5}YF_4$	0.2766	0.0083	-	-	0.1000	0.1404	0.2964
undoped (*shelling*)	$LiYF_4$	0.2258	-	-	0.2098	-	-	0.2964
undoped (*shelling*)	$NaYF_4$	0.2258	-	-	-	0.2000	-	0.2964

5.2.2. Synthesis of Pr^{3+}-co-doped alkali-metal-based MCs

For the synthesis of Pr^{3+}-co-doped alkali-metal-based yttrium fluoride MCs the following chemicals were used: Pr_2O_3 (99.99%), Gd_2O_3 (99.99%), Y_2O_3 (99.99%), HNO_3 (63÷65%), LiF (99.99%), NaF (99%), NH_4F (≥ 99.99%), EDTA (≥ 99%), ethanol (99.8%), and acetone. All reagents were purchased from Sigma Aldrich and utilized without prior purification.

All of the MCs were prepared in accordance with the protocol described in Section 3.2.1.1. The masses of the corresponding solid compounds utilized in the syntheses were provided below in Table 7.

Table 7. Summary for the amount of solid compounds used in MCs syntheses

Dopants	**Host matrix**	**Compound mass [g]**						
		Y_2O_3	**Pr_2O_3**	**Gd_2O_3**	**EDTA**	**LiF**	**NaF**	**NH_4F**
2% Pr^{3+}	$LiYF_4$	0.8299	0.0248	-	0.3945	0.1946	-	0.8333
2% Pr^{3+}, 5% Gd^{3+}	$LiYF_4$	0.7960	0.0248	0.0227	0.3945	0.1946	-	0.8333
2% $Pr^{3+,}$ 30% Gd^{3+}	$LiYF_4$	0.6265	0.0248	0.1362	0.3945	0.1946	-	0.8333
2% Pr^{3+}	$NaYF_4$	0.8299	0.0248	-	0.3945	-	0.3149	0.8333
2% Pr^{3+}, 30% Gd^{3+}	$NaYF_4$	0.6265	0.0248	0.1362	0.3945	-	0.3149	0.8333

5.2.3. dsDNA photodegradation with up-converted UV radiation

Salmon sperm dsDNA was purchased from Sigma Aldrich and used without further purification. The dsDNA solution concentrated at 50 µg mL^{-1} was prepared in Milli-Q quality water (resistivity: 18.2 MΩ cm^{-1} at 25 °C) right before the measurements.

Hoechst 33258 dye was purchased from Sigma Aldrich and used without prior purification. The stock solution of the dye at the concentration of 1 mg mL^{-1} was prepared in Milli-Q quality water (resistivity: 18.2 MΩ cm^{-1} at 25 °C).

5.2.4. Organic-to-aqueous phase transfer

HCl (35÷37%) was purchased from ChemPur (Poland) and used without further purification to prepare the 2 M HCl solution. Ethanol (99.8%) obtained from Sigma Aldrich was utilized for washing the etched NPs, which were dispersed in Milli-Q quality water (resistivity: 18.2 MΩ cm^{-1} at 25 °C).

5.2.5. Cytotoxic properties of the synthesized materials

A549 (human lung carcinoma, CCL-185^{TM}, cancer cell line) and HeLa cell line (human cervix carcinoma, CCL-2^{TM}) were obtained from American Type Culture Collection – ATCC (Rockville, MD, USA). They were all cultured in Dulbecco's Modified Eagle's Medium (DMEM) supplemented with 10% fetal bovine serum (FBS) (Capricorn Scientific, Germany) and 4 mM L-glutamine (Biological Industries, Israel), 100 µg mL^{-1} of penicillin and 100 µg mL^{-1} of streptomycin (Sigma Aldrich, Germany).

Human adenovirus 5 (HAdV-C5 – ATCC® VR-5^{TM}) and herpes simplex virus type 1 (HSV-1 – ATCC® VR-1493™) were delivered by ATCC (Rockville, MD, USA). In the further step, the suspension for virucidal activity validation was incubated with phosphate buffer saline (PBS), purchased from Sigma Aldrich, Germany, as an interfering substance (pH = 7.2).

5.3. Characterization methods

5.3.1. Crystal structure

The crystal structure of all synthesized Pr^{3+}-co-doped alkali-metal-based yttrium fluoride NPs and MCs were investigated with the STOE powder X-ray diffractometer, as already described in Section 4.3.1.

5.3.2. Morphology and size distribution

The TEM images of the NPs were captured using an FEI Tecnai G^2 20 X-TWIN TEM at the Faculty of Chemistry at University of Wrocław, Poland, in accordance with the procedure aforementioned in Section 4.3.2. The NPs size distribution analysis was performed in OriginPro Software as length and width of 100 NPs in the micrographs had been measured in ImageJ Software.

Since the synthesized MCs were expected to be of bigger size in comparison with the NPs, they were investigated with a Jeol JSM-6610LVnx SEM. A drop of each material's suspension was deposited on a piece of carbon tape and evaporated before putting the holder into the microscope chamber. The MCs size distribution analysis was performed in OriginPro Software as length and width of 100 MCs in the micrographs had been measured in ImageJ Software. Additionally, the system was coupled with an Oxford Aztec Energy X-ray energy dispersive spectrometer (EDS), which allowed to simultaneously record the elemental distribution maps throughout the samples.

5.3.3. Vis-to-UV UC emission spectra acquisition

Within the research scope presented in this chapter, the Vis-to-UV UC emission spectra of the dried samples deposited on glass substrates were measured under ambient conditions with the use of the setup described in Section 4.3.3.

5.3.4. Quantitative validation of dsDNA photodegradation *via* up-converted UV radiation

As presented in Section 4.3.4 there was the setup assembled for dsDNA degradation *via* Vis-to-UV UC emission generated by Pr^{3+}-co-doped alkali-metal-based NPs and MCs. In the next step, its remaining concentration in the irradiated solution was estimated in accordance with the modified FADU procedure. The experimental protocol was described in the detail in Section 4.3.5.

5.3.5. Organic-to-aqueous phase transfer

To perform the experiment in aqueous-based environment, the selected NPs needed to be transferred from an organic (hexane) to aqueous phase, which was achieved by etching oleic-acid-capped β-$NaYF_4$ and $LiYF_4$ CS NPs [147]. 5 mL of the dispersion of NPs in hexane was stirred with 20 mL of 2 M HCl solution at room temperature for 2 h. The mixture was then poured into a glass separator to isolate the inorganic phase. The hexane layer was washed three times with distilled water to collect the NPs, remaining after etching. After centrifuging at 9,000 rpm for 15 min and washing with the water-ethanol mixture (1:1 v/v) twice, the pellet was redispersed in 5 mL of water. The success of organic-to-aqueous phase transfer was controlled with a FT-IR vacuum spectrometer Bruker Optic GmbH Vertex70v. The representative FT-IR spectra for the dried samples of β-$NaYF_4$ and $LiYF_4$ NPs before and after acidic etching were recorded in the range between 500÷4000 cm^{-1} and with the resolution of 0.4 cm^{-1}. The NPs concentration was estimated by weighing the solid residue after drying 20 μL of each aqueous suspension, the estimation was performed in triplicate.

5.3.6. Cytotoxicity studies according to EN 14476 standard

Cytotoxicity studies were conducted in accordance with EN 14476 standard, which allows to distinguish cytopathic effects (CPE) caused by a virus from cell damages induced by test formulations [142]. The aqueous suspensions tested in this experiment contained the selected Pr^{3+}-co-doped alkali-metal-based yttrium fluoride NPs and MCs.

For cytotoxicity assessment, A549 and HeLa cell lines at density of $4 \cdot 10^4$ cells mL^{-1} were seeded into 96-well polystyrene plates (ThermoFisher Scientific, USA) and incubated for 24 h. Subsequently, a series of 10-fold dilutions (from 10^{-1} to 10^{-8}) of the formulations at their initial concentration (100% concentrated) were prepared. 50 μL of each dilution was added to wells containing a monolayer of cells – 8 wells per dilution were inoculated. Monitored once a day using an inverted microscope (Olympus Corp., Hamburg, Germany; Axio Observer, Carl Zeiss MicroImaging GmbH) for the observation of cytotoxic effect development, the plates were incubated for 4 days at 37 °C in the atmosphere containing 5% CO_2.

5.3.7. Antiviral assays

5.3.7.1. Virucidal activity of the tested materials

The virucidal activity of the obtained Pr^{3+}-co-doped alkali-metal-based yttrium fluoride NPs and MCs was evaluated against two various human virus types: HAdV-C5 (non-enveloped) and HSV-1 (enveloped). The assessment followed the procedure described in EN 14476 standard in the section *Phase 2/Step 1: Quantitative suspension test for assessing virucidal activity in medical applications* [142]. Accordingly, a disinfectant can be pronounced as virucidal when it achieves a reduction of $\geq 4\log_{10}$ in the viral titer (≥99.99% inactivation) in comparison with the untreated control virus within the specified exposure time.

As per the protocol, one part of test virus stock dispersion (0.1 mL of HAdV-C5 or HSV-1), one part of interfering substance (0.1 mL of PBS), and eight parts (0.8 mL) of the disinfectant (aqueous suspension of Pr^{3+}-co-doped NPs or MCs at their initial 100% concentration) were mixed. After 1-hour-long direct contact, the aliquots were collected and serial dilutions of each mixture (up to 10^{-12}) were prepared, 8 wells per mixture. In the next step, 50 μL of each dilution was added to a microtiter plate containing a confluent monolayer of A549 cells for HAdV-C5 or HeLa cells for HSV-1. The plates were incubated at 37 °C in the atmosphere containing 5% CO_2 and observed daily for 4 days under an inverted microscope to monitor the viral CPE development. At the end of the experiment the residual infectivity was determined.

5.3.7.2. Test of virucidal activity of the synthesized materials under the 447 nm laser irradiation

The selected Pr^{3+}-co-doped alkali-metal-based NPs and MCs in aqueous solutions in a volume of 800 μL at the initial concentration (i.e., 100 %) were mixed in Eppendorf tubes (ThermoFisher Scientific, USA) with 100 μL of PBS as the interfering substance and 100 μL of either HAdV-C5 or HSV-1 virus suspension. In order to perform light-triggered eradication of naked and enveloped virus species, a custom setup was assembled (Fig. 31). It consisted of a 447 nm fiber-coupled CW laser diode (CNI MDL-XD-447) with the output placed 12 cm above a 96-well polystyrene plate. To ensure that the laser impact on virus species and culture cells is infinitesimal, a series of control experiments was conducted to establish such parameters as laser power and exposure time. Finally, the diode emitted the unfocused beam of blue radiation corresponding to the ~1000 J cm^{-2} light dose. After the irradiation, the samples were diluted from 10^{-1} to 10^{-12} and the virucidal activity was tested in the same way as provided in Section 5.3.7.

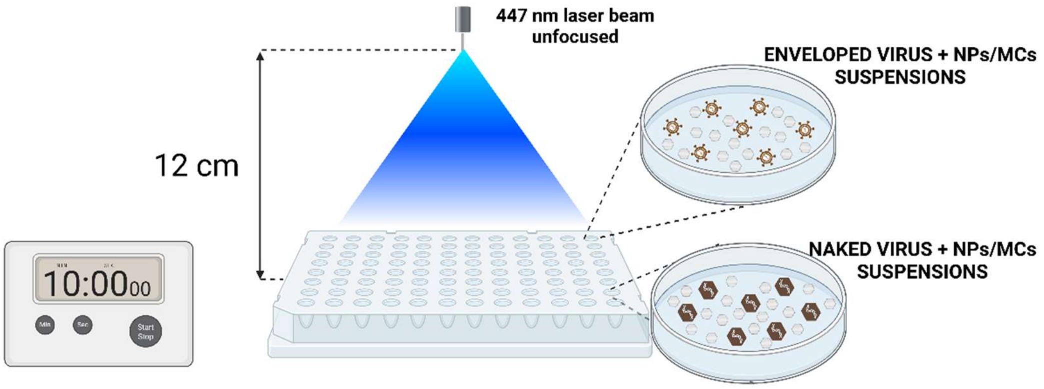

Fig. 31. A scheme of the experiment of virus inactivation via Vis-to-UV UC emission, generated by Pr^{3+}-co-doped NPs and MCs

5.4. Results and discussion

5.4.1. Morphology and structure characterization

In order to optimize the Vis-to-UV UC emission, in this experiment I synthesized a series of inorganic alkali-metal-based yttrium fluoride phosphors differing in size, co-dopants concentration, and internal structure. I successfully obtained Pr^{3+}-based $LiYF_4$, $NaYF_4$, and $Na_{0.5}K_{0.5}YF_4$ crystals at nano- and microscale – all of the materials were listed in Table 8 along with their average size measured based on TEM and SEM images (Fig. 33-37).

Table 8. List of the synthesized Pr^{3+}-co-doped alkali-metal-based yttrium fluoride NPs and MCs with their average size provided

Dopant concentration	**Host matrix**	**Size**	**Shell**	**Length**	**Width**
2% Pr^{3+}	$LiYF_4$	NPs	no	19.9 ± 2.2 nm	16.9 ± 1.9 nm
2% Pr^{3+}@NULL			yes	32.5 ± 4.1 nm	26.9 ± 2.7 nm
2% Pr^{3+},15% Gd^{3+}			no	19.8 ± 2.2 nm	15.1 ± 1.5 nm
2% Pr^{3+},15% Gd^{3+}@NULL			yes	25.0 ± 1.8 nm	21.6 ± 1.3 nm
2% Pr^{3+}	β-$NaYF_4$		no	21.2 ± 0.9 nm	16.7 ± 1.3 nm
2% Pr^{3+}@NULL			yes	35.4 ± 2.3 nm	21.1 ± 1.7 nm
2% Pr^{3+},15% Gd^{3+}			no	20.7 ± 1.4 nm	17.0 ± 1.1 nm
2% Pr^{3+},15% Gd^{3+}@NULL			yes	37.8 ± 3.8 nm	19.4 ± 2.1 nm
2% Pr^{3+}	$Na_{0.5}K_{0.5}YF_4$		no	195 ± 20 nm	56.9 ± 6.5 nm
2% Pr^{3+}	$LiYF_4$	MCs	no	24.1 ± 2.9 µm	14.2 ± 3.0 µm
2% Pr^{3+},5% Gd^{3+}			no	49.2 ± 6.1 µm	31.8 ± 4.7 µm
2% Pr^{3+}	β-$NaYF_4$		no	8.73 ± 0.46 µm	2.02 ± 0.36 µm
2% Pr^{3+},30% Gd^{3+}			no	3.32 ± 0.20 µm	0.98 ± 0.18 µm

The registered XRD patterns of the synthesized NPs and MCs revealed that $LiYF_4$ host matrix formed tetragonal structure (ICSD #27986, Fig. 32a-b). On the contrary, when Na^+ ions were utilized for the synthesis, hexagonal phase β-$NaYF_4$ (ICSD #51916, Fig. 32c-d) was obtained in every case, therefore, it is denoted hereinafter as '$NaYF_4$' for the enhanced clarity of this chapter. The inert shells, epitaxially grown on the NPs surface and marked in the text and in some graphs as 'NULL', formed the same crystal structure as lanthanide-doped C NPs, since there were no foreign peaks in the collected XRD patterns for CS nanoarchitectures. All of these findings imply that the synthetic protocol developed by Abel and co-workers allows for the synthesis of C and CS NPs, regardless of alkali metal utilized during the process [87]. Furthermore, when 50% of Na^+ ions were substituted with K^+ ions, the alkali-metal-mixed $Na_{0.5}K_{0.5}YF_4$ host matrix was formed (Fig. 32e). The XRD pattern resembled the one for β-$NaYF_4$, which means that substituting Na^+ with K^+ ions did not alter the Na-based crystal lattice. It is consistent with the report published by Kale et al. on the influence of various Na^+/K^+ molar ratios in $Na_xK_{1-x}YF_4$ on NIR-to-Vis UC emission enhancement [148].

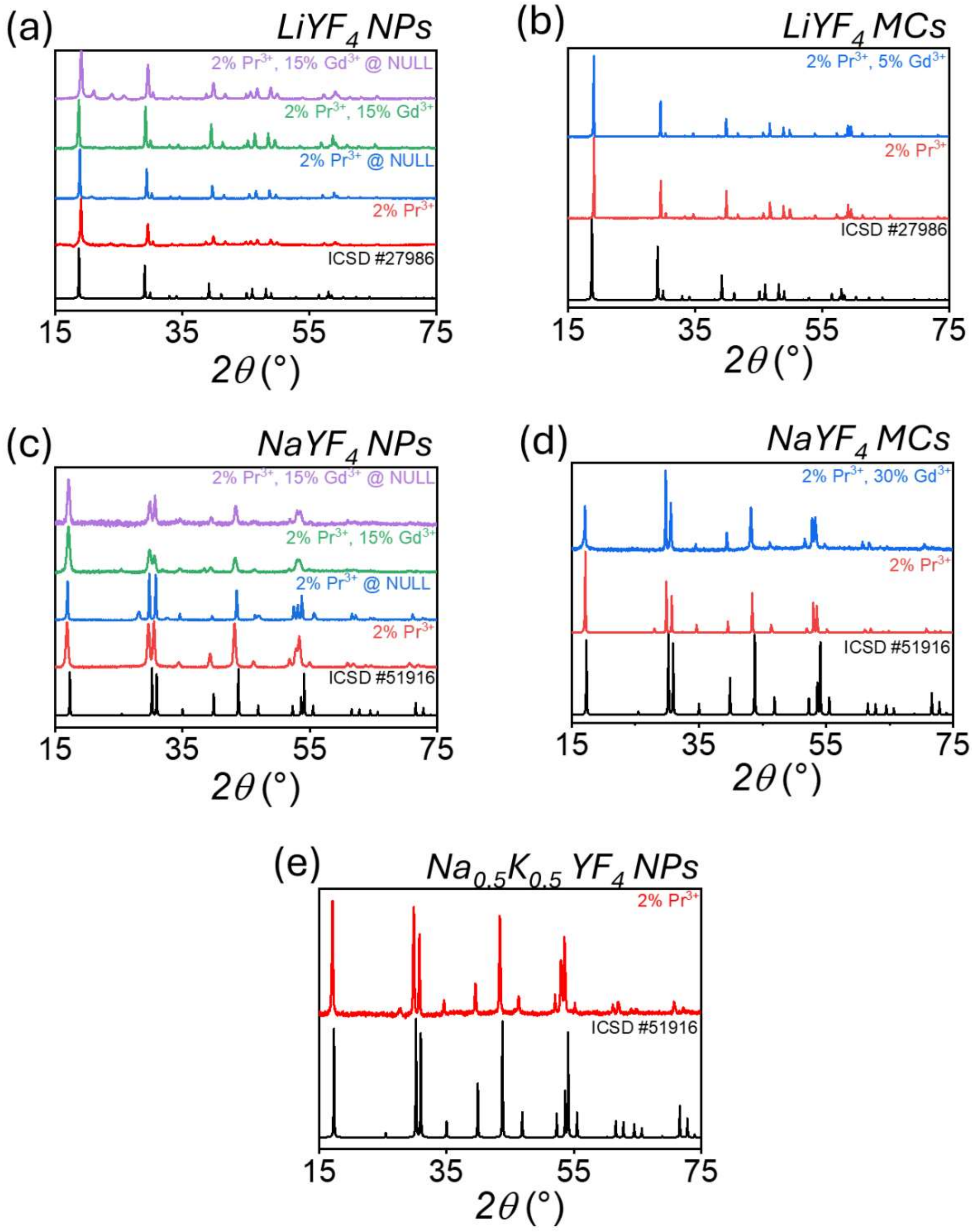

Fig. 32. XRD patterns of Pr^{3+}-co-doped (a) $LiYF_4$ NPs, (b) $LiYF_4$ MCs, (c) $NaYF_4$ NPs, (d) $NaYF_4$ MCs, and (e) $Na_{0.5}K_{0.5}YF_4$ NPs provided with theoretical patterns

Having confirmed the desired crystal structures of the synthesized materials, I examined the formed NPs in terms of morphology and size distribution (Fig. 33-37), whereas the elemental distributions maps were additionally captured for the MCs (see Fig. 36-37). The TEM micrographs revealed that the utilization of the same protocol for the synthesis of $Na_{0.5}K_{0.5}YF_4$ alkali-metal-mixed host matrix resulted in longer, rectangular-shaped Pr^{3+}-doped NPs (195 ± 20 nm long and 56.9 ± 6.5 nm wide) (Fig. 33). For this type of host matrix, both the similar NPs morphology and length-to-width ratio have been reported elsewhere [148]. In the initial synthesis of C NPs monodisperse $LiYF_4$ NPs with tetragonal shape were manufactured, as well as nanorod-like $NaYF_4$ NPs. The mean sizes (length × width) were as provided: 19.9 ± 2.2 × 16.9 ± 1.9 nm for $LiYF_4$:2%Pr^{3+} NPs, 19.8 ± 2.2 × 15.1 ± 1.5 nm for $LiYF_4$:2%Pr^{3+},15%Gd^{3+} NPs, 35.4 ± 2.3 × 21.1 ± 1.7 nm for $NaYF_4$:2%Pr^{3+} NPs, and 20.7 ± 1.4 × 17.0 ± 1.1 nm for $NaYF_4$:2%Pr^{3+},15%Gd^{3+}. Followingly, as $LiYF_4$ or $NaYF_4$ inert shells were grown around the lanthanide-doped C NPs to reduce energy quenching processes, significantly larger CS NPs were formed. The inert shell grew uniformly in all dimensions for $LiYF_4$ NPs, which resulted in $LiYF_4$:2%Pr^{3+}@$LiYF_4$ NPs and $LiYF_4$:2%Pr^{3+}, 15%Gd^{3+}@$LiYF_4$ NPs, with the mean size of 32.5 ± 4.1 × 26.9 ± 2.7 nm and 25.0 ± 1.8 × 21.6 ± 1.3 nm, respectively (Fig. 34). On the other hand, the inert shell growth around $NaYF_4$ C NPs led to the formation of rectangular $NaYF_4$:2%Pr^{3+}@$NaYF_4$ NPs and $NaYF_4$:2%$Pr^{3+|}$,15%Gd^{3+}@$NaYF_4$ nanorods featuring rounded edges, for which the average size was accordingly 35.4 ± 2.3 × 21.1 ± 1.7 nm and 37.8 ± 3.8 × 19.4 ± 2.1 nm (Fig. 35).

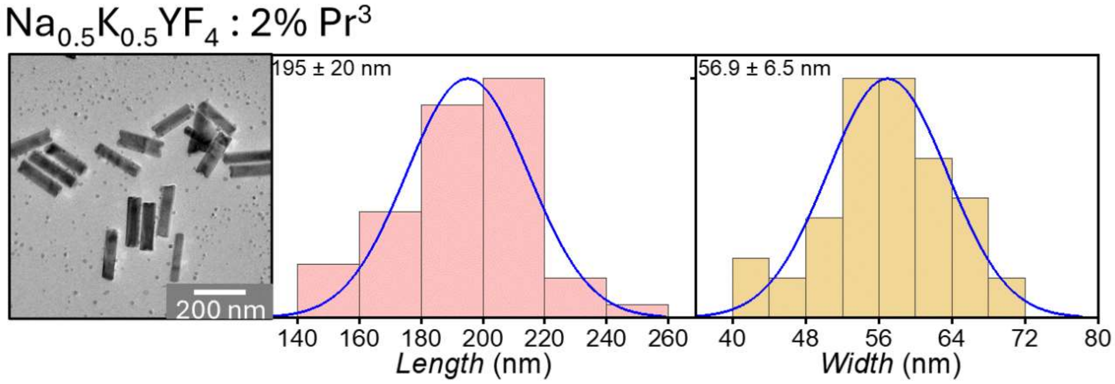

Fig. 33. TEM image (left column), length distribution histograms (middle column), and width distribution histograms (right column) of Pr^{3+}-doped alkali-metal-mixed $Na_{0.5}K_{0.5}YF_4$ NPs

(a) $LiYF_4 : 2\% \ Pr^{3+}$ @ $LiYF_4$ NPs

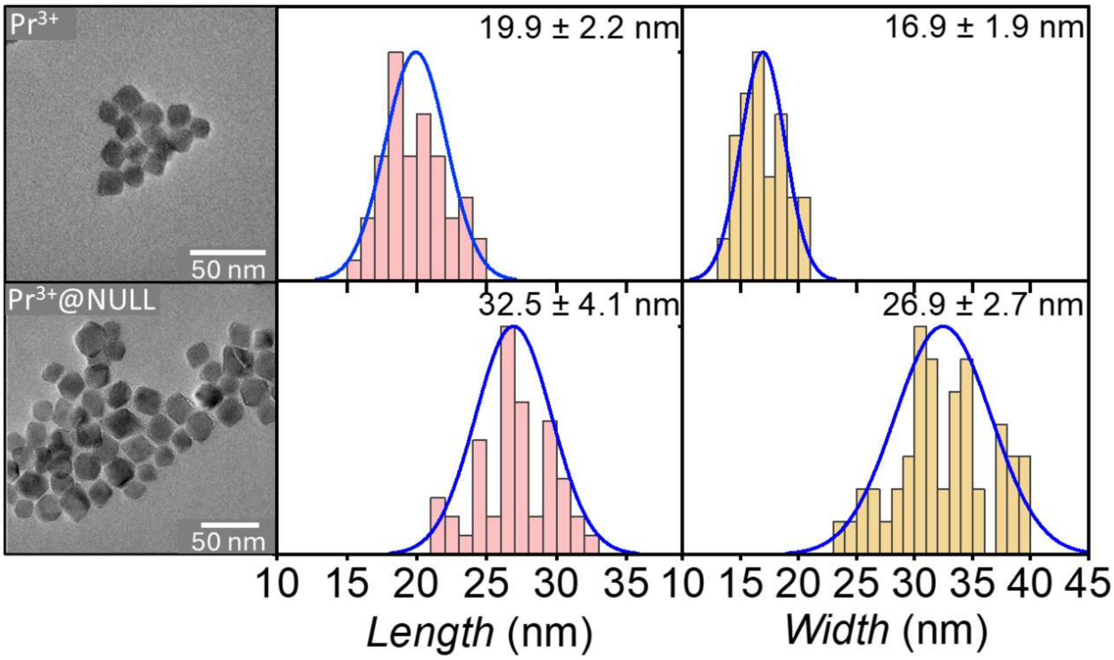

(b) $LiYF_4 : 2\% \ Pr^{3+}, 15\% \ Gd^{3+}$ @ $LiYF_4$ NPs

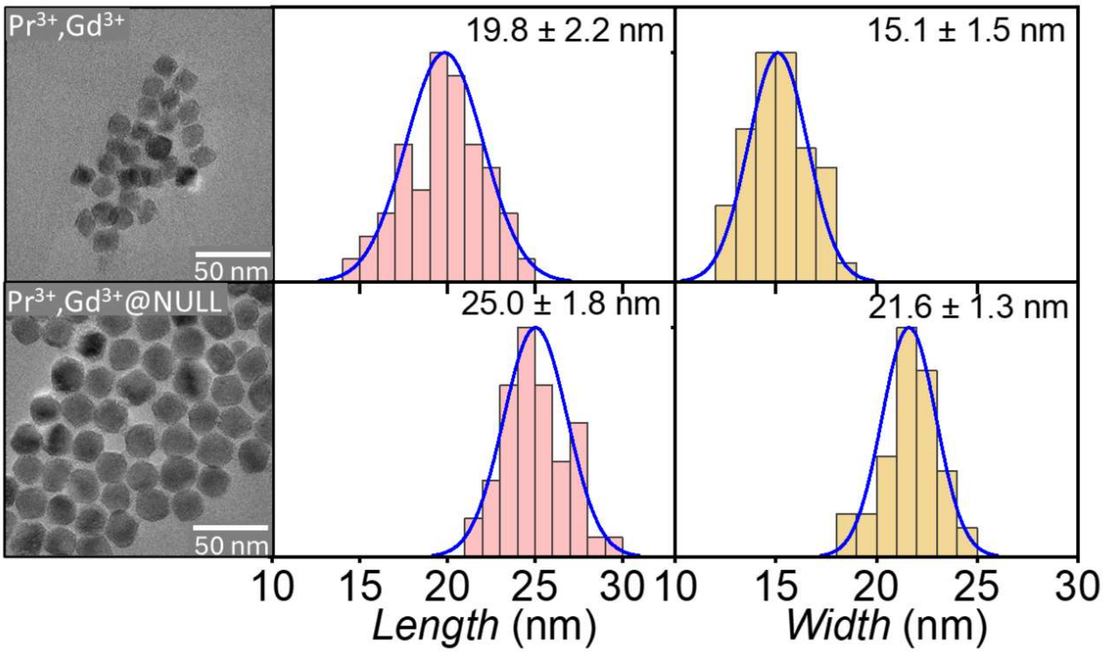

Fig. 34. TEM images (left column), length distribution histograms (middle column), and width distribution histograms (right column) of Li^{+}-based CS NPs (a) Pr^{3+}@NULL (b) Pr^{3+}, Gd^{3+}@NULL

(a) $NaYF_4$: 2% Pr^{3+} @ $NaYF_4$ NPs

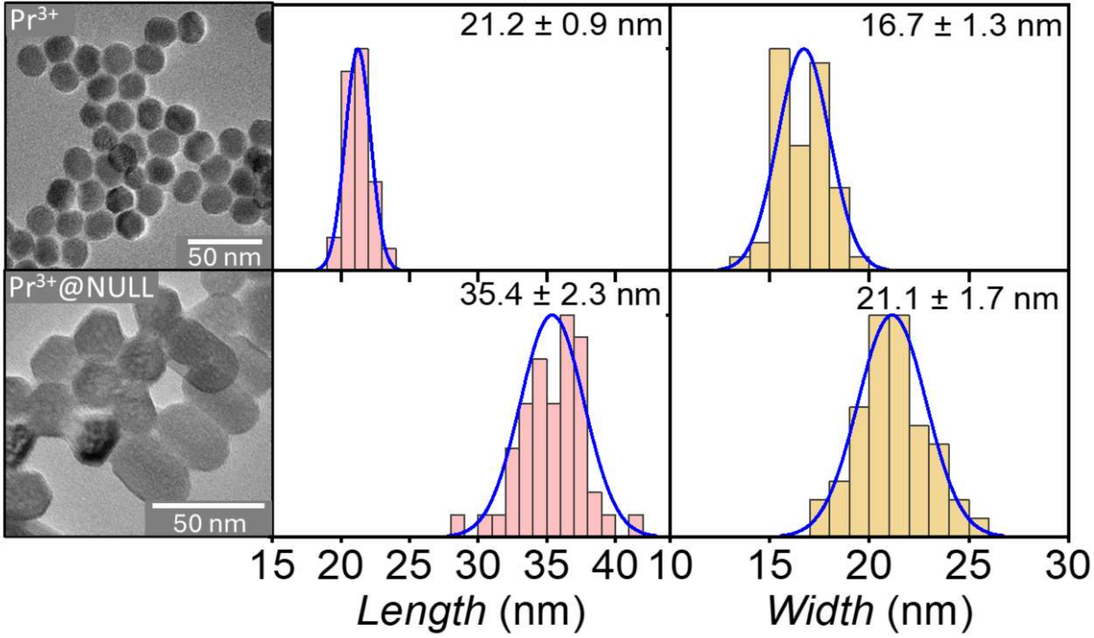

(b) $NaYF_4$: 2% Pr^{3+}, 15% Gd^{3+} @ $NaYF_4$ NPs

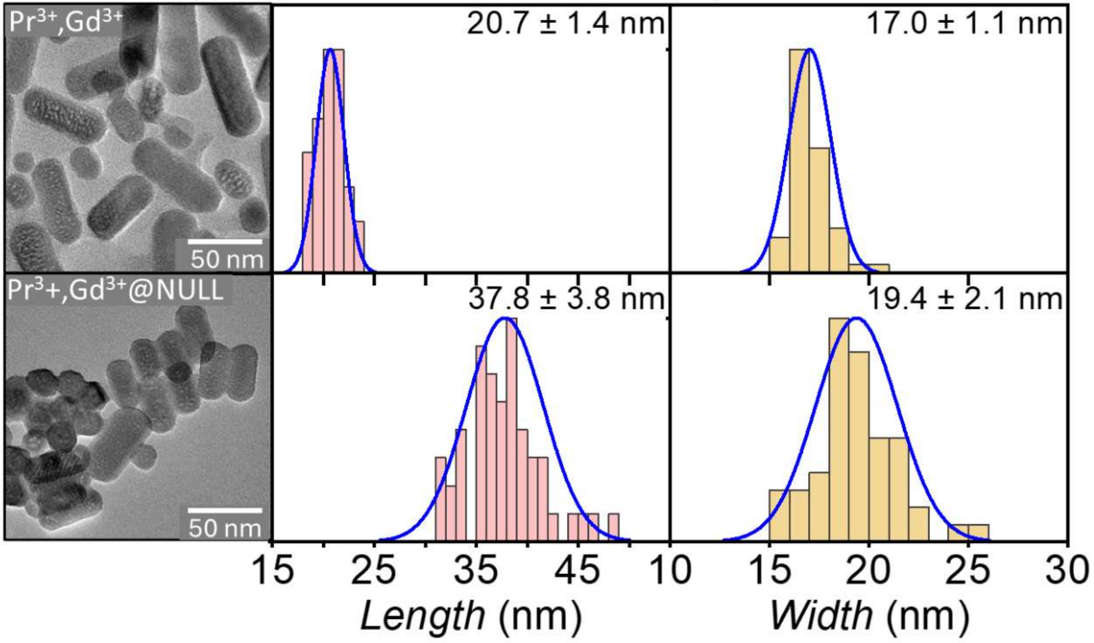

Fig. 35. TEM images (left column), length distribution histograms (middle column), and width distribution histograms (right column) of Na^+-based CS NPs (a) Pr^{3+}@NULL (b) Pr^{3+},Gd^{3+}@NULL

(a) $LiYF_4 : 2\% \ Pr^{3+}$ MCs

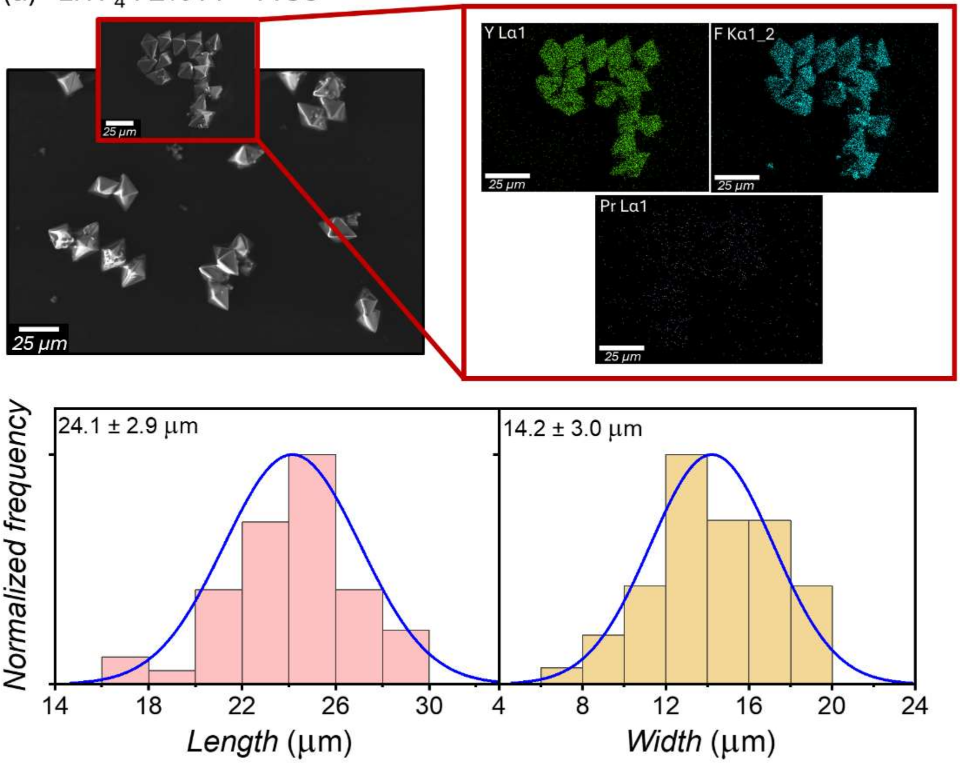

(b) $LiYF_4 : 2\% \ Pr^{3+}, 5\% \ Gd^{3+}$ MCs

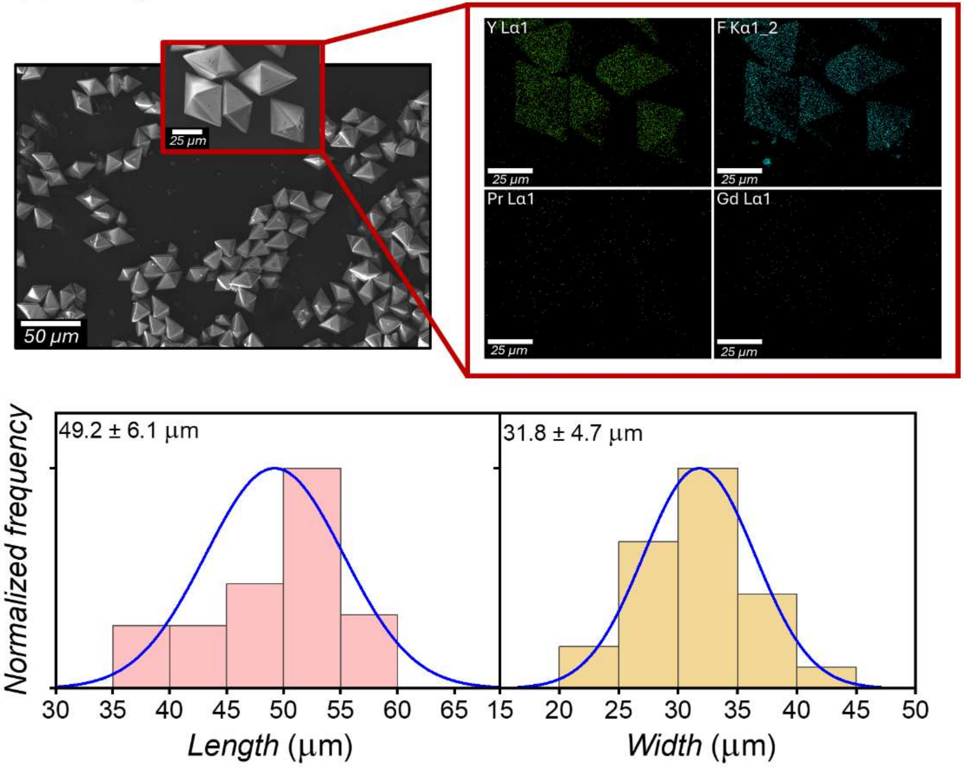

Fig. 36. SEM images and EDS elemental composition maps (upper rows) and length and width (left and right column, respectively) distribution histograms (lower rows) of the synthesized MCs: (a) $LiYF_4$:2% Pr^{3+}, (b) $LiYF_4$:2% Pr^{3+},5% Gd^{3+}

(a) $NaYF_4$: 2% Pr^{3+} MCs

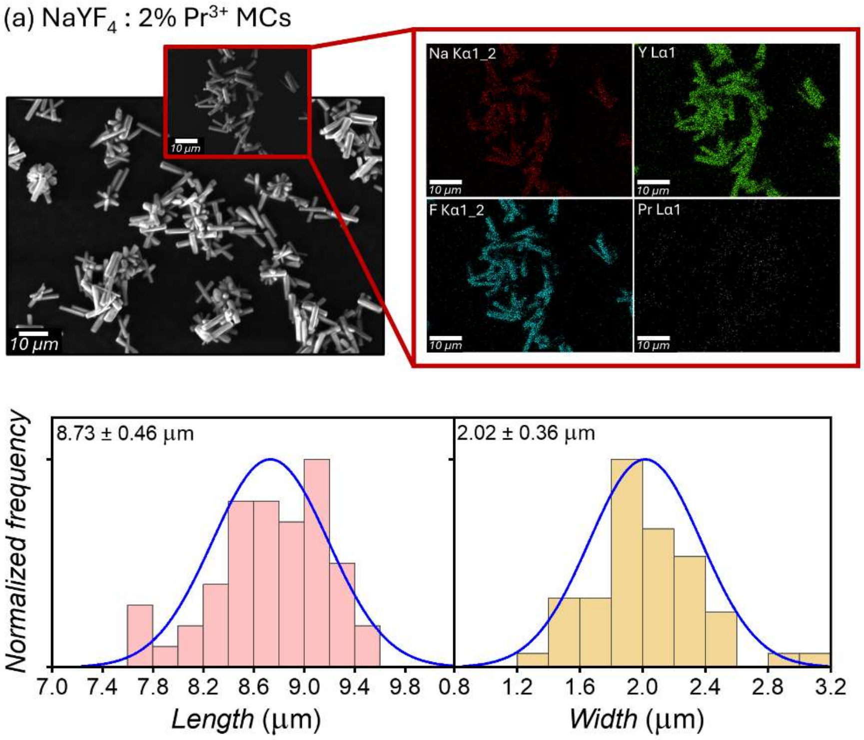

(b) $NaYF_4$: 2% Pr^{3+}, 30% Gd^{3+} MCs

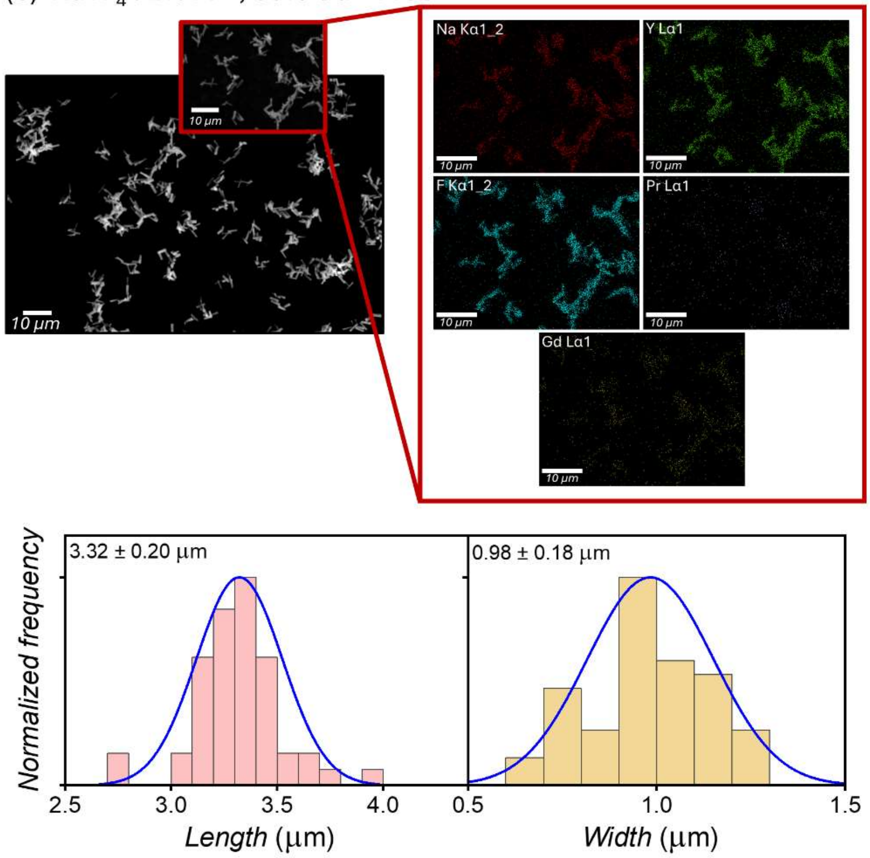

Fig. 37. SEM images and EDS elemental composition maps (upper rows) and length and width (left and right column, respectively) distribution histograms (lower rows) of the synthesized MCs: (a) $NaYF_4$:2% Pr^{3+}, (b) $NaYF_4$:2% Pr^{3+},30% Gd^{3+}

Since the synthesized Pr^{3+}-co-doped MCs were larger than the NPs, SEM technique was utilized to analyze both their morphology and size, along with EDS elemental distribution maps registration (Fig. 36-37). The obtained $LiYF_4$ MCs exhibited the shape of tetragonal bipyramid, with average dimensions of 24.1 ± 2.9 × 14.2 ± 3.0 μm for $LiYF_4$:2%Pr^{3+} MCs and 49.2 ± 6.1 × 31.8 ± 4.7 μm for $LiYF_4$:2%Pr^{3+},5%Gd^{3+} MCs. In contrast, the $NaYF_4$ MCs resembled rods-like structure, measuring 8.73 ± 0.46 × 2.02 ± 0.36 μm in case of $NaYF_4$:2%Pr^{3+} MCs and 3.32 ± 0.20 × 0.98 ± 0.18 μm for $NaYF_4$:2%Pr^{3+}, 30%Gd^{3+} MCs.

5.4.2. Vis-to-UV UC emission spectra

Having successfully analyzed crystal structure and morphology of the Pr^{3+}-co-doped alkali-metal-based yttrium fluoride NPs and MCs, I registered the Vis-to-UV UC emission upon 447 nm laser diode excitation (Fig. 38a-c). The up-converted emission spectra collected from the dried samples of C NPs, CS NPs, and MCs allowed me to select the most promising materials, which would be utilized for the biological experiment focusing on human virus species inactivation. The energy level diagrams of Pr^{3+} ions with the relevant electronic transitions were provided in Fig. 38d.

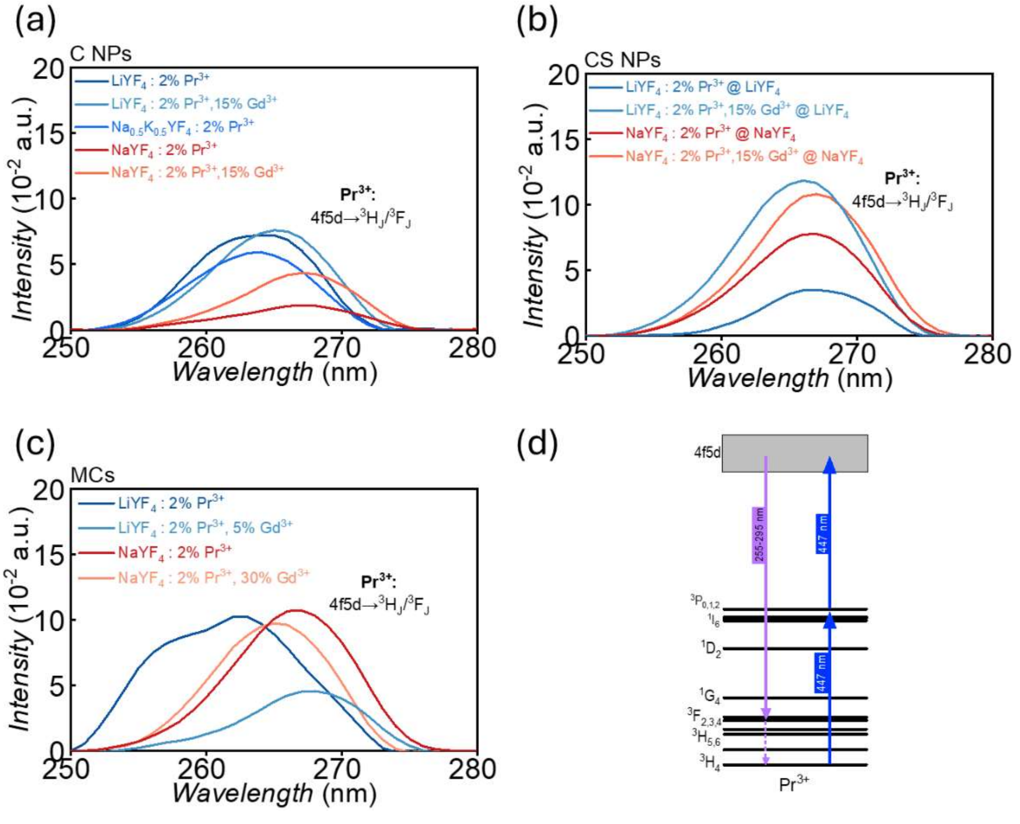

Fig. 38. Vis-to-UV UC emission spectra upon 447 nm laser excitation of the Pr^{3+}-co-doped $LiYF_4$, $NaYF_4$ and $Na_{0.5}K_{0.5}YF_4$ (a) C NPs, (b) CS NPs, and (c) MCs. (d) Energy level structure of Pr^{3+} ions with all relevant electronic transitions

Regardless of the size and host matrix chosen, all materials emitted a broad band spanning between 255÷275 nm, resulting from 4f5d→^3H_J/^3F_J transition in the energy level structure of Pr^{3+} ions (for details see Pr^{3+} ions energy level diagram in Fig. 38d). The emission from this energy level is feasible due to the sequential absorption of 447 nm photons through ^3P_J energy level, which was already proven for these ions not only in Chapter 4 of the doctoral dissertation, but also in research papers focusing on other alkali yttrium fluoride host matrices at the nanoscale, e.g., $BaYF_5$ [149]. Likewise, Gd^{3+} ions incorporated into the host matrix could contribute to UV-C emission, based on reports on up-converted UV-C radiation emission peaking at ca. 275 nm, ascribable to ^6I_J→$^8S_{7/2}$ electronic transition [48,77]. However, the type of host matrix can influence the coordination environment of Y^{3+}, where subtle changes in atomic arrangement may restrict the incorporation of Gd^{3+} ions. The inert shell growth on lanthanide-doped C NPs has been usually recommended to protect optically active centers from prospective interaction with the surroundings, which could simultaneously diminish Vis-to-UV UC emission intensity. Consequently, in case of the CS NPs fabricated by me, UV-C radiation intensity upon 447 nm irradiation was highly likely to increase (Fig. 38a-b). As the particles size was larger, i.e., MCs were considered (Fig. 38c), the registered up-converted emission was not significantly enhanced, as it was expected. One of the possible reasons could be the absorption of up-converted UV radiation by EDTA, a capping agent used in MCs synthesis.

5.4.3. Quantitative validation of dsDNA photodegradation *via* up-converted UV radiation

Since all studied Pr^{3+}-co-doped alkali-metal-based yttrium fluoride NPs and MCs demonstrated UV-C emission attainable through sequential absorption of two 447 nm photons within the ladder-like energy level structure of Pr^{3+} ions, their prospective utility in light-triggered eradication of naked and enveloped virus species was preceded with a proof-of-concept experiment of dsDNA degradation. The results of the evaluation conducted with FADU protocol were shown in Fig. 39a-c, however, for enhanced clarity the values were also provided in Table 9.

The initial dsDNA concentration in each test cuvette was 50.00 ± 2.50 μg mL^{-1}. Upon exposure to the collimated 447 nm CW laser beam, emitting blue photons sequentially absorbed within Pr^{3+} ions energy level structure, up-converted UV-C radiation was generated. The dsDNA concentration decreased after 20 min for all of the irradiated C NPs (Fig. 39a), i.e., by 27.8% (36.11 ± 1.81 μg mL^{-1}) for $LiYF_4$:2%Pr^{3+}, by 13.9% (43.07 ± 2.15 μg mL^{-1}) for $LiYF_4$:2%Pr^{3+},15%Gd^{3+}, by 16.5% (41.77 ± 2.09 μg mL^{-1}) for $NaYF_4$:2%Pr^{3+}, by 26.0% (37.02 ± 1.85 μg mL^{-1}) for $NaYF_4$:2%Pr^{3+},15%Gd^{3+}, and by 25.1% (37.44 ± 1.87 μg mL^{-1}) for $Na_{0.5}K_{0.5}YF_4$:2%Pr^{3+} NPs. The irradiation time extension up to 40 min did not significantly change the concentration for $LiYF_4$:2%Pr^{3+} (37.90 ± 1.90 μg mL^{-1}), $NaYF_4$:2%Pr^{3+},15%Gd^{3+} (35.16 ± 1.76 μg mL^{-1}), and $Na_{0.5}K_{0.5}YF_4$:2%Pr^{3+} NPs (38.74 ± 1.94 μg mL^{-1}). In contrast, $LiYF_4$:2%Pr^{3+},15%Gd^{3+} and $NaYF_4$:2%Pr^{3+} NPs further reduced dsDNA by 6.0% (down to 40.06 ± 2.00 μg mL^{-1}) and 10.3% (down to 36.62 ± 1.83 μg mL^{-1}), respectively. Compared to the C NPs, the CS NPs caused a more significant decrease in dsDNA concentration in the solution exposed to the up-converted UV-C radiation (see Fig. 39b). Specifically, $LiYF_4$:2%Pr^{3+}, 15%Gd^{3+}@$LiYF_4$ and $NaYF_4$:2%Pr^{3+},15%Gd^{3+}@$NaYF_4$ NPs reduced dsDNA to 36.25 ± 1.81 μg mL^{-1} and 41.81 ± 2.09 μg mL^{-1} after 20 min, respectively, and further to 37.70 ± 1.89 μg mL^{-1} and 33.67 ± 1.68 μg mL^{-1} after 40 min, accordingly. However, the inert shell growth on Pr^{3+}-co-doped C NPs (forming $LiYF_4$:2%Pr^{3+}@$LiYF_4$ and $NaYF_4$:2%Pr^{3+}@$NaYF_4$) did not notably affect dsDNA degradation. This suggests that the enhancement of UV-C emissive properties of the nanophosphors was caused by co-doping with Gd^{3+} ions.

The further conducted investigation on Pr^{3+}-co-doped MCs revealed differences between $LiYF_4$ and $NaYF_4$ matrices (Fig. 39c). $LiYF_4$:2%Pr^{3+} MCs reduced dsDNA concentration to 44.39 ± 2.22 μg mL^{-1} after 20 min, and 41.18 ± 2.06 μg mL^{-1} after 40 min. In contrast, $LiYF_4$:2%Pr^{3+},5%Gd^{3+} MCs reduced it to 40.58 ± 2.03 μg mL^{-1} after 20 min, with no further change after 40 min. For $NaYF_4$-based MCs, the solely Pr^{3+}-doped sample reduced the amount of dsDNA by 34.8% (32.62 ± 1.63 μg mL^{-1}) after 20 min and 37.6% (31.22 ± 1.56 μg mL^{-1}) after 40 min. However, $NaYF_4$:2%Pr^{3+},30%Gd^{3+} MCs showed the reduced performance, with dsDNA concentrated at 36.33 ± 1.82 μg mL^{-1} after the 20-min exposure time and 34.96 ± 1.75 μg mL^{-1} after 40-min-long one. The reduction in the efficiency was highly likely to occur due to concentration quenching and ET between Pr^{3+} and Gd^{3+} ions, hindering Vis-to-UV UC efficiency and, consequently, dsDNA degradation process.

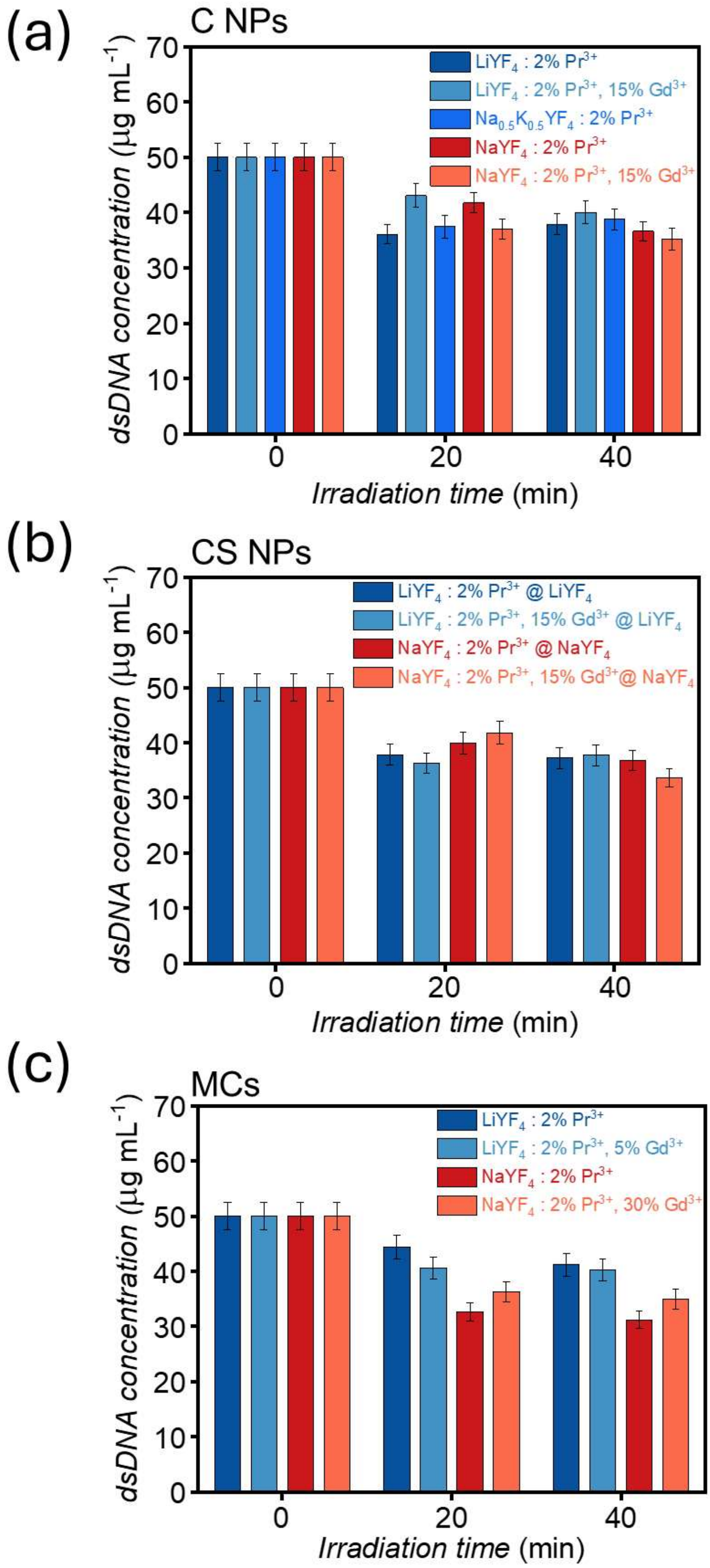

Fig. 39. Summary of quantitative dsDNA photodegradation validation via up-converted UV-C radiation – dsDNA concentration in the solution after exposition to 447 nm CW laser diode for 0, 20 and 40 min in the presence of the synthesized (a) C NPs, (b) CS NPs, and (c) MCs

Table 9. dsDNA concentration before and after its irradiation with a 447 nm CW laser diode in the presence of the synthesized $LiYF_4$, $NaYF_4$, and $Na_{0.5}K_{0.5}YF_4$ NPs and MCs

	Irradiation time (min)		
	0	**20**	**40**
Investigated sample	**dsDNA concentration (μg mL^{-1}) [amount of initial concentration (%)]**		
$LiYF_4$: 2% Pr^{3+} NPs	50.00 ± 2.50 [100.0]	36.11 ± 1.81 [72.2]	37.90 ± 1.90 [75.8]
$LiYF_4$: 2% Pr^{3+} @ $LiYF_4$ NPs		37.82 ± 1.89 [75.6]	37.23 ± 1.86 [74.5]
$LiYF_4$: 2% Pr^{3+}, 15% Gd^{3+} NPs		43.07 ± 2.15 [86.1]	40.06 ± 2.00 [80.1]
$LiYF_4$: 2% Pr^{3+}, 15% Gd^{3+} @ $LiYF_4$ NPs		36.25 ± 1.81 [72.5]	37.70 ± 1.89 [75.4]
$NaYF_4$: 2% Pr^{3+} NPs		41.77 ± 2.09 [83.5]	36.62 ± 1.83 [73.2]
$NaYF_4$: 2% Pr^{3+} @ $NaYF_4$ NPs		39.97 ± 2.00 [79.9]	36.79 ± 1.84 [73.6]
$NaYF_4$: 2% Pr^{3+}, 15% Gd^{3+} NPs		37.02 ± 1.85 [74.0]	35.16 ± 1.76 [70.3]
$NaYF_4$: 2% Pr^{3+}, 15% Gd^{3+} @ $NaYF_4$ NPs		41.81 ± 2.09 [83.6]	33.67 ± 1.68 [67.3]
$Na_{0.5}K_{0.5}YF_4$: 2% Pr^{3+} NPs		37.44 ± 1.87 [74.9]	38.74 ± 1.94 [77.5]
$LiYF_4$: 2% Pr^{3+} MCs	50.00 ± 2.50 [100.0]	44.39 ± 2.22 [88.9]	41.18 ± 2.06 [82.4]
$LiYF_4$: 2% Pr^{3+}, 5% Gd^{3+} MCs		40.58 ± 2.03 [81.2]	40.28 ± 2.01 [80.6]
$NaYF_4$: 2% Pr^{3+} MCs		32.62 ± 1.63 [65.2]	31.22 ± 1.56 [62.4]
$NaYF_4$: 2% Pr^{3+}, 30% Gd^{3+} MCs		36.33 ± 1.82 [72.7]	34.96 ± 1.75 [69.9]

Based on both the capability to emit intense up-converted UV-C radiation and how efficient UV-C-induced dsDNA degradation was, I selected the most promising materials for the experiment of human naked and enveloped virus species inactivation. All of the synthesized CS NPs (i.e., $LiYF_4$:2%Pr^{3+}@$LiYF_4$, $LiYF_4$:2%Pr^{3+},15%Gd^{3+}@$LiYF_4$, $NaYF_4$:2%Pr^{3+}@$NaYF_4$, and $NaYF_4$:2%Pr^{3+},15%Gd^{3+}@$NaYF_4$) were chosen due to the generation of strong UV-C UC signal and higher amount of dsDNA degraded after 40 min of the irradiation with 447 nm CW laser beam, compared to the corresponding C NPs. Among the synthesized MCs within the research scope, $NaYF_4$:2%Pr^{3+} MCs showed the greatest dsDNA degradation rate, even just after 20 minutes of up-converted UV-C emission, therefore, this microphosphor was picked for further biological studies.

5.4.4. Antiviral properties of selected Pr^{3+}-co-doped alkali-metal-based NPs and MCs

The evaluation of antiviral properties of Vis-to-UV UC emission generated by the selected Pr^{3+}-co-doped alkali-metal-based NPs and MCs was decided to be conducted on two common human virus species – HAdV-C5 and HSV-1. Although they have the dsDNA genome, its size is different (HAdV-C5 – 26÷45 kbp, vs. HSV-1 – 152 kbp). Additionally, the genome of HSV-1 is placed in lipid bilayer – the envelope. Infections caused by HSV-1 are fairly ordinary, however, after the first one in the host's organism the virus particles remain latent permanently and the symptoms recurrence occurs with any immune decline [150]. In contrast, HAdV-C5 infects epithelial cells of the upper and lower respiratory tracts, causes their lysis and thus allows progeny copies to spread to neighboring cells [151]. For this study, different types of viruses were selected, as according to European standards, similar effectiveness of a physical or chemical disinfectant against viruses with comparable morphological characteristics can be assumed [142].

Since the biological studies had to be performed in water, there was a need to transform the earlier selected Pr^{3+}-co-doped CS NPs from organic phase to aqueous one. Therefore, the experiment was preceded with acidic etching [147]. The resulting ligand-free CS NPs were dispersed in distilled water to form stable suspensions. The concentration of the materials estimated by the weight of dry solid residues was provided in Table 10 along with the concentration of the diluted samples, used for the intrinsic cytotoxicity studies.

Table 10. Estimated concentration of the chosen Pr^{3+}-co-doped $LiYF_4$ and $NaYF_4$ CS NPs and MCs in water suspension, provided in mg mL^{-1}

		Estimated concentration [%]		
Investigated material	**Size**	**25% of the initial concentration**	**50% of the initial concentration**	**100% of the initial concentration**
$NaYF_4$:2%Pr^{3+}@$NaYF_4$	NPs	7.5	15	30
$LiYF_4$:2%Pr^{3+},15%Gd^{3+}@$LiYF_4$	NPs	8.75	17.5	35
$NaYF_4$:2%Pr^{3+},15%Gd^{3+}@$NaYF_4$	NPs	9.25	18.5	37
$LiYF_4$:2%Pr^{3+}@$LiYF_4$	NPs	5.5	11	22
$NaYF_4$:2%Pr^{3+}	MCs	29.5	59	118

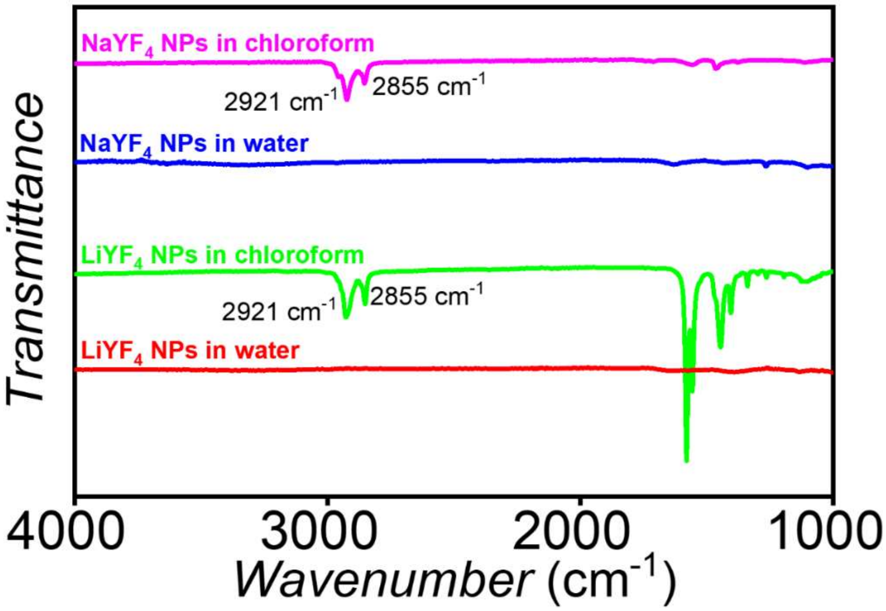

Fig. 40. FT-IR spectra of the Pr^{3+}-co-doped $LiYF_4$ and $NaYF_4$ NPs before and after the organic-to-aqueous phase transfer

In order to verify the complete removal of organic ligands from the surface of the NPs, FT-IR spectra were recorded (Fig. 40). Prior to surface functionalization (denoted in Fig. 40 as 'in chloroform'), $NaYF_4$ and $LiYF_4$ NPs exhibited two peaks at 2921 cm^{-1} and 2855 cm^{-1}, corresponding to the asymmetric and symmetric stretching vibrations of the methylene ($–CH_2–$) group in the long alkyl chain of oleic acid, a ligand utilized during the NPs synthesis [152]. However, these characteristic peaks were no longer observed in the FT-IR spectra after the NPs were transferred from the organic phase to the aqueous one (denoted in Fig. 40 as 'in water'). Therefore, their absence suggests the oleic acid successful removal from the NPs surface, confirming the effective displacement of the –HC=CH– group.

Further, in order to establish cytotoxic effects toward cell cultures, the non-colorimetry-based method described in the EN 14476 standard was utilized. Within the study one found the cytotoxic effects for all Pr^{3+}-co-doped NPs and MCs used at the dilutions up to 10^{-2}. The strong cellular toxicity was observed in the wells containing highly-concentrated suspensions, whereas at further dilutions only a small fraction of cells was destroyed. The reason for intrinsic CPE could be connected with the increased concentration of H^+ ions, remaining after organic-to-water phase transfer, or, more likely, in mechanical damage due to interactions occurring between particles and cells.

In the next step within the research scope, the capability of the selected Pr^{3+}-co-doped NPs and MCs to inactivate HSV-1 and HAdV-C5 viruses was evaluated both before and after the irradiation with the 447 nm CW laser (Fig. 41, for exact efficiency rate values see Table 11). All of the tested materials showed very high (99.99%) virucidal efficiency against enveloped virus HSV-1, even as they were not exposed to laser radiation. The reason supporting the immediate antiviral effect without irradiation could be connected with simple physical contact between the enveloped virus particles and the materials, regardless of their size. As far as the non-enveloped HAdV-C5 virus was concerned, CPE was much weaker. Only $NaYF_4$:2% Pr^{3+} MCs exhibited the inactivation efficiency at 99% when no radiation was utilized. On the contrary, the selected NPs were not virucidal against this pathogen under the same conditions. Even though both virus species have a dsDNA genome, HSV-1 was inactivated by all tested materials at the highest level (≥99.99%) without laser irradiation, while for HAdV-C5 the native cytotoxicity was not observed besides for $NaYF_4$:2% Pr^{3+} MCs. Such results do not support the hypothesis that intrinsic virucidal activity is determined by the number of genetic material strands. However, the lack of the lipid envelope might explain why adenovirus was inactivation-resistant, while herpesvirus, an enveloped pathogen, was relatively easy to eradicate even in the close contact with the materials. This idea finds the support in yet another study, where virus species were classified into three main categories, based on the increasing susceptibility to be neutralized by chemical disinfectants: enveloped, large non-enveloped, and small non-enveloped [153]. Accordingly, herpesvirus could be ascribed to the first group, whereas adenovirus belongs to the second one.

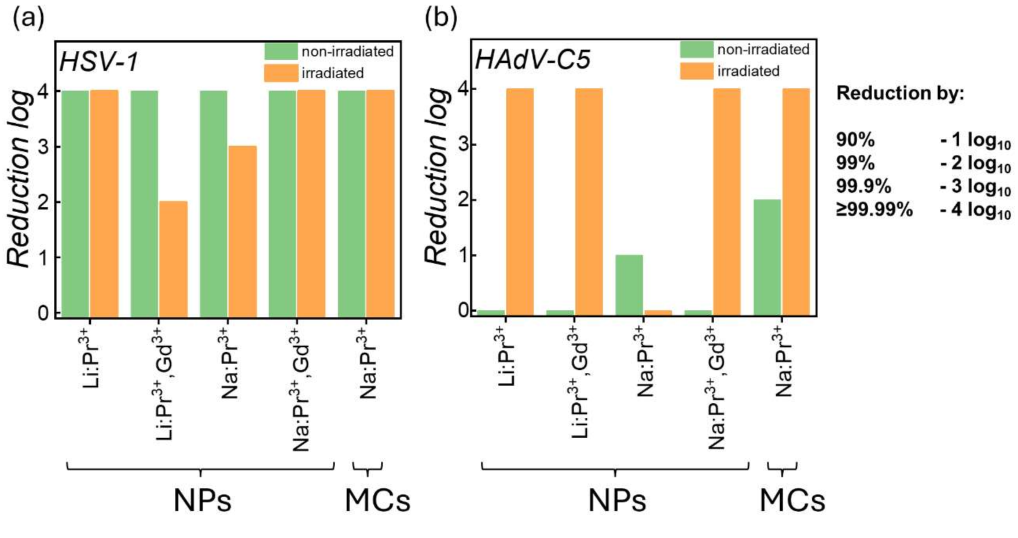

Fig. 41. Virucidal properties of the tested water-suspended $LiYF_4$ and $NaYF_4$ CS NPs and MCs before (green bars) and after (orange bars) the exposition to 447 nm CW laser radiation (~1000 J cm^{-2} light dose) against (a) HSV-1 and (b) HAdV-C5 virus species

Table 11. Virucidal properties of the tested water-suspended $LiYF_4$ and $NaYF_4$ CS NPs and MCs before and after 447 nm CW laser radiation exposition

Investigated material	**Virus cytotoxicity BEFORE laser irradiation**		**Virus cytotoxicity AFTER laser irradiation**	
	HSV-1	**HAdV-C5**	**HSV-1**	**HAdV-C5**
$NaYF_4$:2%Pr^{3+} MCs	≥99.99%	99%	99.9%	≥99.99%
$LiYF_4$:2%Pr^{3+}@ $LiYF_4$ NPs	≥99.99%	0%	99.9%	≥99.99%
$LiYF_4$:2%Pr^{3+},15%Gd^{3+}@$LiYF_4$ NPs	≥99.99%	0%	99%	≥99.99%
$NaYF_4$:2%Pr^{3+}@$NaYF_4$ NPs	≥99.99%	0%	99.9%	0%
$NaYF_4$:2%Pr^{3+},15%Gd^{3+}@$NaYF_4$ NPs	≥99.99%	0%	99.9%	≥99.99%

The results were completely different when the 447 nm CW laser beam was utilized. As already proven, the synthesized CS NPs and MCs were capable to emit UV-C radiation due to the UC process occurring within the ladder-like energy level structure of Pr^{3+} ions. Consequently, it could interact with the selected naked and enveloped human virus species. Since the water suspensions of CS NPs and MCs exhibited the cytotoxic effect on HSV-1 virus, no significant difference was expected to be seen and, indeed, it was experimentally confirmed. However, adenovirus irradiation with the 447 nm CW laser in the presence of Pr^{3+}-co-doped materials resulted in the virus mortality rate rocketing – it increased to over 99.99%. Only the efficiency shown by $NaYF_4$:2%Pr^{3+}@$NaYF_4$ NPs remained at constant level of 0%.

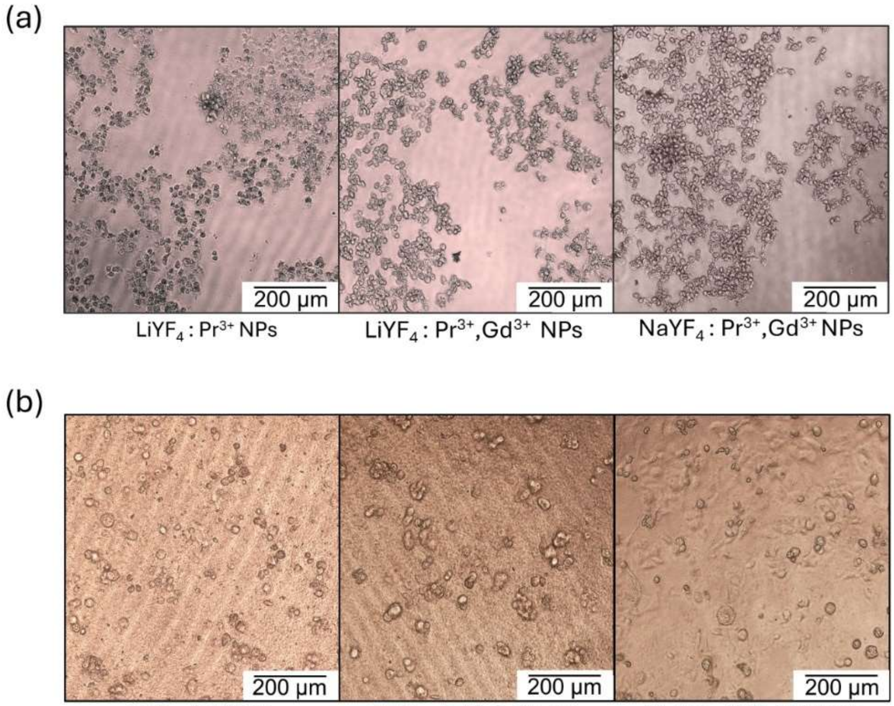

Fig. 42. The impact of the chosen suspensions on HAdV-C5 inoculated into A549 cells (a) before laser irradiation, (b) after laser irradiation. The test formulations were exposed to the 447 nm CW laser diode at ~1000 J cm^{-2} light dose. Reproduced from Fałat et al [154]

The provided results revealed that the synthesized CS NPs and MCs were capable to reduce infectivity of naked virus species after the exposition to 447 nm CW laser radiation. It is highly likely that UV-C radiation emitted *via* UC influenced on structure and morphology of the virus, simultaneously blocking its interaction with the host cells which it was inoculated onto. Consequently, as provided in the optical microscopy photos comparison for chosen NPs (Fig. 42a – before and Fig. 42b – after the exposition to 447 nm laser radiation) neither the cells rounding nor the detachment from the culture dish bottom induced by active virus replication was noticed, which advocates for no CPE. The materials at the nanoscale exhibited also better virucidal activity along with the intrinsic cytotoxic effect of lower magnitude (see Table 11). The observed changes clearly indicated that Vis-to-UV UC process in Pr^{3+}-co-doped alkali-metal-based yttrium fluoride CS NPs and MCs could enhance their germicidal action, even toward the viruses perceived as the most cumbersome to eradicate.

5.5. Conclusions

In this chapter I conducted a comprehensive optimization study on synthesis of Pr^{3+}-co-doped alkali-metal-based yttrium fluoride NPs and MCs, capable to generate Vis-to-UV UC emission of sufficient brightness for commonly known human virus species deactivation purposes. Using wet chemistry techniques, I successfully obtained a series of $NaYF_4$, $LiYF_4$, and $Na_{0.5}K_{0.5}YF_4$ NPs, in some of which nanoarchitecture two crucial components were distinguishable – the optically active Pr^{3+}-based core and the epitaxially grown inert shell for enhancing emissive properties in the region of interest. Some of these NPs were additionally co-doped with Gd^{3+} ions to improve the up-converted UV emission. For comparison, the materials at microscale were synthesized, bearing selected lanthanide ions at the corresponding molar concentrations. Followingly, I registered the Vis-to-UV UC emission spectra of all fabricated NPs and MCs. The band peaking at ca. 275 nm ascribable to the transition occurring within the electronic structure of Pr^{3+} ions was observed in all of them. In the next step, I used the resultant UC luminescence to denature dsDNA in the aqueous solution in order to select the most promising materials for the light-triggered inactivation of naked and enveloped human virus species. For further studies I chose $LiYF_4$ and $NaYF_4$ CS NPs and $NaYF_4$:2% Pr^{3+} MCs, as the up-converted UV-C radiation generated within the 40 min exposure time to the collimated 447 nm CW laser beam significantly reduced the dsDNA concentration. Since the biological tests required to be conducted in water environment, I successfully transferred NPs from organic phase to water by etching them with HCl solution.

The biological experiment was performed on commonly known human virus species – the enveloped HSV-1 and the naked HAdV-C5, both dangerous for human beings. The results suggested that intrinsic virucidal activity was not based on the number of genetic material strands, as both virus species have double-stranded genomes. The intrinsic CPE caused by the selected materials was extremely high for HSV-1 (≥99.99%), even though they were not exposed to 447 nm radiation. The phenomenon could be explained based on the interactions between the materials and the lipid bilayer forming the envelope of herpesvirus. On the other hand, the dark cytotoxicity for the naked adenovirus was not observed for the vast majority of Pr^{3+}-co-doped NPs. It is highly probable then than Vis-to-UV UC affected the HAdV-C5 structure, which reduced its virulence toward the host cells. As a consequence, the investigated materials at the nanoscale exhibited strong photoactivated virucidal activity, reaching the value of 99.9%.

The promising results of the biological experiment show the application potential of Pr^{3+}-co-doped alkali-metal-based yttrium fluoride CS NPs and MCs as a source of up-converted UV-C radiation, prone to provide photoeradication of virus species. With well-established synthetic methods, they can be prepared in the form of dispersions, ready to be modified for various purposes, e.g., development of self-disinfecting light-activated surfaces or sterilizing wound dressings.

5.6. Acknowledgments

This chapter is partially based on the data presented in the research paper *Inactivation of human viruses using VIS-to-UVC up-conversion luminescence from Pr^{3+}-doped fluoride nano- and microcrystals.* **P. Fałat**, A. Chwirot, P. Kuich, M. Nyk, T.Y. Ohulchanskyy, B. Bażanów, D. Wawrzyńczyk. Rare Metals 44, 2025, pp. 4881-4897.

Within the presented research scope I designed and synthesized Pr^{3+}-co-doped yttrium fluoride C and CS NPs and MCs, in which syntheses such alkali metals as Li, Na, and K were utilized. I investigated their crystal structure purity with the invaluable help of B. Cichy. I also registered the SEM images of MCs along with their EDS elemental distribution maps. In the next step, I captured Vis-to-UV UC emission spectra of all synthesized nano- and micromaterials. I also analyzed in detail the data from Vis-to-UV UC-based dsDNA photodegradation – in their gathering process I was supported by P. Kuich. The biological experiment on non-enveloped and enveloped human virus species inactivation was designed and performed under the guidance and supervision of A. Chwirot and B. Bażanów.

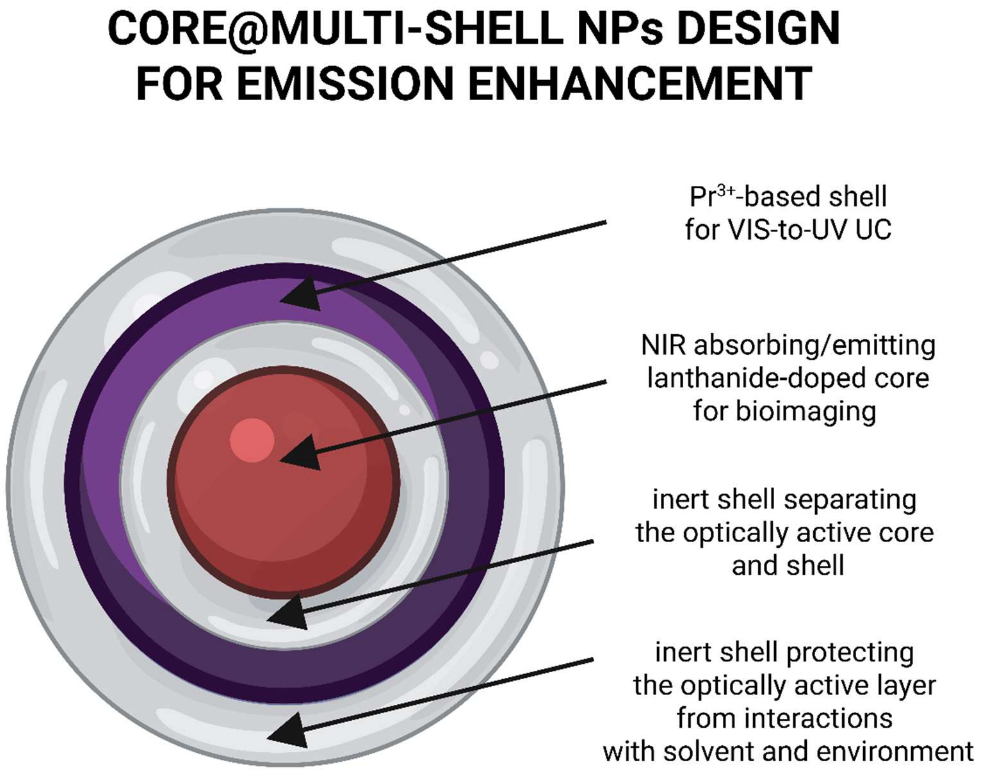

Fig. 43. The cross-section of core@multi-shell NPs synthesized and investigated in the chapter, consisting of the NIR emitting/absorbing core (in red), the inert shell (in gray), and the UV emitting shell (in purple)

Chapter 6

Synthetic design of complex lanthanide-doped core@multi-shell β-NaYF$_4$ nanostructures for concurrent emission in divergent spectral regions

My previous comprehensive studies unveiled that the synthesized β-NaYF$_4$:Pr^{3+},Yb^{3+} and LiYF$_4$:Pr^{3+},Yb^{3+} NPs exhibited an unusual feature of dual optical functionality for concurrent Vis-to-UV UC-based dsDNA photodegradation and NIR-to-NIR DC-based high-contrast bioimaging (*vide* Chapter 4). The epitaxial growth of an additional inert shell on the Pr^{3+}-co-doped β-NaYF$_4$ and LiYF$_4$ NPs resulted in the CS NPs formation with the enhanced intensity of up-converted UV-C radiation, which was successfully employed for human enveloped and naked virus species photoinactivation (*vide* Chapter 5). Hence, having been provided with the promising spectral characteristics of the Pr^{3+}-co-doped C and CS NPs in the wavelength regions of interest, in this chapter I present the results on the advanced engineering of lanthanide-doped core@multi-shell β-NaYF$_4$ nanostructures exhibiting emission in both UV and NIR ranges, thus showing significantly enhanced application potential for theranostics.

The novel approach to the scientific challenge of manufacturing materials that demonstrate concurrent emission in UV and NIR spectral regions stems from the spatial separation of optically active lanthanides. Through highly developed thermal decomposition reaction methods, I synthesize the core@multi-shell β-NaYF$_4$ nanoarchitectures of well-defined size and shape, of which the cross-section scheme is presented in Fig. 43. Doping the core with NIR-emitting and NIR-absorbing lanthanide ions, such as Nd^{3+}, Yb^{3+}, or Tm^{3+}, effectively isolates them from parasitic quenching processes as f-f transitions falling in the NIR range are more prone to be quenched by vibrational modes of solvents or ligand molecules. Having been spatially isolated with the undoped β-NaYF$_4$ shell, the core@shell is covered with the Pr^{3+}-doped shell for Vis-to-UV UC-based therapeutic purposes. The resulting nanostructures have yet another inert shell to reduce the number of defects, depicted as PL intensity diminishing centers. Induced under various excitation wavelengths (447 nm, 808 nm or 980 nm), the appearing UV and NIR emission bands are highly likely to be utilized for antibacterial, antiviral or even anticancer treatments and for optical bioimaging of high contrast, respectively.

The conducted spectral analysis provides thus the solid evidence that lanthanide-doped core@multi-shell β-$NaYF_4$ NPs could be a significant step forward in the design of nanomaterials with dual optical functionality for theranostic applications.

6.1. Introduction to the scientific problem

The intensive research on lanthanide-doped fluoride-based NPs and their broad potential for application in cutting-edge technological solutions has spurred the development of numerous synthetic protocols [155,156]. As briefly revised in Section 3.1, these straightforward methods facilitate the formation of NPs varying in size, shape, and elemental composition, simultaneously ensuring both low size dispersity within the obtained batch and high reproducibility across multiple batches [64]. Furthermore, thermal decomposition reaction of corresponding precursors enables the layer-by-layer NPs synthesis, resulting in the formation of nanostructures of higher complexity, i.e., CS structures. This opens up the possibility of obtaining various spatial distribution of trivalent lanthanide ions within the NPs architecture and, consequently, investigating its influence on their luminescent properties [157].

The initial reports on enhanced up-converted radiation (NIR-to-Vis UC) were provided for core@undoped-shell NPs [38,141]. Later on, active-core@active-shell nanosystems were proposed for such purposes as enhancing UC efficiency [158], minimizing undesired ET processes between trivalent lanthanide dopants [159], improving the functionality of non-contact luminescence-based NPs for temperature and pressure sensing [160], or shifting the excitation wavelength to better suit the prospective bio-related applications in cells and tissues (e.g., changing the excitation source from 980 nm to 808 nm to reduce the heating effect of water present in biological samples) [103,161]. Finally, core@multi-shell NPs were proposed to enable the spatial separation of doping ions for engineering of various photon management processes [162]. For instance, this approach to photon management processes was exploited by Su et al. to realize the sequential absorption of six NIR-I photons, resulting in UV-C emission at ~254 nm from Gd^{3+} ions incorporated into the host matrix forming the outer shell [163]. In the literature, significant emphasis is put also on inert undoped shells incorporated amid the optically active segments of the nanoarchitecture, effectively inhibiting unwanted CR processes between various lanthanide ions, thereby enhancing emissive properties in the wavelength regions of interest [76]. Yet another approach employs the heterostructures combining various host matrices (e.g., β-$NaYF_4$ core and CaF_2 shell), which show low phonon energies and good structural matching in terms of UC emission enhancement [74].

The depicted robust catalog of sophisticated internal fluoride-based nanoarchitectures opens up the possibility of experimenting with photon management processes, which could have a beneficial impact on luminescent properties in specific spectral regions. Therefore, since I had provided the thorough analysis of β-$NaYF_4$:Pr^{3+},Yb^{3+} and $LiYF_4$:Pr^{3+},Yb^{3+} NPs luminescent properties in Chapter 4 and had proved the enhanced up-converted UV-C emission of the Pr^{3+}-co-doped β-$NaYF_4$ and $LiYF_4$ CS NPs in Chapter 5, I was fully motivated to investigate how the mutual separation and spatial distribution of trivalent lanthanide ions within the engineered core@multi-shell NPs influence Vis-to-UV UC and NIR-to-NIR DC emissions. I hypothesized that the utilization of highly-developed method of thermal decomposition of corresponding precursors in high boiling point surfactants enables complex β-$NaYF_4$ core@shell@shell@shell NPs synthesis. Consequently, photon management processes could be engineered to minimize the occurrence of parasitic ET processes between various lanthanide ions, simultaneously leading to stronger emission signals in both UV and NIR spectral regions.

My approach, which does exploit photon management processes engineering, is based on synthesizing β-$NaYF_4$ C NPs bearing 1% Nd^{3+}, 1% Tm^{3+}, or 10% Yb^{3+} ions. In this way, the complete separation of NIR-absorbing/emitting lanthanide ions from solvents and ligand molecules is beneficial to eradicate any peristatic quenching processes [38]. Additionally, earlier optimized and reported in the literature, the molar concentration of lanthanides was chosen to maximize emission intensity in the NIR range and simultaneously reduce the probability of concentration quenching occurrence between neighboring ions [140,164,165]. In the subsequent step, the first undoped shell (depicted in the text and the figures as 'NULL') is epitaxially grown, leading to the CS NPs formation and spatially separating the core from the second shell doped with Pr^{3+} ions for Vis-to-UV UC (thus resulting in core@shell@shell NPs formation, described within the text as 'CSS NPs'). Finally, the last undoped inert shell is deposited (core@shell@shell@shell NPs synthesis, marked within the text as 'CSSS NPs'), significantly reducing the amount of surface defects and thus protecting Pr^{3+} ions from surface quenching. Resultantly, the following core@multi-shell nanostructures are formed (for enhanced text clarity the abbreviated forms are provided in the brackets as they are utilized throughout this chapter):

- $NaYF_4$:1%Nd^{3+}@$NaYF_4$@$NaYF_4$:1%Pr^{3+}@$NaYF_4$ (Nd^{3+}@NULL@Pr^{3+}@NULL),
- $NaYF_4$:10%Yb^{3+}@$NaYF_4$@$NaYF_4$:1%Pr^{3+}@$NaYF_4$ (Yb^{3+}@NULL@Pr^{3+}@NULL),
- $NaYF_4$:1%Tm^{+}@$NaYF_4$@$NaYF_4$:1%Pr^{3+}@$NaYF_4$ (Tm^{3+}@NULL@Pr^{3+}@NULL).

With regard to optical spectroscopy, the emphasis is placed on measurements in the UV-C and NIR spectral regions to validate that the up-converted UV-C radiation generation for prospective therapeutic purposes with the high-contrast NIR-II emission for deep-tissue optical bioimaging could be combined within highly-advanced core@multi-shell nanoarchitectures.

6.2. Materials

For β-$NaYF_4$ core@multi-shell NPs synthesis the following chemicals were used: Nd_2O_3 (99.99%), Pr_2O_3 (99.99%), Tm_2O_3 (99.995%), Y_2O_3 (99.99%), Yb_2O_3 (99.99%), NaOH (≥ 98.0%), NH_4F (≥ 99.99%), acetic acid (pure for analysis, 99.5÷99.9%), oleic acid (technical grade, 90%), octadec-1-ene (technical grade, 90%), methanol (99%), ethanol (99.8%), hexane, chloroform, and acetone. All reagents were purchased from Sigma Aldrich and utilized without prior purification.

All of the β-$NaYF_4$ core@multi-shell NPs series were prepared in accordance with the protocol described in Section 3.1.2. The masses of the corresponding solid compounds utilized in the syntheses were provided below in Table 12 for Nd^{3+}@NULL @Pr^{3+}@NULL, Yb^{3+}@NULL@Pr^{3+}@NULL, and Tm^{+}@NULL@Pr^{3+}@NULL β-$NaYF_4$ NPs, respectively.

Table 12. Amounts of solid compounds utilized to synthesize NPs in each step of the Nd^{3+}@NULL@Pr^{3+}@ NULL, Yb^{3+}@NULL@Pr^{3+}@NULL, and Tm^{3+}@NULL@Pr^{3+}@NULL β-$NaYF_4$ core@multi-shell nanoarchitecture (RE stands for Nd, Yb, and Tm, where appropriate)

Synthesized β-$NaYF_4$ nanostructure	**Compound mass [g]**				
	RE_2O_3	**Y_2O_3**	**Pr_2O_3**	**NaOH**	**NH_4F**
Nd^{3+}	0.0034	0.2236	–	0.2000	0.2964
Nd^{3+}@NULL	–	0.2258	–		
Nd^{3+}@NULL@Pr^{3+}	–	0.2236	0.0033		
Nd^{3+}@NULL@Pr^{3+}@NULL	–	0.2258	–		
Yb^{3+}	0.0394	0.2032	–	0.2000	0.2964
Yb^{3+}@NULL	–	0.2258	–		
Yb^{3+}@NULL@Pr^{3+}	–	0.2236	0.0033		
Yb^{3+}@NULL@Pr^{3+}@NULL	–	0.2258	–		
Tm^{3+}	0.0039	0.2236	–	0.2000	0.2964
Tm^{3+}@NULL	–	0.2258	–		
Tm^{3+}@NULL@Pr^{3+}	–	0.2236	0.0033		
Tm^{3+}@NULL@Pr^{3+}@NULL	–	0.2258	–		

6.3. Characterization methods

6.3.1. Crystal structure

The crystal structure of all synthesized C, CS, CSS, and CSSS β-$NaYF_4$ NPs was investigated with the previously described STOE powder X-ray diffractometer (see Section 4.3.1).

6.3.2. Morphology and size distribution

The TEM images were captured using an FEI Tecnai G^2 20 X-TWIN TEM at the Faculty of Chemistry at University of Wrocław, Poland. The procedure to image the NPs was described in detail in Section 4.3.2. The NPs size distribution analysis was performed in OriginPro Software as the diameter size of 100 NPs in the micrographs had been measured in ImageJ Software.

6.3.3. Spectroscopic features

The Vis-to-UV UC spectra of the dried samples deposited on the glass substrates were recorded under ambient conditions with the custom-assembled setup. The measurement procedure was explicitly explained in Section 4.3.3.

The Vis-to-Vis Stokes emission spectra (induced by 447 nm Xe lamp excitation) of the NPs dispersed in chloroform were recorded with the FLS980 Edinburgh Instruments PL spectrometer, along with the luminescence decay curves at chosen emission wavelengths. Additionally, the selected NPs were investigated in terms of NIR-to-NIR DC under either 808 nm laser diode excitation (MDL-N-808 nm, 8.5 W) or 975 nm laser diode excitation (MDL-N-975 nm, 8.5 W). The laser beam was guided to the spectrometer through a 1 mm thick glass fiber employed with collimation optics.

6.4. Results and discussion

6.4.1. Crystal structure and morphology

Sampling small volumes of the intermediate products (i.e., C, CS, and CSS NPs) after each synthetic step enabled me the thorough analysis of β-$NaYF_4$ core@multi-shell NPs formation process. Primarily, XRD measurements of all dried samples (Fig. 44a-c) revealed that obtained diffraction peaks were in good agreement with the standard XRD pattern for undoped β-$NaYF_4$ host matrix (ICSD #51916), which exhibits hexagonal symmetry and is known to have a beneficial impact on up-converting properties of lanthanide-doped fluoride materials [166]. Importantly, the sequential epitaxial growth of additional layers did not alter the crystal structure of the synthesized nanoarchitectures, thus demonstrating the feasibility of the selected synthetic procedure for obtaining the high phase purity core@multi-shell β-$NaYF_4$ NPs. Additionally, it is noteworthy that within β-$NaYF_4$ host matrix, Nd^{3+}, Yb^{3+}, Tm^{3+}, and Pr^{3+} ions could be incorporated at the selected molar concentration without significant alteration of crystal lattice. It is possible due to the similar ionic radii of the ninefold coordinated Nd^{3+} (1.163 Å), Yb^{3+} (1.042 Å), Tm^{3+} (1.052 Å), and Pr^{3+} ions (1.179 Å), compared to the ionic radius of Y^{3+} ions, which are substituted throughout the crystal lattice (1.075 Å) [124].

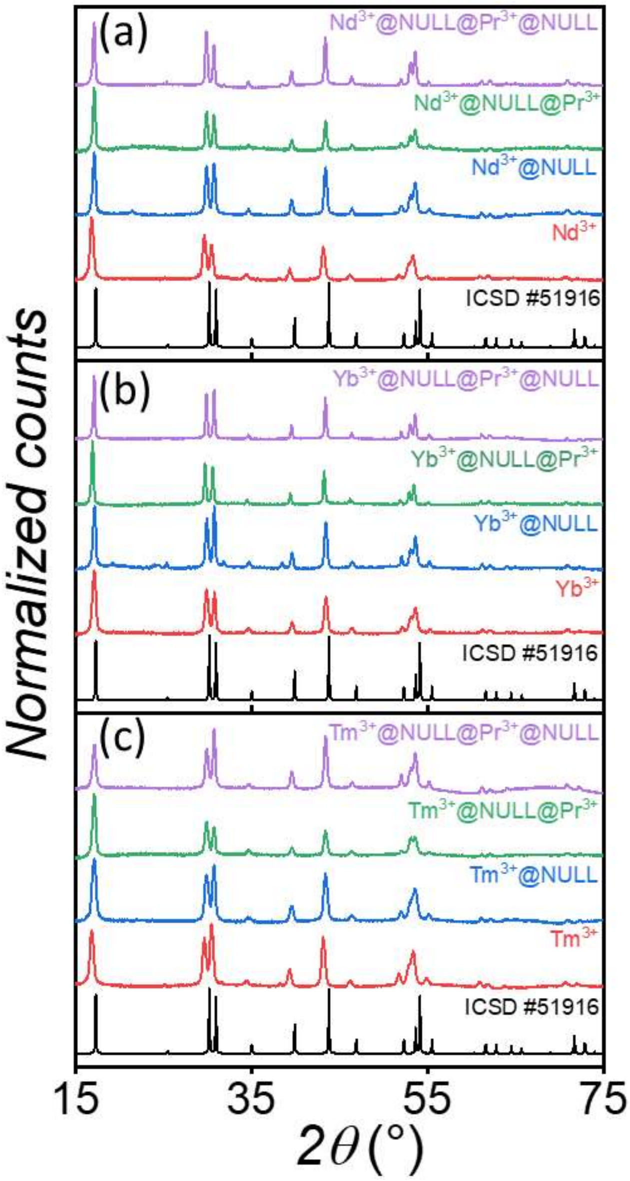

Fig. 44. XRD patterns of (a) Nd^{3+}-co-doped (b) Yb^{3+}-co-doped, and (c) Tm^{3+}-doped core@multi-shell β-$NaYF_4$ NPs series monitored after each step of synthesis vs. theoretical pattern of β-$NaYF_4$ host matrix (ICSD #51916)

Parallelly, the morphology and mean length and width distributions were evaluated based on the TEM measurements for the diluted samples. The TEM images and the mean size distribution histograms were provided in Fig. 45-47 for the formation series of Nd^{3+}-co-doped, Yb^{3+}-co-doped, and Tm^{3+}-co-doped core@multi-shell β-$NaYF_4$ NPs, accordingly. From the outset, all synthesized NPs exhibited size anisotropy, even more noticeable with the deposition of additional shells on the C NPs. The similar formation behavior was reported for other lanthanide-doped core@multi-shell β-$NaYF_4$ nanostructures. The explanation was attributed to the utilization of oleic acid as a capping agent, which promotes the shell growth rather from the six lateral faces of β-$NaYF_4$ host matrix than along the *c* crystallographic direction [167]. The length and width of C NPs doped with Nd^{3+}, Yb^{3+}, and Tm^{3+} ions were 25.2 ± 1.2 × 19.2 ± 1.4 nm, 28.1 ± 1.8 × 17.8 ± 1.4 nm, and 17.2 ± 1.2 × 14.4 ± 1.3 nm, respectively. As the first inert shell was deposited, there was no significant change in the mean length and width of Nd^{3+}@NULL CS NPs (27.7 ± 2.4 × 24.6 ± 2.5 nm), whereas Yb^{3+}@NULL and Tm^{3+}@NULL CS NPs exhibited alterations (57.8 ± 3.8 × 24.3 ± 2.5 nm and 28.4 ± 1.8 × 17.0 ± 1.2 nm, accordingly). The epitaxial growth of the second shell, bearing optically active Pr^{3+} ions for Vis-to-UV UC, promoted the formation of more elongated nanostructures, even though with larger length and width NPs dispersion. The sizes of the intermediate Nd^{3+}@NULL@Pr^{3+}, Yb^{3+}@NULL@Pr^{3+}, and Tm^{3+}@NULL@Pr^{3+} CSS NPs were 43.8 ± 3.1 × 31.5 ± 3.5 nm, 59.7 ± 4.6 × 40.5 ± 3.1 nm, and 35.2 ± 3.1×20.0 ± 1.6 nm, correspondingly. It is worth highlighting that the Yb^{3+}@NULL@Pr^{3+} CSS NPs transformed temporarily from nanorods to nanoellipsoids, highly probably due to acidic etching with oleic acid molecules, occurring at high synthesis temperature [167]. The last deposited inert shell led to CSSS nanorods formation with the average size of 63.7 ± 3.2 × 33.3 ± 2.5 nm for Nd^{3+}@NULL @Pr^{3+}@NULL CSSS NPs, 64.5 ± 4.3 × 44.0 ± 3.8 nm for Yb^{3+}@NULL@Pr^{3+}@NULL CSSS NPs, and 53.5 ± 2.9 × 25.1 ± 2.1 nm for Tm^{3+}@NULL@Pr^{3+}@NULL CSSS NPs.

The detailed analysis of both crystal structure and morphology validates the effectiveness of thermal decomposition protocol described by Abel et al. [87] for synthesizing not only core components, but also allowing for the sequential deposition of additional layers of different elemental composition. Consequently, this approach results in successful formation of lanthanide-doped core@multi-shell β-$NaYF_4$ nanostructures.

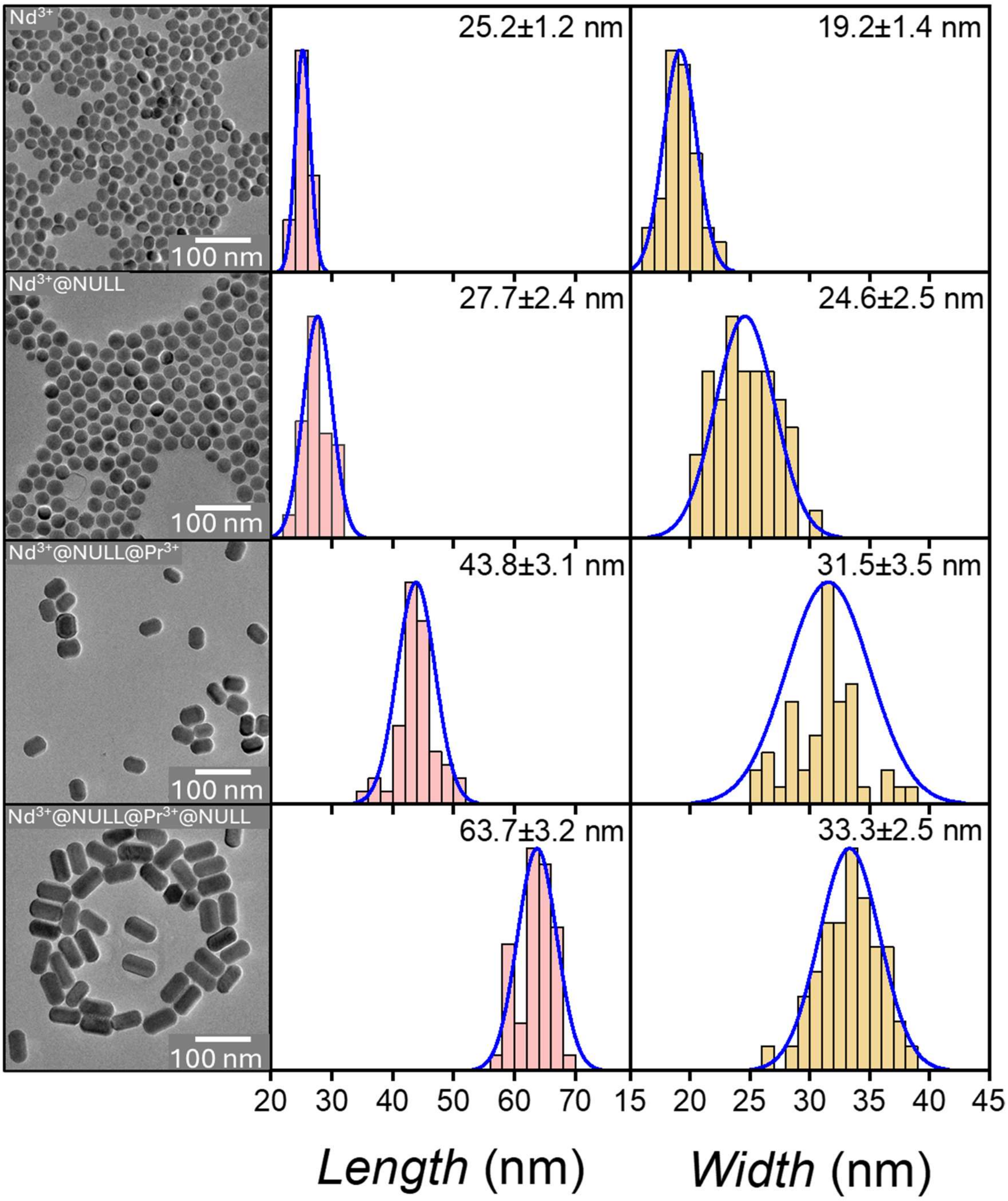

Fig. 45. TEM images (left column), length distribution histograms (middle column), and width distribution histograms (right column) of Nd^{3+}-co-doped C, CS, CSS, and CSSS β-$NaYF_4$ NPs

Yb^{3+}-based β-$NaYF_4$ core@multi-shell NPs formation

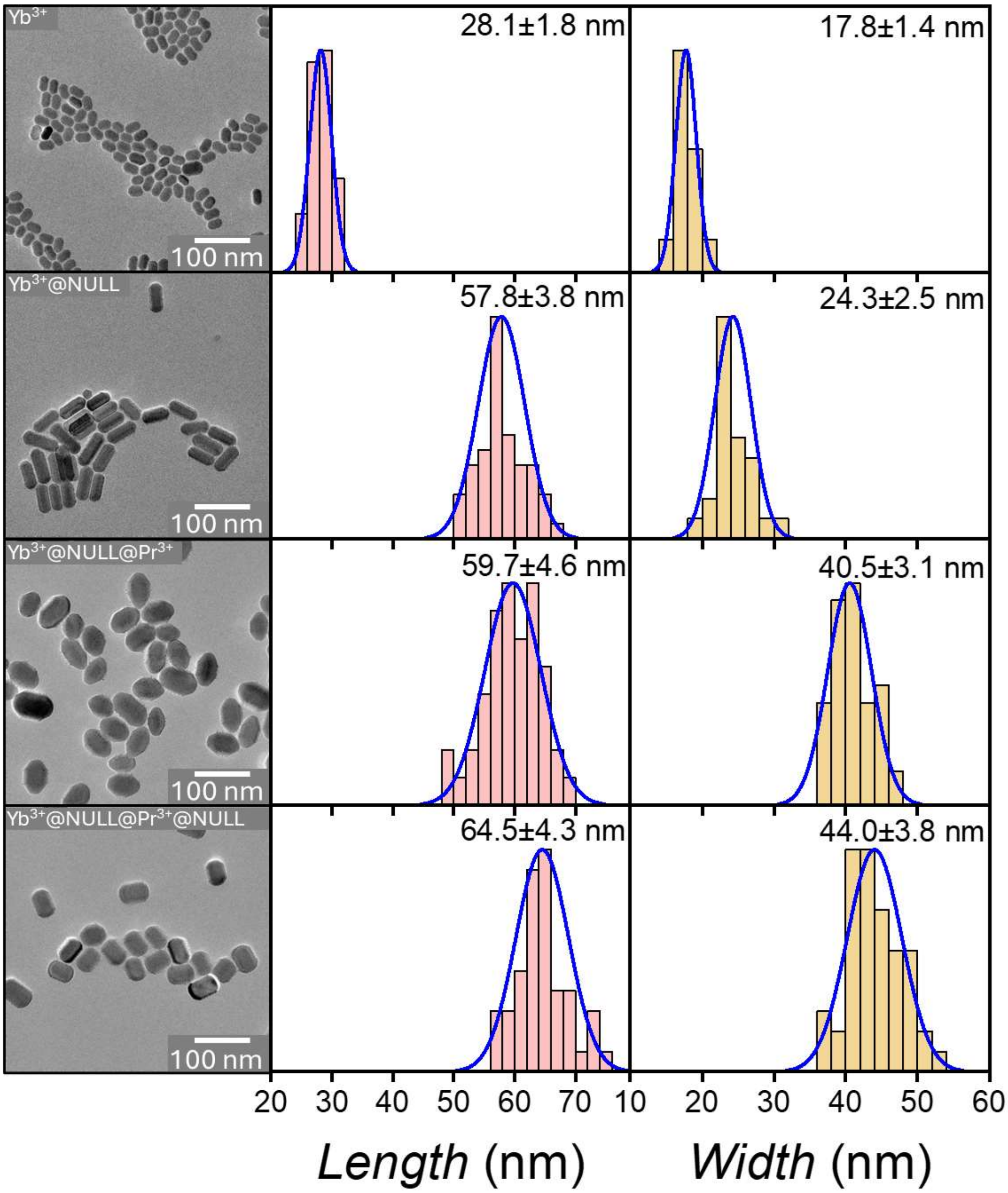

Fig. 46. TEM images (left column), length distribution histograms (middle column), and width distribution histograms (right column) of Yb^{3+}-co-doped C, CS, CSS, and CSSS β-$NaYF_4$ NPs

Tm^{3+}-based β-$NaYF_4$ core@multi-shell NPs formation

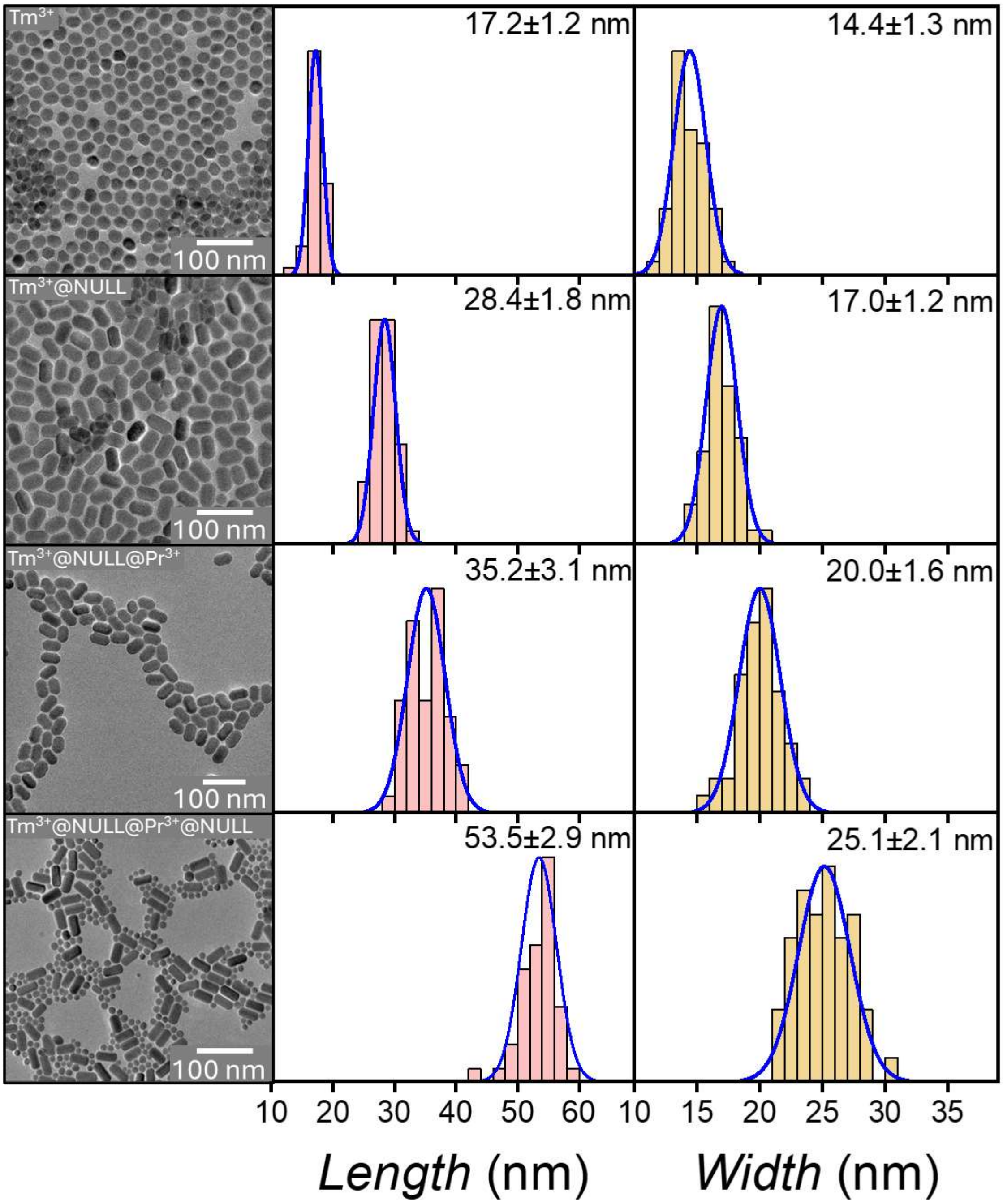

Fig. 47. TEM images (left column), length distribution histograms (middle column), and width distribution histograms (right column) of Tm^{3+}-co-doped C, CS, CSS, and CSSS β-$NaYF_4$ NPs

6.4.2. Spectral characterization

In the next step, I investigated how the designed internal nanoarchitecture, i.e., selection of optically active trivalent lanthanide ions, their spatial distribution, and mutual separation with the undoped β-$NaYF_4$ shell, affects luminescent properties. Having utilized various Vis and NIR excitation sources of different power density, I registered emission spectra of the obtained core@multi-shell β-$NaYF_4$ NPs in divergent spectral regions, including UV, Vis, and NIR emission lines.

In the beginning, I characterized the capability of the CSS and CSSS β-$NaYF_4$ NPs, containing Pr^{3+} ions, to emit up-converted UV radiation upon Vis excitation and the prospective influence of Nd^{3+}, Yb^{3+}, and Tm^{3+} core co-dopants on UV emission. It is noteworthy that the Vis-to-UV UC spectra of CSS and CSSS β-$NaYF_4$ NPs (Fig. 48a-c) could only be interpreted in a qualitative manner, not a quantitative one. Even though the experimental conditions (e.g., optical setup alignment, excitation power, and acquisition time) were maintained during the measurements, I was not able to ensure the equal NPs concentration while depositing them on the glass substrates, thus the emission intensity changes are highly likely to derive from differences in samples concentrations. In the registered emission spectra induced under the 447 nm laser diode excitation, the dried samples deposited on the glass substrate exhibited a broad band peaking at ~270 nm, which could be ascribed to $4f5d \rightarrow {}^3H_J/{}^3F_J$ electronic transition in Pr^{3+} ions, as depicted in the energy level diagram in Fig. 48g. These results are consistent with my previous studies on Vis-to-UV UC of Pr^{3+}-based β-$NaYF_4$ and $LiYF_4$ NPs, described in Chapter 4 [140]. As expected, the emission occurred after the sequential absorption of two 447 nm photons generated by the laser diode. The first photon excited ${}^3P_J$ states in Pr^{3+} ions, which was followed by the population of 4f5d level due to another 447 nm photon absorption. Furthermore, the incorporation of Nd^{3+} or Yb^{3+} ions into the core did not influence on the spectral characteristics of Vis-to-UV UC of Pr^{3+} ions (Fig. 48a-b). Since in the UV spectral range there is no overlay of Nd^{3+} or Yb^{3+} energy levels with the Pr^{3+} ones, one could imply that the process of sequential two-photon absorption and the resultant $4f5d \rightarrow {}^3H_J/{}^3F_J$ transitions were not affected. However, the utilization of the Tm^{3+} ions bearing core led to interesting results (Fig. 48c) and the most possible explanation for this phenomenon is ET from Pr^{3+} to Tm^{3+} ions, occurring across the inert β-$NaYF_4$ shell of the average thickness 4.9 ± 0.9 nm. As a consequence, ${}^1I_6$ and ${}^1D_2$ energy levels in Tm^{3+} ions were excited, hence their depopulation resulted in emission at ~350 nm and ~366 nm, assignable to $^1I_6 \rightarrow ^3F_4$ and $^1D_2 \rightarrow ^3H_6$ electronic transitions, respectively (see energy diagrams of Pr^{3+} and Tm^{3+} ions in Fig. 48g). In general, the appearance of two additional emission bands in UV-A range concurrently with UV-C radiation portrays Pr^{3+},Tm^{3+}-co-doped core@multi-shell β-$NaYF_4$ NPs as materials of highly developed photoinducible disinfecting properties. It is worth recalling herein that the up-converted UV-C radiation generated by Pr^{3+} ions damages dsDNA, which I have already confirmed in Chapter 4 of my doctoral dissertation. On the other hand, UV-A radiation can stimulate endogenous protoporphyrins present in bacteria and viruses to generate ROS, such as hydroxyl radicals or H_2O_2, leading to the eventual apoptosis of pathogenic cells [10,11]. Therefore, the combination UV-A and UV-C emission lines induced upon Vis-to-UV UC process within the presented Tm^{3+}@NULL@Pr^{3+}@NULL β-$NaYF_4$ NPs provides a new insight into materials design for germicidal actions, exploiting various mechanisms of bacteria and virus species inactivation. More information on this ion combination in terms of light-triggered disinfection is also provided in Chapter 8.

As a next stage, I decided to characterize the Stokes emission of the Pr^{3+}-doped CSS and CSSS β-$NaYF_4$ NPs in Vis range, induced upon the exposition to 447 nm photons emitted by the Xe lamp. In the measured spectra (Fig. 48d-f) the typical f-f emission lines for Pr^{3+} bearing materials peaking at ca. 470, 483, 523, 540, 607, 640, and 722 nm were observed, which could be ascribed to $^3P_1 \rightarrow ^3H_4$, $^3P_0 \rightarrow ^3H_4$, $^1I_6 \rightarrow ^3H_5$, $^3P_1 \rightarrow ^3H_5$, $^3P_0 \rightarrow ^3H_6$, $^3P_0 \rightarrow ^3F_2$, and $^3P_0 \rightarrow ^3F_{3,4}$ transitions, respectively, as provided in the energy level structure of Pr^{3+} ions (Fig. 48g). The similar emission bands of Pr^{3+} ions were registered for other compounds at the nanoscale, e.g., LaF_3:Pr^{3+} NPs [168]. Moreover, in the spectra there were no additional peaks ascribable to the electronic transitions occurring in trivalent lanthanide ions doped into the core, hence the inert shell successfully suppressed the ET. The final shelling with the undoped protecting layer slightly enhanced emission intensity in the spectral region of interest for all investigated samples, with the highest for the Tm^{3+}-based β-$NaYF_4$ CSSS NPs. For better insight into Vis-to-Vis Stokes emission occurring from the designed core@multi-shell nanoarchitectures, I recorded luminescence decay curves for the emission bands peaking at 483 and 607 nm and fitted exponential curves (Fig. 49a-f). The determined luminescence LTs of $^3P_0$ energy level spanned between 20÷30 µs (see the exact values in Table 13) and were in the similar time range as the ones reported for Pr^{3+}-doped fluorides [169–171]. It implies that neither the materials nanoarchitecture nor the inert shelling elongated the luminescence LTs. The exemptional LTs of the $^3P_0$ excited state were however found for Tm^{3+}@NULL@Pr^{3+} β-$NaYF_4$ NPs. Compared to the NPs with the Nd^{3+}- and Yb^{3+}-based core, the shorter LTs values (15.270 ± 0.039 μs registered at 483 nm and 16.556 ± 0.052 μs registered at 607 nm) suggest the high probability of ET between Pr^{3+} and Tm^{3+} ions through the inert shell, which is consistent with the additional $^1I_6 \rightarrow {}^3F_4$ and $^1D_2 \rightarrow {}^3H_6$ electronic transitions observed in the Vis-to-UV UC emission spectra of Pr^{3+},Tm^{3+}-co-doped CSS and CSSS β-$NaYF_4$ NPs.

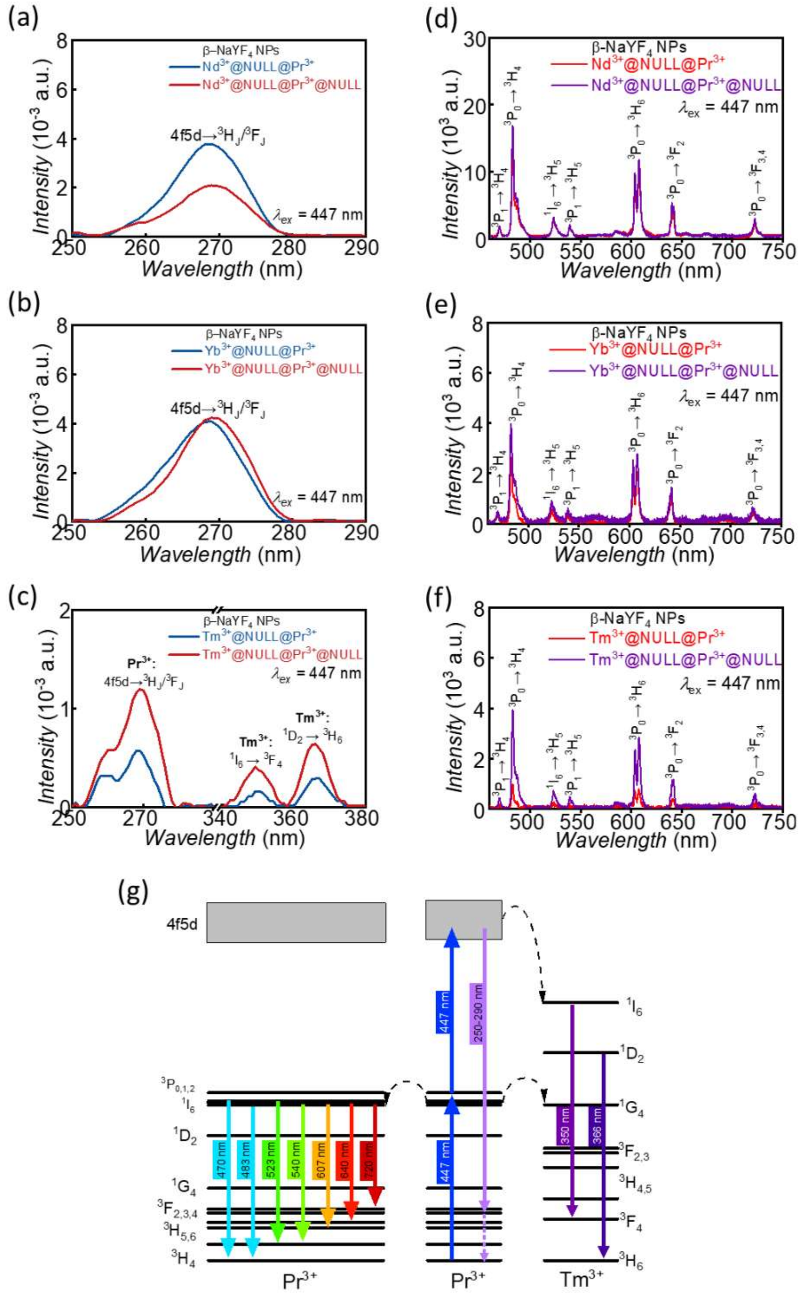

Fig. 48. (a-c) Vis-to-UV UC emission spectra and (d-f) Vis-to-Vis DC emission spectra of Nd^{3+}-co-doped (upper line), Yb^{3+}-co-doped (middle line), and Tm^{3+}-co-doped (lower line) CSS and CSSS β-$NaYF_4$ NPs

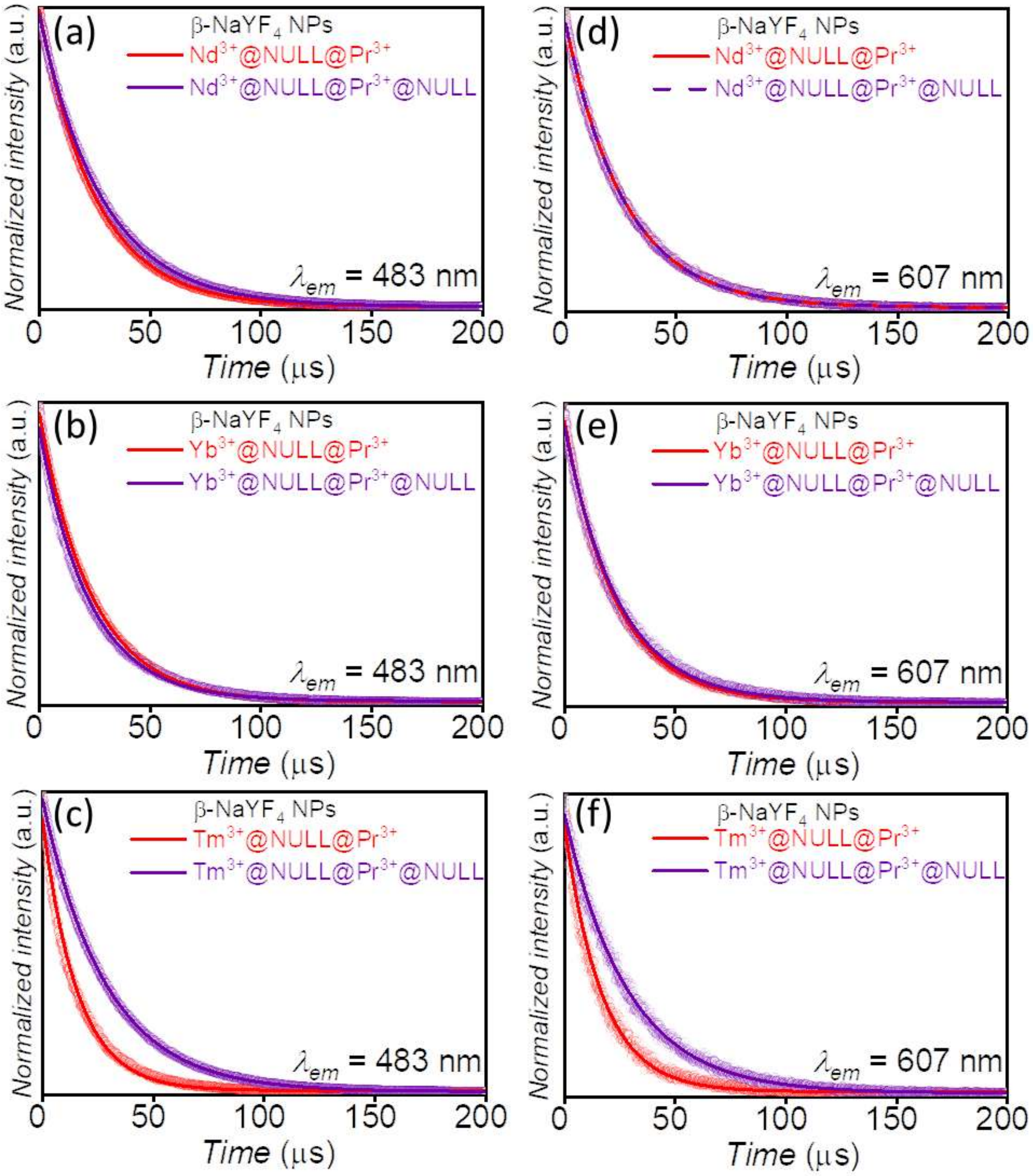

Fig. 49. Experimental luminescence decay curves (points) of the CSS and CSSS β-NaYF$_4$ NPs upon 447 nm excitation (Xe lamp), registered for (a-c) 483 nm and (d-f) 607 nm with the fitted theoretical decay curves (solid lines)

Table 13. Calculated luminescence LTs of Pr^{3+}:$^3P_0$ excited energy levels, measured at 483 and 607 nm, respectively for Nd^{3+}-co-doped, Yb^{3+}-co-doped, and Tm^{3+}-co-doped CSS and CSSS β-NaYF$_4$ NPs

Investigated sample	**τ at 483 nm [μs]**	**τ at 607 nm [μs]**
Nd^{3+}@NULL@Pr^{3+}	25.439 ± 0.013	27.050 ± 0.012
Nd^{3+}@NULL@Pr^{3+}@NULL	28.701 ± 0.018	27.040 ± 0.027
Yb^{3+}@NULL@Pr^{3+}	23.765 ± 0.018	22.901 ± 0.031
Yb^{3+}@NULL@Pr^{3+}@NULL	22.151 ± 0.044	23.936 ± 0.045
Tm^{3+}@NULL@Pr^{3+}	15.270 ± 0.039	16.556 ± 0.052
Tm^{3+}@NULL@Pr^{3+}@NULL	29.100 ± 0.027	29.829 ± 0.055

In the following step of spectroscopic studies I focused on the investigation whether the synthesized core@multi-shell nanoarchitectures exhibit NIR-to-NIR DC, applicable for bioimaging purposes. I was particularly interested to observe the NIR-II emission at ca. 1320 nm, coming from Pr^{3+} ions ($^1G_4 \rightarrow {}^3H_5$ electronic transition) [140], which could be associated with energy transfer from Tm^{3+}, Yb^{3+} or Nd^{3+} ions, doped into the core, to Pr^{3+} ions, incorporated into the optically active shell. The NPs co-doped with Yb^{3+} ions in the core irradiated with the 975 nm laser diode did not exhibit the emission in the region of interest (emission spectrum not shown). On the other hand, the ET exhibiting Tm^{3+}-based β-$NaYF_4$ CSS and CSSS NPs did not show the emission bands in NIR-II region when exposed to 808 nm laser diode irradiation (emission spectrum not shown). In these NPs series, the prospective reason for the lack of ET to Pr^{3+} ions could be linked with the NIR radiation suppression due to the spatial separation of donor and acceptor with the inert shell. For the investigated in the literature $NaYF_4$:Tm^{3+},Yb^{3+}@$NaYF_4$@$NaYF_4$:Er^{3+} CSS NPs the analogous conclusions were drawn, in which the excited states of Tm^{3+} could not be deactivated through ET in NIR spectral region to Er^{3+} ions doped into the outer shell [172].

However, the investigation revealed the noteworthy findings in the NIR region for the Nd^{3+}-based core@multi-shell NPs (Fig. 50a). The 808 nm laser excitation induced $^4I_{9/2} \rightarrow {}^4F_{5/2}$ electronic transition, commonly described in the literature for Nd^{3+} ions [173]. The non-radiative relaxation led to the $^4F_{3/2}$ energy level population and, resultantly, the intensive emission bands at ca. 860, 1050, and 1330 nm were recorded, corresponding to $^4F_{3/2} \rightarrow {}^4I_{9/2}$, $^4F_{3/2} \rightarrow {}^4I_{11/2}$, and $^4F_{3/2} \rightarrow {}^4I_{13/2}$ electronic transitions, respectively (for the detailed overview see the Nd^{3+} energy level structure in Fig. 50b) [108]. Therefore, the Nd^{3+}-based β-$NaYF_4$ core@multi-shell NPs could be considered as interesting candidates for bioimaging nanoprobes, since they were able to exhibit NIR-to-NIR DC emission, favorable for high-contrast bioimaging of biological systems. Such an application of the synthesized Nd^{3+}-based β-$NaYF_4$ CSSS nanoarchitecture seems to be more appealing compared to Yb^{3+}-based nanomaterials. It is due to the fact the 808 nm excitation wavelength for Nd^{3+} ions is less prone to be absorbed by water robustly present in cells than the 980 nm wavelength, commonly used to excite Yb^{3+} ions. Therefore, the utilization of Nd^{3+} instead of Yb^{3+} for the preparation of nanomaterials for bio-related applications allows to avoid the biological tissues overheating [17].

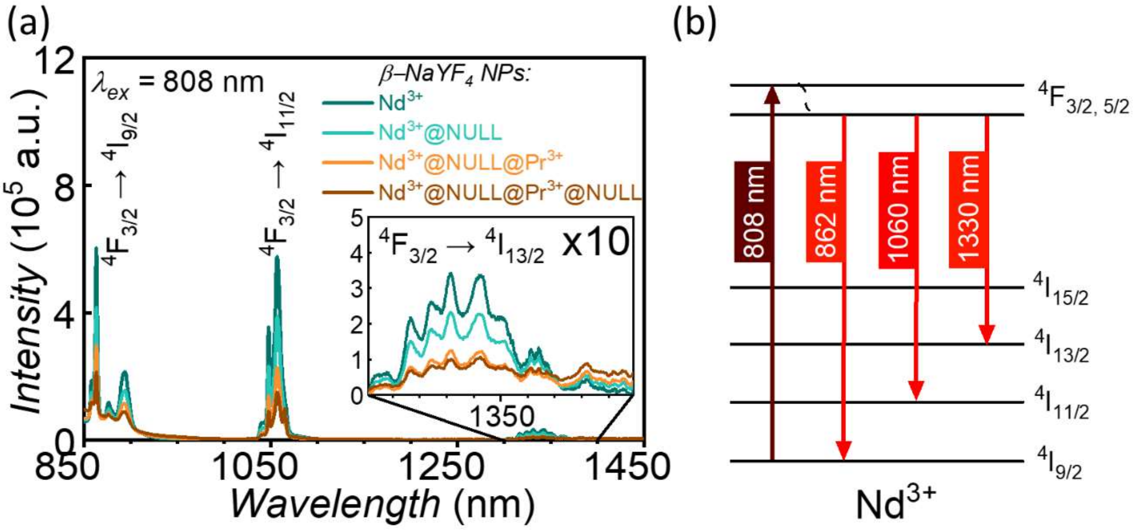

Fig. 50. (a) NIR-to-NIR DC emission of the Nd^{3+}-co-doped β-NaYF$_4$ core@multi-shell NPs series, Inset: the emission band corresponding to $^4I_{9/2}$→$^4F_{5/2}$ electronic at 10-manifold magnification

6.5. Conclusions

In this chapter, I report successful design and synthesis of complex lanthanide-doped β-NaYF$_4$ core@multi-shell nanoarchitectures to realize various photon management processes, resulting in concurrent emission in UV and NIR spectral regions. The conducted spectroscopic analysis proves that Pr^{3+} ions, incorporated into the second shell, are capable to generate UV-C radiation due to sequential absorption of two 447 nm photons. Furthermore, the resulting UV-C emission is barely affected by peristatic quenching processes, hence it could be effectively employed for light triggered germicidal, virucidal, and even anticancer applications. It is worth highlighting that Tm^{3+}-based β-NaYF$_4$ samples provide additional up-converted emission bands in UV-A spectral range. This fact portrays them as a compelling option among the robust collection of UV-emitting phosphors as they simultaneously show UV-A and UV-C lines, having completely different mechanisms of pathogens photoinactivation, which might provide the enhanced therapeutic effect. As far as the luminescent properties in NIR-I and NIR-II spectral regions are considered, the Nd^{3+}-co-doped β-NaYF$_4$ core@multi-shell NPs show the best performance. When excited upon 808 nm, they exhibit emission lines in NIR-I and NIR-II, appropriate for high-contrast bioimaging in biological tissues.

The thorough spectroscopic analysis of the synthesized core@multi-shell NPs provides a broader insight on the luminescent properties of the utilized lanthanide ions and photon management processes. Since Tm^{3+}-based NPs exhibit the best performance in UV range whereas Nd^{3+}-based NPs – in NIR-II range, it is troublesome to designate the nanoarchitecture of the optimal efficiency for prospective theranostic applications. However, it is worth considering to combine the aforementioned Tm^{3+} and Nd^{3+}co-doped nanosystems and study it in detail as a whole. In Nd^{3+}@NULL@Pr^{3+},Tm^{3+}@NULL β-$NaYF_4$ nanostructure, bearing lanthanides of optimized molar concentration, the Nd^{3+}-doped core would be utilized for NIR-to-NIR DC-based optical bioimaging, while Tm^{3+} and Pr^{3+} ions would be co-doped simultaneously into the second shell to enable more efficient ET, leading to UV-A and UV-C emission intensity enhancement for synergic therapeutic effect against bacteria, viruses or even cancer cells.

6.6. Acknowledgments and comments

This chapter is partially based on the data presented in the research paper *Lanthanide doped $NaYF_4$ core@multi-shell nanoparticles: Synthetic strategy for emission in divergent spectral regions.* **P. Fałat**, P. Kuich, M.Y. Tsang, S.J. Zelewski, B. Cichy, M. Samoć, M. Nyk, D. Wawrzyńczyk, Journal of Luminescence 266, 2024, article no. 120284.

Within the research scope I designed and synthesized with the assistance of P. Kuich the lanthanide-based β-$NaYF_4$ core@multi-shell NPs. Later on, I conducted the Vis-to-UV UC emission measurements exploiting the custom optical setup assembled and modified by S.J. Zelewski. Crystal structure characterization with XRD was conducted on the courtesy of B. Cichy. Additionally, under his guidance I registered other spectroscopic features of the synthesized NPs, i.e., Vis-to-Vis Stokes emission, NIR-to-NIR DC emission, and the kinetics of luminescence decay curves.

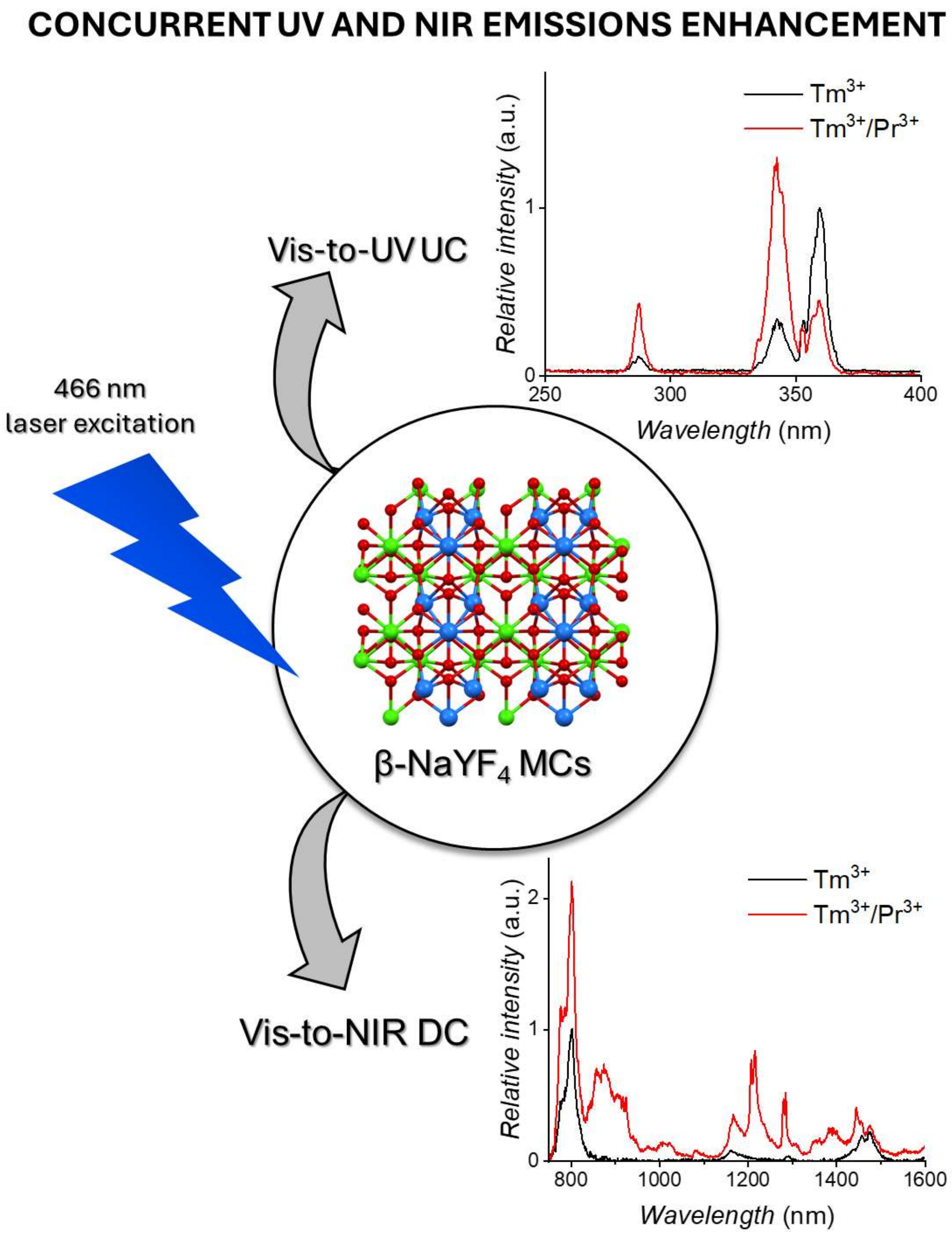

Fig. 51. The graphical representation of the concurrent Vis-to-NIR DC and Vis-to-UV UC emission intensities enhancement in Tm^{3+}-based β-$NaYF_4$ MCs through co-doping with Pr^{3+} ions

Chapter 7

Photon management processes in Tm^{3+},Pr^{3+}-co-doped β-$NaYF_4$ MCs for concurrently enhanced emission in biologically significant spectral regions

Within this part of the doctoral dissertation I focus on Tm^{3+} ions – another lanthanide ions type which is known for the ability to efficiently up-convert to UV radiation as well as to down-convert to NIR radiation under blue Vis irradiation. However, Tm^{3+}-based materials, when intended for theranostic purposes, should exhibit strong PL signals in both UV and NIR spectral ranges. Therefore, within this research I direct my attention toward co-doping with another rare-earth ion as one of the possible strategies to concurrently enhance Stokes and anti-Stokes PL intensity exhibited by Tm^{3+}-based β-$NaYF_4$ MCs. To tune the emission intensity output, I opt for Pr^{3+} ions co-incorporation into the host matrix, since their excitation wavelength matches the energy difference between Tm^{3+}:$^3H_6$ and Tm^{3+}:$^1G_4$ energy levels.

I manufacture the microphosphors through solid state synthesis – a method facilitating the formation of materials exhibiting brighter UC emission. The synthetic procedure does not require organic ligands, which presence might diminish the up-converted UV emission intensity. Although the resulting powder samples are easier to handle and utilize compared to NPs suspended in organic solvents, they typically exhibit poorly defined morphology, which is difficult to control during the synthesis process. I record Vis-to-Vis/NIR DC and Vis-to-UV UC emission spectra for the Tm^{3+} only doped and Tm^{3+},Pr^{3+}-co-doped samples (Fig. 51). With the aim of better understanding of photon management processes emerging within and between the ladder-like energy level structures of the simultaneously excited Tm^{3+} and Pr^{3+} ions, I register PL decay curves at chosen emission wavelengths falling in UV and NIR spectral ranges. The presented methodology provides valuable insights into the synergistic ET mechanisms occurring between Tm^{3+} and Pr^{3+} ions, specifically in terms of their excited-state dynamics. Moreover, it highlights the significant contribution of Pr^{3+} ions to the depopulation of long-lived excited energy levels of Tm^{3+} ions, thus enhancing the ET efficiency.

7.1. Introduction to the scientific problem

As provided in Section 2.3, energy associated with the incident photons undergoes various radiative and non-radiative conversion processes, having been absorbed within electronic structure of lanthanide ions. It usually occurs at the same moment, therefore, the resultant radiation output is registrable as narrow emission bands in a broad part of the electromagnetic spectrum, including UV, Vis, and NIR spectral ranges [157]. Depending on the size of the considered materials, whether in the form of bulk, at the micro- or nanoscale, the synthesized crystals could be employed for novel photonics devices fabrication with the application potential in photovoltaics or telecommunication [174]. The concurrent emission in UV and NIR ranges appears also to be interesting regarding manufacturing of theranostic devices [118]. The results presented in Chapter 4 for Pr^{3+},Yb^{3+}-co-doped β-$NaYF_4$ and $LiYF_4$ NPs clearly depict that the development of such lanthanide-doped materials showing optical bimodality is strongly needed. Nevertheless, the research on their capability to emit strong PL signals in both spectral regions of interest still remains challenging, mostly due to lanthanide ions molar concentration optimization and spatial distribution in hosts (crystalline or vitreous) to both minimize the non-radiative processes occurrence, e.g., concentration quenching *via* CR, and maximize the probability of ET processes needed, for instance, for efficient UC [175].

In the course of work to encounter a solution for the presented scientific challenge, my attention was attracted by the robust ladder-like energy level structure of Tm^{3+} ions (*vide* Fig. 10), within which it is possible to realize a great number of photon management processes [49]. Tm^{3+}-based materials exhibit Vis and NIR Stokes DC emission, resulting from the depopulation of excited energy levels, usually preceded with partial energy loss due to non-radiative relaxation processes. Additionally, when the requirements are met, the sequential absorption of two or more photons is attainable, which leads to the up-converted emission. In the experiments for solely Tm^{3+}-doped materials, Vis-to-UV and NIR-to-Vis UC emissions were registered after the absorption of two blue Vis or NIR photons, accordingly [176,177]. However, exploring alternative approaches to shift the excitation wavelengths and overcoming low absorption could be highly beneficial, as it may broaden the application potential of these materials. One of the possible solutions is to incorporate into the host matrix of choice another lanthanide ion at optimized molar concentration, acting as a SEN and transferring a part of the absorbed energy to an ACT, which eventually emits radiation at the desired wavelength. For instance, the Tm^{3+},Yb^{3+} ions pair exhibits NIR-to-NIR, NIR-to-Vis, and NIR-to-UV UC emission as Yb^{3+} ions are excited with 980 nm radiation, which pictures it as one of the most efficient ETU optical systems. Furthermore, it can be feasibly introduced into vitreous samples and crystalline matrices. The synthesis of materials at the micro- and nanoscale unlocked *in vivo* applications, in which NIR-to-UV UC of the complex multistep mechanism plays a crucial role [178–181]. In another case, the ions combination of Tm^{3+} and Er^{3+} was co-doped into a vitreous host matrix. The 976 nm NIR photons could be harvested by Er^{3+} ions, transferring then energy to Tm^{3+} ions, which eventually emitted radiation at ca. 1800 nm [182]. On the other hand, efficient lasing properties of solely Tm^{3+}-doped materials for telecom applications at ca. 1500 nm are usually severely hindered due to self-termination of the $^3H_4 \rightarrow {}^3F_4$ electronic transition. It does not allow population inversion to occur, which is caused by the extremely high value of Tm^{3+}:$^3F_4$ excited state LT (depending on host matrix type, reaching even up to a several ms), one order of magnitude longer than Tm^{3+}:$^3H_4$ energy level LT (tens or hundreds μs) [183,184]. Therefore, yet another rare earth ions pair was proposed, namely Tm^{3+},Pr^{3+}. Owing to the comparable values of Tm^{3+}:$^3F_4$ and Pr^{3+}:$^3F_2$ excited states energy (*vide infra* the energy level structures of both ions in Fig. 54a), Pr^{3+} ions served as deactivators of Tm^{3+}:$^3F_4$ excited state. It assured a high probability of ET occurrence, which led to the substantial emission enhancement in the targeted spectral range due to PL LT reduction [185]. The described combination was also studied in terms of UV sensitization of Tm^{3+} ions, followed by ET to Pr^{3+} ions, resulting in Vis DC emission from the latter. However, in the literature the influence of Pr^{3+} ions on anti-Stokes UV UC emission from Tm^{3+} ions has been scarcely reported.

Having taken into consideration the current knowledge status on luminescent properties enhancement of Tm^{3+} ions, in this chapter I decide to focus on the Tm^{3+},Pr^{3+} ions pair and its capability for simultaneous improvement of UV UC and NIR DC emissions from Tm^{3+} ions. I opt for incorporating the selected ions combination into β-$NaYF_4$ host matrix, known for its low phonon energy and thus facilitating UC [166,186–188]. The MCs are obtained through solid state synthesis, which according to the literature reports enables manufacturing of materials of brighter UC emission in comparison with hydrothermal methods [91]. The reason standing for it could be connected with the absence of organic ligands on the surface of the material. Such capping agents as citric acid or EDTA could absorb the up-converted UV radiation, hence affecting emission intensity of the microphosphors. In the subsequent step, I investigate them upon 466 nm pulse nanosecond laser, having confirmed that the excitation wavelength matches the energy difference between not only Tm^{3+}:$^3H_6$ and Tm^{3+}:$^1G_4$ energy levels, but also between Pr^{3+}:$^3H_4$ and Pr^{3+}:$^3P_0$, $^1I_6$ [49]. The enhancement of Tm^{3+} ions emission through co-doping with Pr^{3+} ions is attributed to efficient ET between the simultaneously excited ions – a feature particularly valuable for practical applications, given the availability of inexpensive and powerful LEDs emitting at 466 nm. To evaluate this effect, I record Vis-to-NIR PL and Vis-to-UV UC spectra at varying laser power densities, along with PL decay curves for the relevant intermediate excited states. Compared to singly Tm^{3+}-doped material, the Tm^{3+},Pr^{3+}-co-doped β-$NaYF_4$ MCs exhibit significantly enhanced emissions in both the UV-C and NIR spectral regions. These results highlight their potential of a single co-doped material to simultaneously support light-triggered disinfection and deep-tissue bioimaging, paving the way for multifunctional real-life applications.

7.2. Materials

In the synthesis of β-$NaYF_4$ MCs the following chemicals were utilized: NaF (≥99%), YF_3 (≥99%), PrF_3 (99.9%) , TmF_3 (≥99.99%), NH_4F (≥98%), and $(NH_4)HF_2$ (95%). All reagents were purchased from Merck Group and used as received.

The lanthanide-doped β-$NaYF_4$ MCs series was synthesized according to the protocol described in Section 3.2.2.1. The masses of the utilized solid compounds were provided below in Table 14.

Table 14. Summary for the amount of solid compounds used to synthesize the lanthanide-doped β-$NaYF_4$ MCs series

	Compound mass [g]				
Dopants	**NaF**	**YF_3**	**PrF_3**	**TmF_3**	**NH_4F**
1% Tm^{3+}	0.4451	1.5311	-	0.0239	0.5000
5% Tm^{3+}		1.4692	-	0.1197	
1% Tm^{3+}, 1% Pr^{3+}		1.5083	0.0210	0.0239	

7.3. Characterization methods

7.3.1. Crystal structure

In order to verify crystal structure of the synthesized lanthanide-doped β-$NaYF_4$ MCs, the ground materials were analyzed using a Malvern Panalytical Aeris benchtop powder X-ray diffractometer. Each time the smooth layer of the MCs powder was prepared in a sample holder. The filtered $CuK\alpha_1$ radiation operated in the 15÷75° 2θ range in the Bragg-Brentano geometry.

7.3.2. Morphology

The finely ground MCs were sprinkled onto a piece of carbon tape for morphological examination, conducted with a Jeol JSM-6610LVnx SEM, equipped with the Oxford Aztec Energy EDS for detailed elemental composition analysis (see Section 5.3.2 for the procedure).

7.3.3. Spectroscopy features

All spectroscopic studies were conducted using either Edinburgh Instruments FLS900 (for UV and Vis emission) or FLS920 (for NIR emission) spectrometers in ambient air at room temperature. The samples were prepared on a brass holder with a drilled cavity of small dimensions to ensure a consistent volume of each powdered material within the excitation spot. During the measurement series no alterations in the setup were introduced, thus allowing the collected spectra to be interpreted both qualitatively and quantitatively by direct comparison of absolute intensities.

The PL excitation spectra were recorded using a Hamamatsu R928 PMT detector with a 450 W Xe lamp as the excitation source. The Stokes DC emission in Vis and NIR spectral ranges as well as the anti-Stokes Vis-to-UV UC emission were induced using a tunable optical parametric oscillator (OPO) Opotek Opolette HE 355 II (pulse power: 10 mJ, pulse duration: 10 ns, repetition rate: 20 Hz – maximal excitation power density: 300 kW cm^{-2}), based on the third harmonic generation in $YAG:Nd^{3+}$. The setup operated exclusively at the wavelength of 466 nm with the laser beam unfocused. UV and Vis photons emitted by the excited samples were collected with a Peltier-cooled PMT Hamamatsu R928, while NIR photons were gathered with an Hamamatsu R5509-72 PMT, cooled with liquid nitrogen. The appropriate filters, including short-pass, band-pass, long-pass as well as power density filters were used when needed.

The PL decay curves were registered using MCS method, which was already implemented in both Edinburgh Instruments spectrofluorometers.

7.4. Results

7.4.1. Crystal structure and morphology

In this study, the lanthanide-doped β-$NaYF_4$ MCs capable to simultaneously emit in UV and NIR spectral regions under Vis excitation were synthesized. The solely Tm^{3+}-doped β-$NaYF_4$:1%Tm^{3+} MCs and β-$NaYF_4$:5%Tm^{3+} MCs, and the co-doped β-$NaYF_4$: 1%Tm^{3+},1%Pr^{3+} MCs were obtained through solid state synthesis. Quenching effects through CR in the manufactured microphosphors were highly likely to impact on their spectroscopic properties, therefore, the chosen Tm^{3+} and Pr^{3+} ion concentrations were tailored in a way to avoid their occurrence [140]. The patterns of the performed XRD measurements revealed diffraction peaks, ascribable to the ones for standard undoped β-$NaYF_4$ host matrix (ICSD #51916) (Fig. 52). It indicated that the selected lanthanide ions could substitute Y^{3+} ions with no disruption of hexagonal symmetry of the host lattice, which is connected with the comparable ionic radii of ninefold-coordinated Y^{3+} (1.075 Å), Tm^{3+} (1.052 Å), and Pr^{3+} (1.179 Å) ions [124].

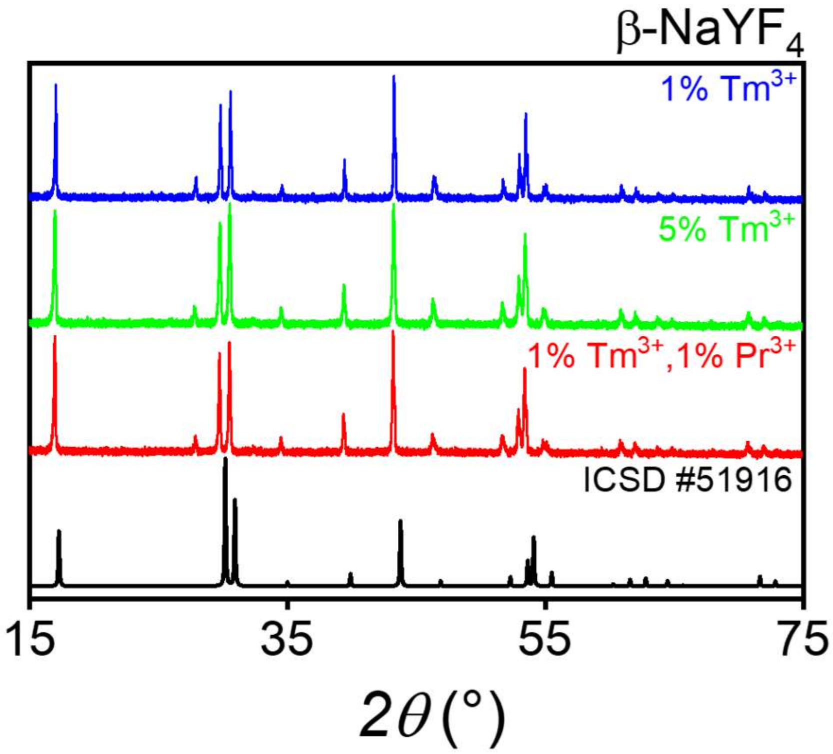

Fig. 52. XRD patterns of the synthesized lanthanide-doped β-$NaYF_4$ MCs. All of the registered patterns were ascribed to the one of undoped β-$NaYF_4$ host matrix (ICSD #51916)

On the contrary, investigated under high-power electron beam (Fig. 53a-c, left column), the finely ground MCs appeared structurally as similar to the already reported and obtained in the same manner lanthanide-doped β-$NaYF_4$ MCs [91,189]. Not to mention, their size and shape were comparable, although solid state synthesis only provides limited control on these parameters, as indicated in the literature. The EDS elemental maps registration (presented in Fig. 53a-c, right column) confirmed that all elements, which were intended to be incorporated into the host matrix, were uniformly distributed across the samples.

(a) β-$NaYF_4$: 1% Tm^{3+} MCs

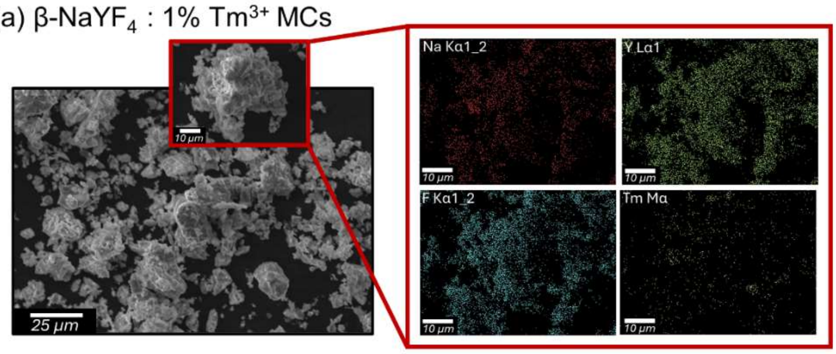

(b) β-$NaYF_4$: 5% Tm^{3+} MCs

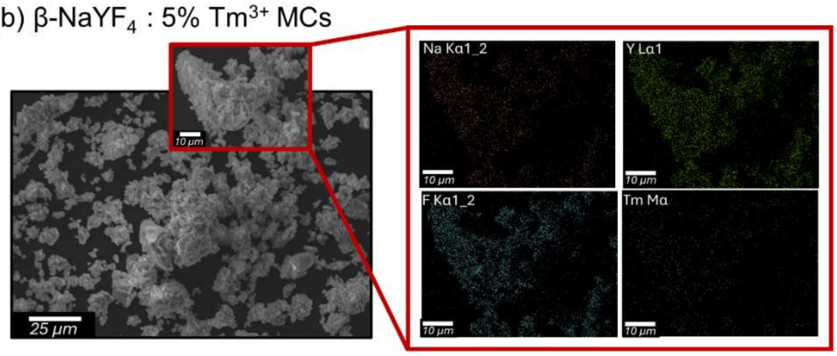

(c) β-$NaYF_4$: 1% Tm^{3+}, 1% Pr^{3+} MCs

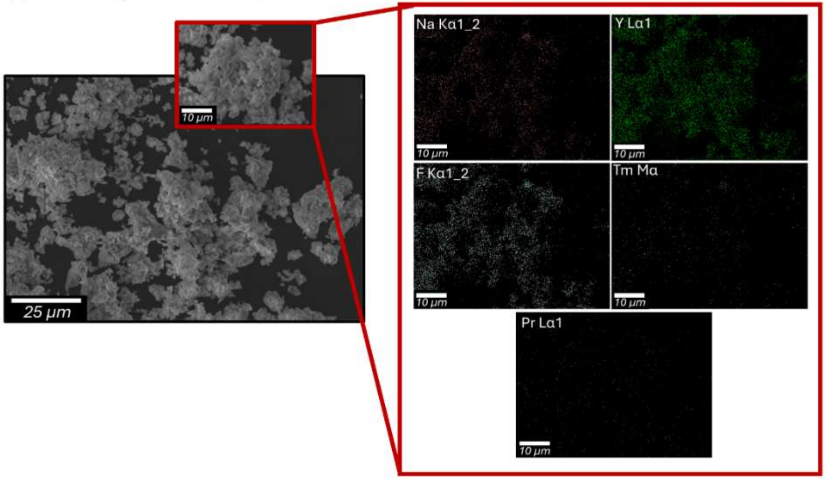

Fig. 53. SEM images (left column) and EDS elemental composition maps (right column) for the synthesized Tm^{3+}-based materials: (a) β-$NaYF_4$:1% Tm^{3+} MCs, (b) β-$NaYF_4$:5%Tm^{3+} MCs, (c) β-$NaYF_4$:1% Pr^{3+},1%Tm^{3+} MCs

7.4.2. Spectroscopic features

Since the synthesized lanthanide-doped powders were classified with regard to crystal structure and morphology as β-$NaYF_4$ MCs, I investigated them in terms of spectroscopy. For better clarity of data analysis within the presented chapter of the doctoral dissertation, the energy level diagrams of Tm^{3+} and Pr^{3+} ions incorporated into β-$NaYF_4$ MCs with all observed electronic transitions and possible pathways leading to emission from the excited energy levels were presented in Fig. 54a-d.

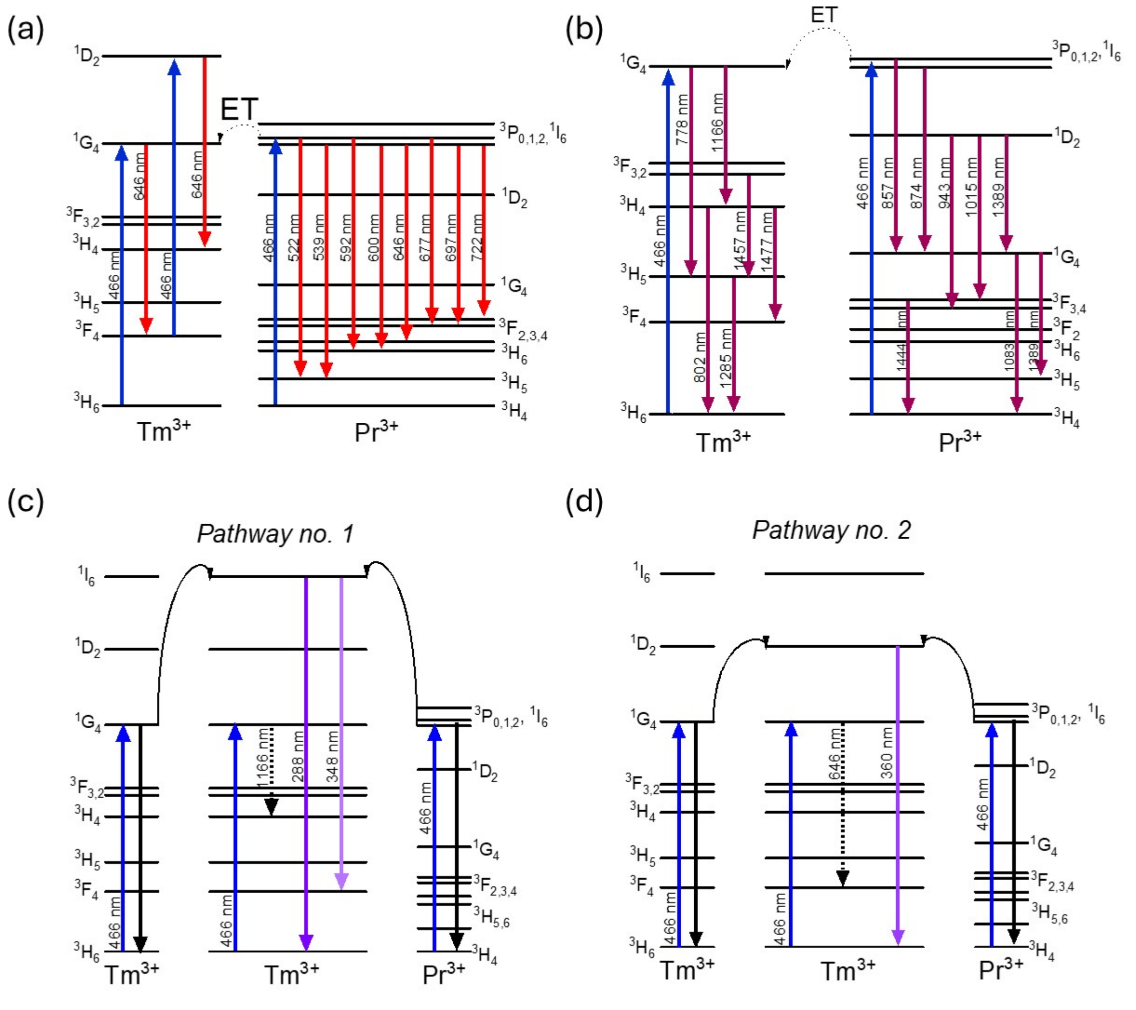

Fig. 54 Energy level diagrams of Tm^{3+} and Pr^{3+}ions with the excitation lines (466 nm) and emission lines in UV, Vis, and NIR spectral ranges: (a) emission lines in Vis, (b) emission lines in NIR, (c)(d) proposed pathways leading to the up-converted Vis-to-UV emission from Tm^{3+}:$^1I_6$ and from Tm^{3+}:$^1D_2$ energy levels

7.4.2.1. PL excitation spectra

The analysis of photon management processes emerging within the energy level structures of the incorporated ions was preceded by the registration of PL excitation spectra for singly Tm^{3+}-doped and Tm^{3+},Pr^{3+}-co-doped MCs in 250÷550 nm spectral range (Fig. 55a-b). The emission monochromator was fixed at 646 nm, since both ions tend to emit at this wavelength – Tm^{3+} ions from Tm^{3+}:$^1G_4$ and Tm^{3+}:$^3D_2$ energy levels whereas Pr^{3+} ions from Pr^{3+}:$^3P_0$ energy level [140,190].

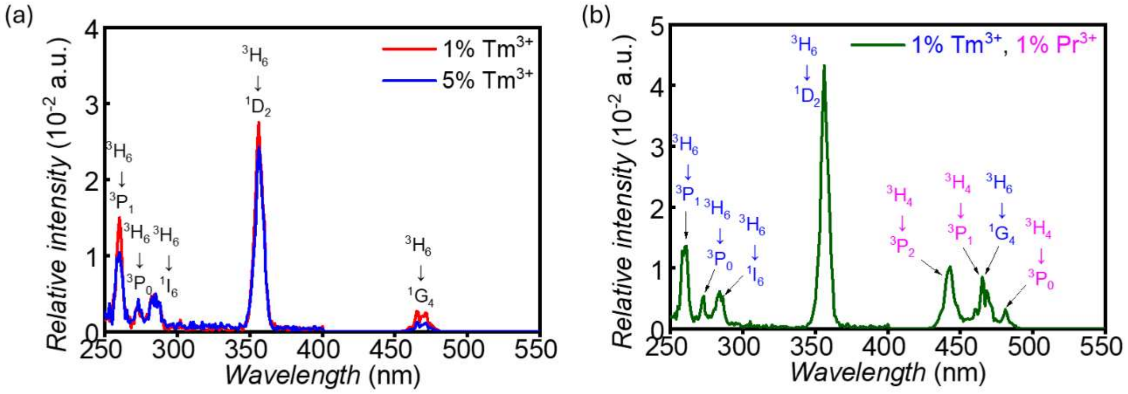

Fig. 55. PL excitation spectra of the synthesized (a) β-$NaYF_4$:1%Tm^{3+} & β-$NaYF_4$:5%Tm^{3+} MCs; and (b) β-$NaYF_4$:1%Tm^{3+},1%Pr^{3+} MCs, monitored at 646 nm

For β-$NaYF_4$:1%Tm^{3+} and β-$NaYF_4$:5%Tm^{3+} MCs (Fig. 55a) the excitation bands peaked at *ca.* 260, 275, 285, 360, and 466 nm, which indicated for $^3H_6 \rightarrow {}^3P_1$, $^3H_6 \rightarrow {}^3P_0$, $^3H_6 \rightarrow {}^1I_6$, $^3H_6 \rightarrow {}^1D_2$, and $^3H_6 \rightarrow {}^1G_4$ electronic transitions, accordingly. It stays in good agreement with the bands observed for Tm^{3+} ions, incorporated into such vitreous host matrices as $LiKB_4O_7$ and potassium zinc aluminoborosilicate [191,192]. As far as the Tm^{3+},Pr^{3+}-co-doped sample was considered, there were two additional bands observed in the excitation spectrum, peaking at ca. 443, and 483 nm, possible to assign to the transitions in Pr^{3+} ions from $^3H_4$ ground state to $^3P_2$, and $^3P_0$ higher energy levels, correspondingly (Fig. 55b). They were also registered as PL excitation lines for various Pr^{3+}-doped vitreous or crystalline materials in the form of bulk, at the micro- or nanoscale, e.g., germanate-based or fluorotellurite glasses, SrF_2:Pr^{3+} powders or YF_3:Pr^{3+} NPs [193–196]. The excitation band at 466 nm was the overlay of the $^3H_6 \rightarrow {}^1G_4$ electronic transition in Tm^{3+} ions and the $^3H_4 \rightarrow {}^3P_1$,$^1I_6$ electronic transitions in Pr^{3+} ions, as already reported for PbF_2 single crystal or La_2O_3 nanorods [197,198]. Therefore, as the simultaneous excitation of two different lanthanide ions incorporated into the host matrix could reveal interesting spectroscopic features connected with photon management processes in Tm^{3+},Pr^{3+}-co-doped β-$NaYF_4$ MCs, I decided to proceed with the investigation utilizing the 466 nm wavelength.

7.4.2.2. Vis-to-Vis/NIR DC emission

In order to analyze photon management processes in the synthesized Tm^{3+}-based β-$NaYF_4$ MCs, the first step was to register the VIS-to-NIR DC emission upon 466 nm laser excitation (Fig. 56a-b).

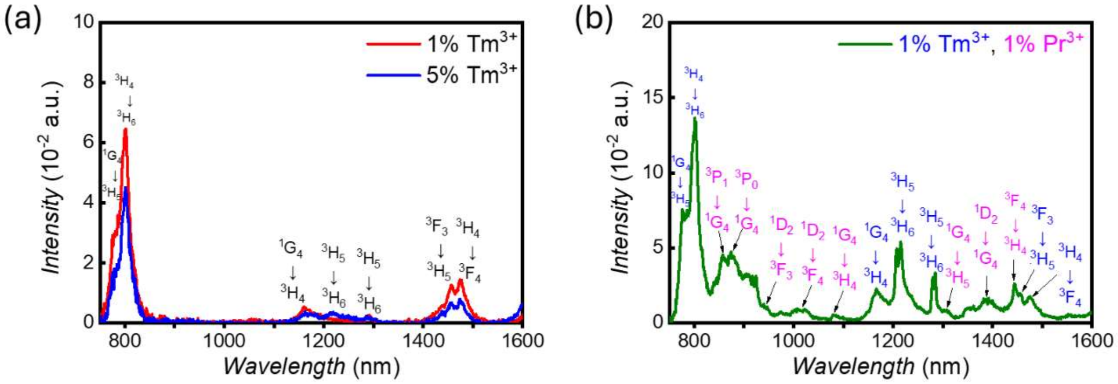

Fig. 56. Vis-to-NIR DC spectra of the synthesized (a) β-$NaYF_4$:1%Tm^{3+} & β-$NaYF_4$:5%Tm^{3+}MCs, (b) β-$NaYF_4$:1%Tm^{3+},1%Pr^{3+} MCs upon 466 nm pulse laser excitation (power density: 200 kW cm^{-2})

The corrected Stokes emission spectra in broad NIR range for both Tm^{3+}-doped samples (Fig. 56a) revealed bands at ca. 778, 802, 1166, 1220, 1285, 1457, and 1477 nm, to which the following electronic transitions could be ascribed: $^1G_4 \rightarrow {}^3H_5$, $^3H_4 \rightarrow {}^3H_6$, $^1G_4 \rightarrow {}^3H_4$, $^3H_5 \rightarrow {}^3H_6$, $^3F_3 \rightarrow {}^3H_5$, and $^3H_4 \rightarrow {}^3F_4$ (for better guidance see the energy level diagram of Tm^{3+} ions in Fig. 54a). The increase of the ions concentration from 1 to 5% led to the intensity decrease by 50% as concentration quenching between neighboring Tm^{3+} ions appeared. For β-$NaYF_4$:1%Tm^{3+},1%Pr^{3+} MCs the additional bands peaking at ca. 857, 874, 943, 1015, 1083, 1308, 1389, and 1444 nm emerged (Fig. 56b), which were ascribable to $^3P_1 \rightarrow {}^1G_4$, $^3P_0 \rightarrow {}^1G_4$, $^1D_2 \rightarrow {}^3F_3$, $^1D_2 \rightarrow {}^3F_4$, $^1G_4 \rightarrow {}^3H_4$, $^1G_4 \rightarrow {}^3H_5$, $^1D_2 \rightarrow {}^1G_4$, and $^3F_4 \rightarrow {}^3H_4$ electronic transitions within the energy level structure of Pr^{3+} ions (see the energy diagram of Pr^{3+} ions in Fig. 54a), respectively. The Pr^{3+} ions co-doping into the host matrix was beneficial for NIR radiation enhancement. The possible mechanism could base on the Pr^{3+} ions capability to transfer energy to Tm^{3+} ions after 466 nm laser excitation, i.e., resonant Pr^{3+}:$^3P_0$,$^1I_6 \rightarrow Tm^{3+}$:$^1G_4$ and Pr^{3+}:$^1G_4 \rightarrow Tm^{3+}$:$^3H_5$ ETs could occur. It should be highlighted that the enhanced emissions at ca. 800 and 1230 nm could be efficiently utilized for *in vivo* bioimaging [199–201].

Consequently, the PL decay curves at two emission wavelengths were recorded in order to gain a better insight into NIR emission kinetics: 802 nm ($^3H_4 \rightarrow {}^3H_6$ electronic transition, Fig. 57a-c) and 1166 nm ($^1G_4 \rightarrow {}^3H_4$ electronic transition, Fig. 57d-f), followed by fitting them with the chosen exponential models and extracting PL LT values of Tm^{3+}:$^3H_4$ and Tm^{3+}:$^1G_4$ excited energy levels (see Table 15).

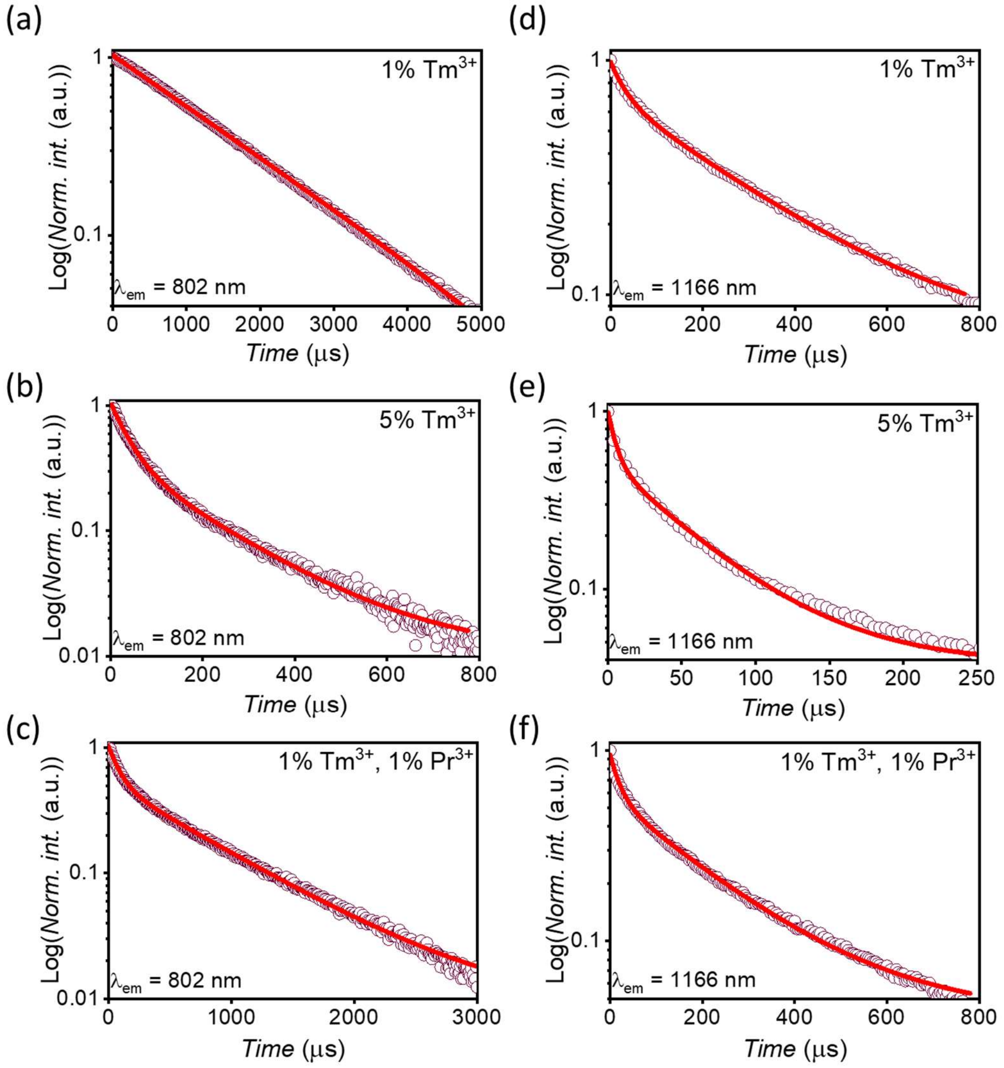

Fig. 57. Luminescence decay curves observed upon ns-pulsed 466 nm laser excitation for the synthesized β-NaYF$_4$:1%Tm^{3+}, β-NaYF$_4$:5%Tm^{3+}, β-NaYF$_4$:1%Tm^{3+},1%Pr^{3+} MCs, registered at (a-c) 802 nm and (d-f) 1166 nm

Table 15. Calculated luminescence LT values for the chosen energy levels of Tm^{3+} ions incorporated into β-NaYF$_4$ measured at corresponding emission wavelengths in NIR spectral range

Dopants	**Energy level**	**λ_{em} [nm]**	**τ_1 [µs]**	**τ_2 [µs]**
1% Tm^{3+}	$^3H_4$	802	1539 ± 7	–
5% Tm^{3+}			37.8 ± 0.6	182.5 ± 3.9
1% Tm^{3+}, 1% Pr^{3+}			90.2 ± 1.3	755.7 ± 6.9
1% Tm^{3+}	$^1G_4$	1166	33.0 ± 1.6	290.9 ± 6.0
5% Tm^{3+}			5.6 ± 0.3	54.6 ± 1.4
1% Tm^{3+}, 1% Pr^{3+}			21.8 ± 0.8	208.5 ± 3.8

The PL decay curve for the Tm^{3+}:$^{3}H_4$ excited state depopulation in β-$NaYF_4$:1%Tm^{3+} MCs was approximated with a monoexponential fit. The extracted PL LT value (τ = 1539.00 ± 7.00 μs) is comparable to the ones measured for Tm^{3+} ions incorporated into other alkali-metal-based fluoride host matrices (τ_{KY3F10} = 1.14 ms, τ_{LiYF4} = 1.44 ms, τ_{LiLuF4} = 1.34 ms or τ_{BaY2F8} = 1.10 ms) [202]. As Tm^{3+} ions concentration in the host increased, the non-exponential decay was registered and approximated with a bi-exponential function. The PL LT consisted of τ_1 and τ_2 components (τ_1 = 37.8 ± 0.6 μs, τ_2 = 182.6 ± 3.9 μs). The non-exponential character of the decay can be explained by CR between neighboring Tm^{3+} ions. Furthermore, when the Tm^{3+},Pr^{3+}-co-doped materials β-$NaYF_4$:1%Tm^{3+},1%Pr^{3+} was investigated, the non-exponential decay was also observed, which was highly likely a result of ET and CR between the electronic levels structures of Tm^{3+} and Pr^{3+} ions. The conducted bi-exponential curve fit gave τ_1 = 90.18 ± 1.30 μs, τ_2 = 755.68 ± 6.92 μs.

The PL decay curves registered at 1166 nm were approximated with the bi-exponential lines (Fig. 57d-f). Upon either increasing the concentration of Tm^{3+} ions or introducing Pr^{3+} ions through co-doping, the appearance of distinct τ_1 and τ_2 clearly indicated that, in addition to radiative processes from this level, non-radiative ET and CR processes also occurred. When Pr^{3+} ions were co-doped into the host matrix along with Tm^{3+} ions, the luminescence LT values for Tm^{3+}:$^{1}G_4$ excited state decreased by approximately 33% compared to MCs doped solely with Tm^{3+} ions at the same concentration (i.e., 1%Tm^{3+} MCs: τ_1 = 33.02 ± 1.58 μs, τ_2 = 290.87 ± 6.01 μs; for 1%Tm^{3+},1%Pr^{3+} MCs: τ_1 = 21.77 ± 0.83 μs, τ_2 = 208.50 ± 3.78 μs). The results demonstrated that the Tm^{3+}:$^{1}G_4$ energy level depopulated more rapidly in the co-doped sample in contrast to the one containing 1% Tm^{3+} ions only. For the 5% Tm^{3+}-doped MCs, the luminescence LT values were determined to be τ_1 = 5.62 ± 0.29 μs and τ_2 = 54.57 ± 1.36 μs. The reduction by 75% could be attributed to CR between neighboring Tm^{3+} ions closely positioned in the crystal lattice at higher concentration.

In the subsequent step, I recorded Vis-to-Vis DC emission spectra upon the pulsed 466 nm excitation (Fig. 58a-b). According to the literature, the first emission band for the solely Tm^{3+} doped MCs at ca. 646 nm was very probable a convolution of two electronic transitions from various excited energy levels, namely $^{1}G_4 \rightarrow {}^{3}F_4$ and $^{1}D_2 \rightarrow {}^{3}H_4$ (see energy level structure of Tm^{3+} ions in Fig. 54b). The phenomenon was already reported for KZABS glasses, exposed to the same wavelength of choice [192]. Not to mention, other Tm^{3+}-doped materials also exhibited such a combination, which was experimentally confirmed with the means of time-resolved spectroscopy [203]. Whereas the former transition was the outcome of the casual Stokes depopulation from Tm^{3+}:$^1G_4$ excited state, the latter occurred prior sequential absorption of two 466 nm photons. The Vis-to-Vis DC emission spectrum of the Tm^{3+},Pr^{3+}-co-doped MCs resembled the one registered for the triply-co-doped $Y_2Si_2O_7$:Pr^{3+},Tm^{3+},Yb^{3+} silicate powder under 447 nm laser diode irradiation (for more details see Chapter 8). While the peaks solely attributed to Tm^{3+} ions emission at approximately 778 and 802 nm were clearly distinct, the additional ones connected with Pr^{3+} ions were also observed. The bands peaking around 522, 539, 592, 600, 677, 697, and 722 nm corresponded to $^3P_1\rightarrow{}^3H_5$, $^3P_0\rightarrow{}^3H_5$, $^3P_1\rightarrow{}^3H_6$, $^3P_0\rightarrow{}^3H_6$, $^3P_1\rightarrow{}^3F_3$, $^3P_0\rightarrow{}^3F_3$, and $^3P_0\rightarrow{}^3F_4$ electronic transitions, respectively (see energy level structure of Pr^{3+} ions in Fig. 54b). The resultant emission at ca. 646 nm was then the effect of three electronic transitions convolution, i.e., $^1G_4\rightarrow{}^3F_4$ (Tm^{3+}), $^1D_2\rightarrow{}^3H_4$ (Tm^{3+}), and $^3P_0\rightarrow{}^3F_2$ (Pr^{3+}). Therefore, the PL decay curves have not been analyzed for both Tm^{3+}-doped and Tm^{3+},Pr^{3+}-co-doped MCs as the accurate separation at 646 nm would be cumbersome.

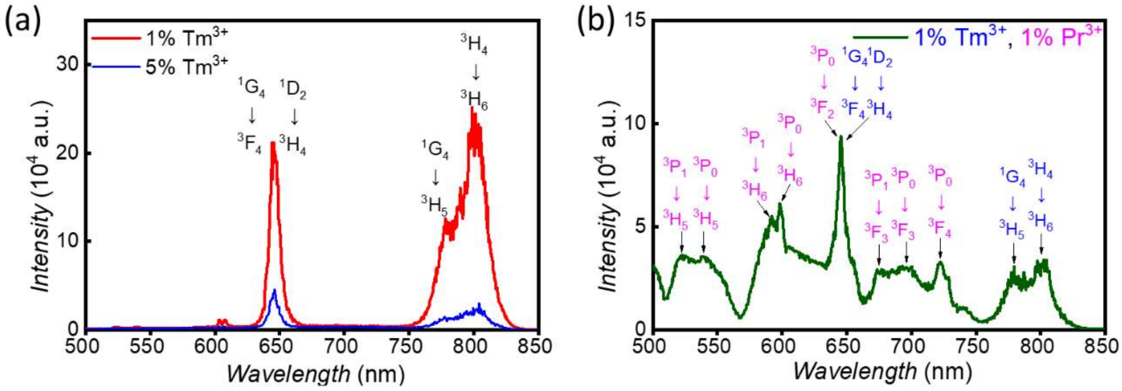

Fig. 58. Vis-to-Vis DC spectra of the synthesized (a) β-$NaYF_4$:1%Tm^{3+} & β-$NaYF_4$:5%Tm^{3+} MCs, (b) β-$NaYF_4$:1%Tm^{3+},1%Pr^{3+}MCs upon 466 nm pulse laser excitation

7.4.2.3. Vis-to-UV UC emission

In the subsequent research phase, anti-Stokes Vis-to-UV UC emission under 466 nm laser excitation in Tm^{3+}-based β-$NaYF_4$ MCs was investigated (Fig. 59). The UV up-converted emission spectra for all samples revealed three bands arising at ca. 288, 348, and 360 nm, associated respectively with $^1I_6\rightarrow{}^3H_6$, $^1I_6\rightarrow{}^3F_4$, and $^1D_2\rightarrow{}^3H_6$ electronic transitions in Tm^{3+} ions. The findings stay in good agreement with the results collected for β-$NaYF_4$ materials, doped with very low amounts of Tm^{3+} ions (i.e., 0.01% and 0.3%).

Additionally, the bands were convergent even with the ones registered in UV spectral range upon NIR excitation for β-NaYF$_4$:Tm^{3+},Yb^{3+} nanotubes [204,205].

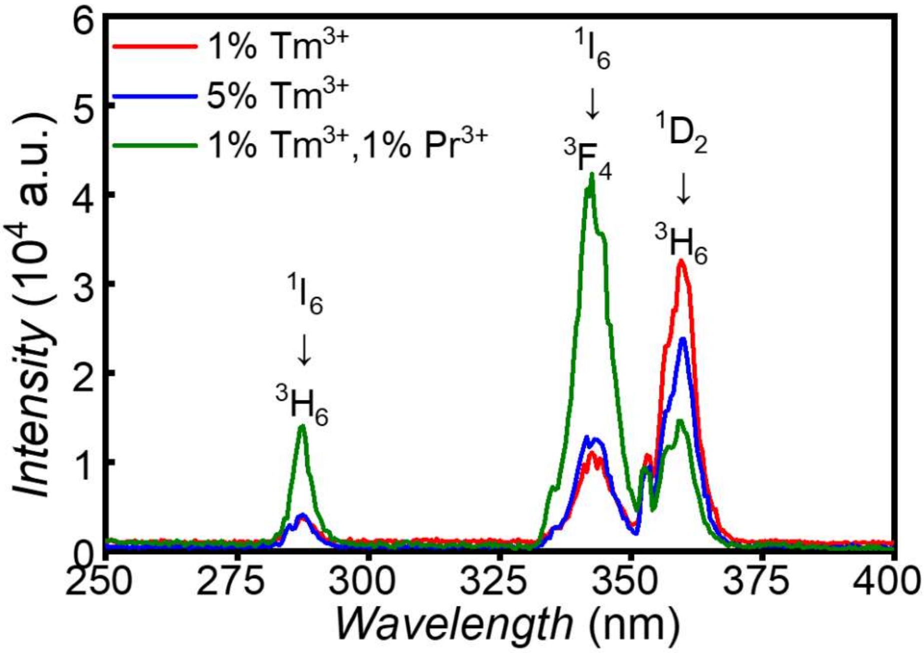

Fig. 59. Vis-to-UV UC spectra of β-NaYF$_4$:1%Tm^{3+}, β-NaYF$_4$:5%Tm^{3+}, and β-NaYF$_4$:1%Tm^{3+},1%Pr^{3+} MCs upon 466 nm pulse laser excitation

It is significant to mention that for all of the investigated MCs, the PL LT measured at ca. 288 and 348 nm showed comparable values (Fig. 60a-f and Table 16), which indicated that the emission was the result of the depopulation occurring from the same Tm^{3+}:^{1}I$_6$ excited state. Oppositely, the PL decay curves at ca. 360 nm were different (Fig. 60g-i and Table 16), thus the UC must have arisen from another excited state, in this case Tm^{3+}:^{1}D$_2$. The presented conclusions align closely with the mechanism standing for Vis-to-UV UC process in Tm^{3+}-doped materials proposed by O'Connor et al, presented in Fig. 54c-d as *Pathway no 1* and *Pathway no 2*, respectively [203]. In β-NaYF$_4$:1%Tm^{3+} MCs, the radiative PL component from these energy levels was dominant as the captured PL decay curves followed a single-exponential trend. The depopulation remained unaffected by parasitic non-radiative energy migration processes ($\tau^{288\ nm} = 95.2 \pm 0.4$ µs, $\tau^{348\ nm} = 88.6 \pm 0.9$ µs, and $\tau^{360\ nm} = 161 \pm 1$ µs). As the higher concentration Tm^{3+} ions was incorporated into the host matrix, the PL decay curves for Tm^{3+}:^{1}I$_6$ excited state required bi-exponential fitting. For these materials, the short components values of luminescence LT were as follows: $\tau_1^{288\ nm} = 18.84 \pm 0.60$ µs, $\tau_1^{348\ nm} = 20.89 \pm 0.31$ µs, and $\tau_1^{360\ nm} = 7.11 \pm 0.18$ µs, with corresponding long components values of $\tau_2^{288\ nm} = 62.35 \pm 3.51$ µs,

$\tau_2^{348\ nm}$ = 74.35 ± 3.18 µs, and $\tau_2^{360\ nm}$ = 48.09 ± 0.56 µs. The Pr^{3+} ions incorporation as a co-dopant significantly shortened the Tm^{3+}:$^1I_6$ excited energy level LT by approximately 40%, compared to β-$NaYF_4$:1%Tm^{3+} MCs. The resulting values were: $\tau_1^{288\ nm}$ = 6.65 ± 0.16 µs, $\tau_2^{288\ nm}$ =58.62 ± 0.24 µs, $\tau_1^{348\ nm}$ = 6.83 ± 0.30 µs, $\tau_2^{348\ nm}$ = 57.08 ± 0.41 µs, $\tau_1^{360\ nm}$ = 28.87 ± 0.35 µs, $\tau_2^{360\ nm}$ = 99.34 ± 2.11 µs.

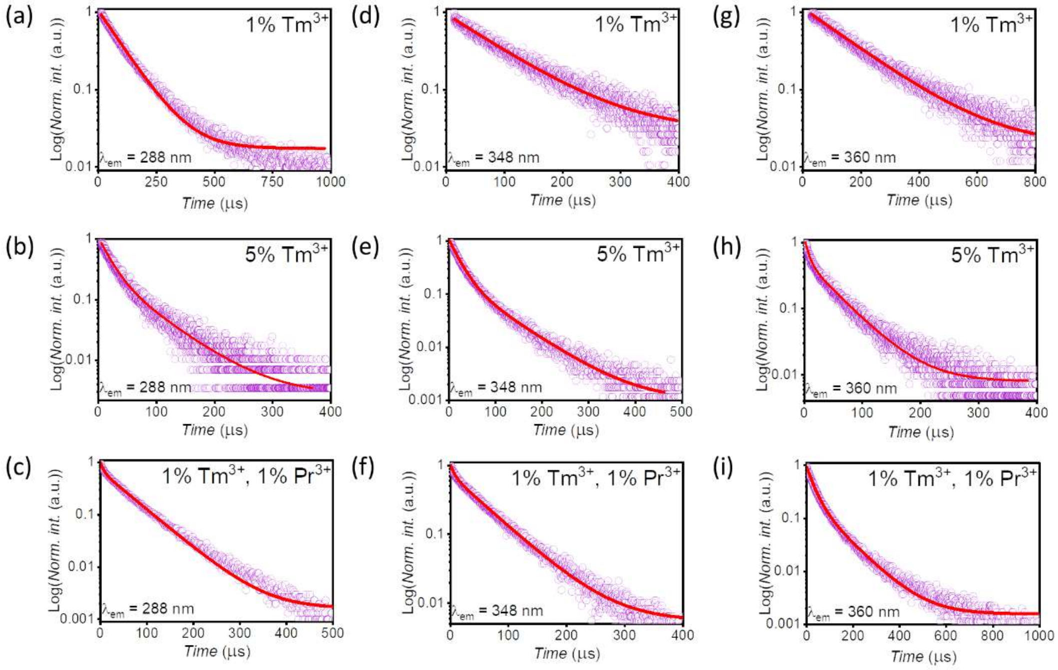

Fig. 60. PL decay curves observed upon ns-pulsed 466 nm laser excitation for the synthesized Tm^{3+}-based β-$NaYF_4$ MCs, registered at (a-c) 288 nm, (d-f) 348 nm, and (g-i) 360 nm

Table 16. Calculated luminescence LT for the chosen energy levels of Tm^{3+} ions measured at corresponding emission wavelengths in UV spectral range

Dopants	Energy level	λ_{em} [nm]	τ_1 [µs]	τ_2 [µs]
1% Tm^{3+}	$^1I_6$	288	95.2 ± 0.4	–
5% Tm^{3+}			18.8 ± 0.6	62.4 ± 3.5
1% Tm^{3+}, 1% Pr^{3+}			6.7 ± 0.2	58.6 ± 0.2
1% Tm^{3+}	$^1I_6$	348	88.6 ± 0.9	–
5% Tm^{3+}			20.9 ± 0.3	74.4 ± 3.2
1% Tm^{3+}, 1% Pr^{3+}			6.8 ± 0.3	57.1 ± 0.4
1% Tm^{3+}	$^1D_2$	360	160.8 ± 1.0	–
5% Tm^{3+}			7.1 ± 0.2	48.1 ± 0.6
1% Tm^{3+}, 1% Pr^{3+}			28.9 ± 0.4	99.3 ± 2.1

The Vis-to-UV UC emission spectra collected for Tm^{3+}-based β-$NaYF_4$ MCs could be interpreted quantitatively and absolute emission intensities can be directly compared, since in each measurement the same amount of the synthesized material was investigated. For the solely Tm^{3+}-doped microphosphors, regardless of the lanthanide ion concentration, the emission intensities at 288 and 348 nm were similar and independent of dopant concentration. Contrastingly, for β-$NaYF_4$:5%Tm^{3+} sample, the emission peaking at 360 nm was slightly diminished. Interestingly, in the case of β-$NaYF_4$:1%Tm^{3+},1%Pr^{3+} MCs, no upconverted emission bands originating from Pr^{3+} ions were observed. This indicates that neither the Pr^{3+}:$^1S_0$ nor the higher-lying Pr^{3+}:4f5d excited states were populated – an outcome that contrasts with the behavior of other Pr^{3+}-based nano- and micro-materials discussed in previous chapters of the doctoral dissertation. The likely explanation lies in the use of a 466 nm laser line during my research stay at Utrecht University, which delivers slightly lower photon energy than the 447 nm laser diode used at my home institution. Consequently, it was insufficient to populate the Pr^{3+}:$^1S_0$ and Pr^{3+}:4f5d higher states and thus did not trigger characteristic upconverted UV emissions from Pr^{3+} ions. Surprisingly, the up-converted UV bands related to Tm^{3+}:$^1I_6$ excited state were four times more intense, while the depopulation of Tm^{3+}:$^1D_2$ excited state to the Tm^{3+}:$^3H_6$ ground state resulted in the band of lower intensity. In other words, the trend was reversed, compared to the solely Tm^{3+}-doped samples. To the best of my knowledge, such a phenomenon has not been previously reported for Tm^{3+},Pr^{3+}-co-doping combination. The intense up-converted UV bands lay within UV-B and UV-C ranges (280÷320 nm/200÷280 nm), which suggests that the co-doped sample could have a considerable potential for biological applications (for more details see Section 2.1.1). The wavelengths from these spectral regions are prone to interact with dsDNA or RNA, causing the formation of photoproducts that prevent them from further replication [115]. Consequently, it makes them possibly more effective for germicidal purposes compared to UV-A radiation (320÷400 nm), which only excites endogenous protoporphyrins generating ROS inside the affected microorganisms [8]. Therefore, the enhanced Tm^{3+}:$^1I_6$ UC emission intensity suggests that β-$NaYF_4$:1%Tm^{3+},1%Pr^{3+} MCs are better suited for prospective germicidal applications relying on Vis-to-UV UC emission than their singly Tm^{3+}-doped counterparts.

I decided to explain the observed phenomenon occurring in β-$NaYF_4$:1%Tm^{3+},1%Pr^{3+} MCs, having gotten acquainted with two possible pathways leading to Vis-to-UV UC in Tm^{3+} ions, analyzed in the detail for β-$NaYF_4$ polycrystalline material by O'Connor and co-workers (see Fig. 54c-d) [203]. Both of them were claimed as ESA, however, there are other reports showing that the sequential absorption of two photons within the ladder-like energy level structure of a single Tm^{3+} ions dominates only in materials with low Tm^{3+} concentration. In the β-$NaYF_4$ crystal lattice with 1% Tm^{3+} concentration, ETU is likely the more efficient mechanism responsible for the observed UV emission. The first absorbed 466 nm photon transferred the electron from Tm^{3+}:$^3H_6$ ground state to Tm^{3+}:$^1G_4$ excited state, which was followed by the radiative depopulation to Tm^{3+}:$^3H_4$ or Tm^{3+}:$^3F_4$ electronic states, observed as 646 nm and 1166 nm photons, respectively. Since the energy gaps between $^3H_4$-$^1I_6$ and $^3F_4$-$^1D_2$ energy levels in Tm^{3+} ions correspond to that between the $^3H_6$ and $^1G_4$ levels, it is likely that the UV emission lines resulted from ET processes, specifically Tm^{3+}:[$^3H_4$,$^1G_4$] → Tm^{3+}[$^1I_6$,$^3H_4$] and Tm^{3+}:[$^3F_4$,$^1G_4$] → Tm^{3+}:[$^1D_2$,$^3H_4$]. This match highly likely allowed for the absorption of an additional photon, promoting electron transitions to higher excited states, however, time resolved spectra should be captured to verify the hypothesis.

The UV UC arose from the sequential absorption of two blue photons, which was verified for the synthesized materials by plotting the dependencies integrated luminescence intensity (I_{int}) vs. the percentage of maximal excitation power ($\%P_{max}$) in double-logarithmic representation (Fig. 61a-f), following the Formula (1.3):

$$I_{int} \propto (\%P_{\max})^x, \tag{1.3}$$

where x slope in the linear fitting formula represents the number of photons involved, yielding a value close to 2 for all materials and the selected wavelengths.

As both Tm^{3+} and Pr^{3+} ions absorb 466 nm blue radiation, co-doping of β-$NaYF_4$ MCs with Pr^{3+} ions significantly altered the trends in the up-converted UV emission from Tm^{3+} ions. Due to higher absorption coefficient, Pr^{3+} ions were highly likely not only to enhance the number of excited Tm^{3+} ions through the Pr^{3+}:$^3P_0$,$^1I_6$ → Tm^{3+}:$^1G_4$ ET, but also to contribute to ETU, populating Tm^{3+}:$^1I_6$ and Tm^{3+}:$^1D_2$ states, from which the emission occurred. As a result, the UV emissions from Tm^{3+}:$^1I_6$ at ca. 288 and 348 nm were more intense in the co-doped MCs than in singly doped β-$NaYF_4$:1%Tm^{3+}, likely due to the lack of the Pr^{3+} ions excited states overlapping with the Tm^{3+}:$^3H_4$ excited energy level

(*Pathway no. 1*, shown in Fig. 54c). In contrast, the UV emission around 360 nm from Tm^{3+}:$^1D_2$ (*Pathway no. 2* in Fig. 54d) decreased about threefold upon Pr^{3+} co-doping, which could be attributed to quenching of the long-lived Tm^{3+}:$^3F_4$ excited energy state through resonant ET to Pr^{3+}:^3F_J states [189]. As Tm^{3+}:$^3F_4$ is known for its long LT) [183,184], it is able to act as an intermediate excited state for ESA or ETU, therefore, its depopulation by Pr^{3+} ions suppressed *Pathway no. 2*, which explains the diminished UC emission intensity at ca. 360 nm from Tm^{3+}:$^1D_2$ energy level.

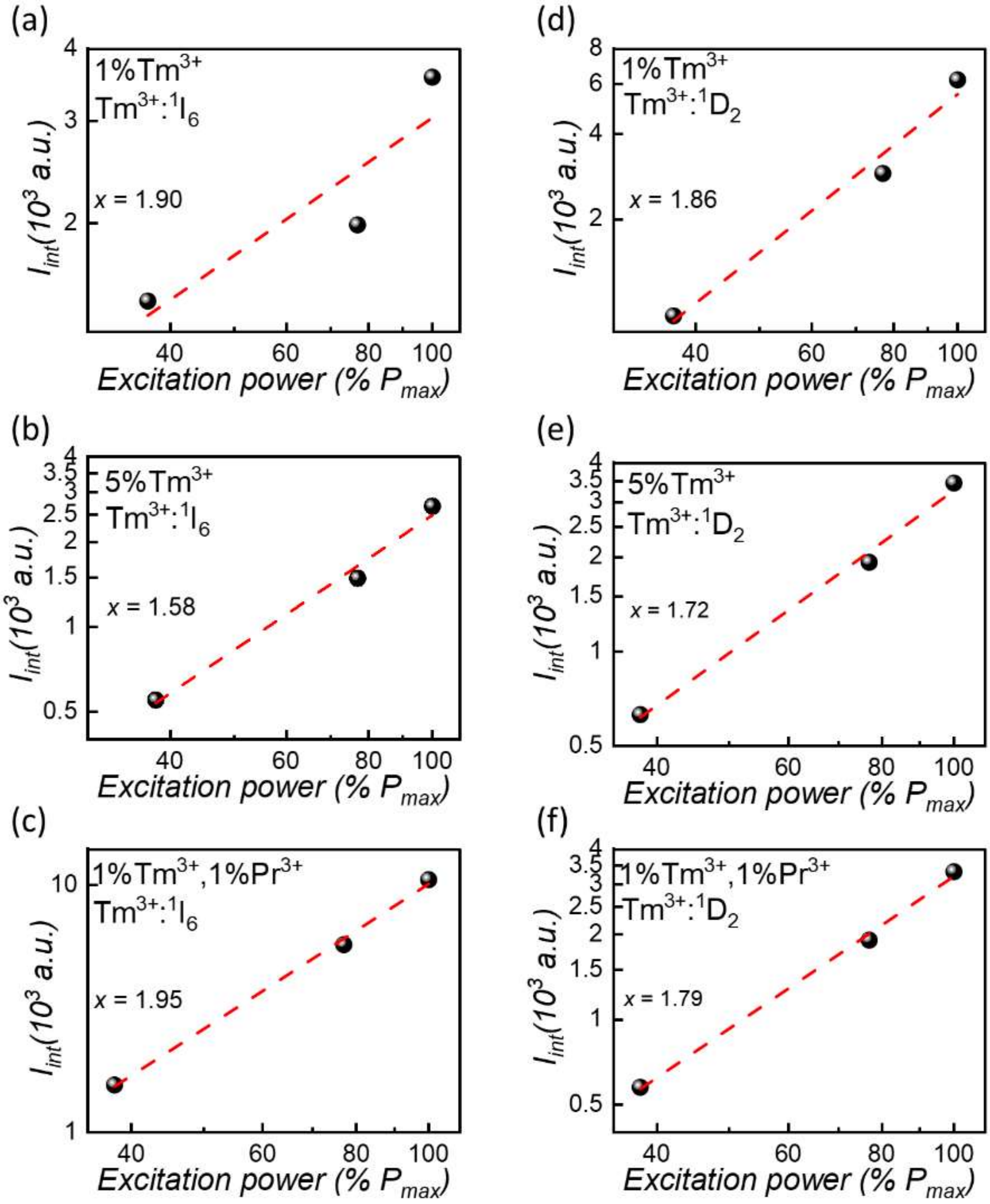

Fig. 61. Log–log plots of integrated emission intensity vs. excitation power with the linear fits (red dashed lines) for the synthesized Tm^{3+}-based β-$NaYF_4$ MCs. The plots were prepared for the up-converted UV emission bands peaking at (a-c) 348 nm and (d-f) 360 nm

7.5. Conclusions

In this part of the research, I revealed how co-doping with Pr^{3+} ions enhances the emissive properties of Tm^{3+}-based β-$NaYF_4$ MCs in two spectral regions of biological importance: UV and NIR. The microphosphors were synthesized through solid-state method and thoroughly characterized in terms of crystal structure and morphology. The first part of the research confirmed that simultaneous excitation of both Tm^{3+} and Pr^{3+} ions with 466 nm photons is feasible, as indicated by their excitation spectra reflecting efficient absorption within their ladder-like energy level structures. Subsequently, the β-$NaYF_4$ MCs were exposed to 466 nm laser excitation, and emission spectra were recorded under identical conditions for Vis-to-NIR DC and Vis-to-UV UC processes. These experiments demonstrated that co-doping with Pr^{3+} ions into the β-$NaYF_4$ host matrix led to an enhancement of the emissive properties in both spectral regions.

The more intense Vis-to-NIR DC emission, especially within the biologically relevant 650÷950 nm window, was attributed to efficient ET from the concurrently excited Pr^{3+} ions to Tm^{3+} ions. This enhancement holds particular significance for bioimaging applications, given the superior tissue penetration capabilities of NIR light in this range. In the case of Vis-to-UV UC, co-doping with Pr^{3+} ions resulted in the enhanced Tm^{3+}:$^1I_6$ UV-C emission, while the Tm^{3+}:$^1D_2$ UV-A emission was notably weakened. The stronger $^1I_6$ emission is ascribed to additional absorption and ET from Pr^{3+} to Tm^{3+} ions, providing alternative excitation pathways. Conversely, the reduction in Tm^{3+}:$^1D_2$ emission intensity is explained by the depopulation of the intermediate Tm^{3+}:$^3F_4$ excited energy state, which plays a crucial role in sequential photon absorption processes leading to the Tm^{3+}:$^1D_2$ state population. Resonant ET from Tm^{3+}:$^3F_4$ to Pr^{3+}:$^3F_2$ effectively disrupts this UC pathway, thus diminishing the UV-A emission.

These findings provide valuable insights into the design of lanthanide-doped materials and the ability to tailor their optical behavior for advanced photonic applications. In particular, the demonstrated co-doping strategy supports the development of theranostic materials capable of concurrent *in vivo* bioimaging (*via* NIR DC) and germicidal action (*via* UV-C UC), opening new pathways for multifunctional optical devices.

7.6. Acknowledgments and comments

This chapter is partially based on the data presented in the research paper *Spectroscopic characterization of UV-C and NIR emitting* Tm^{3+}/Pr^{3+}*-co-doped β-*$NaYF_4$. **P. Fałat*,** A. Meijerink, D. Wawrzyńczyk, (submitted to Optical Materials, under revision, *I am the corresponding author).

The research was conducted under the guidance of Prof. A. Meijerink during my short research stays at Utrecht University in the Netherlands [1-month research stay in July 2023, funded within the framework of SHENG project; 3-month research stay in September-December 2023, funded within the framework of *InterDocSchool* project granted by Polish National Agency of Academic Exchange (NAWA) to the Doctoral School of Wroclaw University of Science and Technology]. I designed β-$NaYF_4$ MCs co-doped with Tm^{3+} and Pr^{3+} ions at the selected concentrations. In the subsequent step, I synthesized and characterized them with regard to crystal structure, morphology, and elemental distribution. I registered the Stokes emission spectra of Vis-to-Vis and Vis-to-NIR DC emission as well as the anti-Stokes emission of Vis-to-UV UC. In order to get a better understanding of photon management processes kinetics occurring in the samples, I registered luminescence decay curves of the selected excited states at chosen emission wavelengths and extracted luminescence LT values.

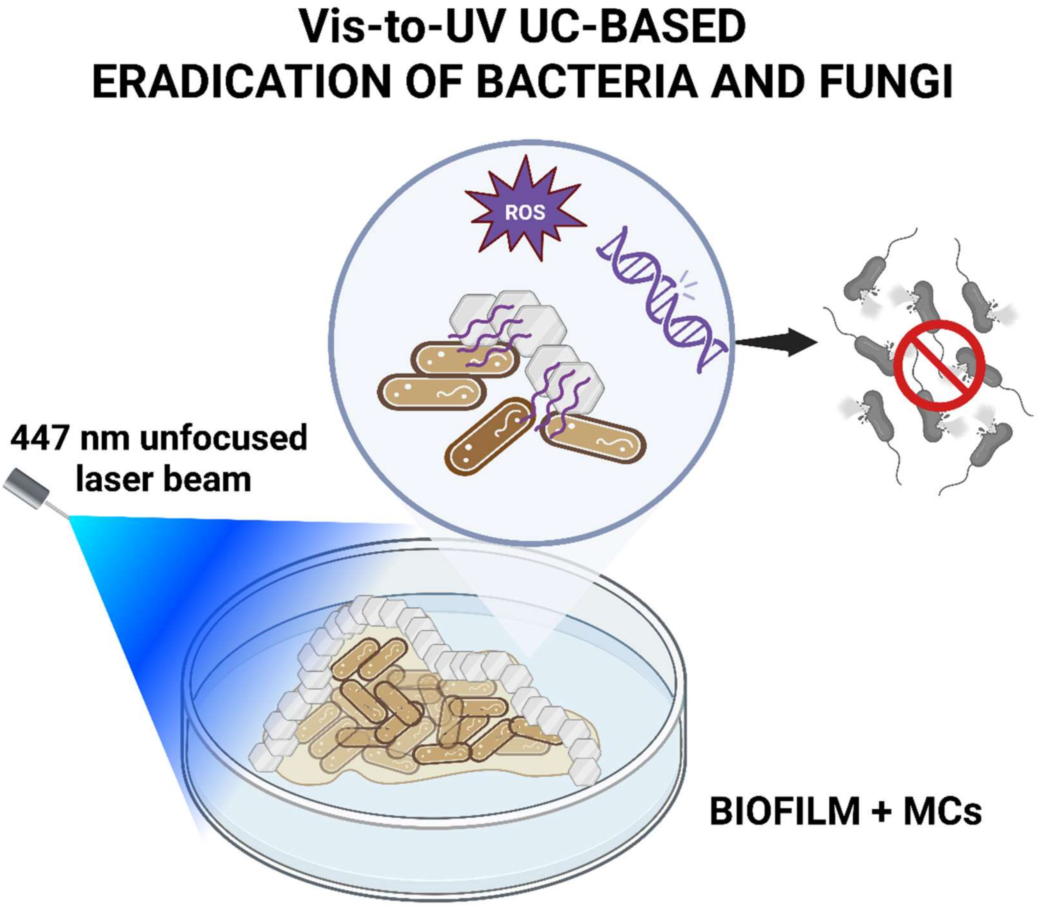

Fig. 62. The general concept of common bacteria and fungi photoinactivation experiment, exploiting enhanced Vis-to-UV UC of lanthanide-doped $Y_2Si_2O_7$ *phosphors*

Chapter 8

Enhancement of photon management processes in Pr^{3+}-doped yttrium silicates by Tm^{3+} and Yb^{3+} co-doping for photoactivated biocidal treatment

This chapter of the doctoral dissertation focuses on the following photon management processes: Vis-to-UV UC, NIR-to-UV UC, and Vis-to-Vis DC occurring in lanthanide-doped yttrium silicates ($Y_2Si_2O_7$) powders and their performance validation in light-triggered germicidal actions. In contrast to Chapter 5, where I thoroughly discuss Pr^{3+}-doped nano- and micromaterials and their efficient utilization against both enveloped and naked virus species, here I describe potential applications of $Y_2Si_2O_7$ powders, obtained through sol-gel synthesis, toward widespread and contagious bacteria and fungi. As these pathogens adhere to commonly-touched surfaces in healthcare facilities and public transportation, they tend to remain biologically active for extended periods, reciprocating at the same time. As a consequence, it poses a serious health hazard to all members of society, regardless of their medical condition.

Within the research scope I foremostly analyze lanthanide co-dopants influence on UC emission in UV range, exhibited by solely Pr^{3+}-doped and Pr^{3+},Tm^{3+},Yb^{3+} co-doped $Y_2Si_2O_7$ powders. When incorporated into $Y_2Si_2O_7$ host matrix, Pr^{3+} ions are prone to sequentially absorb two 447 nm Vis photons and emit broad up-converted UV band with two maxima peaking at ca. 278 and 308 nm (Vis-to-UV UC). An additional up-converted UV-A band from the co-doped Tm^{3+} ions is attainable due to ET to them from Pr^{3+} ions, excited at 447 nm. Further incorporation of Yb^{3+} ions unlocks the same band, however, through the sequential absorption of several 980 nm photons, i.e., NIR-to-UV UC occurs. This functionality introduced into the material considerably improves its effectiveness in light-triggered eradication of such pathogens as *A. baumannii*, *S. aureus*, and *B. cereus* bacteria as well as eukaryotic cells of *C. albicans*, all of them incubated as both planktonic cultures and biofilms (Fig. 62). This kind of behavior is most probably connected with endogenous protoporphyrins, which triggered with UV-A radiation coming from the co-doped Tm^{3+} ions generate ROS prone to interact with microbial cells.

A remarkable feature of the developed triply-co-doped phosphor is the mortality rate of cells in microbial layers after the irradiation with Vis radiation at 500 J cm^{-2} light dose, which is comparable in magnitude to that observed when the pathogenic cells are irradiated with a UV-C-emitting lamp only. Consequently, these findings are encouraging, since an efficient, localized antimicrobial treatment using lanthanide-doped Vis-to-UV up-converting materials could offer a human-health-safe alternative to applications based on direct UV light sources.

8.1. Introduction to the scientific problem

As already highlighted in Chapter 5, antimicrobial resistance occurs as a natural response of viruses, bacteria, and fungi, toward which selected chemical agents are utilized during eradication process, such as disinfectants, antibiotics, or even new types of metallic nanomaterials. As a result, the affected microbes no longer respond to their increasing doses, which leads to the development of multidrug resistant superbacteria, superviruses, and antifungal-resistant strains of fungi [206–208]. This issue emerges as one of the most serious challenges to be faced by modern medicine, which was emphasized by WHO in *Global Strategy for Containment of Antimicrobial Resistance* [135]. Therefore, future-oriented disinfection methods should be based on neither strong oxidizing chemicals nor direct interactions between microorganisms and NPs, but rather on physical stimuli. One of them is UV radiation, killing pathogens at high efficiency rate, which has been confirmed in numerous studies conducted over the years [8]. As outlined in Section 2.1.1, it can be divided into three distinct types, each of them providing different mechanism of microbial cells inactivation. Nevertheless, lamps generating high-power UV radiation (ca. 100 W) used worldwide tend to irradiate the whole room cubature in order to efficiently disinfect biologically contaminated surfaces. They emit radiation at 254 nm, which shows significant human health hazards. As a consequence, in high-power mode they can operate only when nobody is present in the affected zones, so their utilization is greatly limited due to the lack of site specificity [209].

In order to overcome this obstacle, the introduced solution could be based on Vis/NIR-to-UV up-converting phosphors. The studies showing such spectroscopic features were conducted on many lanthanide ions exhibiting sequential absorption of two Vis photons, nevertheless, the great hope has been placed on Pr^{3+} ions [210]. They can generate up-converted UV radiation with high efficiency, when incorporated into such host matrices as Ca_2SiO_4, $LiYF_4$, YBO_3, Y_2SiO_5 or $Y_2Si_2O_7$, just to name a few [211–213]. Interestingly, silicate host matrices (Y_2SiO_5 and $Y_2Si_2O_7$) were reported by Cates et al. as one of the most efficient systems for Vis-to-UV UC emission generation [66,214]. Y_2SiO_5:Pr^{3+} polycrystalline films exhibited the sequential absorption of two Vis photons. The resultant UV emission band, ranging between 260÷360 nm and peaking within the UV-C range, demonstrated significant influence on eradication efficiency of *Pseudomonas aeruginosa* biofilm bacteria and *Bacillus subtilis* spores [66]. On the other hand, the ceramic host matrix alteration from Y_2SiO_5 to $Y_2Si_2O_7$ considerably boosted the up-converted UV emission coming from Pr^{3+} ions [214]. Furthermore, the incorporation of suitable lanthanide ions into a host matrix at optimized concentration allows to engineer the UV emission output, thus the simultaneous combination of diverse emission lines could be essential to enhance light-triggered germs inactivation. Indeed, it was shown for Gd^{3+} ions – their incorporation along with Pr^{3+} ions resulted in an additional up-converted band at ca. 314 nm [66]. On the other hand, the material co-doping with NIR-absorbing lanthanide ions facilitates NIR-to-UV UC emission. The phenomenon occurs due to absorption of multiple (more than 2) NIR photons, in the vast majority of cases followed by immediate ET to ladder-like energy level structure of other lanthanide ions, capable to emit UV radiation (e.g., Tm^{3+},Yb^{3+} ion pair) [178–180]. In essence, it enables a shift in excitation wavelength from Vis to NIR spectral range, which is crucial for potential *in vivo* disinfection, as NIR photons can penetrate deeply through soft tissues and flesh [25]. However, up-converting three or more NIR photons within ladder-like energy level structure of lanthanide ions require laser of higher powers, since their absorption cross-sections in the NIR spectral region are of small magnitude, making the process less probable [43].

Inspired by these findings and knowledgeable about energy level structure of lanthanide ions, I decided to synthesize Pr^{3+}-based $Y_2Si_2O_7$ materials co-doped with Tm^{3+} and Yb^{3+} ions and investigate their emissive properties in terms of the potential enhancement of UV-light-based disinfection. I hypothesized that the photoeradication process could simultaneously employ two various types of UV radiation (i.e., UV-C and UV-A), which interact differently with microorganisms. As a consequence, two different mechanisms of UV inactivation would be utilized. Pr^{3+} ions would emit UV-C bands, deactivating microbial cells through direct interaction with dsDNA, resulting in transcription-inhibiting photoproducts formation. On the contrary, Tm^{3+} ions could generate the radiation from UV-A spectral range, exciting endogenous protoporphyrins so that they could induce ROS generation in living cells [10,11]. The latter would only occur if there was ET between Pr^{3+} ions, sensitized with 447 nm radiation, and Tm^{3+} ions behaving in this pair as an ACT. Additionally, co-doping with Yb^{3+} ions has the potential to enable the material excitation with NIR radiation, thus paving the way to NIR-to-UV UC emission occurring in Tm^{3+} ions only, since there is no energy match between the energy levels in Pr^{3+} and Yb^{3+} ions. After the successful confirmation of the desired spectroscopic features, the application potential of the synthesized materials should be verified against commonly-found bacteria and fungi, being at the same time highly lethal for patients with weakened immune system. Therefore, biocidal capability of up-converted UV radiation is here verified in this investigation on three different bacteria types: *A. baumannii* (responsible for hospital-acquired infections), *B. cereus* (causing foodborne illness), *S. aureus* (leading to purulent and systemic infections) as well as one eucaryotic type, *C. albicans* yeast (inducing thrush in various parts of human body).

8.2. Chemicals and chemicals used

8.2.1. Lanthanide-doped $Y_2Si_2O_7$ synthesis

For the synthesis of lanthanide-doped $Y_2Si_2O_7$ powders the following chemicals delivered by Sigma Aldrich were utilized: Y_2O_3 (99.99%), Yb_2O_3 (99.99%), Pr_2O_3 (99.99%), Tm_2O_3 (99.99%), and TEOS (99.999%). On the contrary, ethanol (99.8%) and HNO_3 (63÷65%) were obtained from Avantor Performance Materials Poland S.A. All of the chemicals were not purified before the usage.

The lanthanide-doped $Y_2Si_2O_7$ powders were prepared in accordance with the protocol described in Section 3.2.3. The masses of the corresponding compounds in the solid form were charted below as Table 17.

Table 17. Amounts of solid compounds used to synthesize lanthanide-doped $Y_2Si_2O_7$ silicates

Synthesized phosphor	**Compound mass [g]**			
	Y_2O_3	**Pr_2O_3**	**Yb_2O_3**	**Tm_2O_3**
$Y_2Si_2O_7$	1.0000	–	–	–
$Y_2Si_2O_7$: 1.2% Pr^{3+}	0.9890	0.0165	–	–
$Y_2Si_2O_7$: 1.2% Pr^{3+}, 0.5% Tm^{3+}, 5% Yb^{3+}	0.9213	0.0165	0.0866	0.0077

8.2.2. Microbial inactivation studies – planktonic cells and biofilm

In the study four various microbial species were utilized: *Acinetobacter baumannii* (PCM 8740), *Bacillus cereus* (PCM 2021), *Staphylococcus aureus* (PCM 2024) – obtained from Polish Collection of Microorganisms, and *Candida albicans* (ATCC 10231) from ATCC. The Mueller–Hinton broth (purchased from Oxoid, UK) was used to incubate the microorganisms in the form of either inoculum or biofilm. Additionally, for *C. albicans* the growth solution was supplemented with 1% of glucose (99.9%, Sigma Aldrich).

BacTiter-Glo™ Assay (Promega Corporation, USA) was used as received from the supplier to assess the viability of planktonic cells.

3-(4,5-dimethylthiazol-2-yl)-2,5-diphenyltetrazolium bromide (MTT) and PBS (at pH = 7.2) were purchased from Sigma Aldrich. Both chemicals were mixed to prepare the MTT reagent at the final concentration of 5 g L^{-1}, which was further utilized for the biofilm viability assessment. Isopropanol (99.9%, Avantor Performance Materials Poland S.A.) and HCl (35÷38%, ChemPur, Poland) were mixed at the ratio of 200:3 (v/v) to obtain the solution of acidic isopropanol for the formed formazan crystals dissolution.

8.2.3. Intracellular ROS generation

2′,7′-dichlorodihydrofluorescein diacetate (DCFDA) (≥97%, Sigma Aldrich) was applied as a solution at the concentration of 50 μM to quantify the capability of the synthesized lanthanide-doped $Y_2Si_2O_7$ powders to generate intracellular ROS.

8.3. Characterization methods

8.3.1. Crystal structure & Rietveld refinement

XRD analysis of the synthesized lanthanide-doped $Y_2Si_2O_7$ microphosphors was carried out using a Bragg–Brentano geometry STOE X-ray diffractometer with $CuK\alpha_1$ radiation, operating within a 2θ range of 10÷80°. The crystal phases and lattice parameters of the resulting materials were determined through Rietveld refinement in FullProf Suite software.

8.3.2. Morphology and elemental analysis

SEM images registration and EDS analysis were performed using the SEM, conjugated with the Oxford Aztec spectrometer. The utilized setup has already been briefly described in Section 5.3.2. The parameters of the conducted analyses remained unchanged throughout the whole experiment.

8.3.3. Spectroscopic features characterization

The Vis-to-Vis DC emission spectra of the powdered samples were recorded with FLS980 Edinburgh Instrument, as indicated in Section 4.3.3. The powders were excited with a 450 W Xe lamp in ambient conditions (λ_{ex} = 447 nm). The anti-Stokes NIR-to-Vis UC emission spectra were captured under the 980 nm CW semiconductor laser diode illumination (8 W, Spectra Laser, Poland).

The Vis-to-UV UC emission spectra of the powdered samples, deposited on glass substrates, were recorded under ambient conditions with the custom-assembled setup, for which the measurement procedure was thoroughly described in Section 4.3.3.

The Vis-to-UV UC luminescence LTs measurements were performed using the above-mentioned experimental setup with a slight modification. The 447 nm CW laser diode was modulated by the square wave generated by the lock-in amplifier. To ensure the high dynamic range, the PMT signal was amplified by a 200 MHz high-impedance voltage amplifier (Femto HVA-200M-40-F) and then measured with a digital oscilloscope (Rohde & Schwarz RTB2K, 300 MHz bandwidth).

8.3.4. Microbial inactivation studies – planktonic cells

Before the start of the experiment planktonic cells of *A. baumannii*, *S. aureus*, *B. cereus*, and *C. albicans* were prepared. A single colony from each species was inoculated into 5 mL of Mueller-Hinton broth; the medium for the *C. albicans* yeast inoculum contained additionally 1% of glucose. The cultures were incubated in dark at 37 °C for 24 h. After this time, they were centrifuged individually for 5 min at 6,000 rpm. The pellets were resuspended in 5 mL of sterile PBS, each time resulting in the inoculum with approximately $1 \div 2 \cdot 10^6$ colony-forming units (CFU mL^{-1}).

BacTiter-Glo™ test [215], which was utilized to estimate the pathogens viability in the planktonic form, is based on the quantification of ATP present in living cells by its reaction with thermostable luciferase. The resultant luminescence signal is directly proportional to the amount of ATP, thus at the same time being proportional to the number of the viable cells currently present in the culture. The reduction in planktonic cell viability can be calculated using the provided Formula (1.4):

$$planktonic\ cell\ viability = \frac{(I_I - I_B) - (I_T - I_B)}{I_I - I_B} \cdot 100\%, \qquad (1.4)$$

where:

I_I – luminescence intensity of the initial sample (the standardized microbial suspension which was neither exposed to the investigated microphosphors nor irradiated);

I_B – luminescence intensity of background (no cells);

I_T – luminescence intensity of the tested sample (the standardized microbial suspension which was exposed to the investigated microphosphors, irradiated or irradiated in the presence of the investigated microphosphors.

Therefore, the studies on photoeradication of the pathogens in the planktonic form *via* Vis-to-UV UC emission were also preceded by:

- estimation of the light irradiation impact on the viability of the investigated pathogenic cells:
  100 µL of a standardized cell suspension of *A. baumannii, S. aureus, B. cereus,* or *C. albicans* was added to each well of a microtiter plate (Thermo Scientific^{TM}). It was then exposed to the unfocused CW laser beam with the peak-power wavelength at 447 nm for 5, 7, and 10 min, which corresponded to the light dose of 250 J cm^{-2}, 350 J cm^{-2}, and 500 J cm^{-2}, respectively. The irradiated inoculum viability was immediately evaluated by BacTiter-Glo^{TM} test. The experiment was performed in triplicate.
- dark cytotoxicity evaluation of the tested microphosphors against the microorganisms in the planktonic form:
  100 µL of a standardized cell suspension in each well of the plate was incubated without shaking in dark at 37°C with 5, 15, or 30 mg of the lanthanide-doped yttrium silicates. The cell viability was assessed using BacTiter-Glo^{TM} test after 1, 4, and 8 h. The experiment was conducted in triplicate.

The studies on the photoinactivation of the tested pathogenic cells in the planktonic form were conducted by transferring 100 µL of a standardized cell suspension into each well of a microtiter plate and adding 15 mg per well or 30 mg per well of undoped $Y_2Si_2O_7$, $Y_2Si_2O_7$:Pr^{3+} or $Y_2Si_2O_7$:Pr^{3+},Tm^{3+},Yb^{3+} powder. These values were selected based on the prior control experiments. In the next step, such an experimental setup was exposed to the unfocused 447 nm CW laser beam for either 5 or 7 min, which corresponded to the light dose of 250 J cm^{-2} or and 350 J cm^{-2}, respectively. After that time, the tested microphosphors were removed so that the planktonic cells viability could be determined by BacTiter-Glo^{TM} test. The untreated pathogenic inocula were incubated under the same conditions and used as a reference. The whole experiment was conducted three times.

8.3.5. Microbial inactivation studies – biofilm

Before the start of the experiment, there was a need to develop the biofilm consisting of the pathogenic cells. Therefore, 100 µL of a standardized cell suspension of *A. baumannii*, *S. aureus*, and *C. albicans* was placed into each well of a pre-sterilized flat-bottom polystyrene 96-well plate and incubated in dark for 4 h. After this time, the supernatant containing non-adhered cells was discarded, and the wells were washed with 100 µL of sterile PBS per well. In the next step, Mueller-Hinton broth was added in the volume of 100 µL per well (the medium was additionally supplemented by 1% of glucose for *C. albicans* yeast) and the plates were incubated at 37 °C for 24 h in dark. In order to purify the developed biofilm, each well was washed with 100 µL of sterile PBS.

The principles of MTT assay test [216], which was used to determine the viability of the pathogens in the biofilm form, are based on the enzymatic conversion of 3-(4,5-dimethylthiazol-2-yl)-2,5-diphenyltetrazolium bromide (MTT) to water-insoluble formazan products by dehydrogenases and oxireductases. These compounds are only present in living cells, hence there is the direct linear proportionality between the cell counts in the considered sample and the amount of formed formazan crystals. In the next step, the crystals are dissolved in acidic isopropanol and the concentration of such a solution can be obtained through absorption measurement at 570 nm. As a consequence, the reduction in biofilm viability can be thus calculated using the Formula (1.5) provided below:

$$biofilm\ cells\ viability = \frac{(A_I - A_B) - (A_T - A_B)}{A_I - A_B} \cdot 100\%, \qquad (1.5)$$

where:

A_I – absorbance of the initial sample (the biofilm before photoinactivation);

A_B – absorbance of background (no cells, 0.015);

A_T – absorbance of the tested sample (the biofilm after photoinactivation).

Therefore, the studies on the biofilm disruption through Vis/NIR-to-UV UC-based photoeradication were also preceded by:

- estimation of the light irradiation impact on viability of the formed biofilm:
  the biofilms of *A. baumannii, S. aureus,* and *C. albicans*, developed in each well of a microtiter plate, were exposed to the unfocused 447 nm (power density: ~800 mW cm^{-2}) or 980 nm laser beam (power density: ~500 mW cm^{-2}). The biofilm was irradiated with the 447 nm wavelength for 5, 7, and 10 min, which corresponded to the light dose of 250 J cm^{-2}, 350 J cm^{-2}, and 500 J cm^{-2}, respectively. On the contrary, the 980 nm radiation illuminated the biofilm for 10 min, hence the total light dose reached 300 J cm^{-2}. The biofilm cultures viability was evaluated by MTT test. The experiment was performed in triplicate.
- dark cytotoxicity evaluation of the tested microphosphors against the biofilm-forming pathogens:
  5, 15 or 30 mg of the tested lanthanide-doped $Y_2Si_2O_7$ powders was added into each well of the microtiter plate containing the developed biofilm of *A. baumannii, S. aureus,* or *C. albicans*. The plate was incubated without shaking in dark at 37 °C. The biofilm cultures viability was evaluated by MTT test after 1, 4, and 8 h. The test was performed in triplicate.

After a series of control experiments, the studies on the photoinactivation of the biofilm-forming pathogens was conducted after adding 30 mg of the tested powders into each well of the microtiter plate containing the developed biofilm of *A. baumannii, S. aureus,* or *C. albicans*. In the next step, they were exposed to the unfocused 447 nm CW laser beam (power density: ~800 mW cm^{-2}) for 10 min, which corresponded to the light dose of 500 J cm^{-2}. In the separate experiment, the undoped and Yb^{3+}-co-doped $Y_2Si_2O_7$ microphosphors were irradiated for 10 min with the unfocused 980 nm laser beam (power density: ~500 mW cm^{-2}), which corresponded to the 300 J cm^{-2} light dose. After this time, the biofilm cultures viability was evaluated by MTT test. As a reference, the biofilm developed under the same conditions and untreated with the radiation was utilized. The whole experiment was conducted three times.

Additionally, there was a control experiment performed in order to compare the efficiency of biofilm photoinactivation through Vis-to-UV UC emission, generated by the synthesized compounds. The biofilms developed by *A. baumannii, S. aureus,* or *C. albicans* in each well of the microtiter plate were directly exposed to UV radiation, no lanthanide-doped microphosphors were added. The radiation of 254 nm wavelength was emitted for 10 min by a 2-wavelength UV lamp Kamus LP254. After this time, the biofilm cultures viability was evaluated by MTT test. As a reference, the biofilm developed under the same conditions and untreated with the radiation was utilized. The whole experiment was performed three times.

8.3.6. Intracellular ROS generation

The experiment principle is based on excitation of protoporphyrins with up-converted UV radiation. Such a situation could occur due to the partial overlap of their absorption spectrum with the UV radiation emitted by silicate $Y_2Si_2O_7:Pr^{3+},Tm^{3+},Yb^{3+}$ (Fig. 63). Therefore, the *S. aureus* biofilm was developed in a pre-sterilized flat-bottom polystyrene 96-well plate, In the next step, 30 mg of $Y_2Si_2O_7$, $Y_2Si_2O_7:Pr^{3+}$ or $Y_2Si_2O_7:Pr^{3+},Tm^{3+},Yb^{3+}$ powders was placed into each well, followed by the exposition to the unfocused 447 nm CW laser beam for 10 min, which corresponded to the light dose of 500 J cm^{-2}. After this time, the irradiated biofilms were incubated with 50 μM DCFDA solution. The oxidative stress was quantitatively measured with the spectrofluorimetric method using a SpectraMax Gemini spectrofluorometer ($\lambda_{ex} = 485$ nm, $\lambda_{em} = 520$ nm) [217].

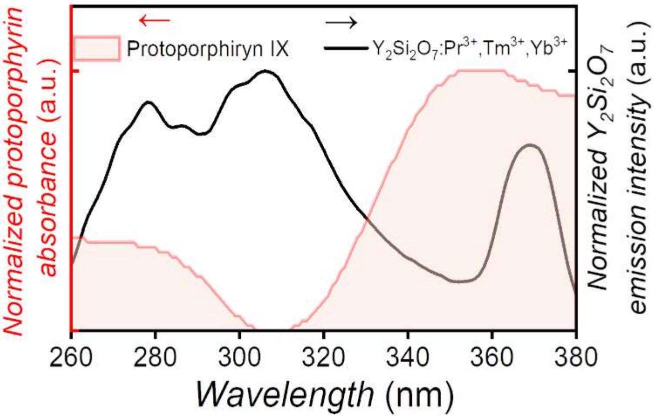

Fig. 63. The VIS-to-UV UC emission spectra of $Y_2Si_2O_7:Pr^{3+},Tm^{3+},Yb^{3+}$ silicate (black line) under 447 nm laser excitation in the comparison with on protoporphyrin IX absorption spectrum (red area)

8.4. Results and discussion

8.4.1. Morphology and crystal structure

In the experiment a series of polycrystalline $Y_2Si_2O_7$ materials co-doped with lanthanide ions (i.e., Pr^{3+}, Yb^{3+}, and Tm^{3+}) was synthesized. Morphology of the resultant white powders was investigated with SEM technique. The undoped and Pr^{3+}-doped materials exhibited highly fused crystallites (Fig. 64a-b), whereas the further concurrent co-doping with Yb^{3+} and Tm^{3+} ions promoted the formation of smaller crystallites (Fig. 64c). For $Y_2Si_2O_7:Pr^{3+}$ and $Y_2Si_2O_7:Pr^{3+},Tm^{3+},Yb^{3+}$ EDS analysis was simultaneously conducted, which revealed the homogenous distribution of lanthanide ions within the samples (Fig. 64b-c). As a consequence, morphology changes could be explained based on crystal lattice alterations occurring due to Pr^{3+}, Yb^{3+}, and Tm^{3+} ions incorporation. The challenging Rietveld refinement of the collected XRD patterns (Fig. 65a-c) allowed to assign the crystal structure of all synthesized materials as $Y_2Si_2O_7$, which in the literature is described as the group of mixed anion silicates [218]. It is characteristic for this group of material that crystal structure usually exhibits low symmetry and every atom has a uniquely defined site. Additionally, the substitution at Y^{3+} sites with ions occurs randomly. As a result, any dopant introduced into the considered host matrix at very low concentration will affect both the reflexes position in XRD patterns and their relative intensity [219]. In this case, X-ray scattering factors of Y^{3+}, Pr^{3+}, Yb^{3+}, and Tm^{3+} ions are of different values, thus the performed Rietveld refinement on the theoretical structure models could only approximate the real structures. Resultantly, the major intensity peaks in the analyzed XRD patterns (depicted for the clarity with asterisks in Fig. 65a-c) do not coincide perfectly with the standard patterns.

Nevertheless, based on Rietveld analysis, it was feasible to distinguish various polymorphs present in the obtained powders. In the undoped material dominated the polymorph of the triclinic phase $P\overline{1}$ (~75%) upon the one with monoclinic $P21/m$ phase (~25%). As Pr^{3+} ions were utilized for the synthesis, the $P\overline{1}$ crystal phase percentage reached ~90%, whereas only ~10% of the material crystallized in the orthorhombic $Pna2_1$ crystal phase. In the recorded XRD patterns the main reflections matched the theoretical pattern mp-581644 (see the Reference pattern in Fig. 65a-b). On the other hand, incorporation of other rare-earth ions into the host matrix resulted in the formation of pure $Y_2Si_2O_7$ triclinic phase $P\overline{1}$ only, which stays in good agreement with the results reported earlier for e.g. Li^+ or Lu^{3+} ions introduced into oxide-based powdered phosphors [66,219,220]. The mechanism responsible for such a behavior could be based on flux effect. It occurs as liquid phase appears at grain boundaries, which allows the crystallite formation rate to increase significantly. Therefore, the crystallites of higher crystal structure are likely to grow during the annealing process [221]. It is worth mentioning that the calculated unit cell parameters for all investigated materials (charted in Table 18) are of comparable values with other related silicate materials, e.g., $Ho_2Si_2O_7$ or $Dy_2Si_2O_7$ [222,223].

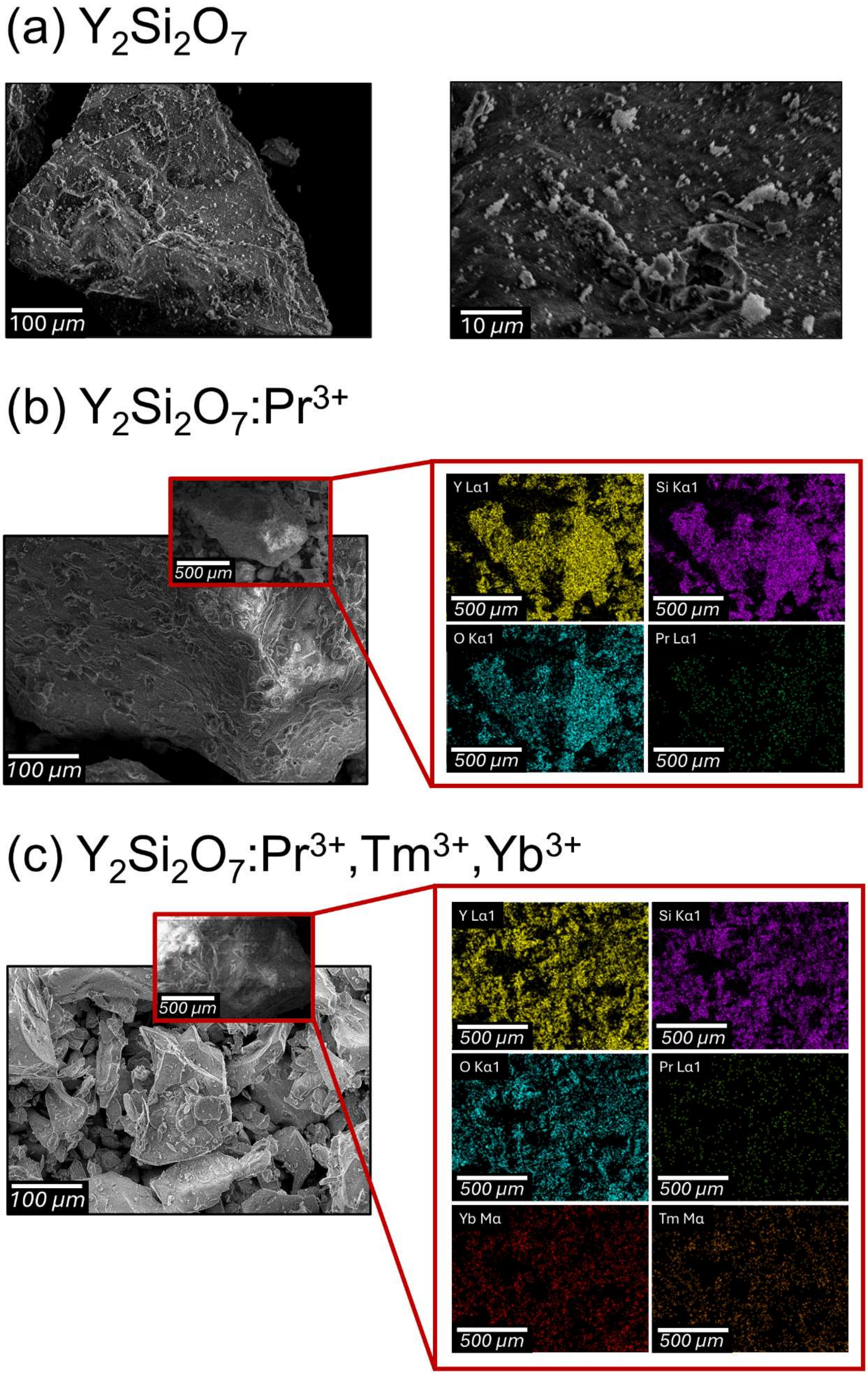

Fig. 64. SEM images (left column) and elemental distribution maps (right column) of (a) Y_2SiO_7, (b) $Y_2Si_2O_7$:Pr^{3+}, and (c) $Y_2Si_2O_7$:Pr^{3+},Tm^{3+},Yb^{3+} powders

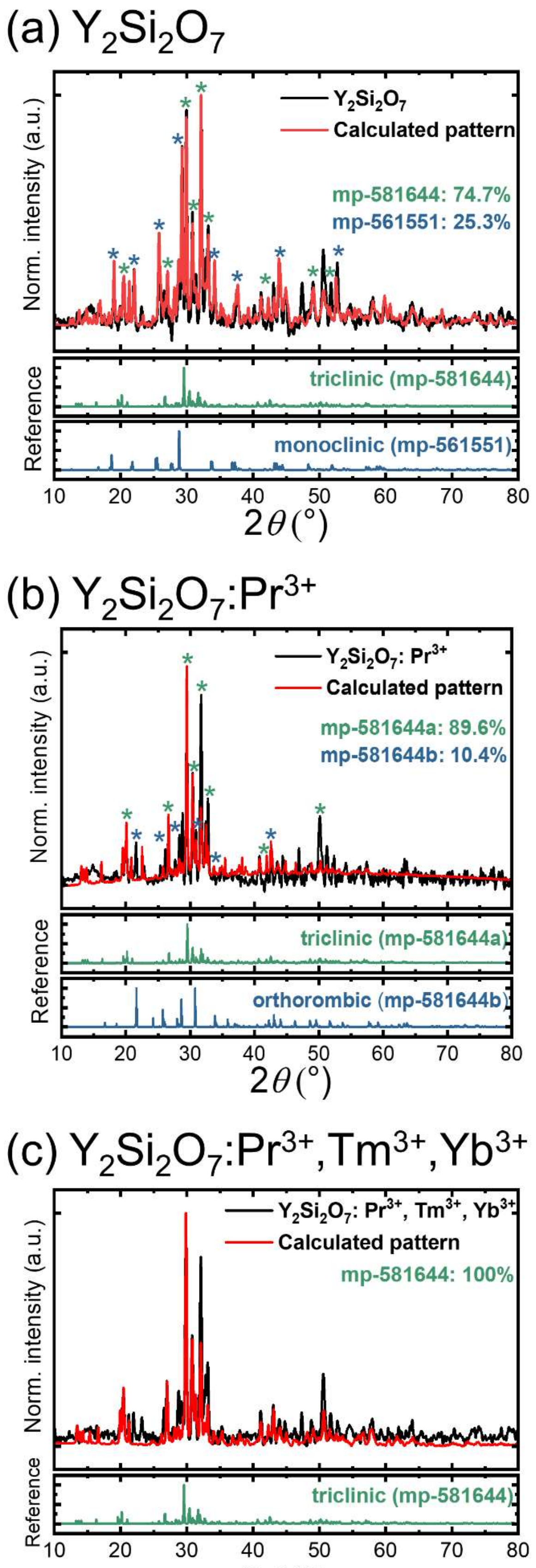

Fig. 65. XRD patterns of (a) $Y_2Si_2O_7$, (b) $Y_2Si_2O_7$:Pr^{3+}, and (c) $Y_2Si_2O_7$:Pr^{3+},Tm^{3+},Yb^{3+} with the theoretical patterns provided as references

Table 18. Cell parameters of the studied undoped $Y_2Si_2O_7$, $Y_2Si_2O_7$:Pr^{3+}, and $Y_2Si_2O_7$:Pr^{3+},Tm^{3+},Yb^{3+} powders calculated in Rietveld refinement

	$Y_2Si_2O_7$ undoped		**$Y_2Si_2O_7$: Pr^{3+}**		**$Y_2Si_2O_7$: Pr^{3+}, Yb^{3+}, Tm^{3+}**
MP card no	**581644**	**561551**	**581644a**	**581644b**	**581644**
Space group	$\boldsymbol{P\bar{1}}$	***P*21/m**	$\boldsymbol{P\bar{1}}$	$\boldsymbol{Pna2_1}$	$\boldsymbol{P\bar{1}}$
***a* (Å)**	6.60208	5.04427	6.53164	6.61358	6.60242
***b* (Å)**	6.63591	8.08721	6.76527	6.66074	6.66096
***c* (Å)**	36.07779	7.3275	36.28017	35.15834	36.10046
***α* (°)**	94.71056	90	94.98871	94.64206	94.53239
***β* (°)**	90.60159	108.5303	90.98531	90.72639	90.61315
***γ* (°)**	92.00661	90	91.81551	92.04543	92.10380

8.4.2. Spectroscopic analysis

Followingly, the thorough spectroscopic analysis of lanthanide-doped $Y_2Si_2O_7$ materials was conducted. For better clarity of the chapter, the energy level diagrams of lanthanide ions co-doped into $Y_2Si_2O_7$ host matrix, i.e., Pr^{3+}, Tm^{3+}, and Yb^{3+}, with all radiative and non-radiative transitions, were presented in Fig. 66a-b.

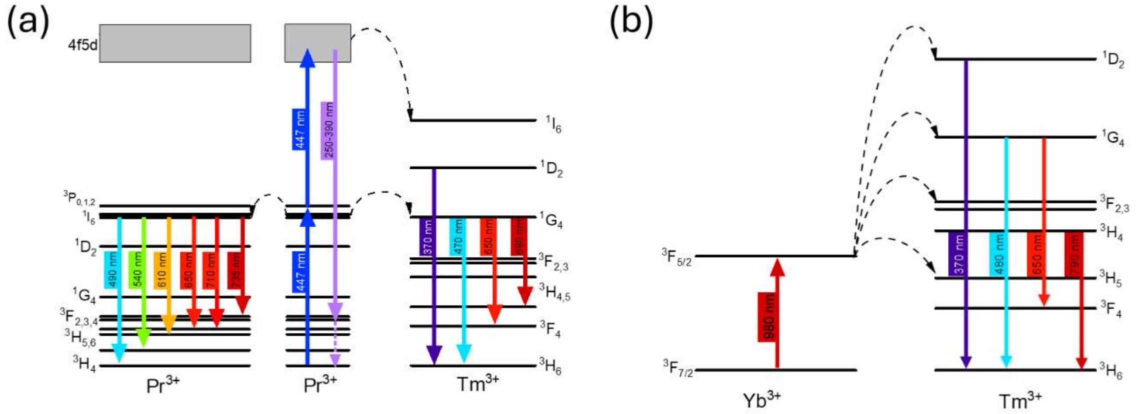

Fig. 66. Energy level diagrams with radiative and non-radiative transitions occurring in (a) Pr^{3+} and Tm^{3+} ions under 447 nm excitation, (b) Yb^{3+} and Tm^{3+} ions under 980 nm excitation

Firstly, when exposed to 447 nm radiation, $Y_2Si_2O_7$:Pr^{3+} exhibited Vis-to-Vis Stokes DC with the bands peaking at ca. 490, 540, 610, 650, 710, and 735 nm, which were ascribable to $^3P_0 \rightarrow {}^3H_4$, $^3P_0 \rightarrow {}^3H_5$, $^3P_0 \rightarrow {}^3H_6$, $^3P_0 \rightarrow {}^3F_2$, $^3P_0 \rightarrow {}^3F_3$, and $^3P_0 \rightarrow {}^3F_4$ electronic transitions within the Pr^{3+} ion energy level structure, respectively (see Fig. 67a for the emission spectrum and Fig. 66a for the energy level structure of Pr^{3+} ions). Besides the emission from Pr^{3+} ions (depicted in black), co-doping with Tm^{3+} ions resulted in the emergence of additional bands at ca. 470, 650, and 690 nm associated with $^1G_4 \rightarrow {}^3H_6$, $^1G_4 \rightarrow {}^3F_4$, and $^1G_4 \rightarrow {}^3H_4$ transitions within the energy structure of Tm^{3+} ions, accordingly (see the emission spectrum in Fig. 67b with highlights in red whereas the energy level structure of Tm^{3+} ions with the electronic transitions – in Fig. 66a).

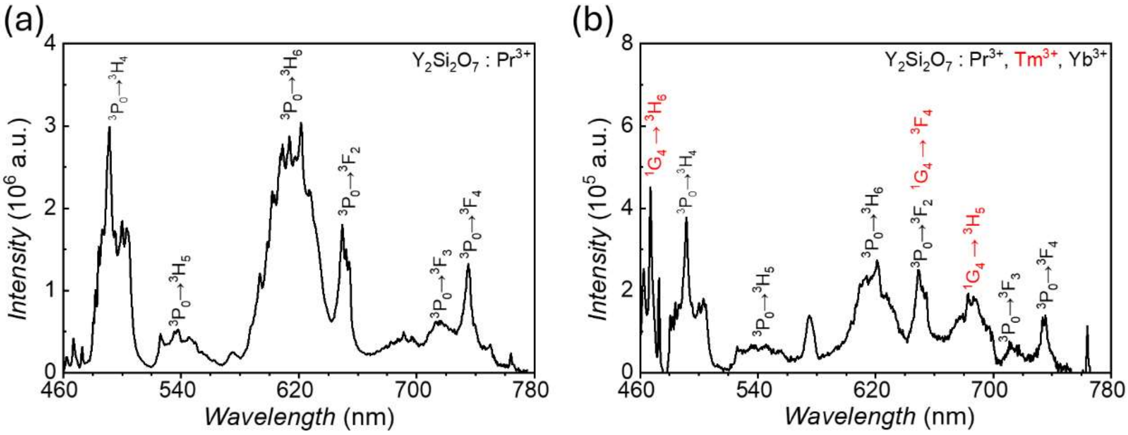

Fig. 67. Vis-to-Vis DC spectra of (a) $Y_2Si_2O_7{:}Pr^{3+}$ and (b) $Y_2Si_2O_7{:}Pr^{3+},Tm^{3+},Yb^{3+}$ phosphors upon 447 nm excitation (Xe lamp)

The resultant emission lines from Tm^{3+} ions were highly likely to be attainable due to ET from the $Pr^{3+}{:}{}^3P_0$ excited state to the $Tm^{3+}{:}{}^1G_4$ energy level (see energy level diagrams in Fig. 66a). To confirm its occurrence, though, the emission kinetics at 610 nm from the $Pr^{3+}{:}{}^3P_0$ excited state was investigated (Fig. 68). Both luminescence decay curves were approximated with the bi-exponential model and the calculated τ_1 and τ_2 were provided in Table 19. A significant shortening of the $Pr^{3+}{:}{}^3P_0$ energy level LT values was observed upon Tm^{3+} ions co-doping – the former was reduced by almost 95% (from 46.22 ± 0.18 μs to 2.70 ± 0.11 μs), whereas the latter by 90% (from 122.20 ± 1.40 μs to 14.56 ± 0.12 μs). Therefore, the collected data strongly supports the hypothesis on ET between these ions.

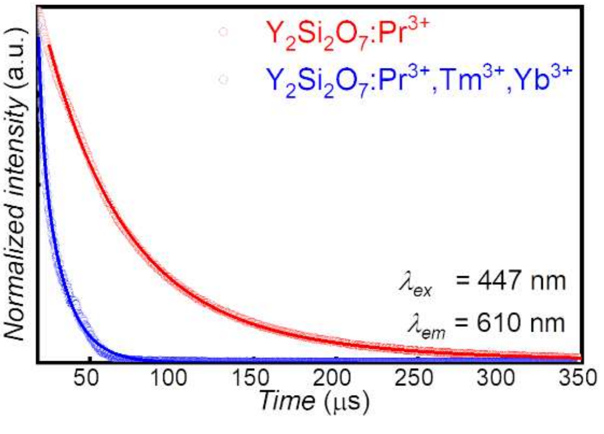

Fig. 68 Luminescence decay curves for $Pr^{3+}{:}{}^3P_0$ excited energy level collected at 610 nm upon 447 nm excitation for the Pr^{3+}-based silicates. The fitted lines represent the bi-exponential model

Table 19. Calculated luminescence LTs for $Pr^{3+}{:}{}^3P_0$ measured at 610 nm upon 447 nm excitation

Investigated phosphor	τ_1 [μs]	τ_2 [μs]
$Y_2Si_2O_7 : Pr^{3+}$	46.22 ± 0.18	122.20 ± 1.40
$Y_2Si_2O_7 : Pr^{3+},Tm^{3+},Yb^{3+}$	2.70 ± 0.11	14.56 ± 0.12

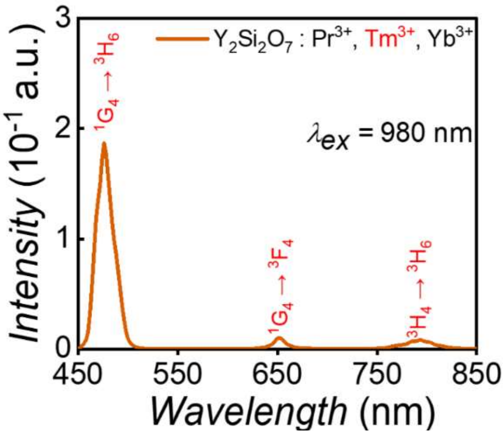

Fig. 69. NIR-to-Vis UC emission spectra for $Y_2Si_2O_7$:Pr^{3+},Tm^{3+},Yb^{3+} induced upon 980 nm laser excitation

In order to prove ET from Yb^{3+} ions to other lanthanides in the sample, $Y_2Si_2O_7$:Pr^{3+}, Tm^{3+},Yb^{3+} material was exposed to 980 nm laser beam, inducing the only one electronic transition possible in Yb^{3+} ions electronic structure. The NIR-to-Vis UC emission spectrum (Fig. 69) was collected, in which three bands peaking at ca. 480, 650, and 790 nm were observed, ascribed to $^1G_4 \rightarrow {}^3H_6$, $^1G_4 \rightarrow {}^3F_4$, and $^3H_4 \rightarrow {}^3H_6$ electronic transitions in Tm^{3+} ions energy level structure (see Fig. 66b), respectively. Since under these conditions there were no UC bands originating from Pr^{3+} ions, the excited Yb^{3+} ions are more susceptible to transfer energy to Tm^{3+} than to Pr^{3+} ions. It stays in fact in good agreement with the published reports on UC in Tm^{3+},Yb^{3+}-co-doped materials [178–180].

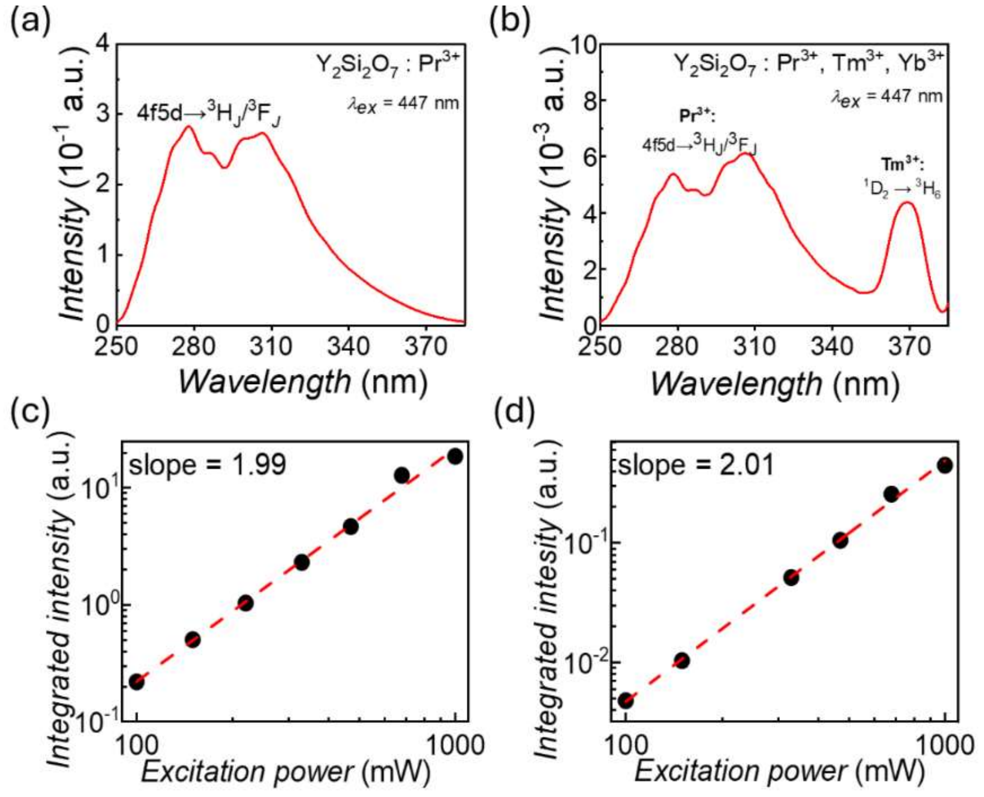

Fig. 70. Vis-to-UV UC emission spectra of (a) $Y_2Si_2O_7$:$Pr^{3+}$and (b)$Y_2Si_2O_7$:Pr^{3+},Tm^{3+},Yb^{3+} upon 447 nm laser irradiation at the power of 1000 mW (left column). Integrated intensity of UV bands emitted by the investigated phosphors (c) $Y_2Si_2O_7$:$Pr^{3+}$and (d)$Y_2Si_2O_7$:Pr^{3+},Tm^{3+},Yb^{3+}upon 447 nm laser excitation plotted against excitation power in log-log scale. The linear fits in red and slope values were provided

As the Vis-to-Vis DC emission spectra were recorded and ET between Pr^{3+} and Tm^{3+} ions was confirmed, the next step was focused on the Vis-to-UV UC emission spectra acqusition upon 447 nm excitation (Fig. 70a-b). The Pr^{3+}-bearing samples emitted in the 250÷390 nm spectral range two overlapping broad bands, with the maximum emission intensity at ca. 278 and 308 nm, which stays in good agreement with the findings reported by Cates et al. for Pr^{3+}-co-doped polymorph, Y_2SiO_5 [66,114,214].

The peaks were the result of the two 447 nm photons sequential absorption, which was also confirmed experimentally by the power dependence registration (Fig. 70c-d), described with the dependency *integrated intensity* vs. excitation power, given as Formula (1.3). When plotted in the log-log scale, the slope values were approximately 2 – i.e., 1.99 for $Y_2Si_2O_7:Pr^{3+}$ and 2.01 for $Y_2Si_2O_7:Pr^{3+},Tm^{3+},Yb^{3+}$ sample. The mechanism is consistent to the one already described for Pr^{3+}-based β-$NaYF_4$ and $LiYF_4$ NPs and MCs (*vide* Chapters 4, 5, and 6). Briefly, the first absorbed blue photon was capable to populate the $^3P_0$ energy level of Pr^{3+} ions, which was proven to show the LT values at μs range, which is sufficient to facilitate absorption of another photon, eventually resulting in 4f5d energy level population. As 4f5d→^3F_J/^3H_J transition occurred, Pr^{3+} ions generated photons falling in UV spectral range (see the energy scheme in Fig. 66a). Additionally, the luminescence decay curves for the up-converted UV radiation emission were registered at 278 and 308 nm for the $Y_2Si_2O_7:Pr^{3+}$ sample (see Fig. 71). The data could be approximated with the single exponential model, resulting in the luminescence LTs equaling 12.34 μs at 278 nm and 8.86 μs at 308 nm.

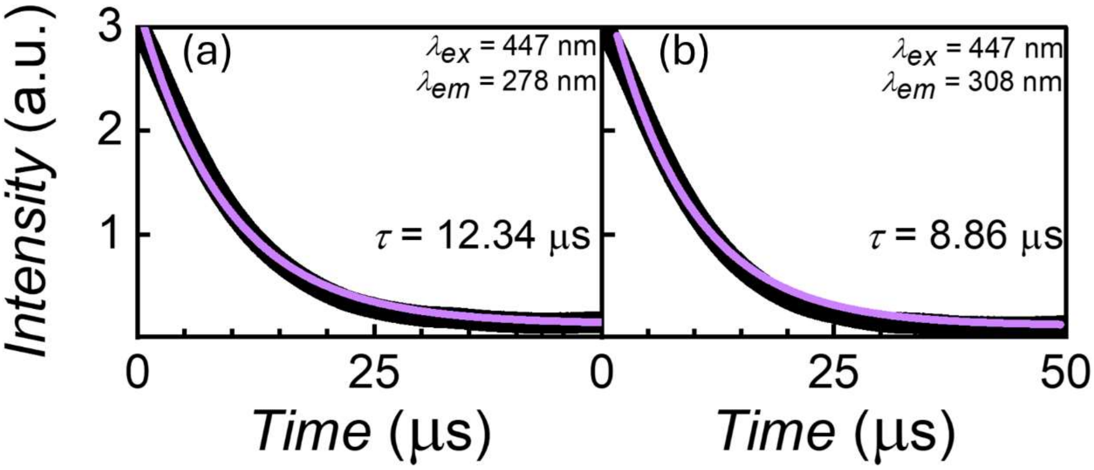

Fig. 71. Vis-to-UV UC luminescence decay curves for $Y_2Si_2O_7:Pr^{3+}$powder upon 447 nm laser excitation, measured at (a) 278 nm and (b) 308 nm. The purple lines represent the single exponential decay fitting model

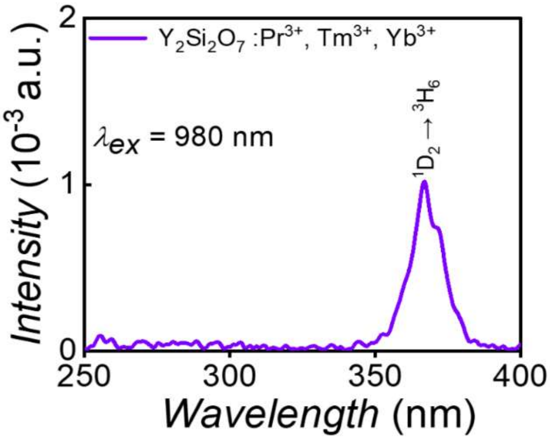

Fig. 72. NIR-to-UV UC emission spectra for $Y_2Si_2O_7$:Pr^{3+},Tm^{3+},Yb^{3+} induced upon 980 nm laser excitation

The incorporation of Tm^{3+} ions into the host matrix provided an additional narrow band at ca. 370 nm, ascribable as $^1D_2 \rightarrow {}^3H_6$ transition occurring in Tm^{3+} ions energy structure. As already mentioned above, its occurrence had to be preceded with ET from the Pr^{3+} ions sensitized by 447 nm photons. Interestingly, the addition of Yb^{3+} ions allowed to shift the excitation wavelength from Vis to NIR spectral range, however, under the 980 nm excitation the up-converted emission fell only in UV-A range, i.e., NIR-to-UV UC emission occurred (Fig. 72). The excited Yb^{3+} ions were capable to perform multiple ET to Tm^{3+} ions, resultant in only one band at ca. 370 nm, associated with $^1D_2 \rightarrow {}^3H_6$ electronic transition (for the mechanism see energy level structures of Tm^{3+} and Yb^{3+} ions in Fig. 66b). In this spectrum no emission coming from Pr^{3+} ions was observed due to the energy mismatch between the photons energy and corresponding energy levels in these ions. The similar conclusion was provided for Pr^{3+},Yb^{3+} co-doped $LiYF_4$ and β-$NaYF_4$ NPs, which was thoroughly described in Chapter 4.

8.4.3. Microbial inactivation studies – planktonic cells

Since the spectroscopic measurements revealed the capability of lanthanide-doped $Y_2Si_2O_7$ silicates to generate UV emission upon Vis or NIR irradiation, the prospective application for light-triggered disinfection was suggested. Therefore, their germicidal performance was validated in a series of proof-of-concept experiments. For the first biological study four different microorganisms in planktonic form were selected: *A. baumannii*, *B. cereus, S. aureus*, and *C. albicans*.

The control samples (exhibiting 100% viability) were the microbial inocula incubated in the dark without the synthesized $Y_2Si_2O_7$ silicates (neither undoped nor lanthanide-doped). The experiment was preceded with the cell viability evaluation upon the irradiation with the 447 nm laser beam. The laser light dose of 350 J cm^{-2} caused no significant cytotoxic effect in the studied microbial cells (mortality rate did not exceed 15 ± 3% for each cell culture). Therefore, it was chosen as the maximal laser light dose to which the cells can be exposed. In the next step, the dark cytotoxicity of the synthesized materials was validated. As presented in Table 20, the cytotoxic effect against the planktonic cells incubated with the compounds, revealed by BacTiter-Glo™ test [215], was in the vast majority of cases statistically insignificant – the mortality usually reached up to 10÷12%. Therefore, 30 mg was the highest amount of each material to be placed into wells.

Table 20. Dark cytotoxicity studies of undoped $Y_2Si_2O_7$, $Y_2Si_2O_7:Pr^{3+}$, and $Y_2Si_2O_7:Pr^{3+},Tm^{3+},Yb^{3+}$ on B. cereus, A. baumannii, S. aureus, and C. albicans in planktonic form

		B. cereus			***A. baumannii***			***S. aureus***			***C. albicans***		
Investigated phosphor	Incubation time [h] / Concentration [mg per well]	1	4	8	1	4	8	1	4	8	1	4	8
undoped $Y_2Si_2O_7$	5	96 ± 3	93 ± 2	91 ± 3	96 ± 2	94 ± 2	94 ± 2	93 ± 3	90 ± 3	90 ± 3	94 ± 2	92 ± 2	91 ± 2
	15	92 ± 3	91 ± 2	89 ± 3	92 ± 2	91 ± 2	90 ± 2	91 ± 2	90 ± 2	88 ± 3	91 ± 2	87 ± 2	82 ± 2
	30	90 ± 3	89 ± 2	86 ± 3	90 ± 3	88 ± 2	86 ± 2	90 ± 2	87 ± 2	86 ± 2	90 ± 2	87 ± 2	86 ± 2
$Y_2Si_2O_7:Pr^{3+}$	5	86 ± 2	86 ± 2	82 ± 2	91 ± 2	90 ± 2	90 ± 2	90 ± 2	88 ± 2	86 ± 2	90 ± 2	86 ± 2	86 ± 2
	15	84 ± 2	84 ± 2	80 ± 3	86 ± 3	86 ± 3	86 ± 3	83 ± 2	83 ± 2	84 ± 3	90 ± 2	86 ± 3	85 ± 2
	30	80 ± 2	80 ± 2	80 ± 3	84 ± 2	84 ± 2	82 ± 2	82 ± 2	80 ± 2	80 ± 2	89 ± 2	86 ± 2	86 ± 2
$Y_2Si_2O_7:Pr^{3+},Tm^{3+},Yb^{3+}$	5	83 ± 3	81 ± 3	80 ± 3	91 ± 2	91 ± 2	90 ± 2	88 ± 2	86 ± 2	84 ± 2	89 ± 2	86 ± 2	82 ± 2
	15	80 ± 3	79 ± 3	76 ± 3	88 ± 2	85 ± 2	86 ± 2	84 ± 2	82 ± 2	81 ± 2	86 ± 2	83 ± 2	80 ± 2
	30	75 ± 3	70 ± 3	70 ± 3	86 ± 2	82 ± 2	81 ± 2	82 ± 2	80 ± 3	80 ± 2	82 ± 2	80 ± 2	80 ± 3

The planktonic cells photoeradication in the presence of Vis-to-UV up-converting lanthanide-doped $Y_2Si_2O_7$ powders (Fig. 73a-h) was carried out under the illumination with the monochromatic 447 nm radiation generated by the unfocused CW laser diode at the output power of 650 mW. There were two various laser light doses chosen, estimated at 250 J cm^{-2} and 350 J cm^{-2}. The results were strongly dependent on the tested material, its concentration in a well, and the irradiation time.

Primarily, the samples were shown to exhibit significant cytotoxic activity against the planktonic culture of *A. baumannii*. With 15 mg of material in each well (Fig. 73a), the exposure to 250 J cm^{-2} reduced the bacterial cell viability by 53.0 ± 1.6%, 29.5 ± 0.9%, and 64.5 ± 1.9% for undoped $Y_2Si_2O_7$, $Y_2Si_2O_7$:Pr^{3+}, and $Y_2Si_2O_7$:Pr^{3+}, Tm^{3+},Yb^{3+}, respectively. The exposure to 350 J cm^{-2} raised the cell mortality to 63.0 ± 1.9%, 39.0 ± 1.2%, and 71.0 ± 2.1% for the corresponding silicates. In comparison with 30 mg of the material per well (Fig. 73b), the irradiation with 250 J cm^{-2} light dose resulted in the reduction in bacterial cells by 85.7 ± 2.6% (undoped $Y_2Si_2O_7$), 83.7 ± 2.6% ($Y_2Si_2O_7$:Pr^{3+}), and 94.2 ± 2.8% ($Y_2Si_2O_7$:Pr^{3+},Tm^{3+},Yb^{3+}). However, the additional light dose of 100 J cm^{-2} (i.e., the total light dose reaching 350 J cm^{-2}) increased cell mortality to a small extent, i.e., to 88.8 ± 2.7%, 86.5 ± 2.6%, and 98.4 ± 3.0%, correspondingly.

The positive photoeradication effect was also demonstrated on *B. cereus* planktonic cells. With 15 mg per each well (Fig. 73c), the photoinduced treatment with the 250 J cm^{-2} light dose reduced the cell count by 53.0 ± 1.6%, 40.5 ± 1.2%, and 76.5 ± 2.3% for $Y_2Si_2O_7$, $Y_2Si_2O_7$:Pr^{3+}, and $Y_2Si_2O_7$:Pr^{3+},Tm^{3+},Yb^{3+}, correspondingly, whereas the exposure to the light dose of 350 J cm^{-2} slightly increased the mortality to 63.5 ± 1.9%, 51.3 ± 1.5%, and 85.6 ± 2.6%, respectively. On the contrary, the addition of 30 mg of the chosen compounds per well (Fig. 73d) and the absorption of 250 J cm^{-2} light dose yielded the mortality rates of 65.3 ± 2.0%, 42.1 ± 1.3%, and 84.8 ± 2.5% for the undoped, the Pr^{3+}-doped, and the Pr^{3+},Tm^{3+},Yb^{3+}-co-doped silicates, respectively. The exposure to the additional light dose of 100 J cm^{-2} (i.e., 350 J cm^{-2} in total) further reduced the cell counts by 68.5 ± 2.1%, 56.1 ± 1.7%, and 95.1 ± 2.9%, consequently.

Since the materials emitted UV radiation upon the exposition to Vis laser beam, the inocula of *C. albicans* yeast cells were also partially annihilated. As 15 mg per well was utilized (Fig. 73e), the 250 J cm^{-2} light dose laser treatment reduced the cell counts by 33.5 ± 0.6%, 18.7 ± 0.6%, and 75.8 ± 2.3% for the undoped, the Pr^{3+}-doped, and the Pr^{3+},Tm^{3+},Yb^{3+}-co-doped silicates, respectively. The irradiation with the total light dose of 350 J cm^{-2} raised the cell mortality to 39.0 ± 1.2%, 21.0 ± 0.9%, and 80.9 ± 2.4%, correspondingly. Additionally, when the materials in the amount of 30 mg per well were used (Fig. 73f), the cell death rates at 80.4 ± 2.4%, 19.7 ± 0.6%, and 77.5 ± 2.3% for undoped $Y_2Si_2O_7$, $Y_2Si_2O_7{:}Pr^{3+}$, and $Y_2Si_2O_7{:}Pr^{3+},Tm^{3+},Yb^{3+}$ were achieved for the illumination with the 250 J cm^{-2} light dose whereas the one with the 350 J cm^{-2} light dose led to the slightly elevated mortality rates of 81.1 ± 2.4%, 31.9 ± 1.0%, and 81.0 ± 2.4%.

Lastly, the impact of the Vis-radiation-triggered germicidal action on Gram-positive *S. aureus* planktonic was shown. The cell reduction of 35.5 ± 1.1%, 22.0 ± 0.7%, and 76.3 ± 2.3% for the 250 J cm^{-2} light dose and of 40.0 ± 1.2%, 20.0 ± 0.6%, and 80.3 ± 2.4% for the 350 J cm^{-2} light dose was observed, as 15 mg per well of the undoped, the Pr^{3+}-doped, and the Pr^{3+},Tm^{3+},Yb^{3+}-co-doped silicates were utilized (Fig. 73g). As 30 mg per well of these materials was used (Fig. 73h), the 38.5 ± 1.2%, 22.5 ± 0.7%, and 80.3 ± 2.4% of the cells population was dead, having been exposed to the laser light dose of 250 J cm^{-2} in the presence of $Y_2Si_2O_7$, $Y_2Si_2O_7{:}Pr^{3+}$, and $Y_2Si_2O_7{:}Pr^{3+},Tm^{3+},Yb^{3+}$ powders. Extending the exposition to the total light dose of 350 J cm^{-2} led to the slight death rate increase, i.e., to 45.5 ± 1.4%, 27.5 ± 0.8%, and 86.0 ± 2.6%, respectively.

As provided above, photoeradication of bacteria and eukaryotic cells in the planktonic form in the presence of lanthanide-doped $Y_2Si_2O_7$ silicates is efficient. The gathered data prove that the UV radiation generated through UC allows to destroy plankton. $Y_2Si_2O_7{:}Pr^{3+}$ phosphor operates well as a light-triggered disinfectant, emitting UV-C radiation upon 447 nm excitation, however, the co-incorporation of Tm^{3+} ions into the host matrix significantly enhances the germicidal performance due to the emission of an additional UV-A band. The remarkable performance of $Y_2Si_2O_7{:}Pr^{3+},Tm^{3+},Yb^{3+}$ phosphor should be highlighted here, since 30 mg of this compound was capable to inactivate almost 98% of *A. baumannii* cells present in the inoculum after the exposition to 447 nm radiation with the total light dose of 350 J cm^{-2}.

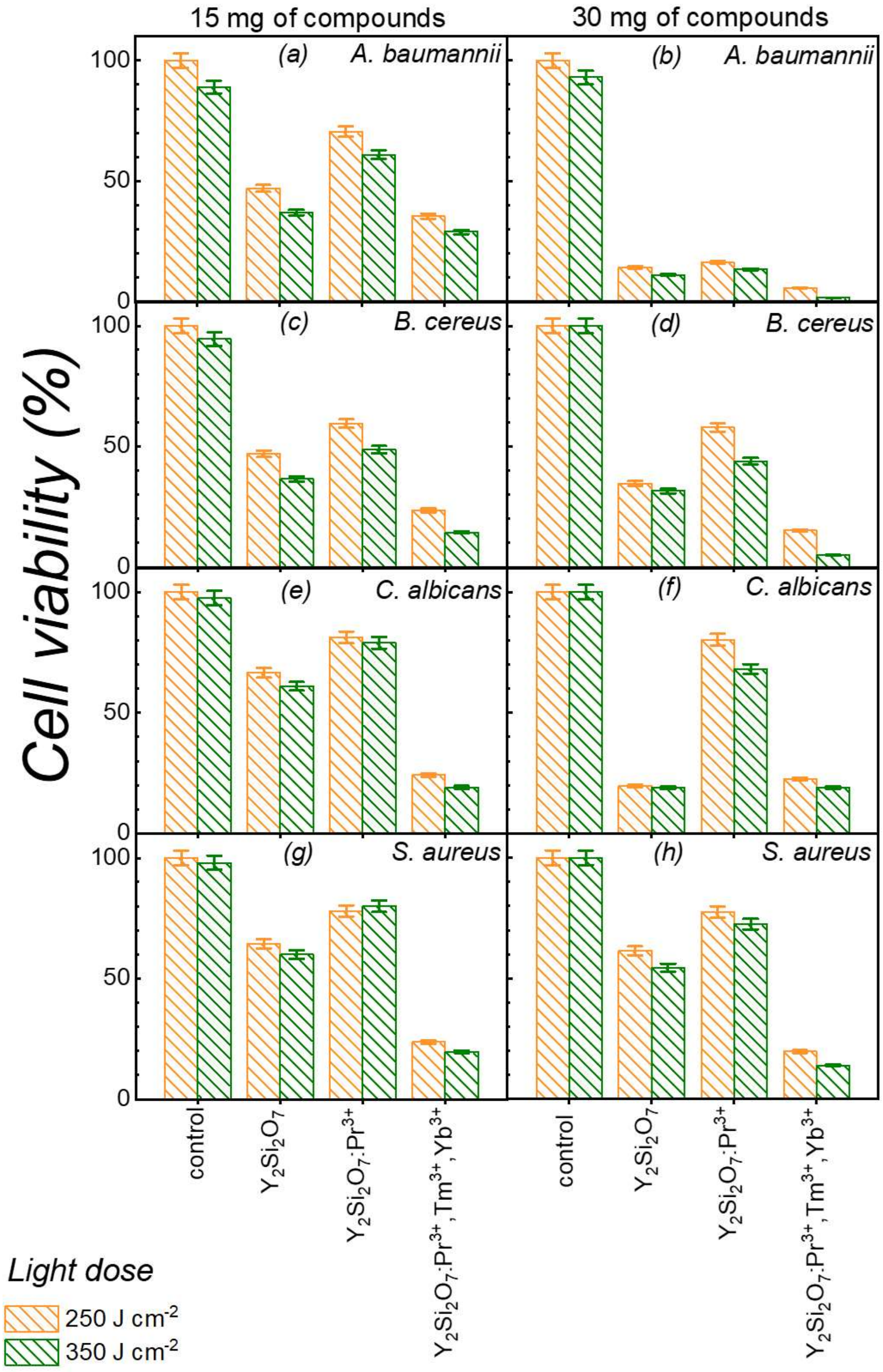

Fig. 73. The effect of the exposition to 447 nm CW laser at 250 J cm^{-2} (orange bars) and 350 J cm^{-2} (green bars) on the viability of (a,b) A. baumannii, (c, d) B. cereus, (e, f) C. albicans and (g, h) S. aureus in the presence of 15 mg (left column) or 30 mg (right column) of undoped $Y_2Si_2O_7$, $Y_2Si_2O_7:Pr^{3+}$, and $Y_2Si_2O_7:Pr^{3+},Tm^{3+},Yb^{3+}$

8.4.4. Microbial inactivation studies – biofilm

In harsh conditions (i.e., lowered humidity, insufficient nutrients concentration, or presence of toxic substances) planktonic microbes tend to transform to biofilm. In such formation the cells are adhered to each other and embedded into a self-produced extracellular polymeric material, which helps them to both attach to surface and survive in the unfavorable environment. As a rule, the produced protective barrier hinders the penetration of antibiotics and disinfectants through the system [224–226]. It makes biofilm eradication more cumbersome in comparison with the one of planktonic cells, hence this formation is more eagerly employed by scientists to study the nature of microbial growth in various conditions [227].

Therefore, within the presented research scope, the synthesized lanthanide-doped $Y_2Si_2O_7$ silicates were also utilized in light-triggered germicidal action against three different microorganisms – *S. aureus*, *A. baumannii*, and *C. albicans*, incubated in biofilm form. The experiment was preceded with the cell viability evaluation upon the irradiation with the 447 nm and 980 nm laser diodes. It was stated that the exposure to total laser light dose of 500 J cm^{-2} for 447 nm radiation and 300 J cm^{-2} for 980 nm radiation caused no significant photocytotoxic effect in all studied biofilm-forming cells (mortality rate did not exceed 14 ± 2% for each cell culture, the detailed results were not shown). In the next step, the dark cytotoxicity of the synthesized materials was validated. As presented in Table 21, the cytotoxic effect against the biofilms incubated with the compounds, revealed by MTT test [216], was in the vast majority of cases statistically insignificant – the mortality reached up to 12÷14%.

Table 21. Dark cytotoxicity studies of undoped $Y_2Si_2O_7$, $Y_2Si_2O_7:Pr^{3+}$, and $Y_2Si_2O_7:Pr^{3+},Tm^{3+},Yb^{3+}$ on A. baumannii, S. aureus, and C. albicans in biofilm form

		A. baumannii			***S. aureus***			***C. albicans***		
Investigated phosphor	Incubation time [h] / Concentration [mg per well]	1	4	8	1	4	8	1	4	8
undoped $Y_2Si_2O_7$	5	97 ± 3	97 ± 3	95 ± 3	96 ± 2	95 ± 2	96 ± 2	96 ± 2	96 ± 3	94 ± 3
	15	93 ± 3	94 ± 3	93 ± 3	93 ± 2	96 ± 2	94 ± 2	93 ± 3	91 ± 3	92 ± 3
	30	93 ± 2	91 ± 2	90 ± 2	92 ± 2	91 ± 3	92 ± 3	92 ± 2	92 ± 2	93 ± 3
$Y_2Si_2O_7:Pr^{3+}$	5	93 ± 2	93 ± 2	93 ± 3	92 ± 2	91 ± 2	91 ± 3	91 ± 2	90 ± 2	90 ± 2
	15	90 ± 2	90 ± 2	90 ± 2	92 ± 2	92 ± 3	92 ± 2	91 ± 2	90 ± 3	90 ± 3
	30	86 ± 2	85 ± 3	86 ± 3	90 ± 2	90 ± 3	90 ± 3	90 ± 2	86 ± 2	88 ± 3
$Y_2Si_2O_7:Pr^{3+},Tm^{3+},Yb^{3+}$	5	90 ± 3	90 ± 3	90 ± 3	90 ± 2	90 ± 3	88 ± 2	90 ± 2	90 ± 3	90 ± 2
	15	90 ± 2	87 ± 2	96 ± 2	90 ± 2	90 ± 2	83 ± 2	88 ± 2	86 ± 2	86 ± 2
	30	89 ± 3	86 ± 2	85 ± 2	88 ± 2	85 ± 2	80 ± 2	86 ± 2	86 ± 2	85 ± 3

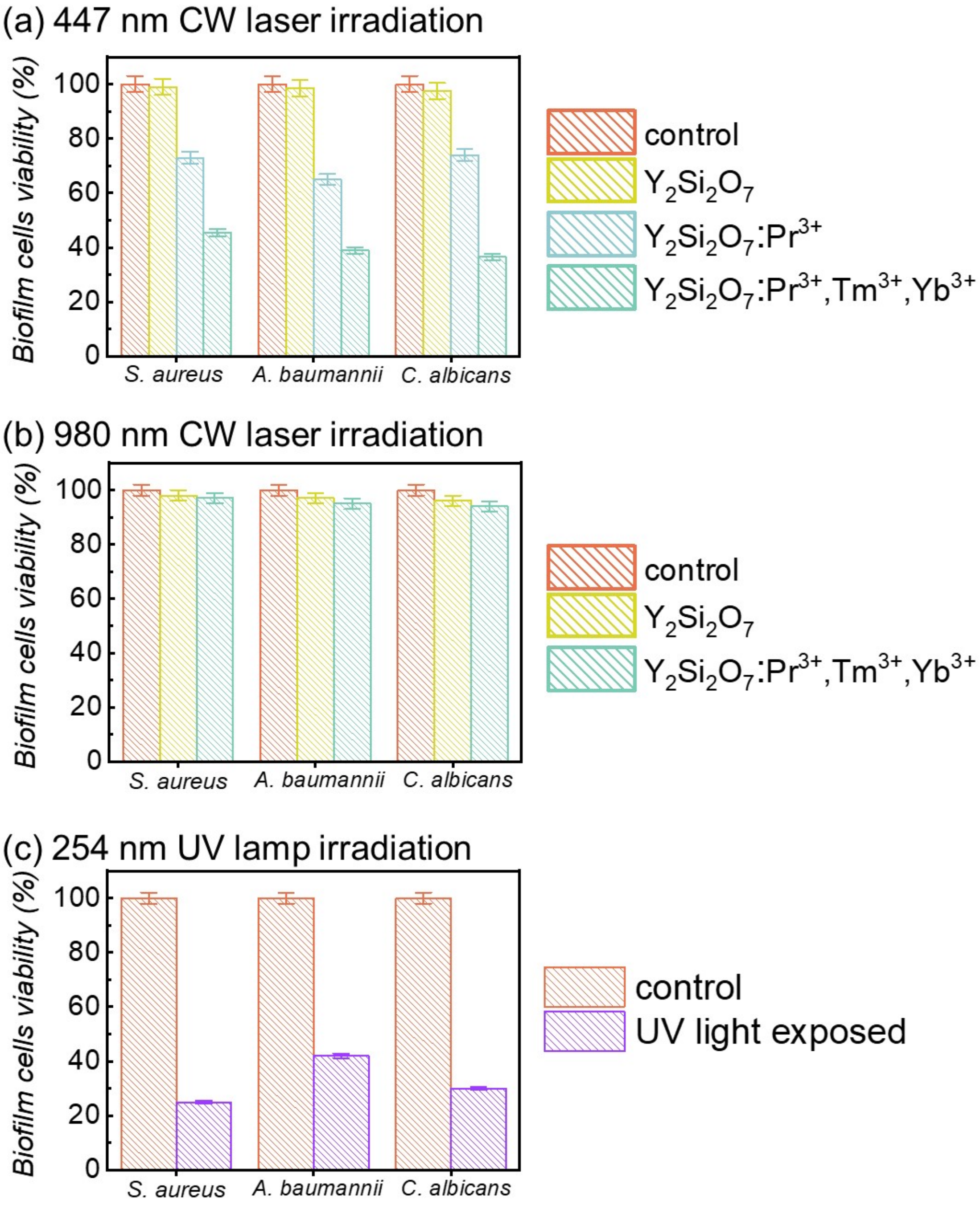

Fig. 74. Biofilm cells viability (S. aureus, A. baumannii, and C. albicans) after exposition to laser diodes (a) 447 nm, total light dose 500 J cm^{-2} and (b) 980 nm, total light dose 300 J cm^{-2} in the presence of undoped $Y_2Si_2O_7$, $Y_2Si_2O_7:Pr^{3+}$, and $Y_2Si_2O_7:Pr^{3+},Tm^{3+},Yb^{3+}$ phosphors (30 mg per well) and without them (control represents non-irradiated cells viability, 100%). (c) Biofilm cells viability after the exposition for 10 minutes to a UV light emitting lamp (254 nm) was evaluated for the comparison

The control samples (exhibiting 100% viability) were the microbials incubated in dark without the synthesized silicates (neither undoped nor lanthanide-doped). The biofilm photoeradication in the presence of 30 mg per well of Vis/NIR-to-UV up-converting $Y_2Si_2O_7$ powders was conducted with the 447 nm laser radiation, delivering the total light dose of 500 J cm^{-2}. As presented in Fig. 74a, the cytotoxicity rate strongly depended on the tested material type. For the solely Pr^{3+}-doped powders the viability was noticeably reduced (falling between 65÷75% for each microorganism type), however, the most significant was observed in the presence of $Y_2Si_2O_7$:Pr^{3+},Tm^{3+},Yb^{3+} phosphor. As it was utilized as a source of up-converted UV light, the viability dropped down to 45.5 ± 2.5%, 39.0 ± 3.0%, and 36.5 ± 2.5% for *S. aureus*, *A. baumannii,* and *C. albicans*, respectively. Interestingly, these values are really close to the ones obtained after the direct irradiation with a UV-emitting lamp operating at 254 nm without the studied silicate powders (Fig. 74c). The reduction in the number of viable biofilm-forming cells dropped by 75.0 ± 2.0% (*S. aureus*), 58.0 ± 2.1% (*A. baumannii*), and 70.0 ± 1.9% (*C. albicans*). It is concludable that the prolonged irradiation time of $Y_2Si_2O_7$:Pr^{3+},Tm^{3+},Yb^{3+} with Vis radiation might significantly reduce the biofilm viability. Therefore, this lanthanide-doped material could be applied in the self-sterilizing photo-activated surfaces, simultaneously being safe for human health.

The enhanced germicidal action could be the cause of the additional emission band from Tm^{3+} ions, peaking in UV-A spectral range (~370 nm), which could excite endogenous protoporphyrins to generate ROS such as hydroxyl radicals and H_2O_2 [10,11]. In order to verify this hypothesis, it was decided to conduct an additional experiment on oxidative stress detection in the bacterial cells after irradiation with 447 nm of the total light dose of 500 J cm^{-2} (Fig. 75). The yield of generated ROS increased by 54 ± 2% for $Y_2Si_2O_7$:Pr^{3+} powder in comparison with the control sample (biofilm without irradiation). It suggests that the photocytotoxicity of the Pr^{3+}-only-doped material combined dsDNA damage (by UV-C radiation) and ROS generation (by UV-A radiation), with the significant predominance of the latter. The application of the Tm^{3+}-co-doped sample resulted in more intense ROS production within microbial cells (70 ± 2%), which

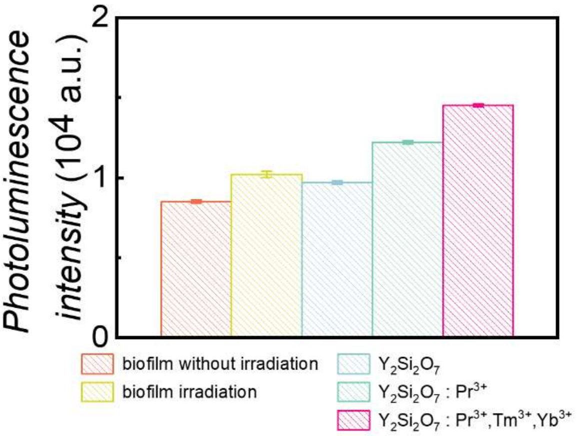

Fig. 75. Effectiveness of ROS generation in biofilm irradiated by 447 nm CW laser diode (power density: 800 mW cm^{-2}) in the presence of the presence of undoped $Y_2Si_2O_7$, $Y_2Si_2O_7$:Pr^{3+}, and $Y_2Si_2O_7$:Pr^{3+},Tm^{3+},Yb^{3+}phosphors

confirmed the reason standing for the enhanced Vis-to-UV UC-driven photoeradication performance.

As already proven within the research scope, the concurrent incorporation of Yb^{3+} ions into $Y_2Si_2O_7$ silicates opens up the possibility to exploit NIR photons instead of Vis radiation for UC process to generate UV-A radiation. Such a shift could be utilized for biological applications in which the incident radiation has to pass the tissue or flesh, impenetrable by Vis photons [157]. Therefore, the NIR-to-UV UC-emission-driven photoeradication of biofilm cells was conducted as a proof-of-concept experiment (Fig. 74b). Since the 980 nm wavelength used in this experiment tends to be absorbed by water, low excitation power density of ~500 mW cm^{-2} was applied to avoid biofilm heating. Consequently, the mortality rate of the tested biofilms in the presence of Pr^{3+},Tm^{3+},Yb^{3+}-co-doped material reached ~6%, which actually was comparable with the measurement uncertainty. In other words, after the absorption of ca. 300 J cm^{-2} NIR radiation dose no significant changes in biofilm cells viability was observed. Such low efficiency of NIR-triggered disinfection could be connected with the fact that NIR-to-UV UC requires multiple photons to be absorbed within the ladder-like structure of lanthanide ions, which actually requires high-power radiation.

8.5. Conclusions

In this chapter, I synthesized and characterized a series of Pr^{3+}-based Vis-to-UV up-converting $Y_2Si_2O_7$ powders for prospective light-triggered antimicrobial inactivation applications. The particular emphasis in the research scope was placed on investigation how lanthanide-ions co-doping influences on spectral characteristics in UV range.

In sol-gel synthesis Tm^{3+} ions were incorporated into the silicate host matrix along with Pr^{3+} ions to enhance Vis-to-UV UC emission, while Yb^{3+} ions were added to unlock NIR-to-UV UC emission. Based on the Rietveld analysis of the collected XRD data, I assigned the powders to the $Y_2Si_2O_7$ host matrix, however, the synthesized materials were the mixture of its polymorphs, since obtaining pure ones is reported in the literature as cumbersome. The captured SEM images and EDS maps confirmed the homogenous distribution of lanthanide ions throughout the samples. In the next step, I investigated UV emission resultant from the sequential absorption of two Vis photons. The incorporation of Tm^{3+} ions into Pr^{3+}-doped powder revealed the Vis-to-UV UC emission falling in both

UV-A and UV-C spectral regions, contrarily to the solely Pr^{3+}-doped one, exhibiting emission exclusively in UV-C range. The emission of up-converted UV-A band at ca. 370 nm from Tm^{3+} ions was preceded with the ET from the already excited Pr^{3+} ions to Tm^{3+} ions in their ground state, which was experimentally confirmed by the shortened values of the Tm^{3+}:$^3P_0$ excited state LT. As Yb^{3+} ions were sensitized with NIR photons, ET occurred only to Tm^{3+} ions, leading to the aforementioned UV-A band emission and no emission from Pr^{3+} ions was revealed due to energy mismatch between energy levels of both lanthanides.

The collected spectra showed the up-converted UV radiation enhancement and the possibility to switch the excitation wavelength from 447 nm (Vis spectral range) to 980 nm (NIR spectral range), as $Y_2Si_2O_7$:Pr^{3+},Tm^{3+},Yb^{3+} was utilized. Knowledgeable on both interactions of each UV radiation subtype with cell organelle and all possibly induced damages, I decided to employ the synthesized phosphors in a series of proof-of-concept biological experiments. Planktonic cells and biofilms of commonly known and microbials (*A. baumannii*, *S. aureus*, *B. cereus*, and *C. albicans*), dangerous for immunosuppressed people, were exposed in the presence of lanthanide-doped silicates to the unfocused beams emitted by CW Vis or NIR laser diodes. Consequently, the UV radiation generated *in situ* upon Vis excitation was able to damage microorganisms not only in planktonic form, but also in the developed biofilms. As previously noted, the incorporated Tm^{3+} ions emitted UV-A radiation, which increased the ROS concentration in the irradiated cells. This process led to a marked increase in the mortality rates of all targeted microbial species, even to as low as 2% for the planktonic cells of *A. baumannii.* On the contrary, NIR-to-UV UC-driven photoeradication of biofilms was not successful as there was a scarce reduction in the cells viability, comparable with the measurement error. Such low efficiency could be connected with the nature of NIR-to-UV UC as the sequential absorption of multiple photons within ladder-like energy level structure requires sources of higher power density within the excitation spot (e.g., focused laser beams). Therefore, high efficiency of light-triggered disinfection was more efficient for Vis-to-UV UC, in which only two photons are needed.

It is worth noting that the mortality rate for the triply-co-doped compound exposed to the 447 nm laser radiation of the 500 J cm^{-2} light dose was comparable to the one registered for biofilm eradication with a UV lamp emitting at 254 nm wavelength operating for 10 min. If the newly developed lanthanide-based powders exhibited the anti-Stokes emission in UV range of higher magnitude, they would present strong competition against UV lamps in real-life biocidal applications, especially in terms of human health safety. For instance, the self-sterilizing surface created by embedding such phosphors into non-toxic polymer matrix could be either perpetually triggered with low-intensity ambient light or on-demand activated with the unfocused Vis laser light. Such a non-chemical microbial inactivation method could be applied even in the presence of humans, providing constant sanitizing effect. Therefore, these findings indicate that the development of lanthanide-doped phosphors technology is strongly desired.

8.6. Acknowledgments and comments

This chapter is partially based on the data presented in the research paper *Enhanced biocidal activity of* Pr^{3+}*-doped yttrium silicates by* Tm^{3+} *and* Yb^{3+} *co-doping.* **P. Falat,** M.Y. Tsang, I.H. Maliszewska, S.J. Zelewski, B. Cichy, T.Y. Ohulchanskyy, M. Samoć, M. Nyk, D. Wawrzyńczyk. Material Advances 4, 2023, pp. 5827-5837.

Within the presented research I optimized the lanthanide ions molar concentration and synthesized $Y_2Si_2O_7$, $Y_2Si_2O_7:Pr^{3+}$, and $Y_2Si_2O_7:Pr^{3+},Tm^{3+},Yb^{3+}$ powders. I conducted the Rietveld refinement of the obtained XRD patterns with the invaluable help of B. Cichy. I captured the Vis/NIR-to-UV UC emission spectra and luminescence decay curves in UV spectral range on the optical setup, which had been assembled by S.J. Zelewski, whereas the studies on Vis-to-Vis Stokes emission and luminescence LTs curves in Vis range were performed on the courtesy of B. Cichy. The verification of the synthesized phosphors germicidal performance and their ROS generation ability with the detailed data analysis were delivered by I.H. Maliszewska.

Chapter 9

Final remarks and future perspectives

9.1. Conclusions

In the presented doctoral dissertation, I focused on the synthesis of lanthanide-doped materials at the nano- and micro-scale, and on the characterization of their luminescent properties for potential biomedical applications. I explored how these materials could be tailored for advanced applications such as high-contrast deep-tissue *in vivo* bioimaging and light-triggered disinfection that is safe for human use.

Firstly, I investigated Pr^{3+},Yb^{3+}-co-doped β-$NaYF_4$ and $LiYF_4$ NPs, demonstrating their dual functionality for Vis-to-UV UC-based dsDNA degradation and NIR-to-NIR DC emission-based *in vivo* bioimaging. Under 447 nm laser excitation, the materials exhibited strong up-converted UV-C emission from Pr^{3+} ions, intense enough to damage dsDNA, as confirmed in proof-of-concept experiments using two independent methods. Conversely, the NIR DC emission facilitated effective *in vivo* bioimaging of a channel drilled in a bovine tooth and overlaid with muscle tissue. Interestingly, the high values of LTs for the chosen Pr^{3+},Yb^{3+}co-doped β-$NaYF_4$ and $LiYF_4$ NPs (ca. 100 μs), highlight their prospective use in time-gated bioimaging.

In the next stage, I investigated various strategies to enhance Vis-to-UV UC luminescence in Pr^{3+}-doped β-$NaYF_4$ and $LiYF_4$ NPs and MCs. By co-doping with another type of lanthanide ion, i.e., Gd^{3+}, and by constructing active-core@inert-shell nanostructures, I significantly enhanced the up-converted UV-C luminescence intensity, making these materials even more effective for light-triggered disinfection, as demonstrated using the FADU assay. Furthermore, experimental evidence confirmed their ability to inactivate human viruses (adenovirus HAdV-C5 and herpes simplex virus HSV-1) upon UV light exposure, showing their utility in light-driven germicidal applications.

Later on, I extended my research to design and synthesis of core@multi-shell β-$NaYF_4$ nanostructures. In this part, I investigated how the spatial distribution of optically active lanthanide ions within nanomaterials of complex architecture can simultaneously enhance emissions in both UV and NIR spectral regions. The results suggest that it is a promising approach for developing multifunctional nanoplatforms that integrate diagnostic NIR bioimaging and UV-based therapeutic capabilities within a single nanosystem.

I also investigated how co-doping of Pr^{3+} ions into β-$NaYF_4$:Tm^{3+} MCs can influence on their concurrent anti-Stokes UV and Stokes NIR PL emissions, occurring under Vis irradiation. For this lanthanide ion pair, efficient ET between Pr^{3+} and Tm^{3+} ions occurred, which led to a noticeable increase in emission intensity in the UV and NIR spectral regions. This approach is valuable for designing lanthanide-doped inorganic phosphors with the potential application in theranostics.

Finally, in the last part of my research, I turned my focus to the development of Pr^{3+}-doped and Pr^{3+},Tm^{3+},Yb^{3+}-co-doped $Y_2Si_2O_7$ powders, which showed great promise for light-triggered antimicrobial applications. By harnessing VIS-to-UV UC, these materials were effective in the inactivation of common bacteria and fungi, responsible for hospital-acquired infections in immunosuppressed patients.

In conclusion, the research conducted within the presented doctoral dissertation shows novel strategies for enhancing luminescent properties of lanthanide-doped colloidal NPs and MCs in powdered form in UV and NIR spectral ranges. The successful utilization in proof-of-concept experiments, i.e., NIR-based *in vivo* bioimaging or light-triggered Vis-to-UV UC-based eradication of human viruses, bacteria, and fungi, portrays them as suitable candidates for real-life biomedical applications.

9.2. Future perspectives

The findings in this doctoral dissertation provide a solid basis for potential implementation of lanthanide-doped materials in advanced biomedical applications. However, continued development is still desired to improve their performance and expand their use in a wider range of fields. Future work should address the following areas:

- development of materials concurrently emitting in UV and NIR spectral regions, co-doped with other lanthanide ions: while I mainly focused on Pr^{3+} and Tm^{3+} ions, it is highly likely that there are other combinations of lanthanide ions that could exhibit PL of higher intensity in spectral regions of interest, when incorporated at optimized molar concentrations into host matrices. For instance, addition of Ho^{3+} or Er^{3+} ions along with Pr^{3+} ions into the host matrix could be an interesting choice as ET processes leading to UV emission enhancement may occur;

- selection of other host matrices: the choice of host matrix for lanthanide ions incorporation is crucial to obtain materials with luminescent properties of high efficiency. Although β-$NaYF_4$, $LiYF_4$, and $Y_2Si_2O_7$ were utilized in this study – the hosts proven to facilitate UC, there are other matrices of lower phonon cut-off energy, e.g., KPb_2X_5 ($\hbar\omega \approx 128\ \mathrm{cm}^{-1}$). It is highly probable that when co-doped with lanthanide ions at the same molar concentration, they can exhibit more intense UV and NIR emission, compared to alkali-metal-based yttrium fluorides counterparts;
- preparation for light-triggered disinfection: the synthesized Pr^{3+}-doped NPs and MCs exhibited promising results in light-activated bacterial and viral inactivation. Since they were utilized in the presented research as water dispersions, further processing is required to improve their functionality and applicability in real life. For instance, one can fabricate photoactive polymeric surfaces by embedding lanthanide-doped inorganic nano- and microphosphors, capable of Vis-to-UV UC, into polymers of high transparency in the region of interest. As a consequence, continuous, strongly localized antimicrobial effect with no simultaneous harm for human health would be observed, even under standard light sources (e.g., a halogen lamp or monochromatic LEDs). Interestingly, I am going to develop this idea within the three-year research project PRELUDIUM, funded by National Science Centre of Poland;
- integration with other functional nanostructures: one of the promising direction for future work is the co-doping or co-encapsulation of lanthanide-doped NPs with other functional NPs. For instance, integrating with plasmonic nanoparticles, such as Ag or Au NPs could enhance Vis-to-UV UC emission *via* plasmonic effects. Similarly, hybrid systems combining lanthanide-doped NPs with quantum dots (e.g., CdSe, CdS or CdTe) or magnetic NPs (e.g., Fe_3O_4) could create multifunctional nanoplatforms suitable for theranostics;
- design of multifunctional theranostic platforms: one could also explore the possibility of integrating these lanthanide-doped NPs and MCs with other therapeutic agents, such as photosensitizers for photodynamic therapy or targeted drug delivery systems. By combining diagnostic and therapeutic functionalities

in a single platform, these materials could provide advances in personalized medicine, offering more precise treatments with minimal side effects.

In conclusion, while the findings of this thesis lay a strong foundation for the development of lanthanide-doped NPs and MCs phosphors with enhanced optical properties for biomedical and photonics applications, there is still significant potential for further innovation. Future research should focus on improving their multifunctionality, optimizing their performance in biological environments, and exploring new composite materials that integrate other nanomaterials with unique properties.

References

[1] J. Zwinkels, *Light, Electromagnetic Spectrum*, in: *Encyclopedia of Color Science and Technology*, Springer Berlin Heidelberg, 2015, pp. 1–8. DOI: 10.1007/978-3-642-27851-8_204-1

[2] M. Beckers, B. Weise, S. Kalapis, T. Gries, G. Seide, C. A. Bunge, *Basics of light guidance*, in: *Polymer Optical Fibres: Fibre Types, Materials, Fabrication, Characterisation and Applications*, Elsevier Inc., 2017, pp. 9–46. DOI: 10.1016/B978-0-08-100039-7.00002-6

[3] E.G. Richard, *The Science and (Lost) Art of Psoralen Plus UVA Phototherapy*, Dermatol. Clin. 38(1) (2020), pp. 11–23. DOI: 10.1016/j.det.2019.08.002

[4] T. Kondo, S. Toya, K. Suzuki, H. Higashi, Y. Saito, *Characterization of Individual Widegap Semiconductor Nanoparticles by Ultraviolet Photoluminescence Microscopy*, J. Phys. Chem. C 128(30) (2024), pp. 12704–12710. DOI: 10.1021/acs.jpcc.4c03229

[5] H. Langhals, *Fluorescence and fluorescent dyes*, Phys. Sci. Rev. 5(8) (2020), article no. 20190100. DOI: 10.1515/psr-2019-0100

[6] A. Pérez-Sánchez, E. Barrajón-Catalán, M. Herranz-López, V. Micol, *Nutraceuticals for skin care: A comprehensive review of human clinical studies*, Nutrients 10(4) (2018), article no. 403. DOI: 10.3390/nu10040403

[7] A. Juzeniene, J. Moan, *Beneficial effects of UV radiation other than via vitamin D production*, Dermatoendocrinol. 4 (2012), pp. 109–117. DOI: 10.4161/derm.20013

[8] A.L. Santos, V. Oliveira, I. Baptista, I. Henriques, N.C.M. Gomes, A. Almeida, A. Correia, Â. Cunha. *Wavelength dependence of biological damage induced by UV radiation on bacteria,* Arch. Microbiol. 195 (2013), pp. 63–74. DOI: 10.1007/s00203-012-0847-5

[9] A. Pecorelli, G. Valacchi, *Oxidative-Stress-Sensitive microRNAs in UV-Promoted Development of Melanoma*, Cancers 14(13) (2022), article no. 3224. DOI: 10.3390/cancers14133224

[10] J.D. Hoerter, A.A. Arnold, D.A. Kuczynska, A. Shibuya, C.S. Ward, M.G. Sauer, A. Gizachew, T.M. Hotchkiss, T.J. Fleming, S. Johnson, *Effects of sublethal UVA irradiation on activity levels of oxidative defense enzymes and protein oxidation in Escherichia coli*, J. Photochem. Photobiol. B 81(3) (2005), pp. 171–180. DOI: 10.1016/j.jphotobiol.2005.07.005

[11] N. Zhao, L.P. Lv, P. Ma, Y.Y. Zhang, J. Deng, Y.Y. Zhang, *A novel exposure mode based on UVA-LEDs for bacterial inactivation*, J. Photochem. Photobiol. B 239 (2023), article no 112641. DOI: 10.1016/j.jphotobiol.2022.112641

[12] B. Dale Wilson, S. Moon, F. Armstrong, *Comprehensive Review of Ultraviolet Radiation and the Current Status on Sunscreens.* J. Clin. Aesthet. Dermatol. 5(9) (2012), pp. 18–23. PMID: 23050030

[13] X. Tang, T. Yang, D. Yu, H. Xiong, S. Zhang, *Current insights and future perspectives of ultraviolet radiation (UV) exposure: Friends and foes to the skin and beyond the skin*, Environ. Int. 185 (2024), article no. 108535. DOI: 10.1016/j.envint.2024.108535

[14] T. Dai, M.S. Vrahas, C.K. Murray, M.R. Hamblin, *Ultraviolet C irradiation: An alternative antimicrobial approach to localized infections?*, Expert Rev. Anti Infect. Ther. 10 (2012), pp. 185–195. DOI: 10.1586/eri.11.166

[15] H.J. Kim, H.W. Yoon, M.A. Lee, Y.H. Kim, C.J. Lee, *Impact of UV-C Irradiation on Bacterial Disinfection in a Drinking Water Purification System*, J. Microbiol. Biotechnol. 33(1) (2023), pp. 106–113. DOI: 10.4014/jmb.2211.11027

[16] Y. González, G. Gómez, G.E. Moeller-Chávez, G. Vidal, *UV Disinfection Systems for Wastewater Treatment: Emphasis on Reactivation of Microorganisms*, Sustainability 15(14) (2023), article no. 11262. DOI: 10.3390/su151411262

[17] T. Koutchma, *UV light for processing foods*, Ozone Sci. Eng. (2008), pp. 93–98. DOI: 10.1080/01919510701816346

[18] Z. Feng, T. Tang, T. Wu, X. Yu, Y. Zhang, M. Wang, J. Zheng, Y. Ying, S. Chen, J. Zhou, X. Fan, D. Zhang, S. Li, M. Zhang, J. Qian, *Perfecting and extending the near-infrared imaging window*, Light Sci. Appl. 10 (2021), article no. 197. DOI: 10.1038/s41377-021-00628-0

[19] M. Manley, *Near-infrared spectroscopy and hyperspectral imaging: Non-destructive analysis of biological materials*, Chem. Soc. Rev. 43(24) (2014), pp. 8200–8214. DOI: 10.1039/c4cs00062e

[20] T.W.L. Scheeren, P. Schober, L.A. Schwarte, *Monitoring tissue oxygenation by near infrared spectroscopy (NIRS): Background and current applications*, J. Clin. Monit. Comput. (2012), pp. 279–287. DOI: 10.1007/s10877-012-9348-y

[21] C. Gong, X. Xue, Q. Zhu, P. Li, X. Wang, J.G. Li, *Simultaneously strong NIR-II and NIR-III luminescence induced by* Cr^{3+}-Yb^{3+}-Er^{3+} *energy transfer in* $KScP_2O_7$

for NIR thermometry, NIR pc-LED and night-vision applications, Ceram. Int. A 50(19) (2024), pp. 35465–35473. DOI: 10.1016/j.ceramint.2024.06.358

[22] A.M. Smith, M.C. Mancini, S. Nie, *Bioimaging: Second window for in vivo imaging*, Nat. Nanotechnol. 4 (2009), pp. 710–711. DOI: 10.1038/nnano.2009.326

[23] X. Zhang, L. An, Q. Tian, J. Lin, S. Yang, *Tumor microenvironment-activated NIR-II reagents for tumor imaging and therapy*, J. Mater. Chem. B 8(22) (2020), pp. 4738–4747. DOI: 10.1039/d0tb00030b

[24] S. Wang, B. Li, F. Zhang, *Molecular Fluorophores for Deep-Tissue Bioimaging*, ACS Cent. Sci. 6(8) (2020), pp. 1302–1316. DOI: 10.1021/acscentsci.0c00544

[25] G. Chen, T.Y. Ohulchanskyy, A. Kachynski, H. Ågren, P.N. Prasad, *Intense visible and near-infrared upconversion photoluminescence in colloidal* $LiYF_4:Er^{3+}$ *nanocrystals under excitation at 1490 nm*, ACS Nano 5(6) (2011), pp. 4981–4986. DOI: 10.1021/nn201083j

[26] B. del Rosal, D.H. Ortgies, N. Fernández, F. Sanz-Rodríguez, D. Jaque, E.M. Rodríguez, *Overcoming Autofluorescence: Long-Lifetime Infrared Nanoparticles for Time-Gated In Vivo Imaging*, Adv. Mater. 28(46) (2016), pp. 10188–10193. DOI: 10.1002/adma.201603583

[27] F. Wang, D. Banerjee, Y. Liu, X. Chen, X. Liu, *Upconversion nanoparticles in biological labeling, imaging, and therapy*, Analyst 135(8) (2010), pp. 1839–1854. DOI: 10.1039/c0an00144a

[28] J.-C.G. Bünzli, S. V. Eliseeva, *Basics of Lanthanide Photophysics*, in: Lanthanide Luminescence (2010), pp. 1–45. DOI: 10.1007/4243_2010_3

[29] G. Tessitore, G.A. Mandl, S.L. Maurizio, M. Kaur, J.A. Capobianco, *The role of lanthanide luminescence in advancing technology*, RSC Adv. 13(26) (2023), pp. 17787–17811. DOI: 10.1039/d3ra00991b

[30] S. A. Cotton, *Lanthanide and Actinide Chemistry*, 3rd ed., John Wiley & Sons, 2009.

[31] S. Mohanty, M. Lederer, S. Premcheska, H. Rijckaert, K. De Buysser, E. Bruneel, A. Skirtach, K. Van Hecke, A.M. Kaczmarek, *Exploring the potential of lanthanide-doped oxyfluoride materials for bright green upconversion and their promising applications towards temperature sensing and drug delivery*, J Mater Chem C 12(31) (2024), pp. 11785–11802. DOI: 10.1039/d4tc01740d

[32] L. Aboshyan-Sorgho, M. Cantuel, S. Petoud, A. Hauser, C. Piguet, *Optical sensitization and upconversion in discrete polynuclear chromium-lanthanide*

complexes, Coord. Chem. Rev. 256(15-16) (2012), pp. 1644–1663. DOI: 10.1016/j.ccr.2011.12.013

[33] G.H. Dieke, H.M. Crosswhite, *The Spectra of the Doubly and Triply Ionized Rare Earths*, Appl. Opt. 2(7) (1963), pp. 675–686. DOI: 10.1364/AO.2.000675

[34] G. Blasse, B.C. Grabmaier, *Luminescent Materials*, Springer Verlag, Berlin (1994). DOI: 10.1007/978-3-642-79017-1

[35] M. H. V. Werts, *Making sense of lanthanide luminescence*, Sci. Prog. 88(2) (2005), pp. 101–131. DOI: 10.3184/003685005783238435

[36] Y. Fan, L. Liu, F. Zhang, *Exploiting lanthanide-doped upconversion nanoparticles with core/shell structures*, Nano Today 25 (2019), pp. 68–84. DOI: 10.1016/j.nantod.2019.02.009

[37] S. Wen, J. Zhou, K. Zheng, A. Bednarkiewicz, X. Liu, D. Jin, *Advances in highly doped upconversion nanoparticles*, Nat. Commun. 9 (2018), article no 2415. DOI: 10.1038/s41467-018-04813-5

[38] X. Chen, D. Peng, Q. Ju, F. Wang, *Photon upconversion in core-shell nanoparticles*, Chem. Soc. Rev. 44(6) (2015), pp. 1318–1330. DOI: 10.1039/c4cs00151f

[39] F. Auzel, *Upconversion and Anti-Stokes Processes with f and d Ions in Solids*, Chem. Rev. 104(1) (2004), pp. 139–173. DOI: 10.1021/cr020357g

[40] F. Auzel, *Materials and devices using double-pumped-phosphors with energy transfer*, Proc. IEEE Int. 61(6) (1973), pp. 758–786. DOI: 10.1109/PROC.1973.9155

[41] N. Bloembergen, *Solid state infrared quantum counters*, Phys. Rev. Lett. 2(3) (1959), pp. 84–85. DOI: 10.1103/PhysRevLett.2.84

[42] X. Cheng, D. Tu, W. Zheng, X. Chen, *Energy transfer designing in lanthanide-doped upconversion nanoparticles*, Chem. Commun. 56(96) (2020), pp. 15118–15132. DOI: 10.1039/d0cc05878e

[43] N.M. Idris, M.K.G. Jayakumar, A. Bansal, Y. Zhang, *Upconversion nanoparticles as versatile light nanotransducers for photoactivation applications*, Chem. Soc. Rev. 44(6) (2015), pp. 1449–1478. DOI: 10.1039/c4cs00158c

[44] X. Xia, E. Sivonxay, B.A. Helms, S.M. Blau, E.M. Chan, *Accelerating the Design of Multishell Upconverting Nanoparticles through Bayesian Optimization*, Nano Lett. 23(23) (2023), pp. 11129–11136. DOI: 10.1021/acs.nanolett.3c03568

[45] J. McKittrick, L.E. Shea-Rohwer, *Review: Down conversion materials for solid-state lighting*, J. Am. Ceram. Soc. 97(5) (2014), pp. 1327–1352. DOI: 10.1111/jace.12943

[46] W.W. Piper, J.A. Deluca, F.S. Ham, *Cascade fluorescent decay in Pr^{3+}-doped fluorides: achievement of a quantum yield greater than unity for emission of visible light*, J. Lumin. 8(4) (1974), pp. 344-348. DOI: 10.1016/0022-2313(74)90007-6

[47] J.L. Sommerdijk, A. Bril, A.W. De Jager, *Two photon luminescence with ultraviolet excitation of trivalent praseodymium*, J. Lumin. 8(4) (1974), pp. 341-343. DOI: 10.1016/0022-2313(74)90006-4

[48] R.T. Wegh, H. Donker, A. Meijerink, R.J. Lamminmäki, J. Hölsä, *Vacuum-ultraviolet spectroscopy and quantum cutting for Gd^{3+} in $LiYF_4$.* Phys. Rev. B 56(12) (1997), pp. 13841-13848. DOI: 10.1103/PhysRevB.56.13841

[49] W.T. Carnall, G.L. Goodman, K. Rajnak, R.S. Rana, *A systematic analysis of the spectra of the lanthanides doped into single crystal LaF_3*, J. Chem. Phys. 90 (1989), pp. 3443-3457. DOI: 10.1063/1.455853

[50] B.R. Judd, *Optical Absorption Intensities of Rare-Earth Ions,* Phys. Rev. 127(3) (1962), pp. 750–761. DOI: 10.1103/PhysRev.127.750

[51] G.S. Ofelt, *Intensities of crystal spectra of rare-earth ions*, J. Chem. Phys. 37 (1962), pp. 511–520. DOI: 10.1063/1.1701366.

[52] M.P. Hehlen, M.G. Brik, K.W. Krämer, *50th anniversary of the Judd-Ofelt theory: An experimentalist's view of the formalism and its application*, J. Lumin. 136 (2013), pp. 221–239. DOI: 10.1016/j.jlumin.2012.10.035.

[53] M. V. DaCosta, S. Doughan, Y. Han, U.J. Krull, *Lanthanide upconversion nanoparticles and applications in bioassays and bioimaging: A review*, Anal. Chim. Acta 832 (2014), pp. 1–33. DOI: 10.1016/j.aca.2014.04.030

[54] K.W. Krämer, D. Biner, G. Frei, H.U. Güdel, M.P. Hehlen, S.R. Lüthi, *Hexagonal Sodium Yttrium Fluoride Based Green and Blue Emitting Upconversion Phosphors,* Chem. Mater. 16(7) (2004), pp. 1244–1251. DOI: 10.1021/cm031124o

[55] A. Aebischer, M. Hostettler, J. Hauser, K. Krämer, T. Weber, H.U. Güdel, H.B. Bürgi, *Structural and spectroscopic characterization of active sites in a family of light-emitting sodium lanthanide tetrafluorides*, Angew. Chem., Int. Ed. 45(17) (2006), pp. 2802–2806. DOI: 10.1002/anie.200503966

[56] J. L. Sommerdijk, *Influence of the host lattice on the infrared-excited blue luminescence of Yb^{3+},Tm^{3+}-doped compounds*, *J. Lumin* **8** (1973), pp. 126–130. DOI: 10.1016/0022-2313(73)90095-1

[57] A.A. Ansari, A.K. Parchur, N.D. Thorat, G. Chen, *New advances in pre-clinical diagnostic imaging perspectives of functionalized upconversion nanoparticle-based nanomedicine*, Coord. Chem. Rev. 440 (2021), article no. 213971. DOI: 10.1016/j.ccr.2021.213971

[58] A. Gnach, T. Lipinski, A. Bednarkiewicz, J. Rybka, J.A. Capobianco, *Upconverting nanoparticles: Assessing the toxicity*, Chem. Soc. Rev. 44(6) (2015), pp. 1561–1584. DOI: 10.1039/c4cs00177j

[59] E.L. Cates, M. Cho, J.H. Kim, *Converting visible light into UVC: Microbial inactivation by Pr^{3+}-activated upconversion materials*, Environ. Sci. Technol. 45(8) (2011), pp. 3680–3686. DOI: 10.1021/es200196c

[60] A.I. Becerro, A. Escudero, P. Florian, D. Massiot, M.D. Alba, *Revisiting $Y_2Si_2O_7$ and Y_2SiO_5 polymorphic structures by ^{89}Y MAS-NMR spectroscopy*, J. Solid. State Chem. 177(8) (2004), pp. 2783–2789. DOI: 10.1016/j.jssc.2004.03.047

[61] J.L.B. Martin, L.F. Williams, M.F. Reid, J.P.R. Wells, *Growth and spectroscopy of lanthanide doped Y_2SiO_5 microcrystals for quantum information processing*, Opt. Mater. 142 (2023), article no. 114093. DOI: 10.1016/j.optmat.2023.114093

[62] Q. Su, S. Han, X. Xie, H. Zhu, H. Chen, C.K. Chen, R.S. Liu, X. Chen, F. Wang, X. Liu, *The effect of surface coating on energy migration-mediated upconversion*, J. Am. Chem. Soc. 134(51) (2012), pp. 20849–20857. DOI: 10.1021/ja3111048

[63] L. Marciniak, D. Hreniak, W. Stręk, F. Piccinelli, A. Speghini, M. Bettinelli, M. Miritello, R. Lo Savio, P. Cardile, F. Priolo, *Spectroscopic and structural properties of polycrystalline $Y_2Si_2O_7$ doped with Er^{3+}*, J. Lumin. 170(2) (2016), pp. 614–618. DOI: 10.1016/j.jlumin.2015.02.015

[64] S. Gai, C. Li, P. Yang, J. Lin, *Recent progress in rare earth micro/nanocrystals: Soft chemical synthesis, luminescent properties, and biomedical applications*, Chem. Rev. 114(4) (2014), pp. 2343–2389. DOI: 10.1021/cr4001594

[65] Z. Qiu, S. Wang, W. Wang, S. Wu. *Polymer Composites Entrapped Ce-Doped $LiYF_4$ Microcrystals for High-Sensitivity X-ray Scintillation and Imaging*. ACS Appl. Mater. Interfaces 12 (2020), pp. 29835–29843. DOI: 10.1021/acsami.0c07765.

[66] S.L. Cates, E.L. Cates, M. Cho, J.H. Kim, *Synthesis and characterization of visible-to-UVC upconversion antimicrobial ceramics*, Environ. Sci. Technol. 48(4) (2014), pp. 2290–2297. DOI: 10.1021/es405229p

[67] X. Gao, G. V. Lowry, *Progress towards standardized and validated characterizations for measuring physicochemical properties of manufactured nanomaterials relevant to nano health and safety risks*, NanoImpact 9 (2018), pp. 14–30. DOI: 10.1016/j.impact.2017.09.002

[68] Y. Zhong, H. Dai, *A mini-review on rare-earth down-conversion nanoparticles for NIR-II imaging of biological systems*, Nano Res. 13 (2020), pp. 1281–1294. DOI: 10.1007/s12274-020-2721-0.

[69] J. Ha, *Design and synthesis of phosphors to improve efficiency for solid state lighting application*, PhD dissertation, Materials Science & Engineering, University of California, San Diego, 2019. PDF available via UC eScholarship

[70] L. Aarts, B.M. Van Der Ende, A. Meijerink, *Downconversion for solar cells in* $NaYF_4$*:Er,Yb*, J. Appl. Phys. 106 (2009), article no. 023522. DOI: 10.1063/1.3177257

[71] M. Wang, G. Abbineni, A. Clevenger, C. Mao, S. Xu, *Upconversion nanoparticles: Synthesis, surface modification and biological applications*, Nanomedicine 7(6) (2011), pp. 710–729. DOI: 10.1016/j.nano.2011.02.013

[72] M. Haase, H. Schäfer, *Upconverting nanoparticles*, Angew. Chem., Int. Ed. 50(26) (2011), pp. 5808–5829. DOI: 10.1002/anie.201005159

[73] G. Chen, H. Qiu, P.N. Prasad, X. Chen, *Upconversion nanoparticles: Design, nanochemistry, and applications in Theranostics*, Chem. Rev. 114(10) (2014), pp. 5161–5214. DOI: 10.1021/cr400425h

[74] K. Prorok, A. Bednarkiewicz, B. Cichy, A. Gnach, M. Misiak, M. Sobczyk, W. Stręk, *The impact of shell host (*$NaYF_4/CaF_2$*) and shell deposition methods on the up-conversion enhancement in* Tb^{3+}*,* Yb^{3+} *codoped colloidal* α*-*$NaYF_4$ *core-shell nanoparticles*, Nanoscale 6(3) (2014), pp. 1855–1864. DOI: 10.1039/c3nr05412h

[75] J. Zhou, Z. Liu, F. Li, *Upconversion nanophosphors for small-animal imaging*, Chem. Soc. Rev. 41(3) (2012), pp. 1323–1349. DOI: 10.1039/c1cs15187h

[76] W. Shao, G. Chen, T.Y. Ohulchanskyy, A. Kuzmin, J. Damasco, H. Qiu, C. Yang, H. Ågren, P.N. Prasad, *Lanthanide-doped fluoride core/multishell nanoparticles*

for broadband upconversion of infrared light, Adv. Opt. Mater. 3(4) (2015), pp. 575–582. DOI: 10.1002/adom.201400404

[77] L. Wang, M. Lan, Z. Liu, G. Qin, C. Wu, X. Wang, W. Qin, W. Huang, L. Huang. *Enhanced deep-ultraviolet upconversion emission of* Gd^{3+} *sensitized by* Yb^{3+} *and* Ho^{3+} *in β-*$NaLuF_4$ *microcrystals under 980 nm excitation.* J. Mater. Chem. C. 1 (2013), pp. 2485–2490. DOI: 10.1039/c3tc00936j

[78] A.B. Andrade, G.F.C. Bispo, Z.S. Macedo, M.E.G. Valerio, *Synthesis and characterization of luminescent* Ln^{3+} *(Ln = Eu, Tb and Dy)-doped* $LiYF_4$ *microcrystals produced by a facile microwave-assisted hydrothermal method*, J. Lumin. 219 (2020), article no 116843. DOI: 10.1016/j.jlumin.2019.116843

[79] E. Andresen, F. Islam, C. Prinz, P. Gehrmann, K. Licha, J. Roik, S. Recknagel, U. Resch-Genger, *Assessing the reproducibility and up-scaling of the synthesis of Er,Yb-doped* $NaYF_4$*-based upconverting nanoparticles and control of size, morphology, and optical properties*, Sci. Rep. 13 (2023), article no. 2288. DOI: 10.1038/s41598-023-28875-8

[80] V.T. Tuyen, B.Q.V. Huy, N.B. Tong, T.T. Ngoc Lam, M. Ferrari, C.T. My Dung, U.T. Dieu Thuy, T.T.T. Van, *Controllable structural and optical properties of* $NaYF_4$*:Tm, Yb microparticles by* Yb^{3+} *doping for anti-counterfeiting*, RSC Adv. 13(28) (2023), pp. 19317–19324. DOI: 10.1039/d3ra02841k

[81] F. Wang, X. Liu, *Recent advances in the chemistry of lanthanide-doped upconversion nanocrystals*, Chem. Soc. Rev. 38(4) (2009), pp. 976–989. DOI: 10.1039/b809132n

[82] M. Quintanilla, E. Hemmer, J. Marques-Hueso, S. Rohani, G. Lucchini, M. Wang, R.R. Zamani, V. Roddatis, A. Speghini, B.S. Richards, F. Vetrone, *Cubic: Versus hexagonal-phase, size and morphology effects on the photoluminescence quantum yield of* $NaGdF_4$*:*Er^{3+}*/*Yb^{3+} *upconverting nanoparticles*, Nanoscale 14(4) (2022), pp. 1492–1504. DOI: 10.1039/d1nr06319g

[83] S. Liu, G. De, Y. Xu, X. Wang, Y. Liu, C. Cheng, J. Wang, *Size, phase-controlled synthesis, the nucleation and growth mechanisms of* $NaYF_4$*:Yb/Er nanocrystals*, J. Rare Earths 36(10) (2018), pp. 1060–1066. DOI: 10.1016/j.jre.2018.01.025

[84] P. Qiu, N. Zhou, H. Chen, C. Zhang, G. Gao, D. Cui, *Recent advances in lanthanide-doped upconversion nanomaterials: Synthesis, nanostructures and surface modification*, Nanoscale 5(23) (2013), pp. 11512–11525. DOI: 10.1039/c3nr03642a

[85] S. Hao, J. Liu, M. Tan, G. Chen, Chapter 7. *Upconversion enhancement using epitaxial core-shell nanostructures*, in: *Upconverting Nanomaterials*, CRC Press 2016, pp. 163–186. DOI: 10.1201/9781315371535-19

[86] J.C. Boyer, F. Vetrone, L.A. Cuccia, J.A. Capobianco, *Synthesis of colloidal upconverting* $NaYF_4$ *nanocrystals doped with* Er^{3+},Yb^{3+} *and* Tm^{3+},Yb^{3+} *via thermal decomposition of lanthanide trifluoroacetate precursors*, J. Am. Chem. Soc. 128(23) (2006), pp. 7444–7445. DOI: 10.1021/ja061848b

[87] K.A. Abel, J.C. Boyer, F.C.J.M. Van Veggel. *Hard proof of the* $NaYF_4/NaGdF_4$ *nanocrystal core/shell structure.* J. Am. Chem. Soc. 131 (2009), pp. 14644–14645. DOI: 10.1021/ja906971y.

[88] W. Gao, R. Wang, Q. Han, J. Dong, L. Yan, H. Zheng, *Tuning red upconversion emission in single* $LiYF_4:Yb^{3+}/Ho^{3+}$ *microparticle*, J. Phys. Chem. C 119(5) (2015), pp. 2349–2355. DOI: 10.1021/jp511566h

[89] T. Jiang, W. Qin, J. Zhou, *Citric acid-assisted phase controlled synthesis of* $NaYF_4:Yb^{3+},Tm^{3+}$ *crystals and their intense ultraviolet upconversion emissions*, J. Fluor. Chem. 156 (2013), pp. 177–182. DOI: 10.1016/j.jfluchem.2013.10.007

[90] D. Wawrzyńczyk, D. Piątkowski, S. Maćkowski, M. Samoć, M. Nyk, *Microwave-assisted synthesis and single particle spectroscopy of infrared down- and visible up-conversion in* Er^{3+} *and* Yb^{3+} *co-doped fluoride nanowires*, J. Mater. Chem. C 3(20) (2015), pp. 5332–5338. DOI: 10.1039/c5tc00468c

[91] S. Fan, S. Wang, L. Yu, H. Sun, G. Gao, L. Hu, *Ion-redistribution induced efficient upconversion in* β*-*$NaYF_4:20\%Yb^{3+},2\%Er^{3+}$ *microcrystals with well controlled morphology and size*, Opt. Express 25(1) (2017), pp. 180–190. DOI: 10.1364/oe.25.000180

[92] A. Meijerink, R. Wegh, P. Vergeer, T. Vlugt, *Photon management with lanthanides*, Opt. Mater. 28(6-7) (2006), pp. 575–581. DOI: 10.1016/j.optmat.2005.09.055

[93] D. Kang, E. Jeon, S. Kim, J. Lee, *Lanthanide-Doped Upconversion Nanomaterials: Recent Advances and Applications*, Biochip J. 14 (2020), pp. 124–135. DOI: 10.1007/s13206-020-4111-9

[94] A. Nadort, J. Zhao, E.M. Goldys, *Lanthanide upconversion luminescence at the nanoscale: Fundamentals and optical properties*, Nanoscale 8(27) (2016), pp. 13099–13130. DOI: 10.1039/c5nr08477f

[95] P.A. Tanner, *Lanthanide Luminescence in Solids*, in: *Lanthanide Luminescence*. Springer Verlag Berlin, Heidelberg 2010, pp. 183–233. DOI: 10.1007/4243_2010_6

[96] X. Chen, Y. Liu, D. Tu, *Lanthanide-Doped Luminescent Nanomaterials: From Fundamentals to Bioapplications.* Springer Verlag Berlin, Heidelberg 2014, DOI: 10.1007/978-3-642-40364-4

[97] A.A. Ansari, V.K. Thakur, G. Chen, *Functionalized upconversion nanoparticles: New strategy towards FRET-based luminescence bio-sensing*, Coord. Chem. Rev. 436 (2021), article no. 213821. DOI: 10.1016/j.ccr.2021.213821

[98] E.S. Tsai, S.F. Himmelstoß, L.M. Wiesholler, T. Hirsch, E.A.H. Hall, *Upconversion nanoparticles for sensing pH*, Analyst 144(18) (2019), pp. 5547–5557. DOI: 10.1039/c9an00236g

[99] N. Chowdhury, N. Riesen, H. Riesen, Yb^{3+} and Er^{3+} Codoped $BaLiF_3$ Nanocrystals for X-ray Dosimetry and Imaging by Upconversion Luminescence, ACS Appl. Nano. Mater. 4(7) (2021), pp. 6659–6667. DOI: 10.1021/acsanm.1c00600

[100] L. Shao, D. Liu, J. Lyu, D. Zhou, N. Ding, R. Sun, W. Xu, N. Wang, S. Xu, B. Dong, H. Song, *Near-infrared-pumped photon upconversion in* $CsPbI_3$ *and* CaF_2*:*Yb^{3+}*/*Ho^{3+} *nanocomposites for bio-imaging application*, Mater. Today Phys. 21 (2021), article no. 100495. DOI: 10.1016/j.mtphys.2021.100495

[101] C. Song, S. Zhang, Q. Zhou, H. Hai, D. Zhao, Y. Hui, *Upconversion nanoparticles for bioimaging*, Nanotechnol. Rev. 6(2) (2017), pp. 233–242. DOI: 10.1515/ntrev-2016-0043

[102] H. Jee, G. Chen, P.N. Prasad, T.Y. Ohulchanskyy, J. Lee, *In situ ultraviolet polymerization using upconversion nanoparticles: Nanocomposite structures patterned by near infrared light*, Nanomaterials 10(10) (2020), article no 2054. DOI: 10.3390/nano10102054

[103] J. Shen, G. Chen, A.M. Vu, W. Fan, O.S. Bilsel, C.C. Chang, G. Han, *Engineering the upconversion nanoparticle excitation wavelength: Cascade sensitization of tri-doped upconversion colloidal nanoparticles at 800 nm*, Adv. Opt. Mater. 1(9) (2013), pp. 644–650. DOI: 10.1002/adom.201300160

[104] A. Yakovliev, T.Y. Ohulchanskyy, R. Ziniuk, T. Dias, X. Wang, H. Xu, G. Chen, J. Qu, A.S.L. Gomes, *Noninvasive Temperature Measurement in Dental Materials Using* Nd^{3+}*,* Yb^{3+} *Doped Nanoparticles Emitting in the Near Infrared Region*,

Part. Part. Syst. Charact. 37(2) (2020), article no. 190445. DOI: 10.1002/ppsc.201900445

[105] B. Dong, S. Xu, J. Sun, S. Bi, D. Li, X. Bai, Y. Wang, L. Wang, H. Song, *Multifunctional* $NaYF_4$*:*Yb^{3+}*,*Er^{3+}*@Ag core/shell nanocomposites: Integration of upconversion imaging and photothermal therapy*, J. Mater. Chem. 21(17) (2011), pp. 6193–6200. DOI: 10.1039/c0jm04498a

[106] Z.L. Wang, J. Hao, H.L.W. Chan, G.L. Law, W.T. Wong, K.L. Wong, M.B. Murphy, T. Su, Z.H. Zhang, S.Q. Zeng, *Simultaneous synthesis and functionalization of water-soluble up-conversion nanoparticles for in-vitro cell and nude mouse imaging*, Nanoscale 3(5) (2011), pp. 2175–2181. DOI: 10.1039/c1nr10090d

[107] M. Wang, C.C. Mi, W.X. Wang, C.H. Liu, Y.F. Wu, Z.R. Xu, C. Bin Mao, S.K. Xu, *Immunolabeling and NIR-excited fluorescent imaging of HeLa cells by using* $NaYF_4$*:Yb,Er upconversion nanoparticles*, ACS Nano 3(6) (2009), pp. 1580–1586. DOI: 10.1021/nn900491j

[108] G. Chen, T.Y. Ohulchanskyy, S. Liu, W.C. Law, F. Wu, M.T. Swihart, H. Ågren, P.N. Prasad, Core/shell $NaGdF_4$:Nd^{3+}/$NaGdF_4$ nanocrystals with efficient near-infrared to near-infrared downconversion photoluminescence for bioimaging applications, ACS Nano 6(4) (2012), pp. 2969–2977. DOI: 10.1021/nn2042362

[109] D. Wang, B. Xue, T.Y. Ohulchanskyy, Y. Liu, A. Yakovliev, R. Ziniuk, M. Xu, J. Song, J. Qu, Z. Yuan, *Inhibiting tumor oxygen metabolism and simultaneously generating oxygen by intelligent upconversion nanotherapeutics for enhanced photodynamic therapy*, Biomaterials 251 (2020), article no. 120088. DOI: 10.1016/j.biomaterials.2020.120088

[110] J. Zhao, D. Zhong, S. Zhou, *NIR-I-to-NIR-II fluorescent nanomaterials for biomedical imaging and cancer therapy*, J. Mater. Chem. B 6(3) (2018), pp. 349–365. DOI: 10.1039/c7tb02573d

[111] Q. Ma, J. Wang, Z. Li, X. Lv, L. Liang, Q. Yuan, *Recent Progress in Time-Resolved Biosensing and Bioimaging Based on Lanthanide-Doped Nanoparticles*, Small 15(32) (2019), article no. 1804969. DOI: 10.1002/smll.201804969

[112] E. Zhao, X. Liu, D. Tang, L. Liu, G. Liu, B. Zhou, C. Xing, *800 nm laser induced white light upconversion of Nd/Yb/Pr triply doped* $NaYF_4$ *through a dual-sensitization strategy*, Mater. Res. Bull. 133 (2021), article no 111027. DOI: 10.1016/j.materresbull.2020.111027

[113] L.R.R. Nunes, H.P. Labaki, F.J. Caixeta, R.R. Gonçalves, *Yb^{3+} influence on NIR emission from Pr^{3+}-doped spherical yttria nanoparticles for advances in NIR I and NIR II biological windows*, J. Lumin. 241 (2022), article no. 118485. DOI: 10.1016/j.jlumin.2021.118485

[114] E.L. Cates, J.H. Kim, *Upconversion under polychromatic excitation: $Y_2SiO_5:Pr^{3+},Li^+$ converts violet, cyan, green, and yellow light into UVC*, Opt. Mater. 35(12) (2013), pp. 2347–2351. DOI: 10.1016/j.optmat.2013.06.030

[115] M. Raeiszadeh, B. Adeli, *A Critical Review on Ultraviolet Disinfection Systems against COVID-19 Outbreak: Applicability, Validation, and Safety Considerations*, ACS Photonics 7(11) (2020), pp. 2941–2951. DOI: 10.1021/acsphotonics.0c01245

[116] C.C. Tseng, C.S. Li. *Inactivation of viruses on surfaces by ultraviolet germicidal irradiation.* J. Occup. Environ. Hyg. 4 (2007) pp. 400–405. DOI: 10.1080/15459620701329012

[117] C. Chen, R. Tian, Y. Zeng, C. Chu, G. Liu, *Activatable Fluorescence Probes for "Turn-On" and Ratiometric Biosensing and Bioimaging: From NIR-I to NIR-II*, Bioconjug. Chem. 31(2) (2020), pp. 276–292. DOI: 10.1021/acs.bioconjchem.9b00734

[118] M. Ploydaeng, N. Rajatanavin, P. Rattanakaemakorn, *UV-C light: A powerful technique for inactivating microorganisms and the related side effects to the skin*, Photodermatol. Photoimmuno. Photomed. 37(1) (2021), pp. 12–19. DOI: 10.1111/phpp.12605

[119] M. D'Abramo, C.L. Castellazzi, M. Orozco, A. Amadei, *On the nature of DNA hyperchromic effect*, J. Phys. Chem. B 117(29) (2013), pp. 8697–8704. DOI: 10.1021/jp403369k

[120] C. Baumstark-Khan, U. Hentschel, Y. Nikandrova, J. Krug, G. Horneck. *Fluorometric Analysis of DNA Unwinding (FADU) as a Method for Detecting Repair-induced DNA Strand Breaks in UV-irradiated Mammalian Cells.* Photochem. Photobiol. 72(4) (2000), pp. 477-484. DOI: 10.1562/0031-8655(2000)0720477faoduf2.0.co2

[121] Y. Guan, R. Shi, X. Li, M. Zhao, Y. Li, *Multiple binding modes for dicationic Hoechst 33258 to DNA*, J. Phys. Chem. B 111(25) (2007), pp. 7336–7344. DOI: 10.1021/jp066344e

[122] S. Majumdar, T. Guha, F. Barman, R. Kundu, *A Basic Method for Hoechst (33258) Staining of Nuclei from Whole Root Tissues of Oryza sativa*, Nat. Acad. Sci. Lett. 43 (2020), pp. 389–392. DOI: 10.1007/s40009-019-00865-3

[123] S.R. Gallagher. *Quantification of DNA and RNA with Absorption and Fluorescence Spectroscopy*. Curr. Protoc. Cell Biol. (2000), pp. A.3D.1-A.3D.8. DOI: 10.1002/cpim.20

[124] R.D. Shannon, *Revised Effective Ionic Radii and Systematic Studies of Interatomie Distances in Halides and Chaleogenides*, Acta Cryst. A 32 (1976), pp. 751-767, DOI: 10.1107/S0567739476001551

[125] Z.P. Bian, D.S. Li, X. Zhao, H. Lin, *Multi-peak emissions of* Pr^{3+}*-doped heavy metal tellurite glasses for laser-driven illumination*, Radiat. Phys. Chem. 151 (2018), pp. 126–132. DOI: 10.1016/j.radphyschem.2018.05.029

[126] F.E. Maturi, A. Gaddam, C.D.S. Brites, J.M.M. Souza, H. Eckert, S.J.L. Ribeiro, L.D. Carlos, D. Manzani, *Extending the Palette of Luminescent Primary Thermometers:* Yb^{3+}/Pr^{3+} *Co-Doped Fluoride Phosphate Glasses*, Chem. Mater. 35(17) (2023), pp. 7229–7238. DOI: 10.1021/acs.chemmater.3c01508

[127] L.J. Borrero-González, G. Galleani, D. Manzani, L.A.O. Nunes, S.J.L. Ribeiro, *Visible to infrared energy conversion in* Pr^{3+}-Yb^{3+} *co-doped fluoroindate glasses*, Opt. Mater. 35(12) (2013), pp. 2085–2089. DOI: 10.1016/j.optmat.2013.05.024

[128] D. Wang, W. Wu, X. Tan, B.A. Goodman, S. Xu, W. Deng, *Upconversion Visible Light Emission in Yb/Pr Co-Doped Yttria-Stabilized Zirconia (YSZ) Single Crystals*, Crystals 11(11) (2021), article no. 1328. DOI: 10.3390/cryst11111328

[129] A.M. Srivastava, *Aspects of* Pr^{3+} *luminescence in solids*, J. Lumin. 169B (2016), pp. 445–449. DOI: 10.1016/j.jlumin.2015.07.001

[130] A. Puccini, N. Liu, E. Hemmer, *Praseodymium-Doped Nanoparticles: Candidates for Near-Infrared-II Double- and Single-Band Nanothermometry*, ACS Mater. Lett. 6(4) (2024), pp. 1327–1337. DOI: 10.1021/acsmaterialslett.3c01554

[131] M. Wang, C. Hu, Q. Su, *Luminescent Lifetime Regulation of Lanthanide-Doped Nanoparticles for Biosensing*, Biosensors 12(2) (2022) article no 131. DOI: 10.3390/bios12020131.

[132] C. Ng, E.C. Almaz, J.C. Simon, D. Fried, C.L. Darling, *Near-infrared imaging of demineralization on the occlusal surfaces of teeth without the interference of stains*, J. Biomed. Opt. 24(3) (2019), article no. 036002. DOI: 10.1117/1.jbo.24.3.036002

[133] M. Tan, B. Del Rosal, Y. Zhang, E. Martín Rodríguez, J. Hu, Z. Zhou, R. Fan, D.H. Ortgies, N. Fernández, I. Chaves-Coira, Á. Núñez, D. Jaque, G. Chen, *Rare-earth-doped fluoride nanoparticles with engineered long luminescence lifetime for time-gated: In vivo optical imaging in the second biological window*, Nanoscale 10(37) (2018), pp. 17771–17780. DOI: 10.1039/c8nr02382d

[134] C.L. Ventola, *The antibiotic resistance crisis: Part 1: Causes and threats.* Pharm. Ther. 40(4) (2015), pp. 277-283. PMCID: PMC4378521

[135] World Health Organization, WHO global strategy for containment of antimicrobial resistance, World Health Organization, 2001.

[136] J. Sizun, M.W.N. Yu, P.J. Talbot. *Survival of human coronaviruses 229E and OC43 in suspension and after drying on surfaces: a possible source of hospital-acquired infections.* J. Hosp. Infect. 46 (2000), pp. 55–60. DOI: 10.1053/jhin.2000.0795.

[137] M.Y.Y. Lai, P.K.C. Cheng, W.W.L. Lim. *Survival of Severe Acute Respiratory Syndrome Coronavirus*. Clin. Infect. Dis. 41 (2005), pp. 67-71. DOI: 10.1086/433186.

[138] A.W.H. Chin, J.T.S. Chu, M.R.A. Perera, K.P.Y. Hui, H.-L. Yen, M.C. Chan, M. Peiris, L.L.M. Poon. *Stability of SARS-CoV-2 in different environmental conditions*, Lancet Microbe 1 (2020) e10. DOI: 10.1016/S2666-5247(20)30003-3.

[139] V. Cagno, P. Andreozzi, M. D'Alicarnasso, P.J. Silva, M. Mueller, M. Galloux, R. Le Goffic, S.T. Jones, M. Vallino, J. Hodek, J. Weber, S. Sen, E.R. Janecek, A. Bekdemir, B. Sanavio, C. Martinelli, M. Donalisio, M.A.R. Welti, J.F. Eleouet, Y. Han, L. Kaiser, L. Vukovic, C. Tapparel, P. Král, S. Krol, D. Lembo, F. Stellacci. *Broad-spectrum non-toxic antiviral nanoparticles with a virucidal inhibition mechanism*, Nat. Mater. 17 (2018), pp. 195–203. DOI: 10.1038/NMAT5053.

[140] M.Y. Tsang, P. Fałat, M.A. Antoniak, R. Ziniuk, S.J. Zelewski, M. Samoć, M. Nyk, J. Qu, T.Y. Ohulchanskyy, D. Wawrzyńczyk, *Pr^{3+} doped $NaYF_4$ and $LiYF_4$ nanocrystals combining visible-to-UVC upconversion and NIR-to-NIR-II downconversion luminescence emissions for biomedical applications*, Nanoscale 14(39) (2022), pp. 14770–14778. DOI: 10.1039/d2nr01680j

[141] S. Fischer, N.D. Bronstein, J.K. Swabeck, E.M. Chan, A.P. Alivisatos, *Precise Tuning of Surface Quenching for Luminescence Enhancement in Core-Shell Lanthanide-Doped Nanocrystals*, Nano Lett. 16(11) (2016), pp. 7241–7247. DOI: 10.1021/acs.nanolett.6b03683

[142] BSI Standards Publication. *Chemical disinfectants and antiseptics-Quantitative suspension test for the evaluation of virucidal activity in the medical area-Test method and requirements* (*Phase 2/Step 1*) BS EN 14476:2013+A2:2019.

[143] D.D. Nguyen, L.T. Phung, H.T.T. Tran, H.T.T. Ly, A.H.M. Vo, N.P. Dinh, P.M. Doan, A.T. Nguyen, L.D. Dang, T.T. Doan, K.T. Pham, H.L. Pham, D.X. Hoang, T.N. Pham, B.T. Tran, T.T.T. Tran, H.T.M. Le, A.N. Pham, A. Antoniou, N.T. Ho, *Molecular subtypes of Adenovirus-associated acute respiratory infection outbreak in children in Northern Vietnam and risk factors of more severe cases*, PLoS Negl. Trop. Dis. 17 (2023), article no. e0011311. DOI: 10.1371/journal.pntd.0011311

[144] Y. Huang, C. Wang, F. Ma, Q. Guo, L. Yao, A. Chen, X. Luo, L. Zheng, *Human adenoviruses in paediatric patients with respiratory tract infections in Beijing, China*, Virol. J. 18 (2021), article no 191. DOI: 10.1186/s12985-021-01661-6

[145] A. Banerjee, S. Kulkarni, A. Mukherjee, *Herpes Simplex Virus: The Hostile Guest That Takes Over Your Home*, Front. Microbiol. 11 (2020), article no. 733. DOI: 10.3389/fmicb.2020.00733

[146] G.A. Wudiri, S.M. Schneider, A. V. Nicola, *Herpes simplex virus 1 envelope cholesterol facilitates membrane fusion*, Front. Microbiol. 8 (2017), article no. 2383. DOI: 10.3389/fmicb.2017.02383

[147] N. Bogdan, F. Vetrone, G.A. Ozin, J.A. Capobianco. *Synthesis of ligand-free colloidally stable water dispersible brightly luminescent lanthanide-doped upconverting nanoparticles*. Nano Lett. 11 (2011), pp. 835–840. DOI: 10.1021/nl1041929

[148] V. Kale, T. Soukka, J. Hölsä, M. Lastusaari. *Enhancement of blue upconversion luminescence in hexagonal* $NaYF_4$*:Yb,Tm by using K and Sc ions.* J. Nanopart. Res. 15 (2013), article no 1850. DOI: 10.1007/s11051-013-1850-8

[149] N. Rebrova, P. Zdeb, K. Lemański, B. Macalik, O. Bezkrovnyi, P.J. Dereń. *Upconversion Luminescence Properties of* Pr^{3+}*-Doped* $BaYF_5$ *Nanoparticles Prepared by Microwave Hydrothermal Method*. Inorg. Chem. 63 (2024), pp. 3028–3036. DOI: 10.1021/acs.inorgchem.3c03821.

[150] A.F. Nikkels, G.E. Pièrard. *Treatment of Mucocutaneous Presentations of Herpes Simplex Virus Infections*, Am. J. Clin. Dermatol. 3(7) (2002), pp. 475-487. DOI: 10.2165/00128071-200203070-00004

[151] S. Pfitzner, J.B. Bosse, H. Hofmann-Sieber, F. Flomm, R. Reimer, T. Dobner, K. Grünewald, L.E. Franken, *Human adenovirus type 5 infection leads to nuclear*

envelope destabilization and membrane permeability independently of adenovirus death protein, Int. J. Mol. Sci. 22(23) (2021), article no. 13034. DOI: 10.3390/ijms222313034

[152] D. Wawrzyńczyk, *Surface functionalization of up-converting $NaYF_4$ nanocrystals with chiral molecules*, RSC Adv. 6(7) (2016), pp. 5558–5565. DOI: 10.1039/c5ra19496b

[153] Q. Lin, J.Y.C. Lim, K. Xue, P.Y.M. Yew, C. Owh, P.L. Chee, X.J. Loh. *Sanitizing agents for virus inactivation and disinfection*, VIEW 1 (2020) e16. DOI: 10.1002/viw2.16

[154] P. Fałat, A. Chwirot, P. Kuich, M. Nyk, T.Y. Ohulchanskyy, B. Bażanów, D. Wawrzyńczyk, *VIS-to-UVC Upconversion of Pr^{3+} Doped Fluoride Nano- and Microcrystals for Inactivation of Human Viruses*, Rare Met. 44 (2025), pp. 4881–4897. DOI: 10.1007/s12598-025-03317-8

[155] R.A. Janjua, W. Ji, N.A. Shah, J. Evans, R. Zhang, S. Zhang, S. He, *Advances in Synthesis Strategies for Lanthanide-Based $NaYF_4$ Upconversion Nanocrystals and Their Applications in Ratiometric Thermometry*, Progress In Electromagnetics Research M 122 (2023), pp. 117–136. DOI: 10.2528/PIERM23112602

[156] Y. Liu, D. Tu, H. Zhu, X. Chen, *Lanthanide-doped luminescent nanoprobes: Controlled synthesis, optical spectroscopy, and bioapplications*, Chem. Soc. Rev. 42(16) (2013), pp. 6924–6958. DOI: 10.1039/c3cs60060b

[157] G. Chen, H. Ågren, T.Y. Ohulchanskyy, P.N. Prasad, *Light upconverting core-shell nanostructures: Nanophotonic control for emerging applications*, Chem. Soc. Rev. 44(6) (2015), pp. 1680–1713. DOI: 10.1039/c4cs00170b

[158] F. Vetrone, R. Naccache, V. Mahalingam, C.G. Morgan, J.A. Capobianco, *The active-core/active-shell approach: A strategy to enhance the upconversion luminescence in lanthanide-doped nanoparticles*, Adv. Funct. Mater. 19(18) (2009), pp. 2924–2929. DOI: 10.1002/adfm.200900234

[159] K. Prorok, M. Pawlyta, W. Stręk, A. Bednarkiewicz, *Energy Migration Up-conversion of Tb^{3+} in Yb^{3+} and Nd^{3+} Codoped Active-Core/Active-Shell Colloidal Nanoparticles*, Chem. Mater. 28(7) (2016), pp. 2295–2300. DOI: 10.1021/acs.chemmater.6b00353

[160] C. Hernández-Álvarez, G. Brito-Santos, I.R. Martín, J. Sanchiz, K. Saidi, K. Soler-Carracedo, Ł. Marciniak, M. Runowski, *Multifunctional optical sensing platform of temperature, pressure (vacuum) and laser power density:*

$NaYF_4$:Gd^{3+},Yb^{3+},Er^{3+} nanomaterial as luminescent thermometer, manometer and power meter, J. Mater. Chem. C 11(30) (2023), pp. 10221–10229. DOI: 10.1039/d3tc01712e

[161] X. Huang, J. Lin, *Active-core/active-shell nanostructured design: An effective strategy to enhance Nd^{3+}/Yb^{3+} cascade sensitized upconversion luminescence in lanthanide-doped nanoparticles*, J. Mater. Chem. C 3(29) (2015), pp. 7652–7657. DOI: 10.1039/c5tc01438g

[162] D. Chen, L. Lei, A. Yang, Z. Wang, Y. Wang, *Ultra-broadband near-infrared excitable upconversion core/shell nanocrystals*, ChemComm 47 (2012), pp. 5898–5900. DOI: 10.1039/c2cc32102e

[163] Q. Su, H.L. Wei, Y. Liu, C. Chen, M. Guan, S. Wang, Y. Su, H. Wang, Z. Chen, D. Jin, *Six-photon upconverted excitation energy lock-in for ultraviolet-C enhancement*, Nat. Commun. 12 (2021), article no 4367. DOI: 10.1038/s41467-021-24664-x

[164] B. del Rosal, U. Rocha, E.C. Ximendes, E. Martín Rodríguez, D. Jaque, J.G. Solé, *Nd^{3+} ions in nanomedicine: Perspectives and applications*, Opt. Mater. 63 (2017), pp. 185–196. DOI: 10.1016/j.optmat.2016.06.004

[165] M. Misiak, K. Prorok, B. Cichy, A. Bednarkiewicz, W. Stręk, *Thulium concentration quenching in the up-converting α-Tm^{3+}/Yb^{3+} $NaYF_4$ colloidal nanocrystals*, Opt. Mater. 35(5) (2013), pp. 1124–1128. DOI: 10.1016/j.optmat.2013.01.002

[166] G.S. Yi, G.M. Chow, *Synthesis of hexagonal-phase $NaYF_4$:Yb,Er and $NaYF_4$:Yb,Tm nanocrystals with efficient up-conversion fluorescence*, Adv. Funct. Mater. 16(18) (2006), pp. 2324–2329. DOI: 10.1002/adfm.200600053

[167] C. Zhang, J.Y. Lee, *Prevalence of anisotropic shell growth in rare earth core-shell upconversion nanocrystals*, ACS Nano 7(5) (2013), pp. 4393–4402. DOI: 10.1021/nn4009214

[168] T.Q. Hoa Tran, M.H. Hoang, T.A.T. Do, A.T. Le, T.H. Nguyen, T.D. Nguyen, M.T. Man, *Nanostructure and photoluminescence dynamics of praseodymium doped hexagonal LaF_3 nanocrystals*, J. Lumin. 237 (2021), article no. 118162. DOI: 10.1016/j.jlumin.2021.118162

[169] X.P. Chen, X.Y. Huang, Q.Y. Zhang, *Concentration-dependent near-infrared quantum cutting in $NaYF_4$:Pr^{3+},Yb^{3+} phosphor*, J. Appl. Phys. 106 (2009), article no. 063518. DOI: 10.1063/1.3224906

[170] B. Herden, A. Meijerink, F.T. Rabouw, M. Haase, T. Jüstel, *On the efficient luminescence of β-Na(La*$_{1-x}$*Pr*$_x$*)F*$_4$, J. Lumin. 146 (2014), pp. 302–306. DOI: 10.1016/j.jlumin.2013.09.072

[171] N. Martin, P. Boutinaud, M. Malinowski, R. Mahiou, J. Cousseins, *Optical spectra and analysis of Pr*$^{3+}$ *in β-NaYF*$_4$, J Alloy Compd. 275-277 (1998), pp. 304–306. DOI: 10.1016/j.acthis.2018.03.007

[172] Y. Fu, T. Sun, J. Li, Y. Tang, Y. Yang, S. Tao, F. Wang, D. Zhang, G. Qin, Z. Jia, D. Zhao, W. Qin, *(S + C)-band polymer waveguide amplifier based on Tm*$^{3+}$ *and Er*$^{3+}$ *layer-doped core-shell nanoparticles* , Opt. Lett. 48(2) (2023), pp. 391-394. DOI: 10.1364/ol.477267

[173] U. Rocha, K. Upendra Kumar, C. Jacinto, J. Ramiro, A.J. Caamaño, J. García Solé, D. Jaque, *Nd*$^{3+}$ *doped LaF*$_3$ *nanoparticles as self-monitored photo-thermal agents*, Appl. Phys. Lett. 104 (2014), article no. 053703. DOI: 10.1063/1.4862968

[174] J.C.G. Bünzli, *Lanthanide Photonics: Shaping the Nanoworld*, Trends Chem. 1(8) (2019), pp. 751–762. DOI: 10.1016/j.trechm.2019.05.012

[175] H. Dong, L.D. Sun, C.H. Yan, *Energy transfer in lanthanide upconversion studies for extended optical applications*, Chem. Soc. Rev. 44 (2015), pp. 1608–1634. DOI: 10.1039/c4cs00188e

[176] A. Gharavi, G.L. McPherson, *Up-conversion luminescence from simultaneously excited pairs of Tm*$^{3+}$ *ions in CsMgCl*$_3$ *crystals*, Chem. Phys. Lett. 200(3) (1992), pp. 279-282. DOI: 10.1016/0009-2614(92)80011-Y

[177] C.M. Trindade, F.G. Rego-Filho, N.G.C. Astrath, C. Jacinto, A.S. Gouveia-Neto, *UV–visible-NIR light generation through frequency upconversion in Tm*$^{3+}$*-doped low silica calcium aluminosilicate glasses using multiple excitation around 1.2 µm*, J. Solid State Chem. 260 (2018), pp. 147–150. DOI: 10.1016/j.jssc.2018.01.012

[178] H.N. Luitel, R. Chand, H. Hamajima, Y.R. Gaihre, T. Shingae, T. Yanagita, T. Watari, *Highly efficient NIR to NIR upconversion of ZnMoO*$_4$*:Tm*$^{3+}$*,Yb*$^{3+}$ *phosphors and their application in biological imaging of deep tumors*, J. Mater. Chem. B 4 (2016), pp. 6192–6199. DOI: 10.1039/c6tb00965d

[179] Z. Liu, K. Zheng, D. Zhao, N. Liu, W. Qin, *Size dependent ultraviolet upconversion in single YF*$_3$*:Yb*$^{3+}$*/Tm*$^{3+}$ *particles*, J. Nanosci. Nanotechnol. 11(11) (2011), pp. 9584–9587, DOI: 10.1166/jnn.2011.5259.

[180] I.R. Martín, V.D. Rodríguez, V. Lavín, U.R. Rodríguez-Mendoza, *Infrared, blue and ultraviolet upconversion emissions in Yb*$^{3+}$*-Tm*$^{3+}$*-doped fluoroindate glasses*,

Spectrochim. Acta A 55(5) (1999), pp. 941-945, DOI: 10.1016/S1386-1425(98)00197-8

[181] D. Li, S. Wen, M. Kong, Y. Liu, W. Hu, B. Shi, X. Shi, D. Jin, *Highly Doped Upconversion Nanoparticles for in Vivo Applications under Mild Excitation Power*, Anal. Chem. 92(16) (2020), pp. 10913-10919. DOI: 10.1021/acs.analchem.0c02143.

[182] K. Suresh, K.V. Krishnaiah, C. Basavapoornima, S.R. Depuru, C.K. Jayasankar, *Enhancement of 1.8 μm emission in* Er^{3+}/Tm^{3+} *co-doped tellurite glasses: Role of energy transfer and dual wavelength pumping schemes*, J. Alloys. Compd. 827 (2020), article no 154038, DOI: 10.1016/j.jallcom.2020.154038

[183] R.M. Percival, D. Szebesta, J.R. Williams, *Highly efficient 1.064 μm upconversion pumped 1.47 μm thulium doped fluoride fiber laser*, Electron. Lett. 30(13) (1994), pp. 1057–1058, DOI:10.1049/el:19940701.

[184] W. Lu, J. Xu, Q. Song, K. Bian, J. Guo, J. Liu, D. Li, P. Liu, C. Zhang, X. Xu, J. Xu, K. Lebbou, Pr^{3+} *deactivation effect to* Tm^{3+} *at ~1.5 μm emission in* $Bi_4Ge_3O_{12}$ *crystals grown by the micro-pulling-down method*, J Lumin 246 (2022), article no 118829. DOI: 10.1016/j.jlumin.2022.118829

[185] Q. Li, Z. Shi, Q. Song, J. Tian, J. Liu, X. Xu, J. Xu, D. Li, K. Lebbou, *The micro-pulling-down growth of Tm:LuAG and Tm,Pr:LuAG crystals and optical properties*, Opt. Mater. 118 (2021), article no 111275. DOI: 10.1016/j.optmat.2021.111275.

[186] J. Shan, W. Kong, R. Wei, N. Yao, Y. Ju, *An investigation of the thermal sensitivity and stability of the* β-$NaYF_4$*:Yb,Er upconversion nanophosphors*, J. Appl. Phys. 107 (2010), article no 054901. DOI: 10.1063/1.3298905

[187] C. Renero-Lecuna, R. Martín-Rodríguez, R. Valiente, J. González, F. Rodríguez, K.W. Krämer, H.U. Güdel, *Origin of the high green upconversion luminescence efficiency in* β-$NaYF_4$:2%Er^{3+},20%Yb^{3+}, Chem. Mater. 23(15) (2011), pp. 3442-3448. DOI: 10.1021/cm2004227

[188] S. Heer, K. Kömpe, H.U. Güdel, M. Haase, *Highly efficient multicolour upconversion emission in transparent colloids of lanthanide-doped* $NaYF_4$ *nanocrystals,* Adv. Mater. 16(23-24) (2004), pp. 2102–2105. DOI: 10.1002/adma.200400772

[189] R.G. Geitenbeek, H.W. de Wijn, A. Meijerink, *Non-Boltzmann Luminescence in* $NaYF_4:Eu^{3+}$*: Implications for Luminescence Thermometry*, Phys. Rev. Appl. 10 (2018), article no 064006. DOI: 10.1103/PhysRevApplied.10.064006.

[190] C. Zhao, X. Kong, X. Liu, L. Tu, F. Wu, Y. Zhang, K. Liu, Q. Zeng, H. Zhang, Li^+ *ion doping: An approach for improving the crystallinity and upconversion emissions of* $NaYF_4:Yb^{3+},Tm^{3+}$ *nanoparticles*, Nanoscale 5(17) (2013), pp. 8084–8089. DOI: 10.1039/c3nr01916k

[191] I.I. Kindrat, B. V. Padlyak, R. Lisiecki, V.T. Adamiv, *Optical spectroscopy and luminescence properties of a* Tm^{3+}*-doped* $LiKB_4O_7$ *glass*, J. Non. Cryst. Solids 521 (2019), article no 119477, DOI: 10.1016/j.jnoncrysol.2019.119477

[192] Ravita, A.S. Rao, *Color tunable photoluminescence in* $KZABS:Tm^{3+}$ *glasses under different sources of excitation for photonic applications*, J. Non. Cryst. Solids 585 (2022), article no 121532, DOI: 10.1016/j.jnoncrysol.2022.121532

[193] M.Y.A. Yagoub, H.C. Swart, P. Bergman, E. Coetsee, *Enhanced* Pr^{3+} *photoluminescence by energy transfer in* SrF_2*:* Eu^{2+}*,* Pr^{3+} *phosphor*, AIP Adv. 6(2) (2016), article no 025204, DOI: 10.1063/1.4941833

[194] M. Kuwik, K. Kowalska, J. Pisarska, W.A. Pisarski, *Spectroscopic Properties of* Pr^{3+}*,* Tm^{3+}*, and* Ho^{3+} *in Germanate-Based Glass Systems Modified by* TiO_2, Materials 16(1) (2023), article no 61. DOI: 10.3390/ma16010061

[195] F. Zhang, Z. Bi, A. Huang, Z. Xiao, *Luminescence and Judd-Ofelt analysis of the* Pr^{3+} *doped fluorotellurite glass*, J. Lumin 160 (2015), pp. 85–89. DOI: 10.1016/j.jlumin.2014.11.047

[196] M. Runowski, P. Woźny, I.R. Martín, V. Lavín, S. Lis, *Praseodymium doped* $YF_3:Pr^{3+}$ *nanoparticles as optical thermometer based on luminescence intensity ratio (LIR) – Studies in visible and NIR range*, J. Lumin. 214 (2019), article no 116571. DOI: 10.1016/j.jlumin.2019.116571

[197] X.S. Zhang, C.Z. Yao, L.F. Li, C.Y. Yan, B.H. Wei, *Facile fabrication and spectroscopic study of the energy transfer effect of* Pr^{3+} *and* Tm^{3+} *co-doped* La_2O_3 *nanorod arrays*, Mater. Lett. 76(1) (2012), pp. 165–168. DOI: 10.1016/j.matlet.2012.02.079

[198] X. Cao, Z. Shi, J. Dong, Q. Song, M. Wu, W. Wang, Q. Li, H. Lin, Y. Xue, Q. Wang, J. Xu, *Enhanced 1.5 μm emission of* Tm^{3+} *via* Pr^{3+} *deactivation in* PbF_2 *crystal*, J. Lumin. 248 (2022), article no 118959. DOI: 10.1016/j.jlumin.2022.118959

[199] O.S. Wolfbeis, *An overview of nanoparticles commonly used in fluorescent bioimaging*, Chem. Soc. Rev. 44(14) (2015), pp. 4743–4768. DOI: 10.1039/c4cs00392f

[200] J. Shen, G. Chen, A.M. Vu, W. Fan, O.S. Bilsel, C.C. Chang, G. Han, *Engineering the upconversion nanoparticle excitation wavelength: Cascade sensitization of tri-doped upconversion colloidal nanoparticles at 800 nm*, Adv. Opt. Mater. 1(9) (2013), pp. 644–650. DOI: 10.1002/adom.201300160

[201] H. Kobayashi, M. Ogawa, R. Alford, P.L. Choyke, Y. Urano, *New strategies for fluorescent probe design in medical diagnostic imaging*, Chem. Rev. 110 (2010), pp. 2620–2640. DOI: 10.1021/cr900263j

[202] P. Loiko, J.L. Doualan, L. Guillemot, R. Moncorgé, F. Starecki, A. Benayad, E. Dunina, A. Kornienko, L. Fomicheva, A. Braud, P. Camy, *Emission properties of* Tm^{3+}*-doped* CaF_2*,* KY_3F_{10}*,* $LiYF_4$*,* $LiLuF_4$ *and* BaY_2F_8 *crystals at 1.5 μm and 2.3 μm*, J. Lumin 225 (2020), article no 117279, DOI: 10.1016/j.jlumin.2020.117279

[203] R. O’Connor, R. Mahiou, D. Martinant, M.T. Fournier, *Luminescence and dynamics in* $Tm^{3+}:NaYF_4$, J. Alloys Compds. 225(1-2) (1995), pp. 107-110, DOI: 10.1016/0925-8388(95)07142-3

[204] P. Villanueva-Delgado, K.W. Krämer, R. Valiente, M. De Jong, A. Meijerink, *Modeling blue to UV upconversion in* β*-*$NaYF_4:Tm^{3+}$, Phys. Chem. Chem. Phys. 18(39) (2016), pp. 27396–27404. DOI: 10.1039/c6cp04347j

[205] Y.Y. Zhang, Y. Wang, J.Q. Deng, J. Wang, S.C. Ni, *Highly efficient* Yb^{3+}/Tm^{3+} *co-doped* $NaYF_4$ *nanotubes: Synthesis and intense ultraviolet to infrared up-conversion luminescence*, Opt. Commun. 312 (2014), pp. 43–46, DOI: 10.1016/j.optcom.2013.09.012

[206] D.I. Andersson, D. Hughes, *Antibiotic resistance and its cost: Is it possible to reverse resistance?*, Nat. Rev. Microbiol. 8 (2010), pp. 260–271. DOI: 10.1038/nrmicro2319

[207] S. McCarlie, C.E. Boucher, R.R. Bragg, *Molecular basis of bacterial disinfectant resistance*, Drug Resist. Updat. 48 (2020), article no 100672. DOI: 10.1016/j.drup.2019.100672

[208] A. Colclough, J. Corander, S.K. Sheppard, S.C. Bayliss, M. Vos, *Patterns of cross-resistance and collateral sensitivity between clinical antibiotics and natural antimicrobials*, Evol. Appl. 12(5) (2019), pp. 878–887. DOI: 10.1111/eva.12762

[209] A.R. Pereira, D.F.O. Braga, M. Vassal, I.B. Gomes, M. Simões, *Ultraviolet C irradiation: A promising approach for the disinfection of public spaces?*, Sci. Total Environ. 879 (2023), article no 163007. DOI: 10.1016/j.scitotenv.2023.163007

[210] L. Li, L. Zi, F. Yang, S. Feng, C. Wang, Y. Yang, *Pr^{3+}-Based Visible-to-Ultraviolet Upconversion. A minireview*, Adv. Phys. Res. 4 (2025), article no. 2400097. DOI: 10.1002/apxr.202400097

[211] P. Lv, L. Li, Z. Yin, C. Wang, Y. Yang, *Visible-to-ultraviolet-C upconverted photon for multifunction via $Ca_2SiO_4:Pr^{3+}$*, Opt. Lett. 47(17) (2022), pp. 4435–4438. DOI: 10.1364/ol.469090

[212] J. Wu, H. Zheng, X. Liu, B. Han, J. Wei, Y. Yang, *UVC upconversion material under sunlight excitation: $LiYF_4:Pr^{3+}$*, Opt. Lett. 41(4) (2016), pp. 792–795. DOI: 10.1364/ol.41.000792

[213] X. Zhao, F. Liu, T. Shi, H. Wu, L. Zhang, J. Zhang, X. Wang, Y. Liu, *Conceptual Ultraviolet-C Light Source Based on Up-Conversion Luminescence*, Adv. Photonics Res. 3(9) (2022), article no. 2200106. DOI: 10.1002/adpr.202200106.

[214] E.L. Cates, F. Li, *Balancing intermediate state decay rates for efficient Pr^{3+} visible-to-UVC upconversion: The case of β-$Y_2Si_2O_7:Pr^{3+}$,* RSC Adv 6(27) (2016), pp. 22791–22796. DOI: 10.1039/c6ra01121g

[215] Promega Corporation, *BacTiter-Glo™ Microbial Cell Viability Assay Instructions for Use of Products G8230, G8231, G8232 and G8233*, Madison, WI, USA: Promega, Available: https://www.promega.com (access date: 21.03.2025).

[216] E. Grela, J. Kozłowska, A. Grabowiecka, *Current methodology of MTT assay in bacteria – A review*, Acta Histochem. 120(4) (2018), pp. 303–311. DOI: 10.1016/j.acthis.2018.03.007

[217] L.R. de Haan, M.J. Reiniers, L.F. Reeskamp, A. Belkouz, L. Ao, S. Cheng, B. Ding, R.F. van Golen, M. Heger, *Experimental Conditions That Influence the Utility of 2'7'-Dichlorodihydrofluorescein Diacetate (DCFH2-DA) as a Fluorogenic Biosensor for Mitochondrial Redox Status*, Antioxidants 11(8) (2022), article no. 1424. DOI: 10.3390/antiox11081424

[218] X. Xu, Z. Xiao, Y. Wang, Y. Yan, J. Shen, Y. Nie, W. You, D. Wu, L. Han, F. Lai, *Structure and upconversion luminescence properties of Pr^{3+}-doped $Y_2Si_2O_7$ phosphor prepared by different methods*, Opt. Mater. 134A (2022), article no. 113191. DOI: 10.1016/j.optmat.2022.113191

[219] A.I. Becerro, A. Escudero, *Revision of the crystallographic data of polymorphic* $Y_2Si_2O_7$ *and* Y_2SiO_5 *compounds*, Phase Transitions 77 (2004), pp. 1093–1102. DOI: 10.1080/01411590412331282814

[220] Z. Sun, Y. Zhou, M. Li, *Effect of* $LiYO_2$ *on the synthesis and pressureless sintering of* Y_2SiO_5, J. Mater. Res. 23 (2008), pp. 732–736. DOI: 10.1557/jmr.2008.0085

[221] E.L. Cates, A.P. Wilkinson, J.H. Kim. *Visible-to-UVC upconversion efficiency and mechanisms of* $Lu_7O_6F_9:Pr^{3+}$ *and* $Y_2SiO_5:Pr^{3+}$ *ceramics*. J. Lumin. 160 (2015), pp. 202–209. DOI: 10.1016/j.jlumin.2014.11.049.

[222] M.E. Fleet, X. Liu, *Rare earth disilicates* $R_2Si_2O_7$ *(R = Gd, Tb, Dy, Ho): type B,* Zeitschrift für Kristallographie 218(12) (2003), pp. 795–801. DOI: 10.1524/zkri.218.12.795.20550

[223] M.E. Fleet, X. Liu, *Structure and complex twinning of dysprosium disilicate* ($Dy_2Si_2O_7$)*, Type B*, Acta Crystallogr. B56 (2000), pp. 940–946. DOI: 10.1107/S0108768100008545

[224] H. Van Acker, P. Van Dijck, T. Coenye, *Molecular mechanisms of antimicrobial tolerance and resistance in bacterial and fungal biofilms*, Trends Microbiol. 22(6) (2014), pp. 326–333. DOI: 10.1016/j.tim.2014.02.001

[225] R. Roy, M. Tiwari, G. Donelli, V. Tiwari, *Strategies for combating bacterial biofilms: A focus on anti-biofilm agents and their mechanisms of action*, Virulence 9(1) (2018), pp. 522–554. DOI: 10.1080/21505594.2017.1313372

[226] H. Wu, C. Moser, H.Z. Wang, N. Høiby, Z.J. Song, *Strategies for combating bacterial biofilm infections*, Int. J. Oral Sci. 7 (2015), pp. 1–7. DOI: 10.1038/ijos.2014.65

[227] R.M. Donlan, J.W. Costerton, *Biofilms: Survival mechanisms of clinically relevant microorganisms*, Clin. Microbiol. Rev. 15(2) (2002), pp. 167–193. DOI: 10.1128/CMR.15.2.167-193.2002

List of figures

List of tables

Appendix

Peer-review research papers included in the doctoral dissertation

1. **P. Fałat**, A. Chwirot, P. Kuich, M. Nyk, Tymish Y. Ohulchanskyy, B. Bażanów, D. Wawrzyńczyk*, VIS-to-UVC Upconversion of* *Pr^{3+}* *Doped Fluoride Nano- and Microcrystals for Inactivation of Human Viruses.* Rare Metals 44, 2025, pp. 4881–4897. DOI: 10.1007/s12598-025-03317-8
2. **P. Fałat,** P. Kuich, M.Y. Tsang, S.J. Zelewski, B. Cichy, M. Samoć, M. Nyk, D. Wawrzyńczyk. *The lanthanide doped* *$NaYF_4$* *nanoparticles core@multi-shell synthetic strategy for up-conversion emission in divergent spectral regions.* Journal of Luminescence 266, 2024, article no. 120284. DOI: 10.1016/j.jlumin.2023.120284
3. **P. Fałat**, M.Y. Tsang, I. Maliszewska, S.J. Zelewski, B. Cichy, T.Y. Ohulchanskyy, M. Samoć, M. Nyk, D. Wawrzyńczyk. *Enhanced biocidal activity of* *Pr^{3+}* *doped yttrium silicates by* *Tm^{3+}* *and* *Yb^{3+}* *co-doping*. Materials Advances 4(22), 2023, pp. 5827-5837. DOI: 10.1039/D3MA00451A
4. M.Y. Tsang, **P. Fałat**, M.A. Antoniak, R. Ziniuk, S.J. Zelewski, M. Samoć, M. Nyk, J. Qu, T.Y. Ohulchanskyy, D. Wawrzyńczyk. *Pr^{3+}**-doped* *$NaYF_4$* *and* *$LiYF_4$* *nanocrystals combining Visible-to-UVC upconversion and NIR-to-NIR-II downconversion luminescence emissions for biomedical applications*. Nanoscale 14(39), 2022, pp. 14770-14778. DOI: 10.1039/D2NR01680J

Peer-review research papers not included in the doctoral dissertation

1. O. Pavlosiuk O., **P. Fałat**, D. Kaczorowski, P. Wiśniewski. *Anomalous Hall effect and negative longitudinal magnetoresistance in half-Heusler topological semimetal candidates TbPtBi and HoPtBi*. APL Materials 8, 2020, article no. 111107. DOI: 10.1063/5.0026956

Conference contributions

1. **P. Fałat**, A. Meijerink, D. Wawrzyńczyk. *Spectroscopic characterization of* *$NaYF_4$**:* *Tm^{3+}/Pr^{3+}* *MCs showing concurrent emission in UV and NIR spectral ranges*. 2nd International Conference on Advanced Materials for Bio-Related Applications, 19.-23.05.2024, Wrocław, Poland ***(oral presentation).***

2. **P. Fałat**, M. Nyk, D. Wawrzyńczyk. *The* *Tm^{3+}* *ions heavy doping effect on Vis-to-UV up-conversion emission of* *Pr^{3+}**-based* *β**-*$NaYF_4$* *and* *$LiYF_4$* *NPs*. 20th International Conference on Luminescence, 27.08.-01.09.2023, Paris, France ***(poster presentation).***

3. **P. Fałat,** M. Nyk, D. Wawrzyńczyk. *Diverse synthetic strategies towards enhanced VIS-to-UV and NIR-to-UV up-conversion performance of lanthanide-doped nanomaterials.* Gordon Research Conference - Upconverting and Related Light-Conversion Materials Aimed at Biomedical, Energy and Quantum Applications, 18.-23.06.2023, Waterville Valley, NH, USA ***(poster presentation).***

4. **P. Fałat**, M.Y. Tsang, S. Zelewski, D. Wawrzyńczyk, M. Nyk. *Lanthanide-doped core-shell nanostructures with enhanced VIS-to-UVC upconverted emission for biomedical applications.* SHIFT 2022 – Spectral sHaping For biomedical and energy applicaTions. 10.-14.10.2022, Tenerife, Canary Island, Spain ***(poster presentation).***

5. **P. Fałat**, M.Y. Tsang, S.J. Zelewski, D. Wawrzyńczyk, M. Nyk. *Various routes for VIS-to-UVC upconverted emission enhancement in lanthanide-doped nano-particles.*18-22.07.2022. 5th International Conference on Application of Optics and Photonics, Guimarães, Portugal ***(oral presentation).***

6. **P. Fałat**, M.Y. Tsang, S.J. Zelewski, E. Wanarska, D. Wawrzyńczyk, I. Maliszewska, M. Nyk. *Improved germicidal performance of Visible-to-UVA/UVC upconversion in lanthanide doped oxyorthosilicates.* PhoBiA Annual Nanophotonics International Conference 2022 - Summer School (PANIC Summer School 2022), 30.05.-03.06.2022, Wrocław, Poland ***(oral presentation).***

7. **P. Fałat**, M.Y. Tsang, S.J. Zelewski, E. Wanarska, D. Wawrzyńczyk, I. Maliszewska, M. Nyk. *Antimicrobial effect of UVC radiation generated via upconversion in lanthanide doped* Y_2SiO_5 *phosphors.* 1st International Conference on Advanced Materials for Bio-Related Applications, 16.-19.05.2022, Wrocław, Poland ***(poster presentation).***

8. **P. Fałat**, M.Y. Tsang, S.J. Zelewski, E. Wanarska, D. Wawrzyńczyk, I. Maliszewska, M. Nyk. *The upconversion generated UV-C radiation in lanthanide ions bearing orthosilicates for light triggered antibacterial treatment.* 5th International Symposium on Nanoparticles, Nanomaterials and Applications (ISN^{2}A,) 24.-27.01.2022, Caparica, Portugal ***(oral presentation).***

9. **P. Fałat**, M.Y. Tsang, S.J. Zelewski, D. Wawrzyńczyk, M. Nyk. *Enhanced emission intensity in lanthanide-based materials co-doped with* Li^+ *ions.* 19th International Conference on Luminescence (ICL2020), 26-30.07.2021, hybrid conference: online/Chanchung, China ***(poster presentation).***

10. **P. Fałat**, M.Y. Tsang, S.J. Zelewski, D. Wawrzyńczyk, M. Nyk. *Emission intensity enhancement of lanthanide-based materials co-doped with* Li^+ *ions.* 15th International Conference on Materials Chemistry (MC15), 12.-15.07.2021, an online event ***(poster presentation).***

11. **P. Fałat,** M.Y. Tsang, S.J. Zelewski, D. Wawrzyńczyk, M. Nyk. *Stokes and anti-Stokes emission enhancement in Y_2SiO_5:Pr ceramics co-doped with Li^+ ions.* |PhoBiA Annual Nanophotonics International Conference 2021 (PANIC 2021), 26.-28.05.2021, an online event ***(oral presentation).***

Awards

03/2025	Nomination for the participation as Young Researcher in *74th Lindau Nobel Prize Meeting in Chemistry* in Lindau, Germany
04/2024	Financial support for the long-term internship at TU Dresden & Fraunhofer IFAM within the *Research Grants – One-Year Grants for Doctoral Candidates* project, funded by German Academic Exchange Service (DAAD)
06/2023	Financial support for the 3-month research stay at Utrecht University, the Netherlands, within *InterDocSchool* project, funded by Polish National Agency of Academic Exchange (NAWA)
06/2021	Financial support from International Centre for Diffraction Data (ICDD) for participation in the Workshop on Total Scattering for Nanotechnology To.Sc.Al'And held in Granada, Spain (20.-24.09.2021)

Accepted research grants proposals

12/2024	National Science Centre PRELUDIUM 23 research grant *POLY-LLAMA: Functional POLYmeric surfaces for Light-triggered LAnthanide-doped-Materials-Aided disinfection* Role in the project: Principal Investigator Project budget: 209 999 PLN Planned project duration: 36 months Planned project start: 01.10.2025

Participation in research projects

10/2020 – 09/2023	**Wroclaw University of Science and Technology**: Polish-Chinese joint research project SHENG: *Concurrent Photon Upconversion and Cutting in Lanthanide Doped Nanoparticles for Biomedical* Applications, funded by National Science Centre of Poland (grant no. 2018/30/Q/ST5/00634 Principal Investigator: Dominika M. Wawrzyńczyk, DSc, PhD, Eng Role in the project: PhD candidate – scholarship holder

Research stays abroad

10/2024 – 09/2025
(ongoing)

Chair of Materials Science and Nanotechnology, Technical University Dresden, Germany & Fraunhofer Institute for Manufacturing Technology and Advanced Materials Dresden, Germany
Supervisors:
Prof. Gianaurelio Cuniberti & Dr.-Ing. Nadine Eißmann
The long-term internship has been fully funded within the framework of the program *Research Grants – One-Year Grants for Doctoral Candidates*, granted by German Academic Exchange Service (Deutscher Akademischer Austauschdienst, DAAD) after the successful application in the call in November 2023.

09/2023 – 12/2023

Condensed Matter & Interfaces Group, Utrecht University, the Netherlands
Supervisor: Prof. Andries Meijerink
The short-term research stay was fully funded within the framework of *Task 2. Foreign mobility of WUST doctoral students* of *InterDocSchool* project, granted by Polish National Agency of Academic Exchange (NAWA) to Doctoral School of Wrocław University of Science and Technology. The research stay was granted after the successful application in May 2023.

07/2023

Condensed Matter & Interfaces Group, Utrecht University, the Netherlands
Supervisor: Prof. Andries Meijerink
The short-term research stay was fully funded within the SHENG project *Concurrent Photon Upconversion and Cutting in Lanthanide Doped Nanoparticles for Biomedical Applications*, funded by National Science Centre of Poland (*vide supra*).